Observation of the Top Quark in Proton-Antiproton Collisions at a Center of Mass Energy of 1.8 TeV

by

Douglas Andrew Glenzinski

A dissertation submitted to The Johns Hopkins University
under the guidance of Professor Bruce A. Barnett and
in conformity with the requirements for the degree of
Doctor of Philosophy

Baltimore, Maryland
November, 1995

Abstract

We report on the search for top quark production in $\overline{p}p$ collisions at $\sqrt{s} =$ 1.8 TeV using the CDF detector at the Fermilab TeVatron. We assume Standard Model couplings and search for an excess of events consistent with the decay $t\bar{t} \rightarrow W^+bW^-\bar{b}$. We utilize the excellent resolution of the SVX silicon vertex detector to identify the presence of b quarks via their secondary displaced vertex. We observe 32 candidate events in which 40 jets are identified as b-quark-jets. The background is estimated to be 10.0 ± 2.8 tagged jets. The probability that a background fluctuation can account for the observed excess is 2.8×10^{-6}, which corresponds to 4.5σ on a Gaussian distribution. These data firmly establish the existence of the top quark.

We use a kinematic fitting procedure to directly determine the top quark mass. We measure $M_t = 175 \pm 11$ GeV/c^2. Assuming the measured mass we calculate the $t\bar{t}$ production cross section to be $\sigma_{t\bar{t}} = 6.2 \pm 1.9$ pb. Both the measured mass and the cross section are consistent with Standard Model expectations.

Acknowledgements

Finally, at long last, that page, that single page which is all mine. That one page on which I am allowed to wax lyrical about anything in any manner I'd like. That one page that shall escape being analyzed and criticized for every detail down to the last comma, the last period. And I can say quite truthfully that with this one exceptional page I'd feel quite impudent if I used it any way other than to acknowledge and thank the many, many people who helped me.

There are, literally, hundreds of people to whom I am thankful, of which the ommission of any is a regretful oversight. But I've only one page, and so I begin with these people, the ommission of whom would be a brutish oversight. First, I am very grateful to my advisor, Bruce, without whose support I'd still be grading lab reports in the basement of Bloomberg. I hope he enjoyed having me as a student as much as I enjoyed having him as an advisor. Second, I must thank Rick. I am profoundly grateful for his patience, encouragement and impressively thorough knowledge of a wide range of physics topics, about every one of which I attempted to pester him with questions. Third, I must thank Joe. I am extremely grateful for his trusting me with so much responsibility — I flatter myself by thinking that this had only a little to do with the accute shortage of help with which we were always faced. I hope that I have learned at least some small portion of those things I most admire in them... thoroughness, diligence, and creativity.

I am additionally grateful to all those people of the CDF collaboration. There are 1000s of man-years invested in that detector and it was a real privelege to be able to work with this vast collection of expertise. One of the distinct advantages of working in such a large collaboration is the chance to learn from these experts, all of whom were patient enough to teach those who asked. In particular, the people of the SVX′ group. I am exceedingly grateful to you all. I enjoyed every minute of our designing, building, installing, commissioning, and (finally) analyzing the data of the SVX′ detector. I am also grateful to the people of the Electroweak and

Top Working Groups, who patiently listened to and thoughtfully questioned my analyses. And I thank all those who helped me to find gainful employment upon finishing this tome... especially Bill, Henry, Paul, and finally John, to whom I am especially grateful for having helped me put together a respectable talk.

Beyond the world of physics, I am very grateful to my parents, who instilled in me a confidence and determination in all my endeavors, and to the rest of my family — Jane, Jeff, and my grandparents — all of whom were nothing but supportive in this endeavor. Thank you very very much. And I am more than thankful for Margaret — whose love and friendship I don't think I could have done without. All of you helped me to forget about physics when it was good to do so, and were astoundingly understanding when I saw fit to work through most all hours of the day. Again, I thank you.

A special thanks is in order for Mrs. Dufrain, my 7th grade science teacher, who so impressed upon me the fun of science that I've continued to study it for the last 15 years.

Finally, there's a long list of people with whom I drank, laughed (not necessarily in that order), played ultimate, soccer, and basketball, and generally just let off steam. I thank each of them. They know who they are.

Contents

1 Introduction **1**

1.1 **Standard Model** 1

1.2 **Top Quark Production at the TeVatron** 7

1.3 **Search Strategy** 11

1.4 **Dissertation Outline** 16

2 Experimental Apparatus **17**

2.1 **The Fermilab TeVatron** 17

2.2 **Run 1A and Run 1B** 21

2.3 **The Collider Detector at Fermilab** 22

3 Analysis **34**

3.1 **Sample Selection** 34

3.1.1 **Identification of the Primary Event Vertex** 35

3.1.2 **Muon Selection** 36

3.1.3 **Electron Selection** 36

3.1.4 **Final Event Selection** 38

3.1.5 **Control Samples** 41

3.1.6 **Monte Carlo Samples** 45

3.2 **Development the SVX B-tag Algorithm** 48

3.2.1 **Generator Level Study of B Hadron Decay in Top Quark Events** 49

3.2.2 Monte Carlo Simulation of the SVX′ Detector 70
3.3 Algorithm Optimization 100
3.3.1 Track Selection Studies 100
3.3.2 Final Algorithm Optimization 104
3.4 Algorithm Performance in Control Samples 108
3.5 Acceptance for a Standard Model Top Quark 115
3.5.1 Determination of $A_{t\bar{t}}$ 115
3.5.2 Determination of ϵ_{trig} and $\epsilon_{lepton\ id}$ 116
3.5.3 Determination of $\epsilon_{|z_{pvtx}|}$ 118
3.5.4 Determination of ϵ_{tag} 120
3.6 Results 142
3.7 Background Estimate 143
3.7.1 Estimate of the $Wb\bar{b}$, $Wc\bar{c}$, and Wc Contributions . . . 144
3.7.2 Estimate of Mistag Contribution 148
3.7.3 Estimate of F_{non-W} Contribution 151
3.7.4 Estimate of WW, WZ and $Z \to \tau\tau$ Contributions . . . 152
3.7.5 Additional Checks of Background Estimate 159
3.7.6 Significance of Observed Excess 162
3.8 Kinematic Distributions of Candidate Events 166
3.9 Cross Section Measurement 176
3.10 Direct Determination of the Top Quark Mass 179
3.11 Conclusion 191

List of Figures

1.1 Feynman diagrams of interactions mediated by the (a) weak force, (b) the electromagnetic force, and (c) the strong force. 3

1.2 A picture of a CDF two jet event. 6

1.3 Pictorial representation of a $\overline{p}p$ interaction as understood in the parton model. 8

1.4 The relative contribution to the total NLO $t\overline{t}$ production cross section at the Fermilab TeVatron for the processes $gg \rightarrow t\overline{t}$ and $q\overline{q} \rightarrow t\overline{t}$ as a function of top mass. 10

1.5 Tree level diagram for $t\overline{t}$ production from $q\overline{q}$ annihilation. 12

1.6 Tree level diagram for dominant background process in the search for $t\overline{t}$ production at the Fermilab TeVatron. 14

1.7 Schematic of an SVX B-tag. 15

2.1 Layout of the Fermilab TeVatron Accelerator Complex. 19

2.2 A flow chart describing each of the steps involved in accelerating protons to 900 GeV at the Fermilab TeVatron. 20

2.3 A cross-sectional view of the CDF detector from the side. 23

2.4 Transverse view of the CTC endplate. 26

2.5 An isometric projection of a single SVX barrel. 27

2.6 An SVX ladder used in barrel construction. Each barrel is made up of 48 ladders—12 ladders per layer over 4 layers. 28

2.7 The (biased) residual distribution for the SVX′ detector. 29

2.8 Schematic of a single CDF central calorimeter wedge. 30

3.1 Transverse mass distribution for W + ≥ 1 jet sample after all selection cuts for the electron and muon samples separately. 42

3.2 Invariant mass distribution for $Z \to ee$ and $Z \to \mu\mu$ events selected as discussed in Section 3.1.5. 46

3.3 Schematic of an SVX B-tag. 50

3.4 Properties of B jets in heavy top quark decay (M_{top} = 160 GeV/c^2). 51

3.5 The distance between a given track and the B jet axis in $\eta - \phi$ space. 54

3.6 The P_T distribution for tracks in B-jets from top quark decay. . . . 55

3.7 The impact parameter, d_0, distribution for tracks in B-jets from top quark decay. 56

3.8 The impact parameter significance, $S_{d_0} = d_0/\sigma_{d_0}$, distribution for tracks in Bjets from top quark decay. 57

3.9 A schematic showing the merging, or "sharing", of clusters. 59

3.10 The minimum separation in $\Delta r\phi$ at the innermost layer of the SVX (L0) for tracks in B-jets from top quark decay. 60

3.11 The minimum separation in $\Delta r\phi$ at the outermost layer of the SVX (L3). 61

3.12 The integrated and differential distributions of the minimum road size, centered on a given track, required to include four (a), three (b), and two (c) hits from some other track(s). 62

3.13 The integral and differential P_T distributions for the three highest P_T tracks. 64

3.14 The integral and differential S_{d_0} distributions for the three most significantly displaced tracks. 65

3.15 The differential and integral S_{d_0} distributions for the three highest P_T tracks. 66

3.16 The differential and integral P_T distributions for the three most significantly displaced tracks. 67

3.17 Schematic of a charged particle passing through one layer of the SVX. 72

3.18 The total cluster charge, Q_{TOT}, corrected for the track pathlength through the silicon for shared and unshared clusters. 74

3.19 The total cluster length and cluster charge distribution for isolated tracks. 75

3.20 Core charge distributions for clusters where one core strip (top) or both core strips (bottom) are included in the cluster and where additional strips are absent (left) or present (right). The histograms are the data and the smooth curves are fits. 77

3.21 Top plot: Charge on core strip nearest the track intersection point when there are no adjacent additional strips (dotted) and when adjacent strips are present (points). Bottom plot: Charge on core strip farthest from track intersection point when there are no adjacent additional strips (dotted) and when adjacent strips are present (points). 79

3.22 Top plot: Charge on core strip farthest from the track intersection point when there are additional strips adjacent to the *other* core strip (points) and when no additional strips are present (dotted). Bottom plot: Charge on core strip nearest the track intersection point when there are additional strips adjacent to the *other* core strip (points) and when no adjacent strips are present (dotted). 80

3.23 Probability for having only one core strip in a cluster as a function of the track's intersection point between the core strips for three different ranges of core charge. 82

3.24 Clockwise from the upper left: The total core charge, Q_{core}, distribution and the fraction of that charge deposited on the left core strips, F_L, as a function of the track intersection point, x_{int}, measured relative to the left core strip, for different ranges Q_{core}. The F_L profile distribution of the upper right plot is reproduced in the bottom plot (dotted) for comparison. 83

3.25 The multiplicity of additional strips to the right (solid) and left (dotted) of the core strips. 85

3.26 The number of additional strips to the right of the core cluster, N_R, versus the number of additional strips to the left, N_L. 87

3.27 The mean number of additional strips to the right (left) of the core strips, $N_{R/L}$, for all clusters, as a function of the charge deposited on the right (left) core strip, $Q_{R/L}$. 88

3.28 The mean number of additional strips, for all clusters *with at least one additional strip*, as a function of the charge deposited on the nearest core strip. 89

3.29 Charge distribution for the first additional strip when *only* one additional strip is present (top) and when there are *more than* one additional strips present (bottom) for data (solid) and MC (dotted). . . 90

3.30 Core charge distributions ($Q_{core} = Q_L + Q_R$) for clusters with no additional strips, $N_{strip} \leq 2$ (top), and for all clusters (bottom) for data (solid) and MC (dotted). 93

3.31 Charge distribution of core strip ($Q_{R/L}$) adjacent to additional strips when additional strips are present ($N_{R/L} > 0$) for data (solid) and MC (dotted). 94

3.32 Fraction of core charge deposited on the left core strip as a function of Δx_{int}, measured from the center of that strip. Data (solid) and MC (dotted) distributions are compared for clusters with $Q_{core} < 150$ ADC (a) and with $Q_{core} \geq 150$ ADC (b). The error bars represent the RMS of the F_L distribution in each bin. 95

3.33 The multipliciy of additional strips, N_{add}, averaged over the right and left sides, for data (solid) and MC (dotted). 97

3.34 Charge distributions (in ADC counts) for the second through fifth additional strips, when present, for data (solid) and MC (dotted). . 98

3.35 Distribution of the number of strips included in a cluster (ie. cluster length) for a variety of incidence angles in the $r - \phi$ plane for data (dashed) and MC (solid). 99

3.36 The optimization criteria, S^2/B, as a function of 24 sets of track selection cuts. 105

3.37 The optimization criteria, S^2/B, as a function of 27 sets of various track and vertex selection cuts. 107

3.38 A comparison of the discovery potential for three sets of B-tag algorithm cuts. 109

3.39 A flow chart of the final B-tag algorithm. The relevant cuts are given in Figure 3.40. 110

3.40 The list of cuts used in the final B-tag algorithm. A flow chart of the algorithm is given in Figure 3.39. 111

3.41 The $psuedo - c\tau$ distribution for tagged electron jets in data and Monte Carlo. 113

3.42 The $c\tau_{eff}$ distribution for a sample of generic jets collected with the 50 GeV trigger threshold. We fit the distribution to a combination of heavy flavor tags and background tags. 114

3.43 The efficiency of the isolation cut, $I_{cal} < 0.1$, as a function of the instantaneous luminosity in the event. 117

3.44 The CMUP trigger efficiency as a function of the muon isolation, I_{cal} and the number of jets in the event. 119

3.45 The z_{pvtx} distribution for all run 1B data. 121

3.46 The $\epsilon_{|z_{pvtx}|}$ as a function of the total integrated luminosity and the number of jets in the event. 122

3.47 The $e-\mu$ invariant mass distribution for all electron jets with an away side tag required. The data points include a background subtraction. 127

3.48 The B-tag efficiency, as determined using the two methods described in Section 3.5.4, is plotted versus the E_T^{ejet} (top). The weighted average scale factor as a function of E_T^{ejet} is also plotted (bottom). . . 130

3.49 A comparison between tags in electron jets with an away tag required (points) and $b\overline{b}$ Monte Carlo (histogram) for various kinematic properties of the tracks included in the secondary vertex tag. 132

3.50 A comparison between tags in away jets (points) and $b\overline{b}$ Monte Carlo (histogram) for various kinematic properties of the tracks included in the secondary vertex tag. 133

3.51 The fraction of taggable electron jets (with an away tag required) as a function of the total integrated luminosity. 134

3.52 The double tag rate is plotted as a function of the instantaneous luminosity (top) and the total integrated luminosity (bottom). . . . 136

3.53 The estimated fraction of pre-tagged electron jets that are B-jets, F_B, as a function of the instantaneous luminosity (top) and the total integrated luminosity (bottom). 137

3.54 The excess tagging rate, XS_{ejet}, is plotted as a function of the instantaneous luminosity (top) and the total integrated luminosity (bottom). 138

3.55 The excess tagging rate for a run 1A B-enriched sample as a function of run number. 140

3.56 Tree level diagram of a generic multijet event. A heavy flavor quark pair results from a gluon splitting to a $b\bar{b}$ or $c\bar{c}$ pair. 146

3.57 We compare the heavy flavor tagging rate (per event) observed in data and measured in a HERWIG Monte Carlo sample of generic jets. 147

3.58 Tree level diagram for Wc production. This is dominated by the process $sg \to Wc$, with a $\sim 10\%$ contribution from $dg \to Wc$. . . . 149

3.59 Regions used to determine the fraction of events in the signal region (D) due to non-W sources, such as $b\bar{b}$ 155

3.60 B-tagging results using 100 pb^{-1} of data. The $W+ \leq 2$ jets bins are expected to have a very small $t\bar{t}$ contribution. The $W+ \geq 3$ jets bins are our search region, where Standard Model $t\bar{t}$ production might significantly contribute. 158

3.61 The distributions are (A) the total number of tags from 100 million Monte Carlo background experiments, (B) the total number of double tags from all experiments, and (C) the total number of double tags in experiments with at least 40 tags total. The arrows indicate where our data lie. 167

3.62 Flow chart describing the iteration procedure used to correct the background estimate of Section 3.7 for a $t\bar{t}$ contributions. The procedure yields that $80 \pm 7\%$ ($75 \pm 7\%$) of the tagged jets (events) are from $t\bar{t}$ production. 168

3.63 The solid histogram is the $c\tau$ of tagged jets in the signal region for a $t\bar{t}$ + background Monte Carlo. The points are the data. The two distributions are normalized to the same number of events. The hatched histogram is the background shape normalized to its relative contribution. 171

3.64 The solid histogram is the E_T of tagged jets in the signal region for a $t\bar{t}$ + background Monte Carlo. The points are the data. The two distributions are normalized to the same number of events. The hatched histogram is the background shape normalized to its relative contribution. 172

3.65 The solid histogram is the number of tracks included in the vertex for tagged jets in the signal region for a $t\bar{t}$ + background Monte Carlo. The points are the data. The two distributions are normalized to the same number of events. The hatched histogram is the background shape normalized to its relative contribution. 173

3.66 The histogram is the transverse mass distribution of the lepton and neutrino (whose momentum is estimated using the missing E_T vector) for a $t\bar{t}$ Monte Carlo. The points are the data. The two distributions are normalized to the same number of events. The last bin includes overflows. 174

3.67 The solid histogram is the **H** distribution $\left(= \Sigma E_T^* + \not\!\!E_T + P_T^{lep}\right)$ for tagged events in the signal region for a $t\bar{t}$ + background Monte Carlo. The open points are the pre-tagged data and the solid points are the tagged data. The two tagged distributions are normalized to the same number of events. The hatched histogram is the background shape normalized to its relative contribution. 175

3.68 Total $t\bar{t}$ production cross section for $\overline{p}p$ collisions at $\sqrt{s} = 1.8$ TeV as a function of top mass as measured (points) and calculated in Reference [29] (solid curve). Estimates of the theoretical uncertainty are given as dashed lines. 177

3.69 Jet energy balancing after the application of jet energy corrections. 183

3.70 The resulting M_t distribution from a Monte Carlo sample generated assuming a top mass of 170 GeV/c^2 using the standard jet corrections (top) and additionally including those jet corrections specific to top decay (bottom). 184

3.71 The resulting reconstructed M_t distribution using the fitting procedure described in the text on a Monte Carlo sample of $t\bar{t}$ events passing all the event selection criteria. 185

3.72 The resulting reconstucted mass distribution for a $W+$ multijet Monte Carlo sample. This is used as the background shape in the fitting procedure described in the text. 186

3.73 The resulting mass distribution of the B-tagged $W + 4$ jet events assuming the $t\bar{t}$ hypothesis. 188

3.74 The total $t\bar{t}$ production cross section, $\sigma_{t\bar{t}}$, evaluated at the measured value of the top quark mass, $M_t = 175 \pm 6 \pm 9$ GeV/c^2 (point) and theory curve of Reference [29] (solid curve). Estimates of the theoretical uncertainties are drawn as dashed lines. 190

List of Tables

1.1 The elementary forces postulated by the Standard Model. 2

1.2 The elementary particles postulated by the Standard Model. 4

1.3 Branching ratios for the various $t\bar{t}$ decay modes assuming Standard Model Couplings. 13

2.1 Comparison of SVX and SVX′ 33

3.1 Cuts used to select the high P_T, inclusive central muon sample. . . 37

3.2 Cuts used to select the high P_T, inclusive central electron sample. . 39

3.3 The event yields after application of all selection criteria. 43

3.4 Cuts used to select a B-enriched sample for measuring efficiency of Btag algorithm. 44

3.5 Summary of B jet decay properties (mean values) from the various Monte Carlo conditions for $t\bar{t}$ events (M_{top} = 160 GeV/c^2). Our default configuration is given in the first column. 53

3.6 The acceptance as a function of P_T and S_{d_0} cuts for B jets in $t\bar{t}$ events (M_{top} = 160 GeV/c^2), per B jet. 63

3.7 Breakdown of tracks according to the number of SVX hits associated with the track. 102

3.8 Results of optimizing pointback probability using the criteria S^2/B and subject to constraints on the efficiency. 103

3.9 Combined geometric and kinematic acceptances for $t\bar{t}$ events at various assumed top quark masses, M_t. 118

3.10 The trigger and lepton identification efficiencies as measured using $Z \to \ell\ell$ ($\ell = e$ or μ) events. The errors are statistical only. 120

3.11 The fraction of $t\bar{t}$ events passing all event selection criteria with at least one tagged B-jet. All uncertainties include statistical and systematic errors added in quadrature. 141

3.12 The total $t\bar{t}$ event detection efficiency. All uncertainties include statistical and systematic errors added in quadrature. 141

3.13 B-tagging results using 100 pb^{-1} of data. 142

3.14 Summary of numbers used in estimating the $W+$ heavy flavor background contribution as a function of jet multiplicity. 150

3.15 The parameters and binning used to parameterize the mistag rate. . 150

3.16 Comparison of the number of observed negative tags to the number predicted using the mistag parametrization in a variety of control samples. 152

3.17 A comparison between the number of negative tags observed, N_{-tag}^{obs}, and predicted, N_{-tag}^{pred}, as a function of several variables not used in the mistag parametrization. 153

3.18 The fraction of non-W, F_{non-W}, events passing all event selection criteria as a function of jet multiplicity. The errors are statistical only. 154

3.19 The total event acceptances and per event tagging efficiencies used to estimate the WW, WZ, and $Z \to \tau\tau$ background contributions. 154

3.20 The expected number of tagged *jets* for each background source. Estimates and observations based on 100 pb^{-1} of CDF data. 157

3.21 B-tagging results from a $Z+$ multijet sample using 100 pb^{-1} of CDF data. 162

3.22 The input parameters used to calculate the per event tagging efficiencies expressed in equation 3.21. The errors are statistical only. . . . 165

3.23 We compare the per event tagging efficiencies yielded from the "first principles" calculation to those observed directly from the Monte Carlo. 165

3.24 The total $t\bar{t}$ production cross section, $\sigma_{t\bar{t}}$, as a function of top quark mass, M_t, for $\overline{p}p$ collisions at $\sqrt{s} = 1.8$ TeV. 178

3.25 Number of events surviving various cuts used to isolate a sample from which to directly determine the top quark mass. 180

3.26 Systematic uncertainties investigated in direct determination of top quark mass using B-tagged $W+ \geq 4$ jet data. 189

Chapter 1

Introduction

Over the past two decades the Standard Model (SM) has enjoyed outstanding success [1] - [5]. It is arguably one of the most comprehensive and predictive scientific theories ever postulated. Elementary particle physicists use the SM to describe the elementary constituents of matter (ie. those particles out of which all other matter is made) and the forces with which those constituents interact. The Standard Model is described in considerable detail elsewhere [6] [7] [8]. Below, we include a brief description of those aspects salient to this work.

1.1 Standard Model

The Standard Model postulates two types of elementary constituent matter, *leptons* and *quarks*, which interact through the four forces known as the **strong**, **electromagnetic**, **weak**, and **gravitational** forces. Each force, in turn, is "mediated", or carried, by a particle known as a *boson*. The strong, electromagnetic, weak, and gravitational forces are mediated by a gluon (g), photon (γ), intermediate vector boson ($W^{\pm}$ or Z^0), and graviton, respectively. The strength of each force is characterized by a coupling constant, α_i, where the subscript, i, denotes the particular force with which the coupling constant is associated. Table 1.1 lists the four elementary forces and their associated mediating boson(s) and coupling constants. For

force	**boson**	**coupling constant**
strong	gluons (g)	$\alpha_S = \begin{cases} \approx 1, \text{for large distances} \\ < 1, \text{for small distances} \end{cases}$
electromagnetic	photon (γ)	$\alpha = \frac{1}{137}$
weak	intermediate bosons ($W^{\pm}$, Z^0)	$\alpha_W = 10^{-5}$
gravitational	graviton	$\alpha_G = 10^{-38}$

Table 1.1: The elementary forces postulated by the Standard Model.

the physics discussed here, the gravitational force is too weak to play an important role, and so is discussed no further. An example of a process mediated by each of the weak, electromagnetic, and strong forces is given in Figure 1.1.

All observable matter in the universe is composed of the elementary particles known, in the SM, as leptons and quarks. The most commonly known lepton (ℓ) is the electron (e). There also exist leptons known as the *muon* (μ) [9] and the *tau* (τ) [10]. The electron, muon, and tau all carry integral electric charges, $-1\,|e|$ and are spin $\frac{1}{2}\hbar$ particles obeying Fermi-Dirac statistics. Each of these has an electrically neutral partner particle known as a neutrino (ν_e, ν_μ, or ν_τ) [11]. Table 1.2 lists the three lepton "families". The e, μ, and τ participate in interactions involving the electromagnetic and weak forces, while neutrino interactions are mediated by only the weak force. Each lepton has an anti-particle of equal mass but opposite charge.

Analogously, the SM postulates 3 families of quarks (q). These are shown in Table 1.2. The existence of the down (d), up (u), strange (s), charm (c), and

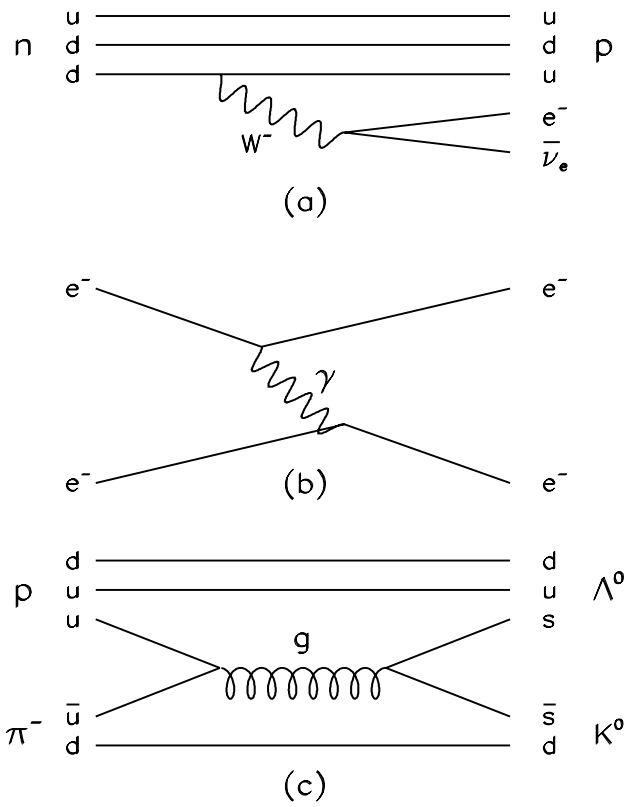

Figure 1.1: Feynman diagrams of interactions mediated by the (a) weak force, (b) the electromagnetic force, and (c) the strong force.

$$\begin{pmatrix} e \\ \nu_e \end{pmatrix} \qquad \begin{pmatrix} \mu \\ \nu_\mu \end{pmatrix} \qquad \begin{pmatrix} \tau \\ \nu_\tau \end{pmatrix}$$

The 3 lepton families of the Standard Model

$$\begin{pmatrix} \text{up} \\ \text{down} \end{pmatrix} \quad \begin{pmatrix} \text{charm} \\ \text{strange} \end{pmatrix} \quad \begin{pmatrix} \text{top} \\ \text{bottom} \end{pmatrix}$$

The 3 quark families of the Standard Model

Table 1.2: The elementary particles postulated by the Standard Model.

bottom (b) quarks has been experimentally verified [12] - [15]. The existence of the top quark (t) has not previously been experimentally verified and is the subject of this work. Quarks have fractional electric charge, $+\frac{2}{3}|e|$ for the u and c, and $-\frac{1}{3}|e|$ for the d, s, and b, and are spin $\frac{1}{2}\hbar$ particles obeying Fermi-Dirac statistics. Quarks also have a "color charge", the strong force analog to the electric charge of the electromagnetic force. There are three color charges somewhat whimsically called "red", "green", and "blue"*. Quarks participate in interactions involving the strong, electromagnetic, and weak forces. Each quark has an anti-particle ($\overline{\text{q}}$) of equal mass but opposite charge.

Through the strong interaction, quarks form bound states known as *hadrons*, which are categorized according to whether they are triple-quark bound states (qqq), known as *baryons*, or quark-anti-quark bound states ($\text{q}\overline{\text{q}}$), known as *mesons*. The most familiar baryons are the proton and neutron, which are composed of the triple-

*Note that there is *one* electric charge, called "minus" (-), which has an anticharge, "plus" (+).

quark bound states, uud and udd, repectively.

It is important to note that the mediating bosons of the strong force, gluons, also carry color charge. This is in contrast to photons, which mediate the electromagnetic force, but do not carry an electric charge. This has the important consequence that gluons can interact directly *with themselves.* This difference between the photon and the gluon accounts for the differences in the behavior (for lack of a better word) of the electromagnetic and strong forces.

The electromagetic-interaction potential is of the form $-\alpha/r$. Thus, it decreases as the participating particles move farther apart — as r get larger, the strength of the electromagnetic interaction gets smaller. On the other hand, the strong-interaction potential has an additional term and is of the form $-\alpha_S/r + kr$. Thus, as the participating quarks move farther apart, the strength of the strong-interaction increases. This has the important consequence that quarks are not observed as free particles, but are confined to only exist as constituent members of hadronic bound states, as discussed above. This means that as a $q\overline{q}$ pair is pulled apart, the strong-interaction coupling increases and therefore the energy density of the color field between the quarks will increase. Eventually, the energy density will be large enough to produce a new $q\overline{q}$ pair. Thus, instead of splitting the initial hadron into its constituent quarks, an additional hadron is produced. At the high energy colliders used by elementary particle physicists, this has the effect that the quarks participating in the initial collision fragment into "jets" of hadrons [16]. Figure 1.2 shows a two jet event recorded with the CDF detector at Fermilab. Because gluons also carry color charge, they too will produce jets. Experimental evidence for the existence of gluons was first provided by the observation of three jet events in e^+e^- collisions [17].

Although quarks have not been observed as free particles[†], their existence is inferred from scattering experiments [12] which reveal that the proton has structure. In fact, from these experiments we can extract the proton structure func-

[†]With the possible exception given in Reference [18].

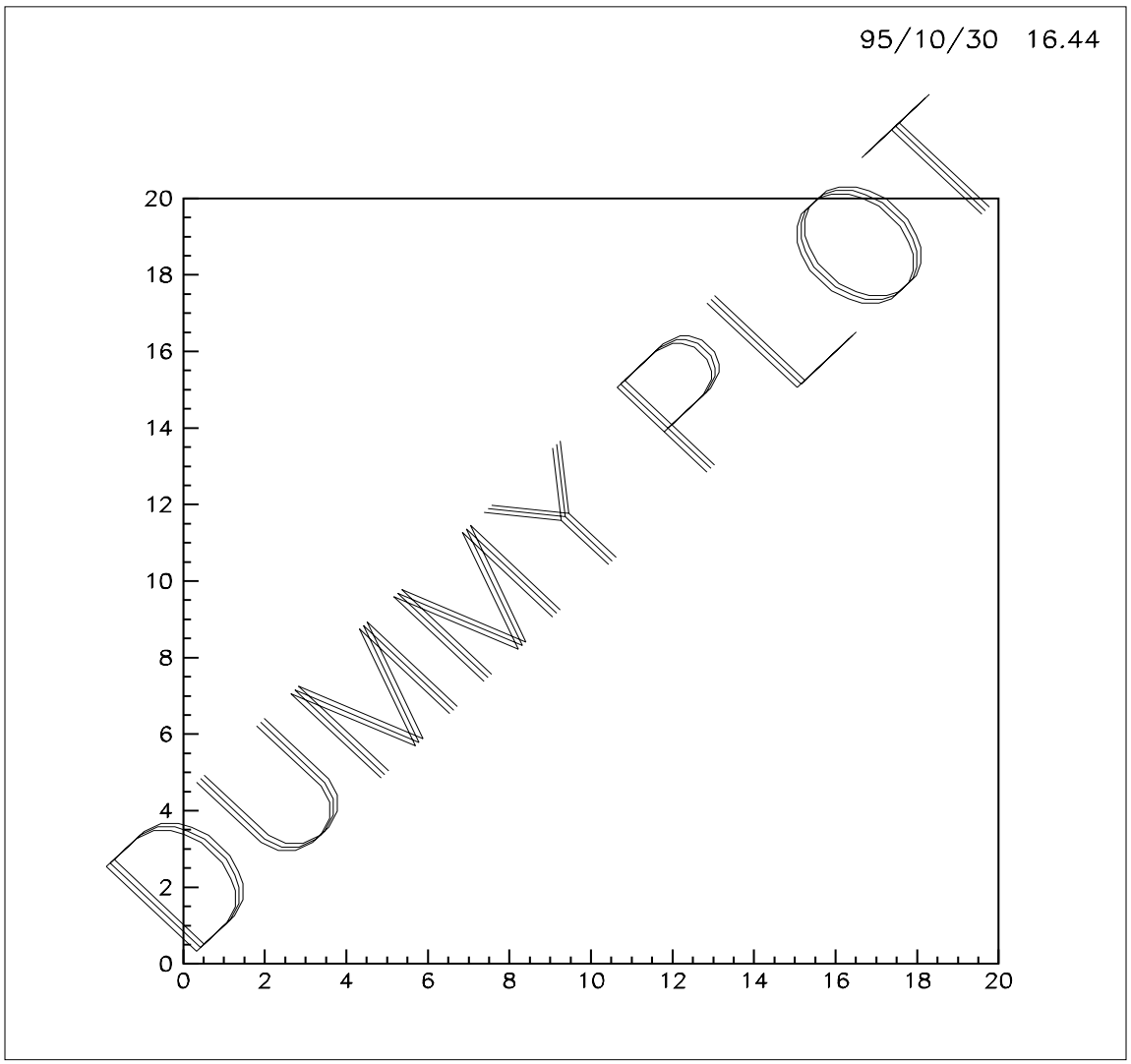

Figure 1.2: A picture of a CDF two jet event in the plane transverse to the $\overline{p}p$ beam line.

tion, $F_p(i, \mathrm{x}_i; \mathbf{Q}_p)$, which gives the probability that the constituent parton (quark or gluon) i carries a fraction, x_i, of the total proton momentum, $\mathbf{Q}_p$ [19]. Scattering experiments also verify that quarks are "point-like", which implies that they are structureless, elementary particles. The idea that hadronic structure is described by point-like spin $\frac{1}{2}\hbar$ constituents is known as the parton model [20], which factorizes a hadronic interaction cross section calculation into two pieces. We pictorially represent a process involving the interaction of two hadrons as shown in Figure 1.3. We mathematically express this cross section as

$$\frac{d^3\sigma}{dx_p dx_{\overline{p}} dcos\theta} = \sum_{i,j} F_p(i, \mathrm{x}_i; \mathbf{Q}_1) \cdot F_{\overline{p}}(j, \mathrm{x}_j; \mathbf{Q}_2) \cdot \frac{d\sigma_{ij\to ab}}{dcos\theta}. \tag{1.1}$$

The first piece of Equation 1.1 involves the structure functions of the incoming hadrons of Figure 1.3. It describes the probability that within the incoming hadron p ($\overline{p}$), there is a parton, i (j), carrying momentum fraction x_i (x_j). The sum is over all partons, i, j, within each of the incoming hadrons p and $\overline{p}$, respectively. The second piece of Equation 1.1 is the short distance cross section for the process $ij \to ab$, where i and j are constituent partons of the incoming hadron and a and b are the resulting outgoing partons, again, as shown in Figure 1.3. In this work, we are interested in the specific case of $\overline{p}p \to t\bar{t}X$, where X generically refers to the rest of the partons in the event — that is, everything else *except* the $t\bar{t}$ pair.

1.2 Top Quark Production at the TeVatron

Ever since the discovery of the b quark in 1977 [15], high energy physicists have been searching for its partner known as the top quark. It is required in the Standard Model as the weak isospin partner of the b quark. Indeed, experiments confirm that the b quark is a member of a weak iso-doublet [21], thus *requiring* the top quark to exist if the SM is to remain viable. The mass of the top quark is not predicted within the framework of the SM, but direct searches at the TeVatron collider at Fermilab have placed a lower limit on its mass of 131 GeV/c^2 [22] at the 95% confidence level.

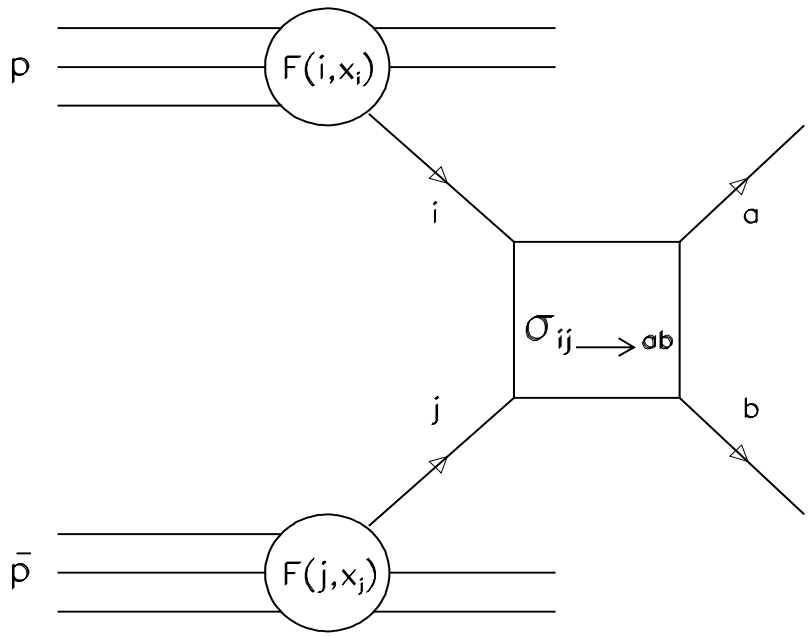

Figure 1.3: Pictorial representation of a $\overline{p}p$ interaction as understood in the parton model. The proton (anti-proton) structure function is given by $F(i, \mathrm{x}_i)$ ($F(j, \mathrm{x}_j)$). The short distance cross section for the reaction $ij \to ab$ is given by $\sigma_{ij \to ab}$.

Recently, CDF has reported direct evidence for top quark production and measured a top quark mass of $M_t = 174 \pm 10^{+13}_{-12}$ GeV/c^2 [23] [24]. Precision electroweak measurements favor a top quark mass of $M_t = 177 \pm 11^{+18}_{-19}$ [25].

In $\overline{p}p$ collisions top quarks are expected to be produced in pairs by both gluon-gluon fusion,

$$gg \rightarrow t\overline{t} \tag{1.2}$$

and $q\overline{q}$ annihilation

$$q\overline{q} \rightarrow t\overline{t}. \tag{1.3}$$

Each of these subprocesses is of order α_S^2 $(\mathcal{O}(\alpha_S^2))$ and is calculated in References [26]. Cross sections have been calculated to next-to-leading order (NLO), $\mathcal{O}(\alpha_S^3)$, in References [27]. As discussed in Reference [28], the $\mathcal{O}(\alpha_S^2)$ and $\mathcal{O}(\alpha_S^3)$ corrections are large, predominantly due to initial state gluon brehmsstrahlung, and are approximately 10% (70%) for the $q\overline{q}$ (gg) channel. Figure 1.4 shows the relative contribution of the gg and $q\overline{q}$ channels to the NLO production cross section for a top mass in the range $90 < M_t < 200$ GeV/c^2 [28]. For a top mass of 175 GeV/c^2, $q\overline{q}$ annihilation is the dominant production mechanism at $\sqrt{s} = 1.8$ TeV, having a cross section almost an order of magnitude larger than the gg channel. A more accurate estimate of the NLO cross section is calculated using a resummation method and yields cross sections ranging from 16.9 pb at a top quark mass of 140 GeV/c^2 to 2.26 pb at a top quark mass of 200 GeV/c^2 [28]. More recently, the NLO resummation calculation has been repeated using the Principle Value Resummation technique [29] and yields consistent results with improved uncertainties.

In $\overline{p}p$ collisions at $\sqrt{s} = 1.8$ TeV, there are a variety of production mechanisms which yield single top quarks. The dominant one is the $W-$gluon fusion process, which produces single top quarks via

$$qg(W^+g) \rightarrow q't\overline{b}, \tag{1.4}$$

where an incoming quark, q, radiates the W boson. Since these processes are expected to have significantly reduced cross sections with respect to the gg and $q\overline{q}$

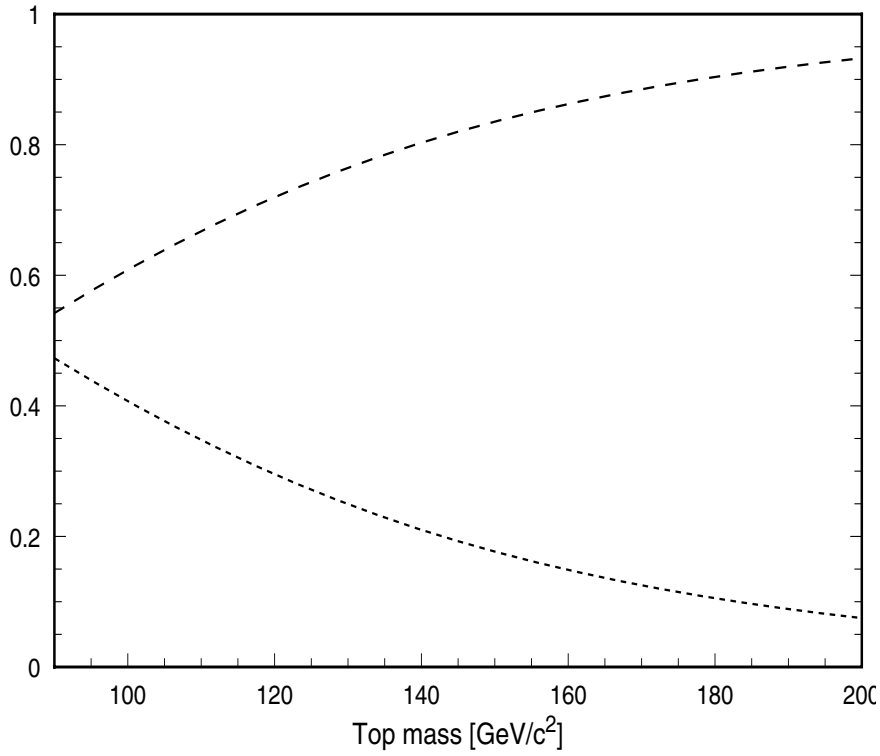

Figure 1.4: The relative contribution to the total NLO $t\bar{t}$ production cross section at the Fermilab TeVatron for the processes $gg \rightarrow t\bar{t}$ (bottom curve) and $q\bar{q} \rightarrow t\bar{t}$ (top curve) as a function of top mass.

processes [30], we do not considered them any further.

1.3 Search Strategy

In this search we assume Standard Model couplings so that the top quark predominantly decays into a W boson and a b quark. For masses greater than about 85 GeV/c^2, both the W boson and the b quark are real.

The tree level production and decay diagram is given in Figure 1.5. The final event topology is determined by the W decays. Table 1.3 lists the braching ratios for each of the possible final states. CDF employs a variety of counting experiments to exploit as many decay channels as possible [31] [32] [33]. Here we consider only those final states which contain a single high P_T electron or muon from a leptonically decaying W and ≥ 3 jets from the hadronization of the two b quarks and the hadronic decay of the remaining W. This "lepton plus jets" mode has a total branching ratio of $\sim 30\%$, with feed-down from semi-leptonic τ decays accounting for $\sim 5\%$ of this.

Higher order W production, where the W is recoiling against significant jet activity, as shown in Figure 1.6, is the dominant background source. The background rate is 2-10 times larger than the event rate from top quark production. This ratio can be considerably improved by requiring that at least one of the jets in the event is identified as a B jet. Any jet thus identified is labelled as "B-tagged". The long lifetime of B hadrons ($\langle c\tau_B \rangle \approx 450\ \mu m$) [34] and the boost they receive from the decay of a heavy top quark allow for the B hadrons to typically travel some distance from the primary vertex before decaying. As shown in Figure 1.7, the signature of such a decay is the presence of a secondary vertex, displaced from the primary vertex, in the event. In the analysis discussed here, we utilize the excellent resolution of the silicon vertex (SVX) detector to partially reconstruct the secondary displaced vertex of the decaying B hadron. Our dominant background source is then "W plus heavy flavor", where one of the gluons in Figure 1.6 splits into a $c\overline{c}$ or $b\overline{b}$ pair.

We therefore define as our signal sample those events with a high P_T, isolated

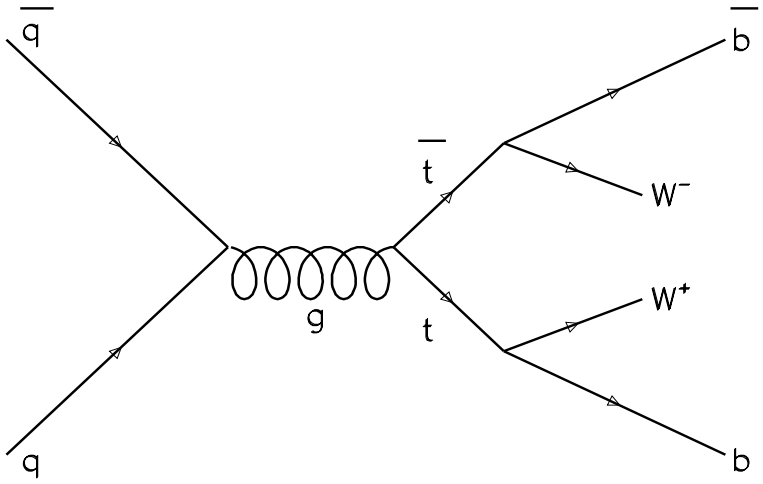

Figure 1.5: Tree level diagram for $t\bar{t}$ production from $q\bar{q}$ annihilation.

decay mode	branching ratio
$t\bar{t} \to (q\bar{q}'b)(q\bar{q}'\bar{b})$	36/81
$t\bar{t} \to (q\bar{q}'b)(e\nu\bar{b})$	12/81
$t\bar{t} \to (q\bar{q}'b)(\mu\nu\bar{b})$	12/81
$t\bar{t} \to (q\bar{q}'b)(\tau\nu\bar{b})$	12/81
$t\bar{t} \to (e\nu b)(\mu\nu\bar{b})$	2/81
$t\bar{t} \to (e\nu b)(\tau\nu\bar{b})$	2/81
$t\bar{t} \to (\mu\nu b)(\tau\nu\bar{b})$	2/81
$t\bar{t} \to (e\nu b)(e\nu\bar{b})$	1/81
$t\bar{t} \to (\mu\nu b)(\mu\nu\bar{b})$	1/81
$t\bar{t} \to (\tau\nu b)(\tau\nu\bar{b})$	1/81

Table 1.3: Branching ratios for the various $t\bar{t}$ decay modes assuming Standard Model Couplings. Under this assumption and in the mass region of interest $BR\,(t \to Wb) \approx 100\%$, with the subsequent decays of the W bosons determining the final event topology. Here, q is taken to be any light quark — d, u, s, c.

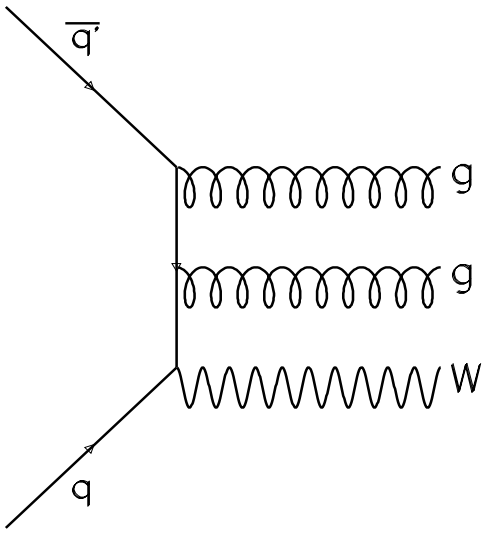

Figure 1.6: Tree level diagram for dominant background process ("W plus heavy flavor") in the search for $t\bar{t}$ production at the Fermilab TeVatron.

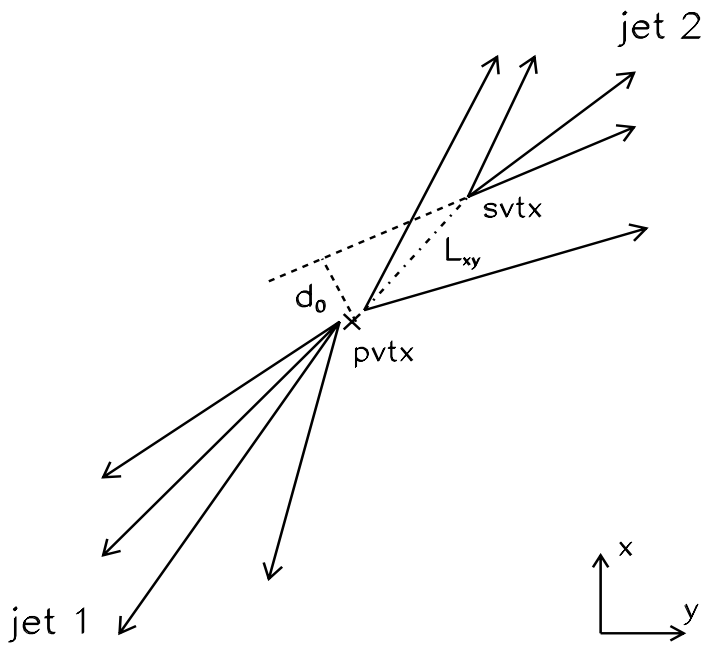

Figure 1.7: Schematic of an SVX B-tag. The presence of a long lived particle in jet 2 is signaled by the presence of a secondary vertex (svtx), whose transverse displacement, L_{xy}, is measured in the $x - y$ plane of the detector. We identify tracks associated with the secondary vertex by requiring a large impact parameter, d_0, with respect to the primary vertex (pvtx).

lepton (electron or muon), missing transverse energy, $\not\!\!E_T$ (signalling the neutrino), and ≥ 3 jets (a.k.a. "W + ≥ 3 jets"). We take as our top quark candidate events all such events in which we've identified the presence of a b quark by tagging its displaced vertex. Since top quarks in the mass range we are interested in tend towards larger jet multiplicity and since the production cross section for W + n jet events falls as $\sim 1/\alpha_S^n$, we define as our control sample those events with a high P_T, isolated lepton, missing transverse energy, and ≤ 2 jets (a.k.a. "W + 1 or 2 jets"). We expect the control region to be dominated by background and so can use this sample to verify our background estimates.

1.4 Dissertation Outline

This dissertation proceeds as follows. In Chapter 2 we discuss the Fermilab accelerator complex, which produces the necessary $\overline{p}p$ collisions, and the CDF detector used to study these collisions. Chapter 3 describes the analysis. We begin with a detailed study of b quark decays in top quark events and proceed with a detailed study of signal formation in the SVX detector. With these things in hand, we next develop and optimize a B-tag algorithm. The probability that a Standard Model top quark event passes all the event selection criteria and is tagged by the B-tag algorithm is then calculated as the total $t\bar{t}$ detection efficiency. We conclude the chapter with a discussion of our observations and their significance, and a measurement of the top quark mass and production cross section.

Chapter 2

Experimental Apparatus

2.1 The Fermilab TeVatron

The CDF detector operates in a high luminosity hadron environment at the Fermilab TeVatron Accelerator. The TeVatron layout is diagrammed in Figure 2.1. The accelerator employs conterrotating beams of protons and anti-protons with energies of 900 GeV each to achieve a center of mass energy equal to 1.8 TeV. Due to various accelerator limitations, the protons must go through several accelerator stages before reaching the maximum energy.

The accelerator string is shown in Figure 2.2. The protons are first extracted from a hydrogen gas bottle and accelerated to 750 keV in a Cockcroft-Walton accelerator as H^- atoms. The electrons are then stripped off and the protons are accelerated to a kinetic energy of 200 MeV in a Linac 150 meters in length. They are next transferred to the Booster ring, a synchrotron with a circumference of 475 meters, where they reach an energy of 8 GeV. Afterwards, they are injected into the Main Ring, a synchrotron with a circumference of 6300 meters, where they are boosted to an energy of 150 GeV. Finally, the protons are injected into the TeVatron, which lays just below the Main Ring, where they reach their peak energy of 900 GeV. This whole process takes about one minute, with the typical yield being

approximately 10^{12} protons divided into 6 equally spaced "bunches".

Not all of the protons extraced from the gas bottle continue through the entire acceleration process. Some are used to create anti-protons. The protons used in making anti-protons are taken through the Linac, Booster, and Main Ring components of the accelerator string exactly as described above except that in the Main Ring they are only accelerated to 120 GeV. The protons are then extracted from the Main Ring and focussed onto a copper foil to produce anti-protons. Only anti-protons with an energy near 8 GeV are collected and sent to the Debuncher/Accumulator where they are stochasticly cooled to reduce their momentum spread and "stacked". This process continues until there are about $\sim 6.0 \times 10^{11}$ anti-protons in the "stack", enough to begin injection into the Main Ring and eventually into the TeVatron. The TeVatron operates with 6 anti-proton bunches, each containing approximately 7.0×10^{10} anti-protons.

The instantanious luminosity of the TeVatron [35] is given in equation 2.1 as

$$\mathcal{L}_{inst} = \frac{3\gamma f B N_P N_{\overline{p}} F}{\beta(\epsilon_p + \epsilon_{\overline{p}})} \tag{2.1}$$

where the parameters are given as

$\gamma \equiv$ relativistic factor of the proton (1066 at 1 TeV)

$f \equiv$ frequency of revolution (47.7 kHz)

$B \equiv$ number of proton and anti-proton bunches (6)

$N_p \equiv$ number of protons per bunch ($\sim 10^{11}$)

$N_{\overline{p}} \equiv$ number of anti-protons per bunch ($\sim 7.0 \times 10^{10}$)

$\beta \equiv$ a single valued function of the azimuth position, related to the emittence, evaluated at the interaction point

$\epsilon_{p\ (\overline{p})} \equiv$ 95% normalized transverse emittence of the proton (anti-proton) beam

$F \equiv$ form factor related to the bunch length at the interaction point and to β.

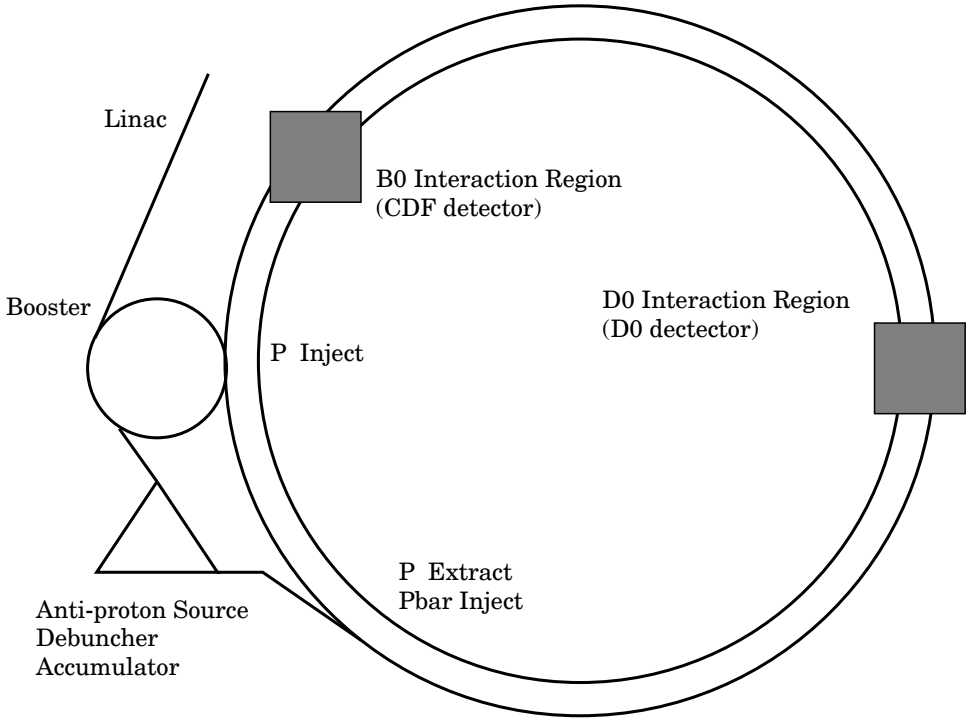

Figure 2.1: Layout of the Fermilab TeVatron Accelerator Complex.

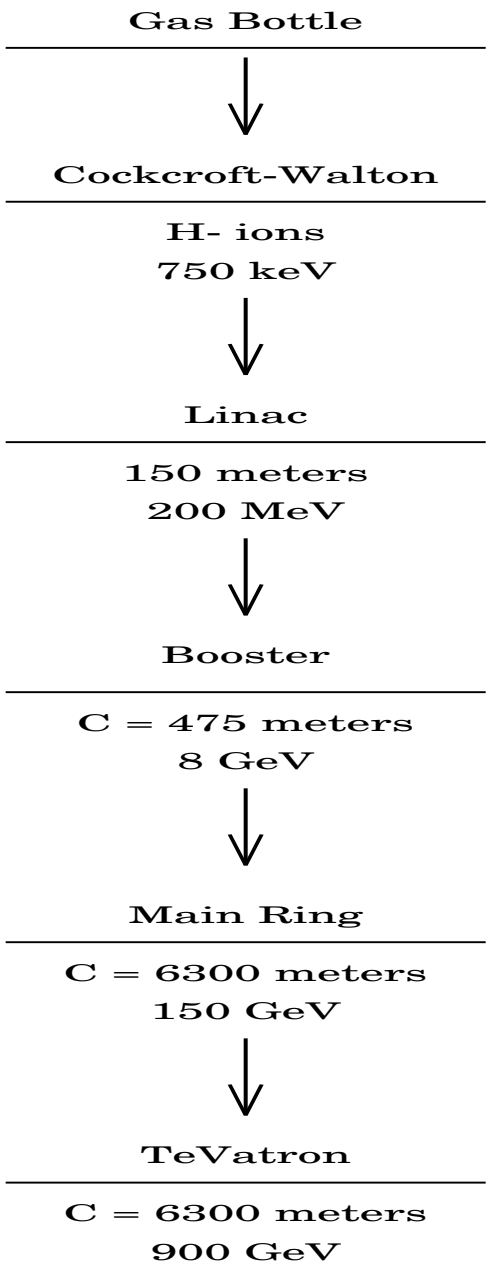

Figure 2.2: A flow chart describing each of the steps involved in accelerating protons to 900 GeV at the Fermilab TeVatron.

Assuming the emittences of the protons and anti-protons to be equal in equation 2.1 gives a luminosity that is proportional to two distinct quantities:

1. $\frac{N_p}{\epsilon_p} \equiv$ the phase space density of the protons
2. $BN_{\overline{p}} \equiv$ the availability of anti-protons.

It is these quantities and the accelerator effects that determine them that limit the luminosity. Fermilab has begun a five year program to improve the luminosity of the TeVatron by improving these quantites [35]. For a more detailed discussion of the relevant accelerator characteristics and the Fermilab upgrade, the reader is referred to [36], [37].

2.2 Run 1A and Run 1B

In this analysis we use 100 pb^{-1} of data collected with the CDF detector at the Fermilab Tevatron. The data is collected during two distinct periods of TeVatron operation. The 1992-93 run is generally known as "Run 1A" while the 1994-95 run is generally known as "Run 1B". The average instantaneous luminosity of a run 1A (run 1B) store is 3×10^{30} (7×10^{30}) cm^{-2}/s. The CDF detector is largely the same for the two runs. The difference most affecting this analysis is the replacement of the SVX detector with the SVX$'$ detector. This is discussed more fully in Section 2.3.

2.3 The Collider Detector at Fermilab

The Collider Detector at Fermilab (CDF) is a general purpose 1.4 Tesla solenoid detector built to analyze proton anti-proton collisions at a center of mass energy of 1.8 TeV. It employs several tracking systems within a magnetic field for momentum analysis and various calorimeter systems to sample the energy of the outgoing particles and jets. The detector is symmetric about the interaction point and in the azimuth angle, and consists of three main sub-systems: the central detector, the endplug detectors, and the forward detectors. A cross-sectional view of one quadrant of the CDF detector is depicted in Figure 2.3. We define a coordinate system that has the positive z-axis pointing along the beamline in the direction of the protons. The positive y-axis is normal to the plane of the accelerator while the x-axis is defined to lie in the plane of the accelerator and has its positive direction defined to yield a right-handed coordinate system. The azimuth angle, ϕ, and the polar angle, θ, are the traditionally defined spherical coordinates. We additionally define the psuedorapidity, $\eta = -ln\,(tan\,(\theta/2))$.

A four level trigger system is employed to reduce the event acceptance rate to 1-2 Hertz (a factor of $\sim 10^5$ in reduction). The first 3 levels (0-2) are hardware triggers employed within the frontend readout electronics and reduce the event rate by a factor of $\sim 10^4$ while incurring a minimal deadtime. The Level 0 trigger requires a coincidence crossing of the proton anti-proton bunches. The Level 1 trigger decision is based on calorimeter and muon chamber information. It is set true is there are a pair of contiguous calorimerter towers over threshold, or if there exists a candidate muon stub in one of the central muon chambers (CMU, CMP, or CMX). The Level 2 decision is based on calorimeter, tracking, and muon information. The tracking information is obtained from the Central Fast Tracker (CFT) [38], which relies on the fact that, due to the Loretz angle of the CTC superlayers (cf. Figure 2.4), tracks with a transverse momentum, P_T, greater than 1 GeV/c have ionization drift times of < 40 nsec. The CFT uses lookup tables of hit patterns to determine the

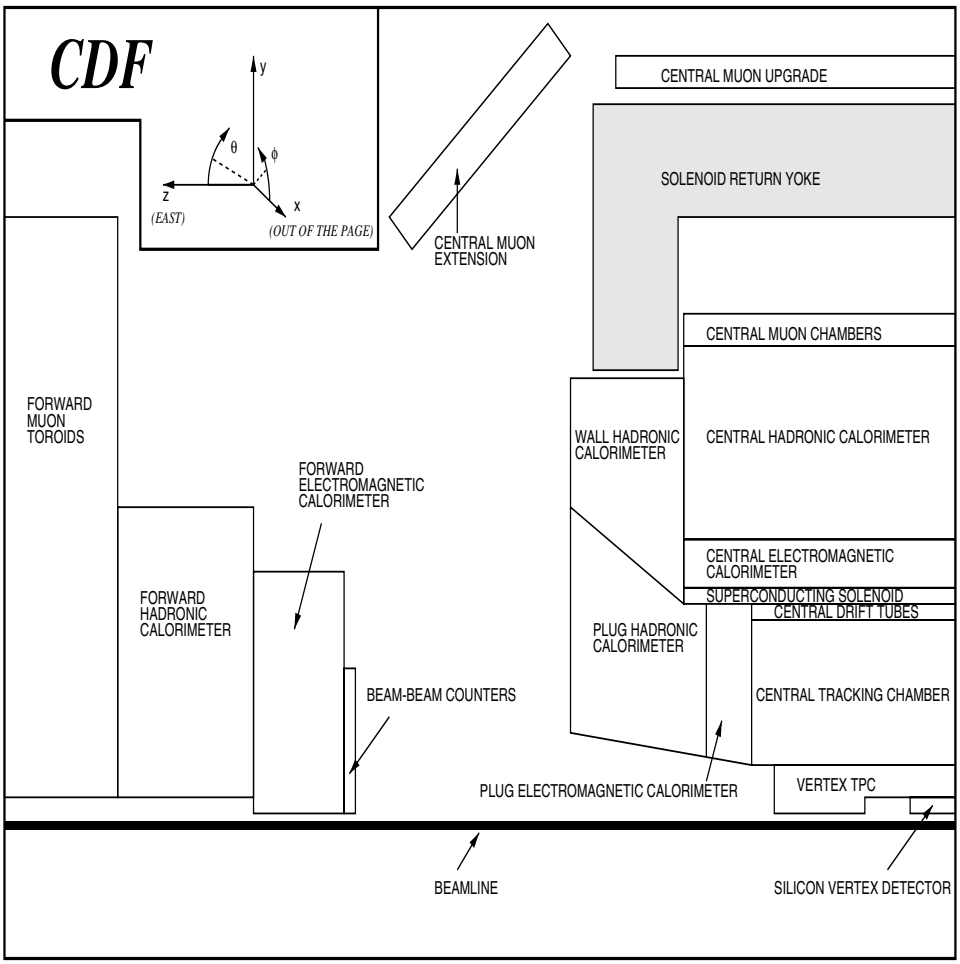

Figure 2.3: A cross-sectional view of the CDF detector from the side. The interaction region is in the lower right hand corner of the figure. The detector is forward-backward symmetric about the interaction region.

P_T of a candidate track in bins of 2.2, 2.7, 3.4, 4.7, 7.5, 12.0, 18.0, 27.0 GeV/c (these are the 90% efficiency points). The CFT has a nominal P_T resolution given by $\delta P_T/P_T^2 = 0.035$ (GeV/c). The CFT tracks are then used in conjuction with calorimeter and muon information to identify electron and muon candidates. Jet clustering is also done at Level 2. An event is accepted at Level 2 if there exists an electron or muon candidate, or if there exists significant jet activity. A Level 2 accept initiates a full detector readout. The scan time is on the order of 30 msec and incurrs 10% deadtime. The final trigger Level 3 is a VAX ALPHA based filter algorithm. The event rate out of the Level 3 is $1-2$ Hertz. Events accepted at Level 3 are written to tape. The 145k channels of the detector are read out, digitized, and recorded by the CDF Data AcQuisition (DAQ) sytem. Signals from the various detector components are read out on the front end by either a custom-made, crate-based analog system known as RABBIT, or the standard commercial crate-based FASTBUS.

The central detector consists of a solenoid magnet, a steel yoke, tracking chambers, a pre-radiator, electromagnetic calorimetry, hadronic calorimetry, and muon chambers. It covers the region $-1.3 < \eta < 1.3$, is symmetric in azimuth, and extends 7.3 meters along the beamline.

The central detector tracking system utilizes a large cylindrical axial wire drift chamber (CTC), with an outer radius of 1.32 meters and a length of 3.21 meters, in combination with a primary event vertex tagging device (VTX), both immersed in a 1.4 Tesla magnetic field, to obtain charged particle tracking information with a momentum resolution of $\delta P_T/P_T^2 = 0.002$ (GeV/c). In addition, a silicon microstrip detector (SVX) placed near the interaction region allows for the tagging of decay vertices of long lived particles. A superconducting coil 3 meters in diameter and 5 meters in length generates the 1.4 Tesla magnetic field.

The CTC is segmented into 9 "superlayers" as shown in Figure 2.4. There are 5 superlayers consisting of 12 sense wires aligned parallel with the z-axis (the axial layers). These alternate with 4 superlayers consisting of 6 sense wires tilted

3° relative to the z-axis (the stereo layers). Together these superlayers allow 3-D tracking. The resolution of the CTC averaged over all layers is $\sim$ 400 μm. For tracks with $|\eta| < 1.0$, the track finding efficiency is greater than 95%.

The SVX figures prominently into this analysis and merits a more thorough discussion. The geometry and layout of the SVX are shown in Figure 2.5. Table 2.1 is a comparative summary of the features of SVX and SVX′ . The two detectors are very similar. Differences will be noted below parenthetically. The SVX consists of two barrels aligned along the beam direction with a gap of 2.15 cm between them at $z = 0$. Each barrel consists of four concentric layers of silicon strip detectors segmented into twelve 30° wedges. Each layer is composed of 12 ladders (cf. Figure 2.6) 25.5 cm long. There are $12 \times 4 \times 2 = 96$ ladders on the complete detector. Each ladder contains three 8.5 cm long single sided silicon wafers. The readout strips of the silicon are aligned parallel with the barrel axis. This provides 2-D tracking information in the $r - \phi$ plane. The front end readout circuit provides sparse mode readout, so that only strips significantly over threshhold are read out. Additionally, the readout circuit allows for a hardware subtraction of the leakage current strip by strip. Typical gains are $\sim$ 15(21) mV/fC. The SVX(′) has a signal to noise ratio of 10 (15), a resolution of 15(13) μm and a hit efficiency of 98(99)% per layer. Figure 2.7 shows the residual distribution for the SVX′ detector. Utilizing SVX and CTC information yields impact parameter resolutions asymptotically approaching 15 (13) μm. The P_T resolution of the combined SVX-CTC system is $\delta P_T/P_T = \sqrt{(0.0009 P_T)^2 + (0.0066)^2}$, where P_T is measured in units of GeV/c.

The central electromagnetic calorimetry (CEM) utilizes alternating layers of lead and scintillator arranged in a projective tower geometry with $\Delta\eta \times \Delta\phi = 0.1 \times 15°$ The towers extend 18 radiation lengths and have an energy resolution of $\sigma_E/E = 13.5\%/\sqrt{E}$ where E is measured in units of GeV. In each CEM tower, wire proportional strip chambers (CES and CEW) located at shower maximum provide shower shape information. The central hadronic calorimetry (CHA) utilizes alternating layers of iron and scintillator. It is located immediately behind, and shares the same

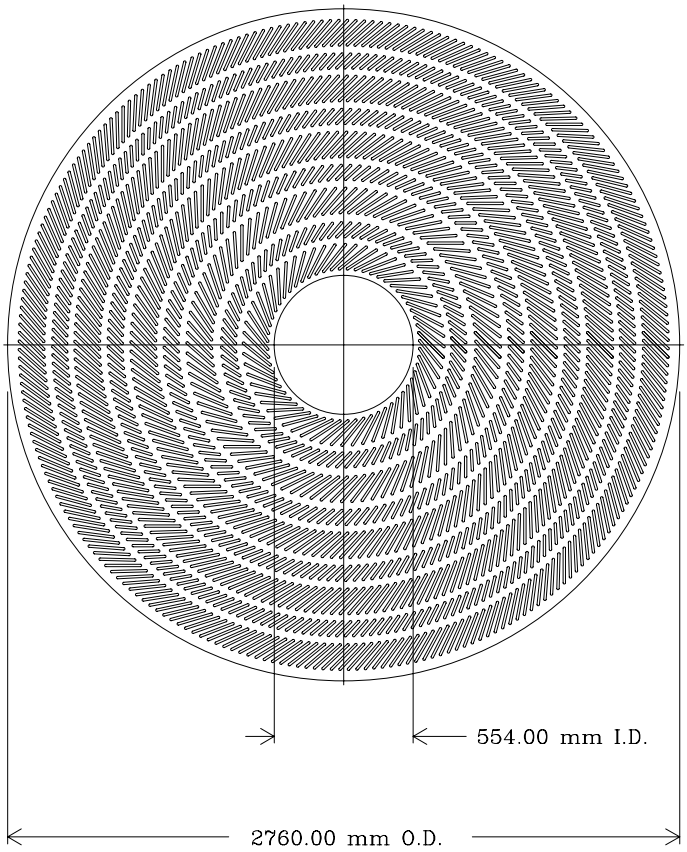

Figure 2.4: Transverse view of the CTC endplate demonstrating the 9 superlayer geometry. The wire planes are titled 45° relative to the radial to account for the Lorentz angle of the ionization drift velocity.

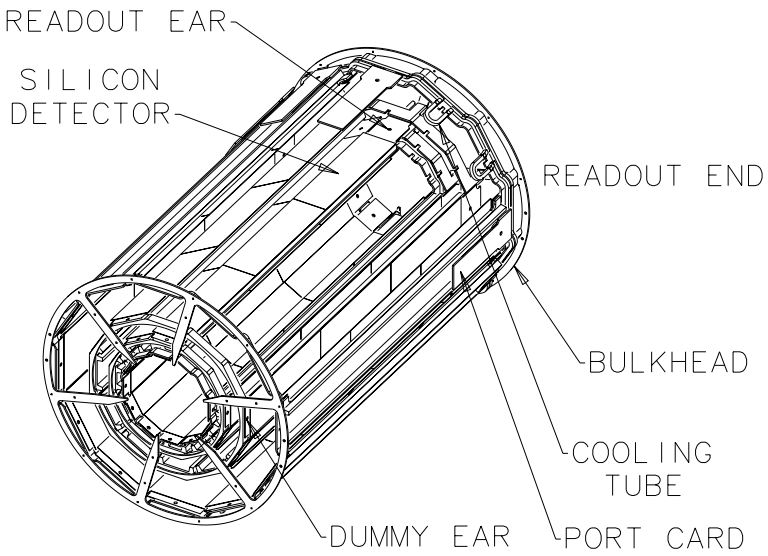

Figure 2.5: An isometric projection of a single SVX barrel. Some ladders of the outer layers have been left off to allow for a view of the inner layers. The SVX detector is composed of two such barrels laid end to end, with their readout ends facing one another at $z = 0$.

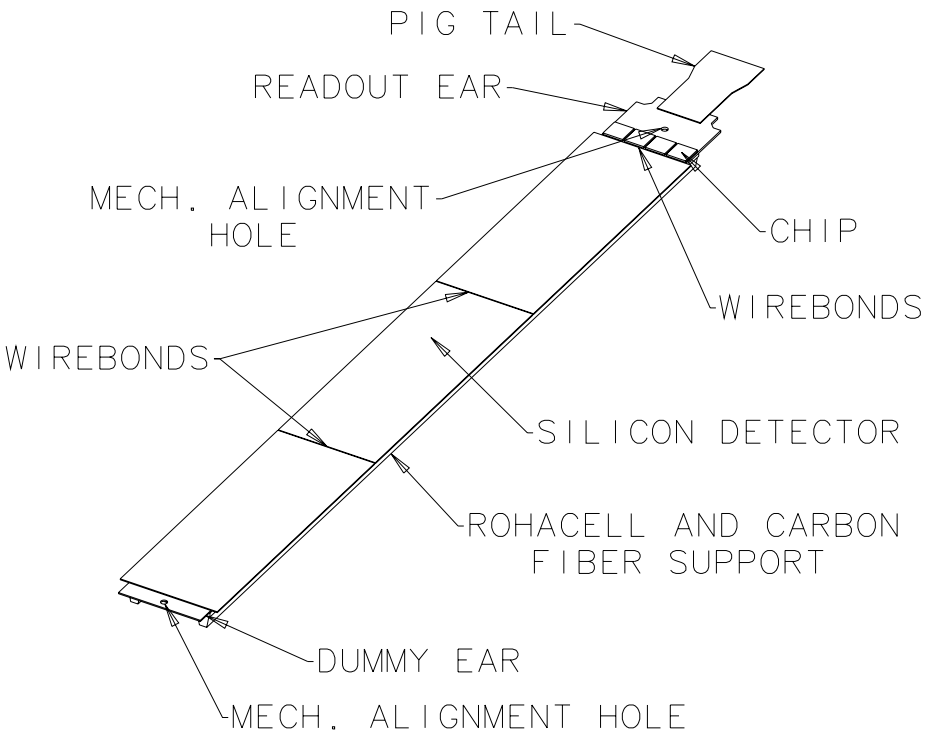

Figure 2.6: An SVX ladder used in barrel construction. Each barrel is made up of 48 ladders—12 ladders per layer over 4 layers.

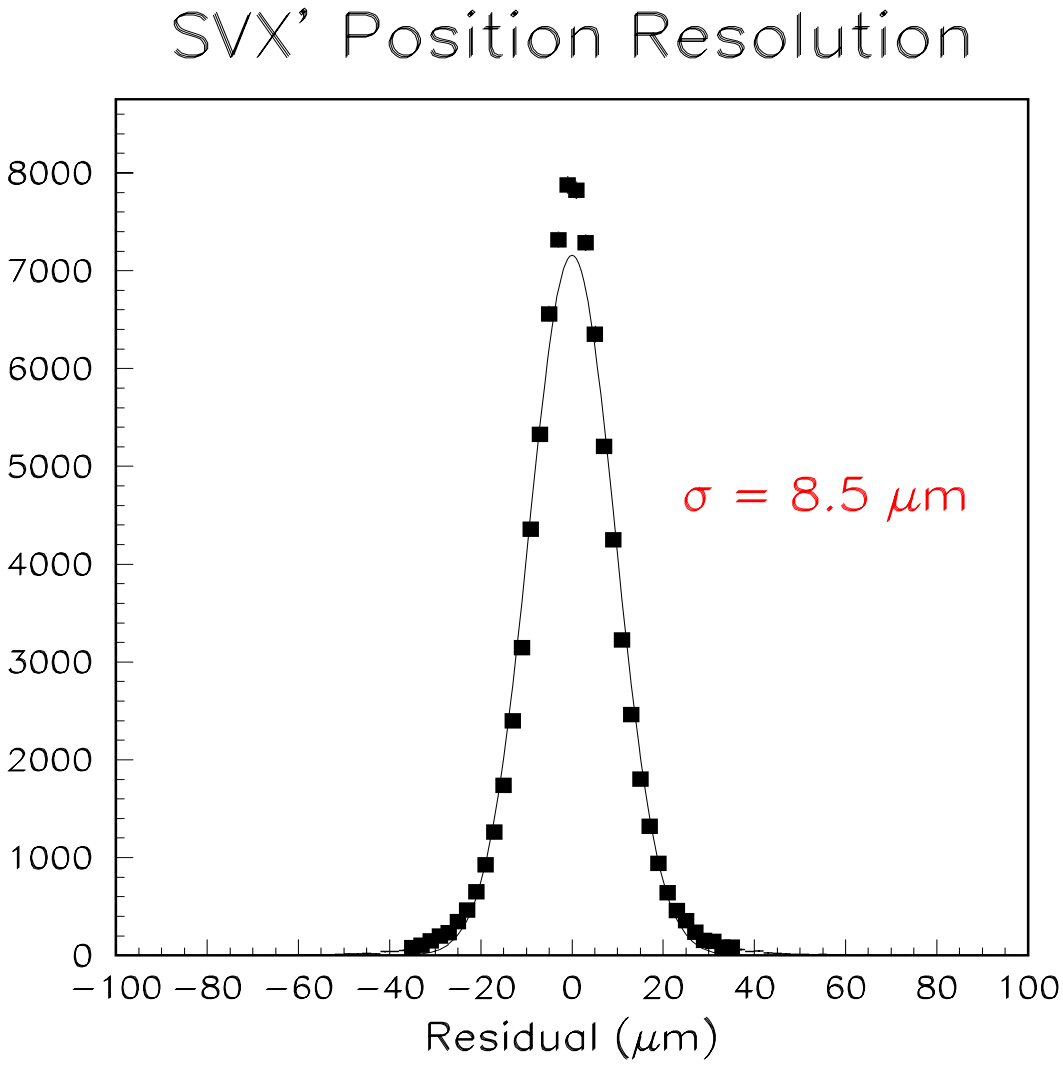

Figure 2.7: The (biased) residual distribution for the SVX′ detector.

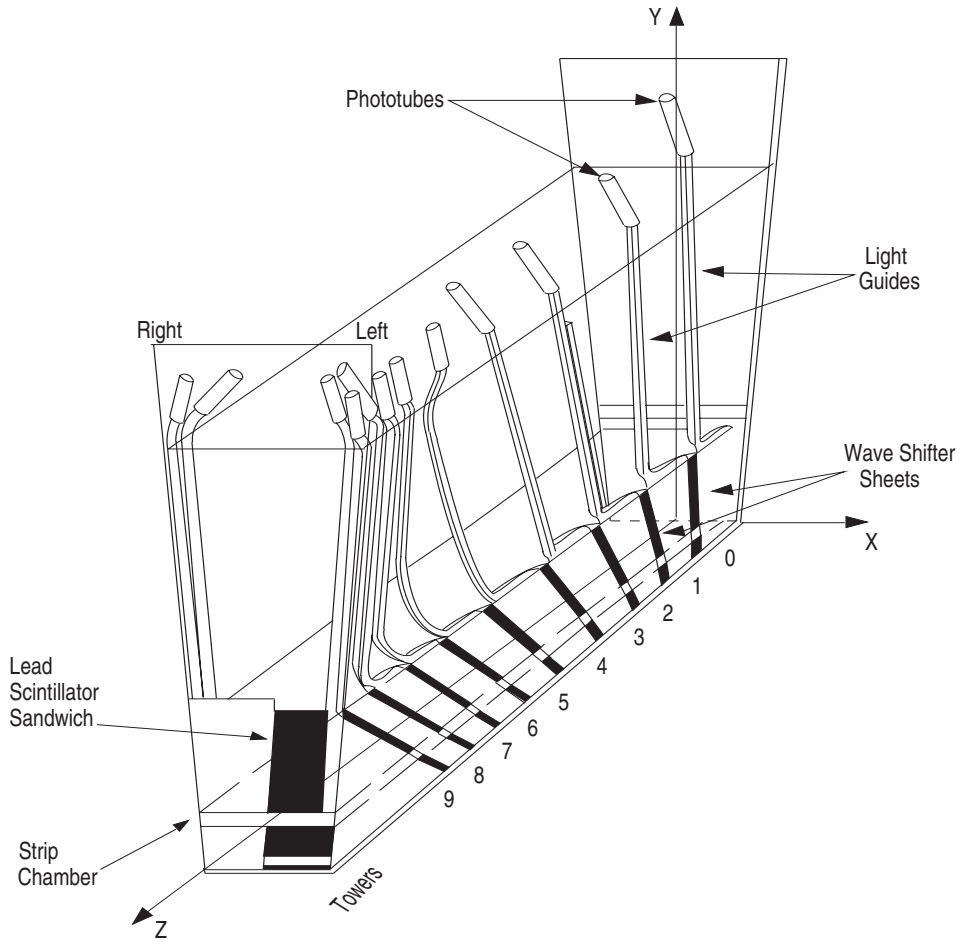

Figure 2.8: Schematic of a single CDF central calorimeter wedge. Each wedge is composed of 10 towers. A single tower spans $\Delta\eta \times \Delta\phi = 0.1 \times 15^{\circ}$. Wire proportional strip chambers are located at shower maximum.

geometry and segmentation as, the the electromagnetic calorimetry. The resolution of the CHA is $\sigma_E/E = 70\%/\sqrt{E}$. A single central calorimeter wedge is represented in Figure 2.8.

The central muon chambers (CMU, CMP, CMX) use drift chambers operating in streamer mode to measure the transverse momentum of muons. The CMU chambers are situated at the end of the CHA and are segmented as $\Delta\eta \times \Delta\phi = 0.1 \times 12.6°$. The CMP chambers are situated behind an additional 0.6 meters of steel. The additional steel reduces the rate of hadronic punchthrough by a factor of 30. Approximately 84% of the solid angle for $|\eta| < 0.6$ is covered by the CMU system, 63% by the CMP system, and 53% by both. The CMX chambers cover 71% of the solid angle in the region $0.6 < |\eta| < 1.0$ and increase the muon acceptance by 25% relative to the CMU + CMP systems only. The CMU, CMP and CMX chambers have a momentum resolution of 13% for muons with a transverse momentum greater than 8 GeV/c.

The endplug detectors consist of electromagnetic and hadronic calorimeters (the PEM and PHA respectively) and cover the region $10° < \theta < 30°$. The endplug detectors rest flush against the central detector to extend the total coverage in the central region to $-2.4 < \eta < 2.4$. The PEM has a resolution of $\sigma_E/E = 28\%/\sqrt{E}$ and the PHA has a resolution of $\sigma_E/E = 140\%/\sqrt{E}$.

The forward detectors cover the small angle region from $1.7° < \theta < 10°$ and consist of electromagnetic calorimeters (FEM), hadronic calorimeters (FHA), and steel toroid muon spectrometers (FMU). The energy resolutions of the FEM, FHA, and FMU are similar to those of the PEM, PHA, and CMU respectively.

The luminosity of the accelerator is monitored by a plane of scintillators mounted immediately in front of the FMU. These are known as the beam-beam counters (BBC) and they cover the region $0.32° < \theta < 4.47°$. The instantaneous luminosity is calculated as

$$\mathcal{L}(t) = \frac{R_{BBC}(t)}{\sigma_{BBC}} \tag{2.2}$$

where

$R_{BBC} \equiv$ the BBC hit rate at time t

$\sigma_{BBC} \equiv$ the BBC total cross section.

The integrated luminosity is found by integrating both sides of Equation 2.2 over time. The integrated luminosity for the 1992 run is estimated to be 20 pb^{-1}, while the integrated luminosity for the 1993 run is estimated to be 80 pb^{-1}. The overall uncertainty in the integrated luminosity is 3.3% [39] for the 1992 run and 10% for the 1993 run.

The CDF detector is described in more detail in reference [40].

Feature	SVX	SVX′
channels	46080	
z coverage	51.1 cm	
gap at z=0	2.15 cm	
radius L0	3.0049 cm	2.8612 cm
radius L1	4.2560 cm	
radius L2	5.6872 cm	
radius L3	7.8658 cm	
overlap L0	-1.26 deg (gap)	0.17 deg (0.24 strip)
overlap L1	0.32 deg (4 strip)	
overlap L2	0.30 deg (4 strip)	
overlap L3	0.04 deg (0 strip)	
silicon	one-sided	
	DC	AC, FOXFET bias
passivation	none	polyimide
atmosphere	Ar/Ethane+H20	dry nitrogen
readout chip	SVX IC Rev.D	SVX IC Rev.H3
sampling	quadruple	double
noise	2200 electrons	1300 electrons
gain	15 mv/fc	21 mv/fc
reset/integrate	3.5 μs	
readout time	2.7 μs	2.1 μs
rad limit	15-20 KRad	$>$ 1 MRad
bad channels	2.93%	1.73%
occupancy typical	7%-10%	5%
occupancy max	12%-20%	25%

Table 2.1: Comparison of SVX and SVX′

Chapter 3

Analysis

3.1 Sample Selection

In this search we assume Standard Model couplings so that the top quark predominantly decays into a W boson and a b quark. As discussed in Section 1.3, in this analysis we consider only those final states which contain a single high P_T electron or muon from a leptonically decaying W, and ≥ 3 jets from the hadronization of the two b quarks and the hadronic decay of the remaining W. This "lepton plus jets" mode has a total branching ratio of $\sim 30\%$. We require that we identify at least one b quark in the event using the SVX detector. Our dominant background source is then "W plus heavy flavor", where the W is recoiling against significant jet activity.

We define as our signal sample those events with a high P_T, isolated lepton (electron or muon), missing transverse energy, $\not\!\!E_T$ (signalling the neutrino), and ≥ 3 jets (a.k.a. "W + ≥ 3 jets"). We take as our top quark candidate events all such events in which we've identified the presence of a b quark by tagging its displaced vertex. We define as our control sample those events with "$W + 1$ or 2 jets". We expect the control region to be dominated by background and so can use this sample to verify our background estimates.

3.1.1 Identification of the Primary Event Vertex

Our analysis strategy relies on our ability to identify the displaced vertices characteristic of the long-lived b quarks in top quark decay. This identification is dependent on the resolution with which we can measure the position of the primary interaction vertex of the event. At the CDF interaction region, primary vertices are Gaussian distributed parallel to the beam axis with $\sigma_{||} \sim 30$ cm and perpendicular to the beam axis with $\sigma_{\perp} \sim 35$ μm. The beam axis and the CDF detector axis are not parallel and have a relative slope of ~ 5 μm/cm in the horizontal plane and ~ -3 μm/cm in the vertical plane. The beam axis, at the nominal interaction point, $z = 0$, is displaced from the detector axis by $200 - 1200$ μm ($400 - 1000$ μm) in the horizontal (vertical) plane. Due to changing TeVatron conditions both the slopes and displacements drifted during the course of data taking, but are measured on an run-by-run basis to accuracies of ~ 4 μm/cm for the slope and ~ 10 μm for the displacement.

We determine the primary vertex on an event-by-event basis using a weighted fit of SVX tracks and the event vertex z position as determined using VTX information. Corrections for the beam offset and slope are accounted for. Tracks with large impact parameters are removed from the fit using an iterative procedure. The impact parameter, d_0, is defined as the distrance of closest approach to the candidate vertex in the $r - \phi$ plane. This procedure yields uncertainties of $6 - 36$ μm in the transverse components of the primary vertex.

Because of the high luminosity conditions, about 50% of events contain multiple interaction vertices separated along the beam axis. In these events, we calculate for each vertex the scalar sum of the transverse momentum of all tracks associated to it. The vertex with which the greatest total transverse momentum is associated is used as the interaction vertex. All tracks used in the vertex fit and subsequent analysis are required to extrapolate to within 5 cm of this vertex along the beam axis — $|z_{trk} - z_{vtx}| < 5$ cm. The primary lepton in the events, selected as described below,

are associated with the chosen vertex 99.9% of the time. Using CTC information, a track's extrapolated z coordinate is determined with a resolution of 6 mm for tracks with $P_T > 2$ GeV/c.

3.1.2 Muon Selection

A high P_T, inclusive, central muon data sample is collected using the multilevel trigger system described in Section 2.3. The Level 1 trigger simply requires a track segment in one of the central muon chambers. The Level 2 trigger requires that this track segment be matched to a track with $P_T > 7.5$ GeV/c reconstructed in the CTC by the CFT. The combined Level 1 and Level 2 trigger efficiency is measured using $Z \rightarrow \mu\mu$ events and is found to be $\epsilon_{CMU/CMP} = 0.863^{+0.027}_{-0.031}$ and $\epsilon_{CMX} = 0.696^{+0.045}_{-0.049}$ for the CMU/CMP and CMX systems respectively. The software Level 3 trigger requires that a track with $P_T > 18$ GeV/c extrapolate to the track segment in the CMU/CMP (CMX) muon chambers to within $\Delta x = r\Delta\phi < 5(10)$ cm and that the energy deposited in the CHA tower traversed by the track be consistent with expectations for minimum ionizing particles, $E_{CHA} < 6$ GeV. Using 100 pb^{-1} of integrated luminosity yields a sample of 745k events. Starting from the inclusive sample we make additional cuts to reduce backgrounds from cosmic rays, decays in flight, and hadronic punchthrough. These cuts are given in Table 3.1. Using $Z \rightarrow \mu\mu$ events we measure the efficiency of these cuts to be 0.959 ± 0.007.

3.1.3 Electron Selection

High P_T, inclusive, central electrons are collected online by requiring at Level 1 a CEM cluster with $E_T > 6$ GeV and at Level 2 that a track reconstructed in the CTC by the CFT, with $P_T > 7.5$ GeV/c, be matched to a CEM cluster with $E_T > 9$ GeV and $E_{CHA}/E_{CEM} < 0.125$. The combined Level 1 and Level 2 trigger efficiency is measured to be 0.919 ± 0.004 using $Z \rightarrow ee$ events. The software trigger at Level 3 requires that the reconstructed CEM cluster have $E_T > 18$ GeV and that a reconstructed track with $P_T > 18$ GeV/c be matched to it. Using 100 pb^{-1} of

Selection cuts to identify $W \rightarrow \mu\nu$ sample:

cut description	selection criteria
transverse momentum of the muon track as measured in CTC:	$P_T > 20.0$ GeV/c
energy deposited in CEM tower traversed by muon:	$E_{CEM}(\mu - tower) < 2.0$ GeV
energy deposited in CHA tower traversed by muon:	$E_{CHA}(\mu - tower) < 6.0$ GeV
sum of energy deposited in CEM+CHA tower traversed by muon:	$E_{CEM}(\mu - tower)+$ $E_{CHA}(\mu - tower) > 0.1$ GeV
impact parameter with respect to the primary event vertex:	$d_0 < 0.3$ cm
distance between the primary event vertex and the muon track along the z axis:	$\lvert z_{p.vertex} - z_\mu \rvert < 5.0$ cm
matching between the track segment in the muon chamber and the extrapolated CTC track:	$\lvert x \rvert_{CMU} < 2.0$ cm, $\lvert x \rvert_{CMP,CMX} < 5.0$ cm
total event selection efficiency:	$\epsilon_\mu = 0.959 \pm 0.007$

Table 3.1: Cuts used to select the high P_T, inclusive central muon sample. The total event selection efficiency is measured using a sample of $Z \rightarrow \mu\mu$ events.

integrated luminosity yields a sample of 570k events.

Offline we make addtional cuts to reduce backgrounds from charged hadrons. These cuts are given in Table 3.2. We measure the efficiency of these cuts to be 0.84 ± 0.02 using $Z \rightarrow ee$ events.

3.1.4 Final Event Selection

We identify our final event sample by requiring a high P_T, isolated electron or muon and missing transverse energy, $\not\!\!E_T$, greater than 20 GeV. High P_T muons and electrons are identified as described above. If a particular event has more than one lepton candidate, we take as the primary lepton in the event the lepton with the largest P_T. We make a cut on the isolation of the primary lepton since we expect it to originate predominantly from the leptonically decaying W. The isolation variable used, I_{cal}, is defined as the transverse energy in a cone of $R = \sqrt{(\Delta\phi)^2 + (\Delta\eta)^2} = 0.4$ centered on the lepton but excluding the energy in the calorimeter tower traversed by the lepton. We require that $I_{cal}/E_T^{electron} < 0.1$ and $I_{cal}/P_T^{muon} < 0.1$ for electrons and muons respectively. This cut reduces our $t\bar{t}$ acceptance by 13% and 19% in the electron and muon channels respectively. The leptonic decay of a W also includes a neutrino, which will pass undetected through the CDF volume resulting in an imbalance of energy in the transverse plane of the detector. We calculate the $\not\!\!E_T$ by subtracting from zero the vector sum of all transverse energies in calorimeter towers with $|\eta| < 3.6$. Only towers with a *total energy*, $E = E_T/sin\theta$, above detector specific thresholds are included in the sum. The thresholds range from 100 MeV for the CEM and CHA, to 800 MeV for the FHA. The $\not\!\!E_T$ resolution is given approximately as $0.7\sqrt{\Sigma E_T}$ GeV$^{1/2}$, where ΣE_T is the *scalar* sum of the transverse energies included in the $\not\!\!E_T$ calculation measured in units of GeV. If there is a primary muon in the event, we correct the $\not\!\!E_T$ calculation by vectorially adding the E_T of the calorimeter tower traversed by the muon and vectorially subtracting the P_T of the muon as measured in the CTC.

Finally, we remove Z candidate, photon conversion candidate, and dilepton can-

Selection cuts to identify $W \rightarrow e\nu$ sample:

cut description	selection criteria
transverse energy deposited in CEM tower traversed by electron:	$E_T > 20$ GeV
ratio of energy deposited in CHA to CEM in tower traversed by electron:	$E_{had}/E_{em} < 0.05$
ratio of CEM energy to total momentum as measured in the CTC:	$E/P > 1.8$
the distance between the CES shower position and the extrapolated CTC track in $r\phi$:	$\|x\|_{CES} < 1.5$ cm
the distance between the CES shower position and the extrapolated CTC track in $r\phi$:	$\|z\|_{CES} < 3.0$ cm
a χ^2 comparison of CES shower profile and expectations from test beam data:	$\chi^2_{CES} < 10$
a comparison of lateral shower profile in CEM and expectations from test beam data:	$L_{shr} < 0.2$
the distance between the primary event vertex and the electron track along the z axis:	$\|Z_{p.vertex} - Z_e\| < 5.0$ cm
total event selection efficiency:	$\epsilon_e = 0.84 \pm 0.02$

Table 3.2: Cuts used to select the high P_T, inclusive central electron sample. The total event selection efficiency is measured using a sample of $Z \rightarrow ee$ events.

didate events. The cuts used to identify Z candidate and photon conversion candidate events are discussed below. To keep the two analyses orthogonal, we remove by hand any event passing all of the dilepton cuts described in references [24] [23] [31]. Table 3.3 gives the final event yields as a function of the jet multiplicity. The jet clustering algorithm uses a cone size of $R = \sqrt{(\Delta\phi)^2 + (\Delta\eta)^2} = 0.4$ and is described in detail in reference [41]. The jet multiplicity of the event is calculated as the number of jets in the event with $E_T > 15$ GeV and $|\eta| < 2.0$. Figure 3.1 shows the transverse mass distributions of the final sample for events with at least one jet. The Jacobian peak characteristic of W decay is evident.

After the initial sample selection described above, we identify the second leg of candidate $Z \rightarrow ee$ and $Z \rightarrow \mu\mu$ events using the following cuts.

In the electron sample:

$E_T > 10$ GeV

$E/P < 2.0$

$E_{CHA}/E_{CEM} < 0.12$

$I_{cal} < 0.2$

$75\ \text{GeV}/c^2 < M_{ee} < 105\ \text{GeV}/c^2$

In the muon sample:

$P_T > 10\ \text{GeV}/c$

$E_{CHA} < 10.0(6.0)$ GeV

$E_{CEM} < 5.0(2.0)$ GeV

$I_{cal} < 0.2$

$|x|_{CMU,CMP,CMX} < 5.0$ cm

$75\ \text{GeV}/c^2 < M_{\mu\mu} < 105\ \text{GeV}/c^2$

The second electron leg is allowed to be in the CEM, PEM, or FEM detectors. The second muon leg is allowed to be in the CMU, CMP, or CMX detectors. Additionally, any track traversing a fiducial volume absent of muon coverage is a candidate second

leg if $|\eta| < 1.1$ and it passes the above cuts. For such candidates, known as Central Minimum IOnizing particles (CMIO), the cuts on E_{CHA} and E_{CEM} are tighter and are given above paranthetically.

In the electron sample, we identify the primary electron as having originated from a $\gamma \rightarrow ee$ conversion if there exists an oppositely charged partner track passing these cuts

distance between track pairs in $r-\phi$ plane at tangent point:	$\lvert\Delta(r\phi)\rvert < 0.30$ cm
difference in polar angle at tangent point:	$\lvert\Delta cot\theta\rvert < 0.06$
conversion radius:	$-20cm. < R_{conv} < 50$ cm

To identify those conversion events in which the partner track remains undetected, we removed events in which the primary electron satisfies the cuts

number of expected VTX hits:	$N_{VTX}^{exp} \geq 3$
occupancy of VTX:	$\frac{\text{no. of hits found}}{\text{no. of hits expected}} < 0.2.$

The removal algorithm is over-efficient so that some electrons are mistakenly identified as having originated from a photon conversion. We measure this removal over-efficiency to be $\epsilon_{over} = 0.022 \pm 0.004$ using a sample of $Z \rightarrow ee$ events. Using an idependently identified sample of conversions, we measure the real conversion removal efficiency to be $\epsilon_{conv} = 0.907 \pm 0.038$. Neither of these efficiencies exhibit a dependence on the E_T of the candidate electron.

3.1.5 Control Samples

In order to develop and understand a Btag algorithm it is necessary to quantify both the algorithm efficiency and backgrounds. This is done using both data and

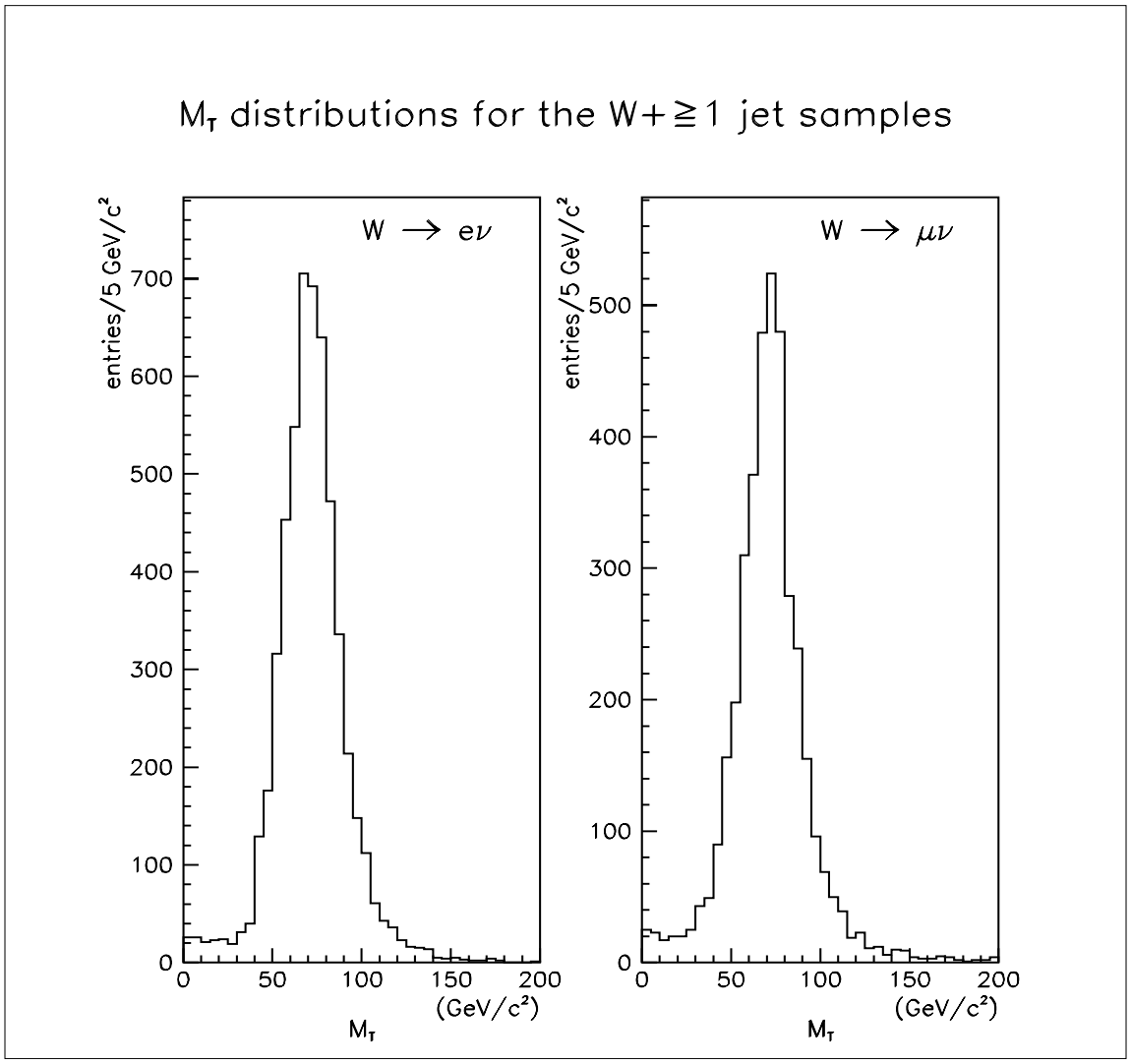

Figure 3.1: Transverse mass distribution for W + $\geq$ 1 jet sample after all selection cuts for the electron and muon samples separately.

jet multiplicity	electrons	muons	total
$1jet$	5640	3891	9531
$2jets$	846	623	1469
$\geq 3jets$	159	137	296

Table 3.3: The event yields after application of all selection criteria including Z, γ conversion, and dilepton candidate removal. Figure 3.1 shows the resulting transverse mass distributions for the electron and muon samples separately.

Monte Carlo samples. Additionally, we use several control samples to help verify our understanding of the backgrounds to the search. Below, these control samples are briefly described and their selection given.

The B-enriched low P_T inclusive electron sample is used to measure the efficiency of the Btag algorithm. The sample selection begins at the trigger level by requiring at Level 1 a CEM cluster with $E_T > 8$ GeV and at Level 2 a CEM cluster with $E_T > 9$ GeV matched to a track with $P_T > 9.2$ GeV/c and $E_{CHA}/E_{CEM} < 0.125$. To further enhance the fraction of events containing a B hadron decay we select only those events passing the cuts listed in Table 3.4. Using ~ 60 pb^{-1} of run 1B data yields approximately 171k events passing all selection criteria.

The inclusive jet samples provide B depleted samples in which we derive and systematically verify our background estimates for the Btag algorithm. These samples require a single tower over threshold at trigger Level 1 and a localized cluster of energy at trigger Level 2. The trigger thresholds used are 20, 50, 70, 100, and 140 GeV. A sixth inclusive jet trigger requires that the scalar sum E_T, ΣE_T, of the event be greater than 300 GeV.

Since the dominant production mechanisms for W and Z^0 bosons in association with jets are very similar, we expect the heavy flavor content of these two samples to be very similar. The "Z plus jets" sample thus provides a natural place in which to

Cuts used to identify $B \rightarrow eX$ enriched sample

cut description:	selection criteria:
transverse energy deposited in CEM tower traversed by electron:	$E_T > 10$ GeV
ratio of CEM energy to total momentum as measured in CTC:	$E/P > 1.8$
distance between CES shower position and the extrapolated CTC track in $r\phi$:	$\|\Delta x\| < 1.5$ cm
distance between CES shower position and the extrapolated CTC track in $r\theta$:	$\|\Delta z\| < 3.0$ cm
comparison of lateral shower profile in CEM and expectations from test beam data	$L_{shr} < 0.2$
isolation of candidate electron track:	$I_{cal} > 0.1$
missing transverse energy:	$\not\!\!E_T < 20$ GeV

Table 3.4: Cuts used to select a B-enriched sample for measuring efficiency of Btag algorithm. Conversion candidate events are removed using the cuts discussed in Section 3.1.4. We require the presence of another jet in the event with $|\eta| < 2.0$, $E_T > 15$ GeV and separated from the electron by ≥ 2.5 units in $\eta - \phi$ space.

look for any anomolous source of background tags not considered in the background estimate. The sample is selected by requiring the primary lepton in the events to pass the cuts described in Sections 3.1.2 and 3.1.3. The second leg is identified using the cuts

In the electron sample:

$E_T > 10$ GeV

$E/P < 2.0$

$E_{CHA}/E_{CEM} < 0.10$

$I_{cal} < 0.1$

$75\ \text{GeV}/c^2 < M_{ee} < 105\ \text{GeV}/c^2$

In the muon sample:

$P_T > 10\ \text{GeV}/c$

$E_{CHA} < 6.0$ GeV

$E_{CEM} < 2.0$ GeV

$I_{cal} < 0.1$

$|x|_{CMU,CMP,CMX} < 5.0$ cm

$75\ \text{GeV}/c^2 < M_{\mu\mu} < 105\ \text{GeV}/c^2$

The second electron leg is allowed to be in the CEM, PEM, or FEM detectors. Both muon legs are allowed to be in the CMU, CMP, or CMX detectors. For muons, the second leg is also allowed to be a CMIO if $|\eta| < 1.1$ and it passes the above muon cuts. The invariant mass distribution for the electron and muon samples together is shown in Figure 3.2.

3.1.6 Monte Carlo Samples

Our analysis employs a variety of Monte Carlo event generators. In determining the $t\bar{t}$ acceptances and efficiencies as discussed in Section 3.5, the B-tag efficiency discussed in Section 3.5.4, and some of the background estimates discussed in Sec-

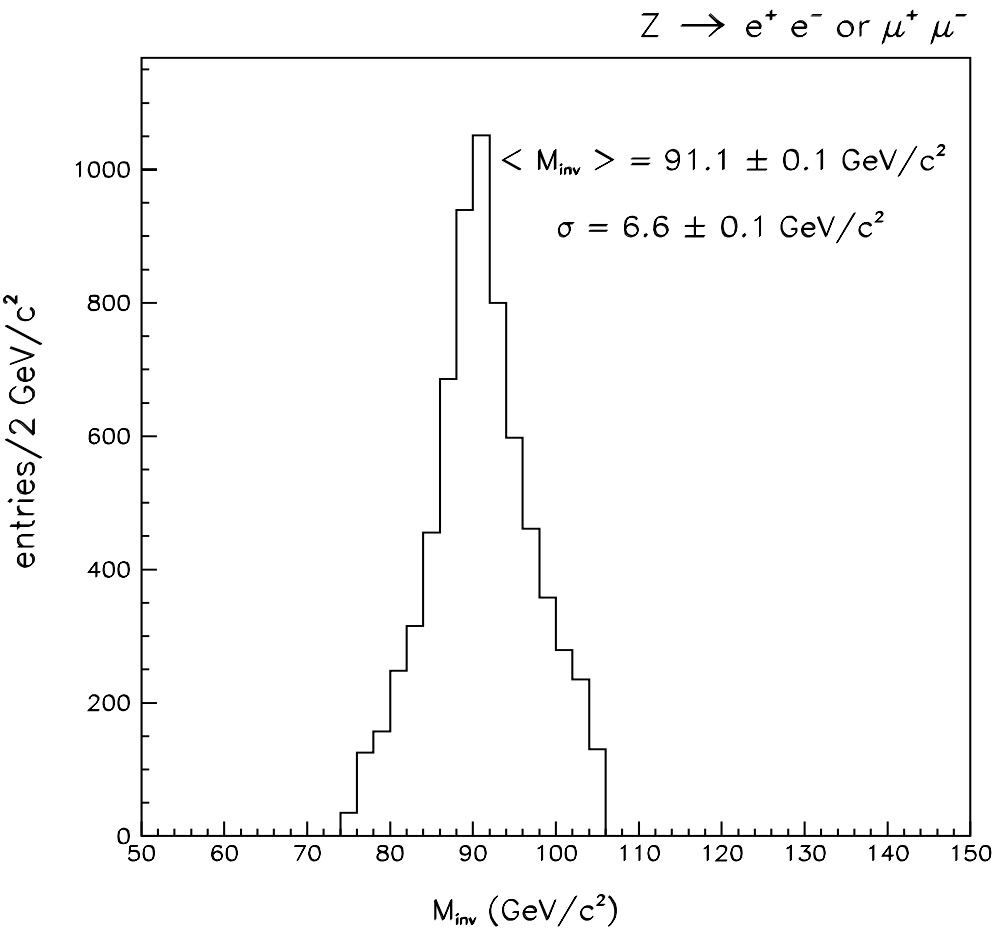

Figure 3.2: Invariant mass distribution for $Z \to ee$ and $Z \to \mu\mu$ events selected as discussed in Section 3.1.5.

tion 3.7, we use the PYTHIA Monte Carlo [42] version 5.6. PYTHIA is a parton-shower Monte Carlo program and is based on leading-order QCD matrix elements for the hard-scattering process, approximately coherent gluon emission, and independent string-fragmentation of the outgoing partons as modeled by JETSET [43] [44]. The effects of minimum bias and underlying events are also included [45] and are tuned to the data. In generated samples of $t\bar{t}$ and $b\bar{b}$ events, we use the CLEO Monte Carlo program [46] to model the decay of B-hadrons.

The HERWIG Monte Carlo generator [47] is used to help determine the mass of the top quark, as discussed in Section 3.10, to estimate some of the backgrounds discussed in Section 3.7, and to assign several systematic errors by comparison to PYTHIA. The HERWIG generator is based on leading order QCD matrix elements for the hard scattering process, followed by coherent parton shower evolution, hadronization, and an underlying event model based on data.

The ISAJET Monte Carlo generator [48] is used to assign systematic errors by comparison to PYTHIA as discussed in Section 3.2.1.

All Monte Carlo samples are processed through a full detector simulation, which models detector responses, efficiencies, and resolutions. Finally, these samples are subjected to the same analysis path as the data, including event reconstruction and selection.

3.2 Development the SVX B-tag Algorithm

As discussed in Section 1.3, after sample selection we expect the signal to noise ratio to be $S/N \sim 1/5$ for events with ≥ 3 jets. To improve this ratio we require that we identify at least one b quark in the event. We employ the excellent position resolution of the SVX detector to "tag" the displaced vertices from b quark decay.

In this Section we discuss the development and optimization of the SVX B-tag algorithm. Figure 3.3 is a schematic representation of an SVX B-tag. Since the SVX has only $r-\phi$ readout, we are sensitive only to displacements in the plane transverse to the beam axis. We define the transverse decay length as

$$L_{xy} = \sqrt{(x_{pvtx} - x_{svtx})^2 + (y_{pvtx} - y_{svtx})^2} \tag{3.1}$$

where

$x_{pvtx}\,(y_{pvtx}) \equiv$ the x (y) coordinate of the primary interaction vertex in the event relative to the nominal interaction point $(0,0,0)$

$x_{svtx}\,(y_{svtx}) \equiv$ the x (y) coordinate of the displaced secondary vertex in the event relative to the nominal interaction point $(0,0,0)$.

We sign L_{xy} by taking the vector dot product of the unit vector $\hat{L_{xy}}$, which points along the vector connecting the primary interaction vertex and the displaced secondary vertex, with the unit vector $\hat{j}$, which points along the axis of the jet with which the secondary vertex is associated.

Some of the tracks originating from the B decay are displaced from the primary $\overline{p}p$ interaction vertex as evidenced by their large impact parameters. Tracks not originating from the B decay extrapolate back to the primary vertex. The primary goal in developing the SVX B-tag algorithm is to identify the decay tracks while discriminating against tracks *not* associated with the B hadron decay. Obviously we want to maximize the efficiency for identifying B jets while minimizing the fake tag or "mistag" rate. Due to detector resolutions and tracking errors, we do not

always discrimnate against tracks *not* associated with the B decay. Mistags arise when such tracks intersect far enough away from the primary vertex to construct a false displaced vertex. These false vertices are not physical and so have an L_{xy} distribution that is symmetric about zero. The vertices from B-decay are real, and should have only $+L_{xy}$ displacements. However, due to detector effects, there is a small $-L_{xy}$ contribution even for B-decays. As discussed more thoroughly in Section 3.7, mistags constitute a major source of background.

The development of the B-tag algorithm takes place in four parts. In Section 3.2.1 we begin with a generator level study of B hadrons from top quark decay. In Section 3.2.2 we develop an accurate simulation of the SVX′ detector. In Section 3.3.1 we develop several sets of cuts to identify high quality tracks. Finally, in Section 3.3.2 we choose the final algorithm based on "discovery probability".

3.2.1 Generator Level Study of B Hadron Decay in Top Quark Events

We begin our development of a B-tag algorithm by characterizing the decay of B hadrons in top quark decay. We use as our default generator PYTHIA [42] with a top quark mass of 160 GeV/c^2. We use the CLEO Monte Carlo [46] to model the decay of the B jets and the Peterson parameterization [49] [50] to model the fragmentation and hadronization of the b quark. We begin at the generator level in order to isolate the decay kinematics of the B hadrons from detector effects. We additionally investigate any systematic effects due to uncertainties in initial state radiation, fragmentation parameters, and B hadron decay tables. Figure 3.4 shows several kinematic distributions for B hadrons from the decay of 160 GeV/c^2 top quarks. The B hadrons are well boosted with an average P_T of 40 GeV/c and 80% of them lie in the region $|\eta| < 1.0$. The combination of the long B lifetime and the boost from a heavy top quark decay results in a mean transverse displacement of $< L_{xy} >= 0.34$ cm from the primary interaction vertex. The mean transverse displacement of the sequentially decaying charmed hadron is 0.18 cm from the B

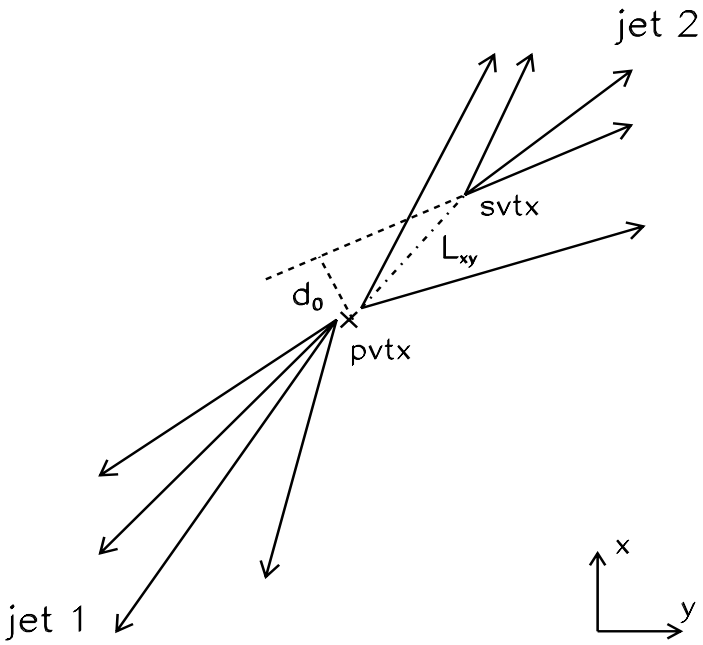

Figure 3.3: Schematic of an SVX B-tag. The presence of a long lived particle in jet 2 is signaled by the presence of a secondary vertex (svtx), whose transverse displacement, L_{xy}, is measured in the $x - y$ plane of the detector. We identify tracks associated with the secondary vertex by requiring a large impact parameter, d_0, with respect to the primary vertex (pvtx).

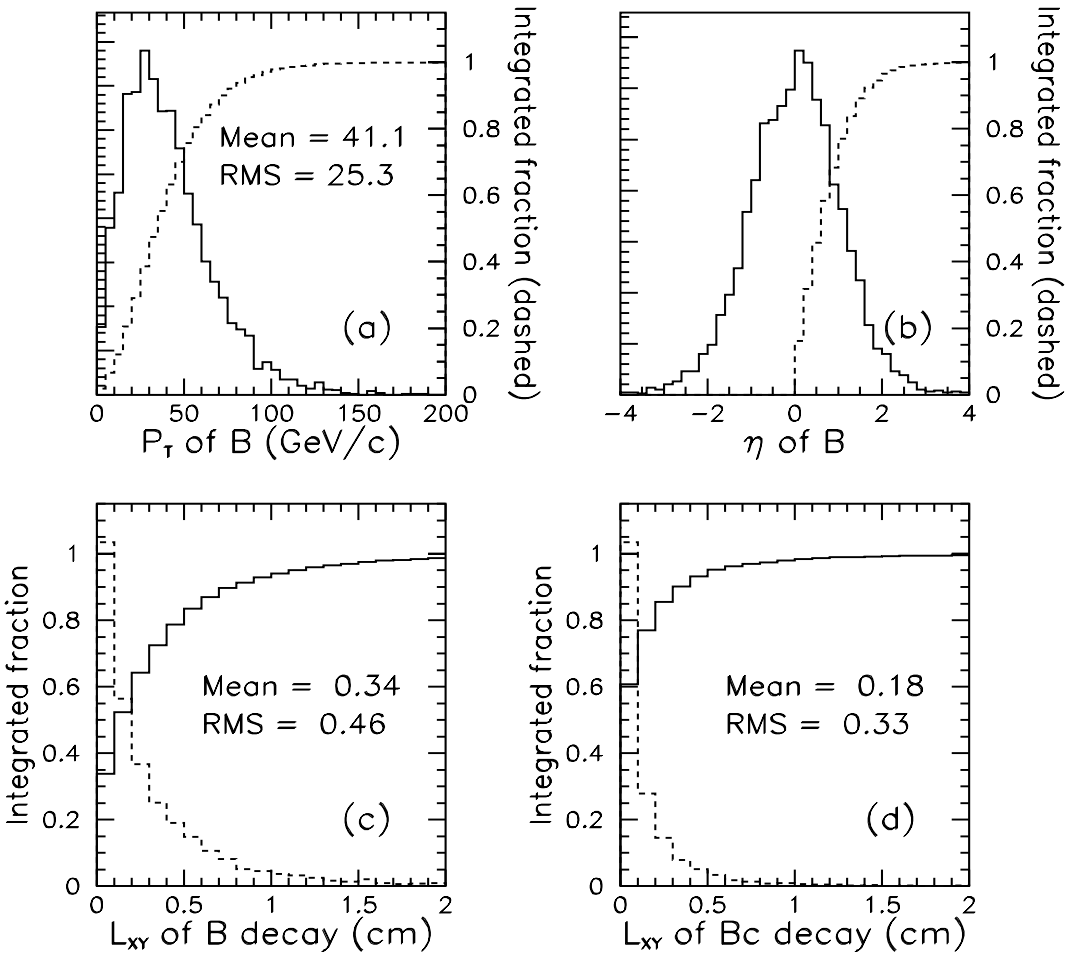

Figure 3.4: Properties of B jets in heavy top quark decay (M_{top} = 160 GeV/c^2). The P_T and η distributions of the B jet are shown in (a) and (b). The transverse decay length, L_{xy}, of the B hadron from the primary vertex is shown in (c) and the L_{xy} distribution of the charmed hadron with respect to the B decay vertex is shown in (d). For each plot both the differential and the integrated distributions are shown.

decay vertex. Displacements as large as this are readily resolvable using the SVX, which has a vertex resolution on the order of 30 μm.

In studying the structure of B jets we consider only those particles which are readily detectable and easily associated with the B jet experimentally. We consider the stable charged particles $\pi^{\pm}$, $K^{\pm}$, $p^{\pm}$, $e^{\pm}$, and $\mu^{\pm}$ and require that they lie within a cone of $\Delta R = \sqrt{\Delta\phi^2 + \Delta\eta^2} < 0.4$ around the B jet axis. In practice, tracks with $P_T < 0.4$ GeV/c curl in the CDF magnetic field and tend to be poorly measured. Therefore, we only consider tracks with $P_T > 0.5$ GeV/c. Tracks are classified according to whether they're associated with 1) the fragmentation and hadronization of the b quark, "prompt tracks", 2) the B decay vertex, "B tracks", or with 3) the sequential charm decay vertex, "BC tracks".

The kinematic distributions considered are cone size, P_T, impact parameter, impact parameter significance ($S_{d_0} = d_0/\sigma_{d_0}$), and minimum $r\phi$ separation of a given track at each layer of the SVX. The distribution means are summarized in Table 3.5, where the effects of various systematic changes are also summarized. The cone size is defined as the distance between a given track and the B jet axis in $\eta - \phi$ space and is plotted in Figure 3.5. A cone size of $\Delta R < 0.4$ retains 90% of tracks from B decay, while rejecting 65% of prompt tracks.

Figure 3.6 shows the P_T distributions. Tracks from B decay have a mean P_T of 5.4 GeV/c, while the prompt tracks have a much softer distribution with a mean P_T of < 3.0 GeV/c. As demonstrated in Figures 3.7 and 3.8 the tracks from B decays have impact parameter distributions with long tails. In Figure 3.8 we parameterize the impact parameter measurement error as $\sigma_{d_0} = \sqrt{10^2 + 13^2 + (60/P_T)^2}\mu$m, where the first, second, and third terms correspond to the error on the position of the primary interaction vertex, the intrinsic SVX resolution, and the multiple scattering contribution respectively.

As illustrated in Figure 3.9, in the SVX, tracks whose charge clusters are very near one another ($\Delta r\phi \leq 240$ μm) will have those clusters merged or "shared". As a result, the cluster centroid is systematically shifted so that tracks with many shared

MC		PYTHIA				ISAJET	HERWIG
quantity	source	default	softer	harder	no-ISR	default	default
P_T of B hadron		41	37	43	41	43	37
	prompt	2.94	3.30	2.50	3.20	3.07	3.64
no. of tracks	B vertex	2.50	2.49	2.54	2.53	2.50	2.51
in cone 0.4	c vertex	2.42	2.36	2.42	2.48	2.34	2.41
P_T	prompt	2.97	3.13	2.91	2.97	2.43	2.81
(GeV/c)	B vertex	5.43	5.24	5.73	5.56	5.93	5.15
in cone 0.4	c vertex	5.39	5.04	5.58	5.37	5.55	4.90
minimum	prompt	0.12	0.12	0.12	0.12	0.11	0.11
$\Delta r\phi$	B vertex	0.12	0.11	0.11	0.11	0.10	0.10
(cm.)	c vertex	0.11	0.11	0.11	0.11	0.10	0.10
Eff:$P_T > 2$ GeV/c,$S_{d_0} > 3$.		0.55	0.53	0.56	0.55	0.54	0.54

Table 3.5: Summary of B jet decay properties (mean values) from the various Monte Carlo conditions for $t\bar{t}$ events (M_{top} = 160 GeV/c^2). Our default configuration is given in the first column.

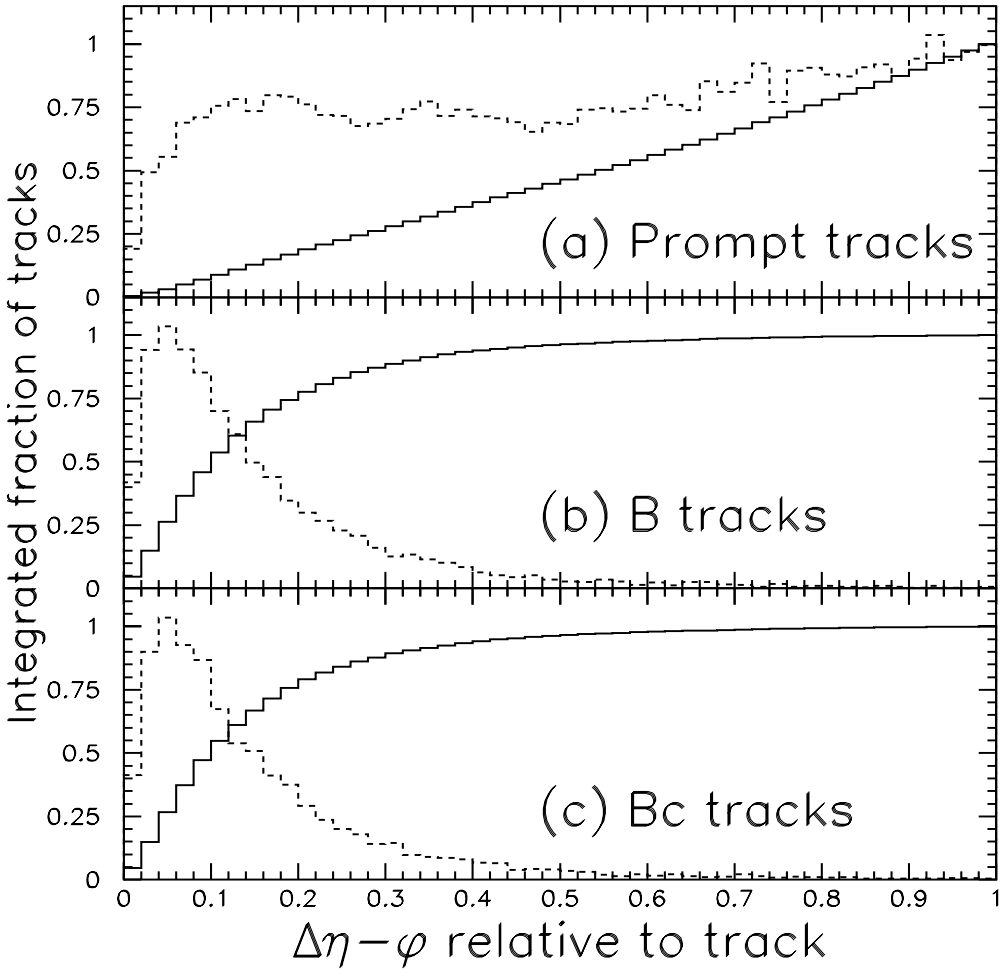

Figure 3.5: The distance between a given track and the B jet axis in $\eta - \phi$ space for fragmentation tracks (a), B decay tracks (b), and sequential charm decay tracks, BC tracks (c). In each plot, we show the integral (solid) and differential (dashed) distributions.

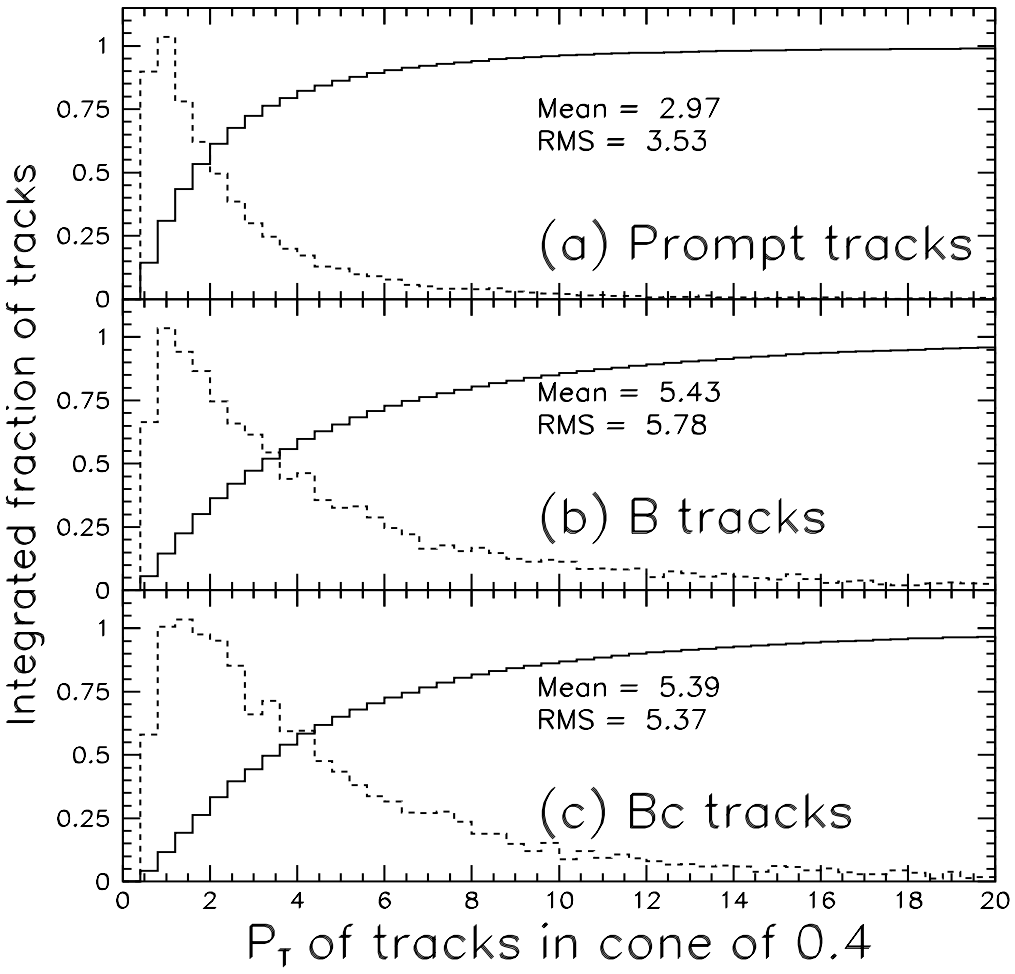

Figure 3.6: The P_T distribution for fragmentation (a), B decay (b), and sequential charm decay (c) tracks. Both the integral (solid) and differential (dashed) distributions are shown.

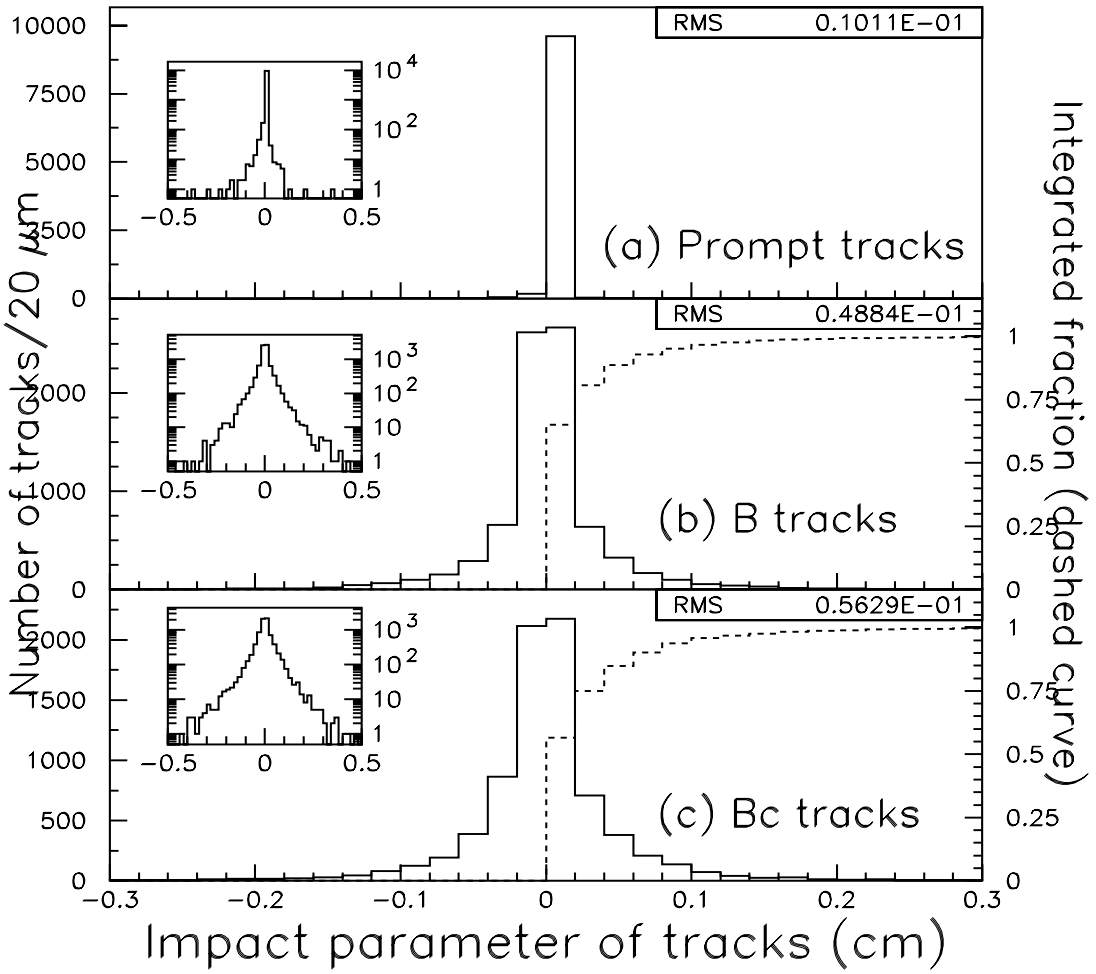

Figure 3.7: The impact parameter, d_0, distribution for fragmentation (a), B decay (b), and sequential charm decay (c) tracks. The sign of d_0 is given by the sign of the charge of the particle. Both the integral (dashed) and differential (solid) distributions are shown. Note that the integral distribution is for $|d_0|$.

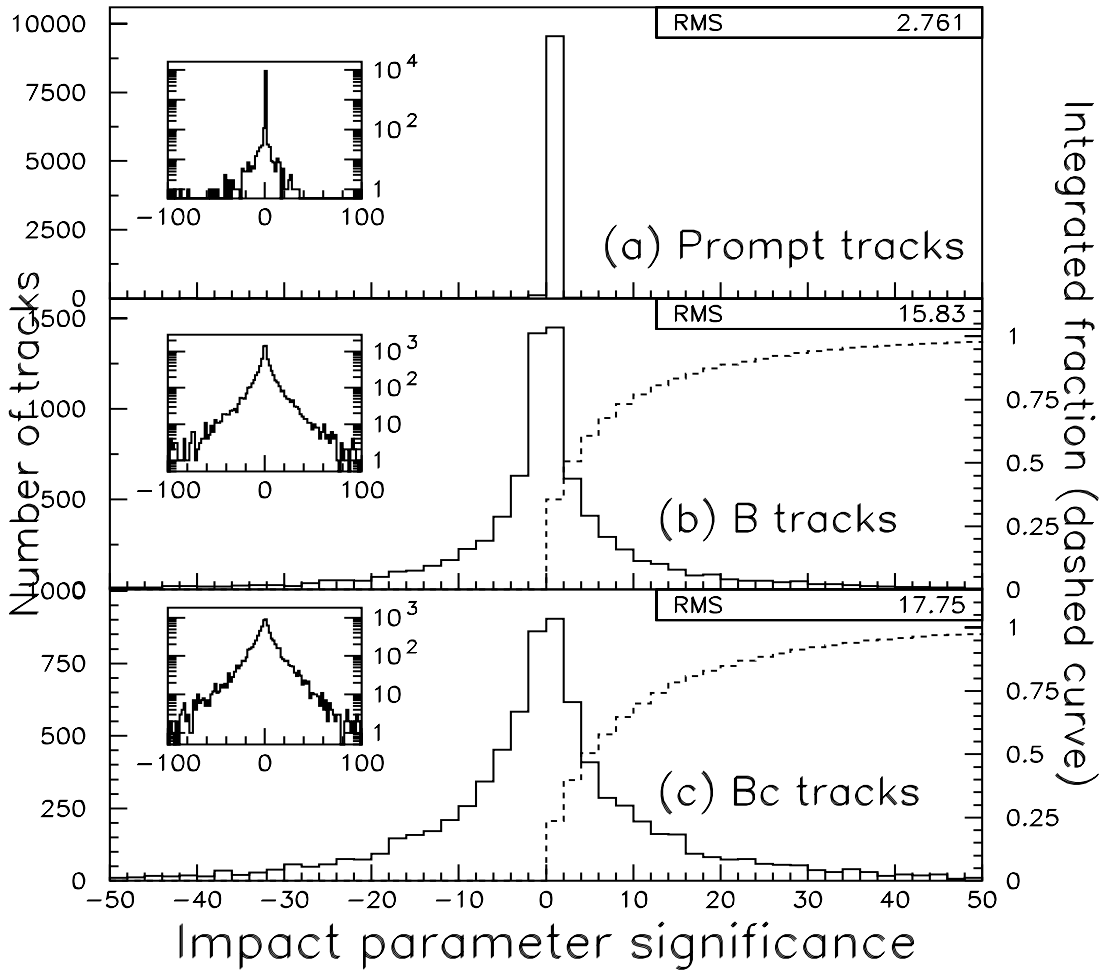

Figure 3.8: The impact parameter significance, $S_{d_0} = d_0/\sigma_{d_0}$, distribution for fragmentation (a), B decay (b), and sequential charm decay (c) tracks. Both the integral (dashed) and differential (solid) distributions are shown. Note that the integral distribution is for $|S_{d_0}|$.

clusters are poorly measured. To better understand the effects of cluster sharing in B jets from top quark decay, we calculate, for each track, the distance in the $r-\phi$ plane to the nearest other track at the inner (L0) and outer (L3) layers of the SVX. These distributions are shown in Figures 3.10 and 3.11 respectively. At layer 0, clusters from decay tracks lie within 240μm of some other cluster 35% of the time. It is interesting to note that the nearest cluster is as likely to be associated with a fragmentation track as it is with a decay track. The average separation at layer 0 is about 0.6 mm and scales linearly with the detector radius. We quantify the effects of sharing multiple clusters by defining for each track a minimum search road, centered on that track, in which N clusters from some other track(s) are found. We consider $N = 2, 3, 4$. The integral distributions are given in Figure 3.12. We find that 15% of tracks have 2 clusters within 240μm of some other track - i.e. have 2 shared clusters - and 5% share all 4 clusters.

We conduct a generator level B-tag optimization by calculating the acceptance for several sets of kinematic cuts. We measure the fraction of B jets passing various track multiplicity, P_T, and impact parameter significance cuts. The strategy is to *loosen* the kinematic cuts as much as possible, but to require that *at least three tracks* pass all the cuts. Mistagged vertices tend to have low track multiplicity. By requiring more tracks in the vertex we hope to keep the mistag rate low. We tally a B jet as "tagged" if at least three tracks survive a "first pass" set of loose cuts to yield a 3 track vertex (3tk vtx), or if two tracks survive a "second pass" set of tight cuts ($P_T > 2.0$ GeV/c and $S_{d_0} > 3.0$) to yield a 2 track vertex (2tk vtx). We require the tracks to be within a cone of $\Delta R < 0.4$ about the B jet axis and consider for the "first pass" the cut combinations $P_T > 0.5, 1.0, 1.5, 2.0$ GeV/c and $S_{d_0} > 2.0, 2.5, 3.0$. For a given set of pass 1 - pass 2 cuts we calculate the acceptance as the fraction of B jets which are tagged. The resulting acceptances are given in Table 3.6. In order to quantify the effects of cluster sharing, we repeat the acceptance determinations with the added requirement that tracks have a minimum $\Delta r\phi$ separation of > 240 μm from the nearest other track. Comparing the best

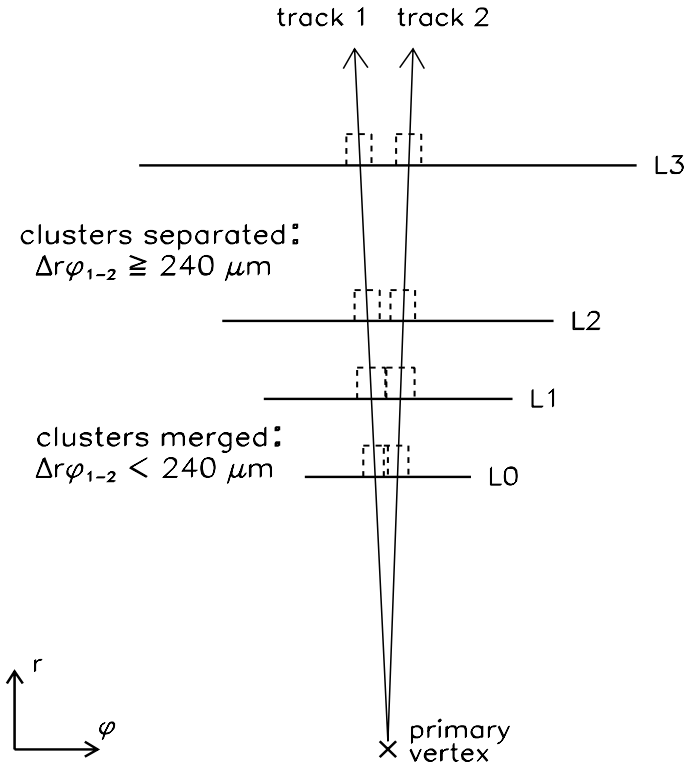

Figure 3.9: A schematic showing the merging, or "sharing", of clusters. When two tracks intersect a layer of the SVX within $< 240\mu$m of each other, their individual charge clusters will be merged. This is demonstrated in layers 0 and 1 above. At the outer layers the clusters are far enough apart to be individually resolved.

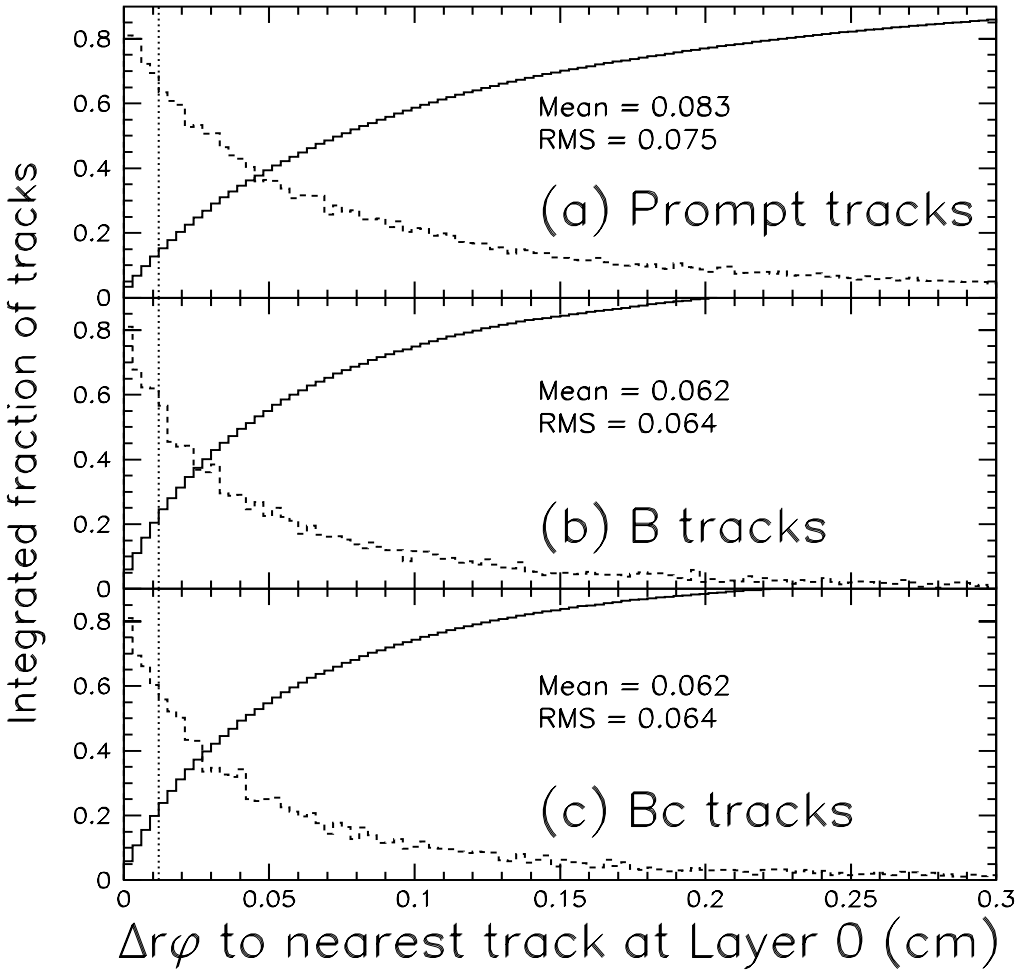

Figure 3.10: The minimum separation in $\Delta r\phi$ at the innermost layer of the SVX (L0) for fragmentation (a), B decay (b), and sequential charm decay (c) tracks. Both the integral (solid) and differential (dashed) distributions are shown. The dotted line corresponds to $\Delta r\phi = 120$ μm - a 2 strip separation.

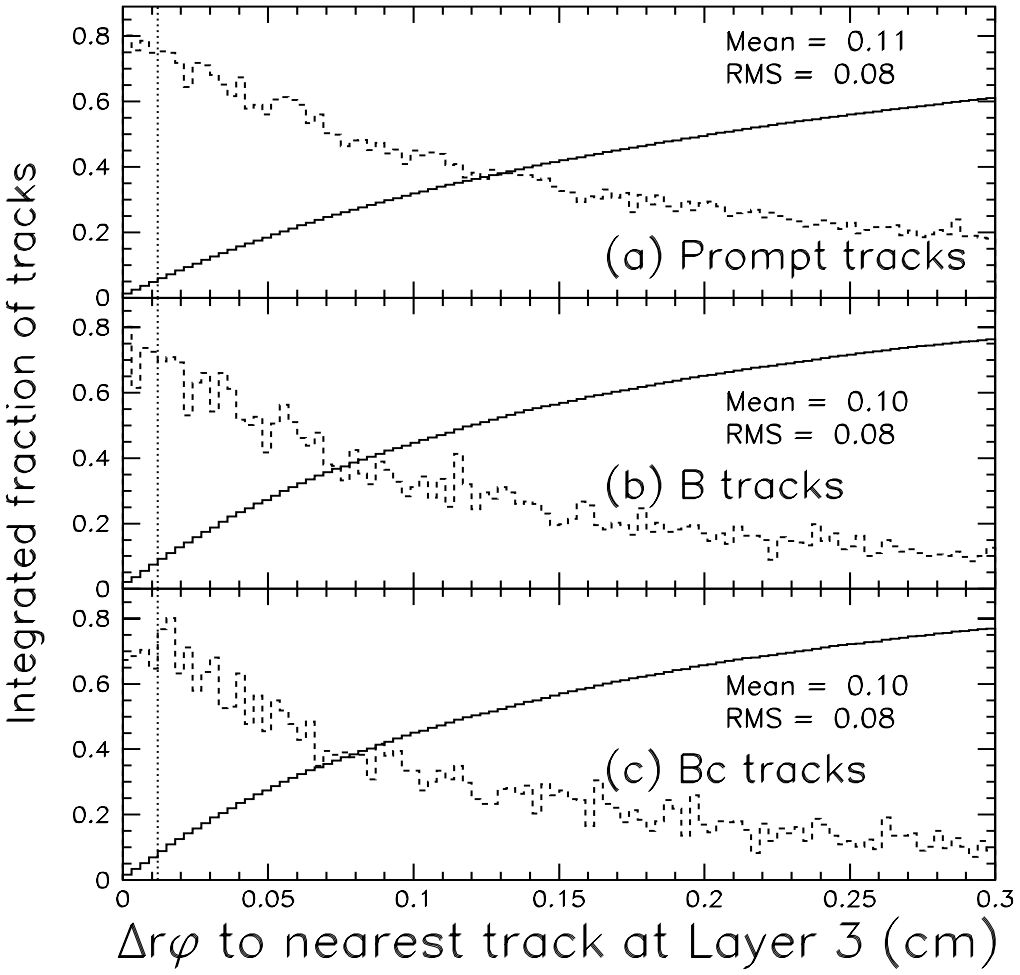

Figure 3.11: The minimum separation in $\Delta r\phi$ at the outermost layer of the SVX (L3) for fragmentation (a), B decay (b), and sequential charm decay (c) tracks. Both the integral (solid) and differential (dashed) distributions are shown. The dotted line corresponds to $\Delta r\phi = 120$ μm - a 2 strip separation.

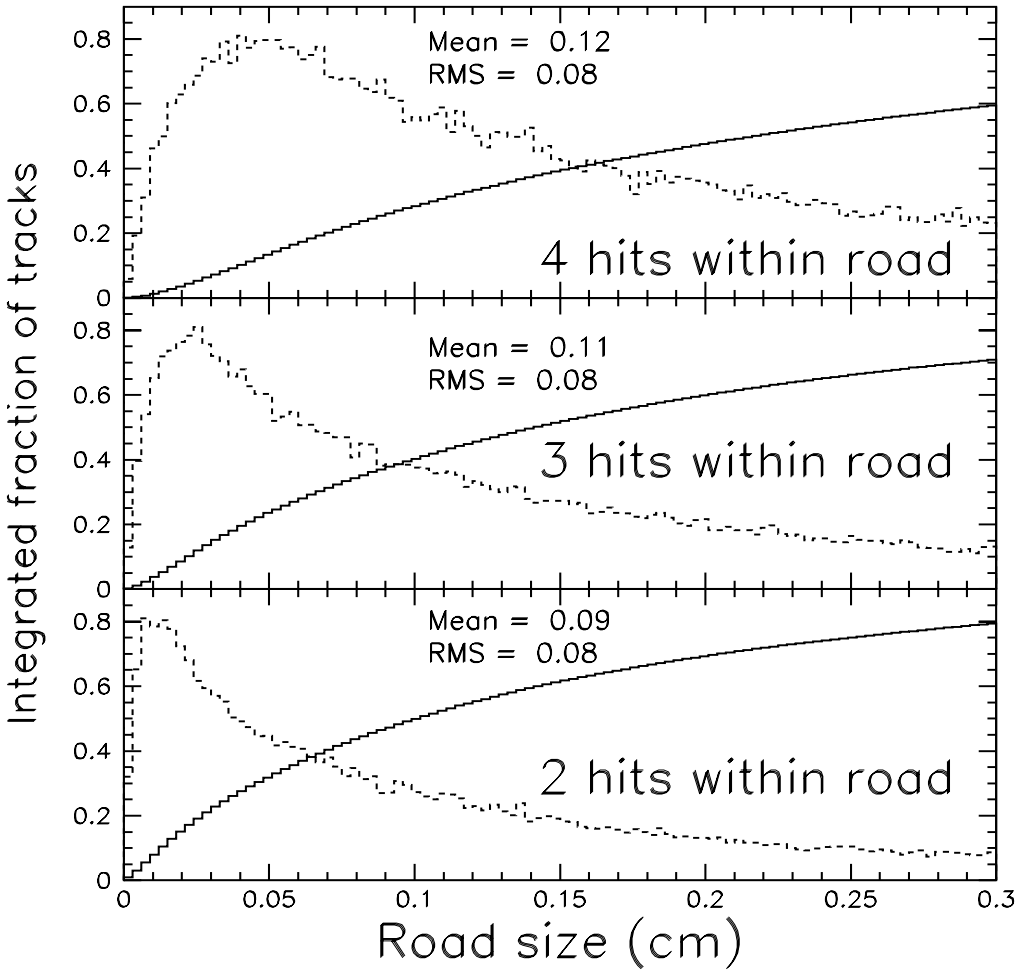

Figure 3.12: The integrated (solid) and differential (dashed) distributions of the minimum road size, centered on a given track, required to include four (a), three (b), and two (c) hits from some other track(s).

and worst acceptances, we find a difference of 20% (relative) in acceptance and a substantial increase in the fraction of 3 track vertices as the P_T requirement is loosened. In addition, we find the minimum separation requirement reduces the acceptance by 17% relative. The effects of individual P_T (S_{d_0}) cuts can be drawn from Figure 3.13 (3.14), which shows the P_T (S_{d_0}) distributions for the three highest P_T (S_{d_0}) tracks. The tracks with highest P_T each have similar S_{d_0} distributions and vice versa as demonstrated in Figures 3.15 and 3.16.

$P_T \geq$	$S_{d_0} \geq$	$\Delta r\phi \geq 0.$		$\Delta r\phi \geq 0.024$ cm	
		total	3tk vtx	total	3tk vtx
0.5	2.0	0.64	0.56	0.55	0.45
GeV/c	2.5	0.60	0.50	0.52	0.39
	3.0	0.58	0.46	0.50	0.35
1.0	2.0	0.61	0.52	0.52	0.40
GeV/c	2.5	0.58	0.46	0.49	0.35
	3.0	0.57	0.43	0.48	0.32
1.5	2.0	0.58	0.45	0.49	0.33
GeV/c	2.5	0.56	0.41	0.48	0.29
	3.0	0.56	0.37	0.47	0.27
2.0	2.0	0.56	0.39	0.47	0.28
GeV/c	2.5	0.55	0.35	0.46	0.25
	3.0	0.55	0.32	0.46	0.23

Table 3.6: The acceptance as a function of P_T and S_{d_0} cuts for B jets in $t\bar{t}$ events ($M_{top} = 160$ GeV/c^2) per B jet.

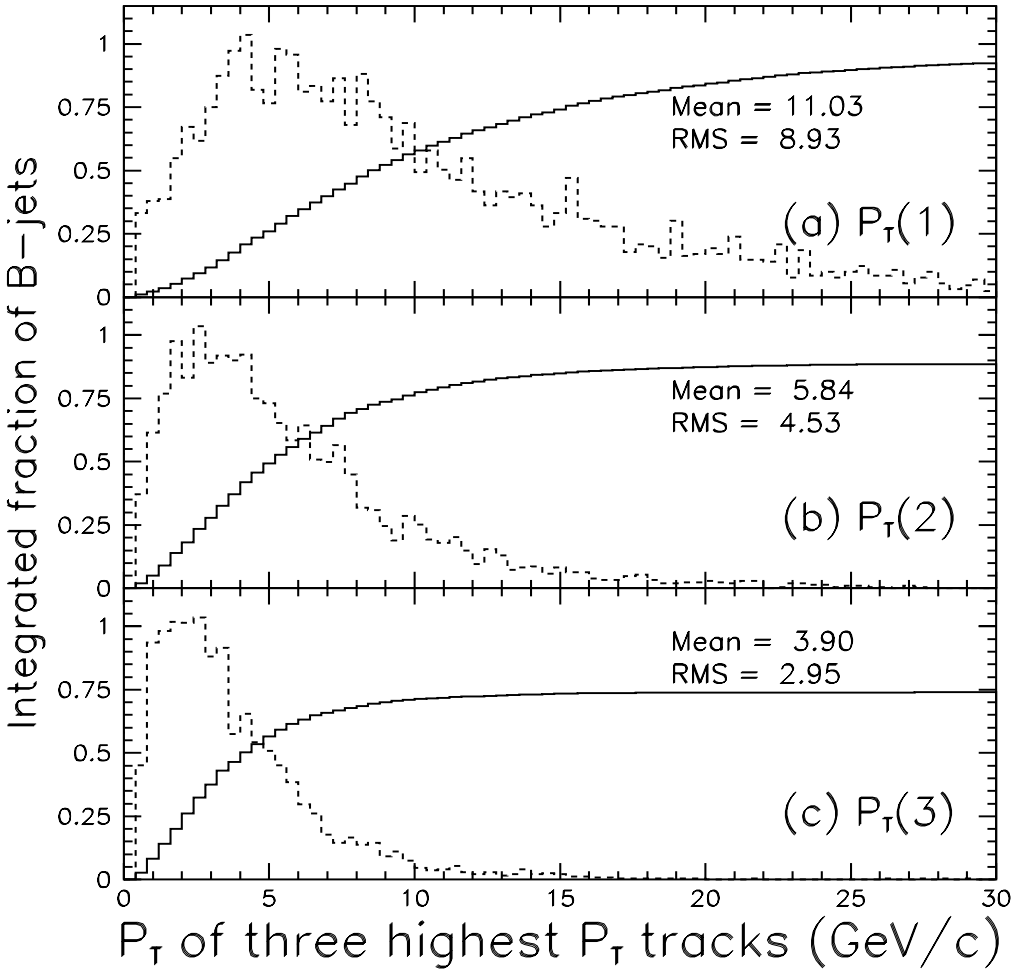

Figure 3.13: The integral (solid) and differential (dashed) P_T distributions for the three highest P_T tracks. Only tracks from B and sequential charm decay are considered.

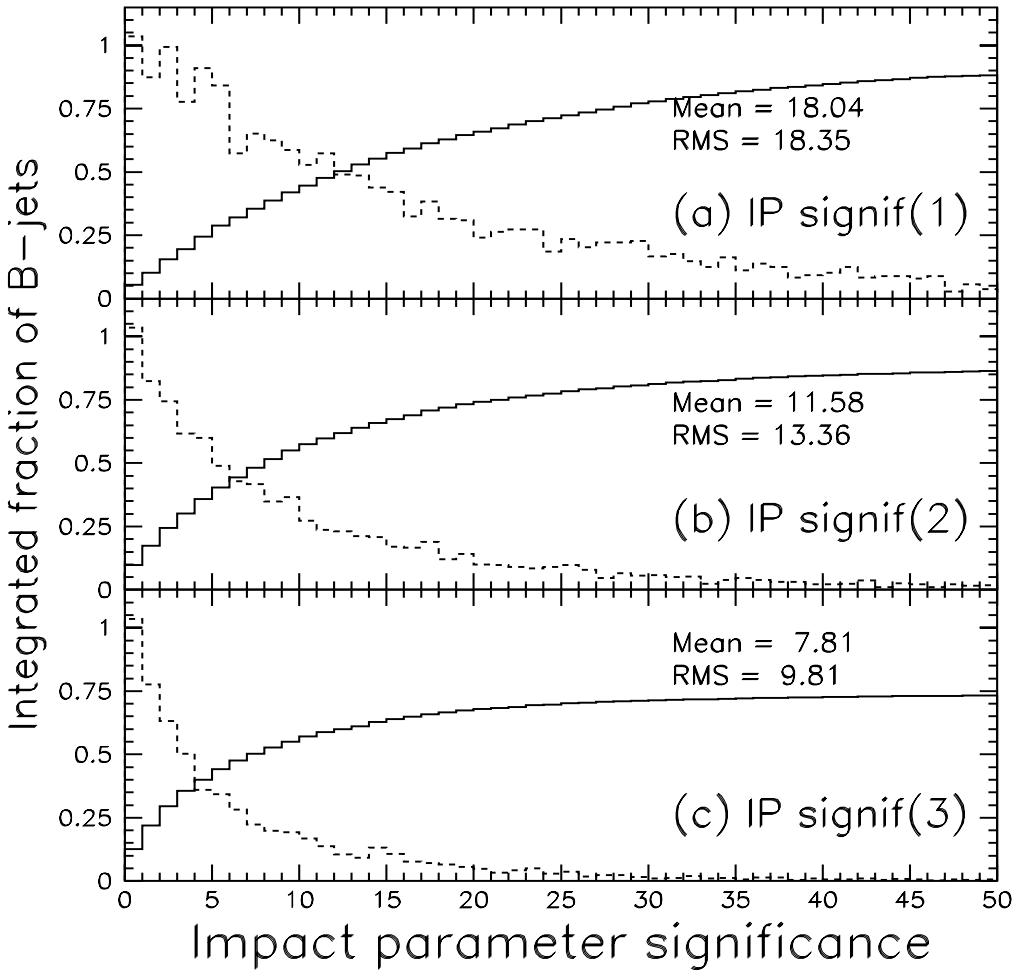

Figure 3.14: The integral (solid) and differential (dashed) S_{d_0} distributions for the three most significantly displaced tracks. Only tracks from B and sequential charm decay are considered.

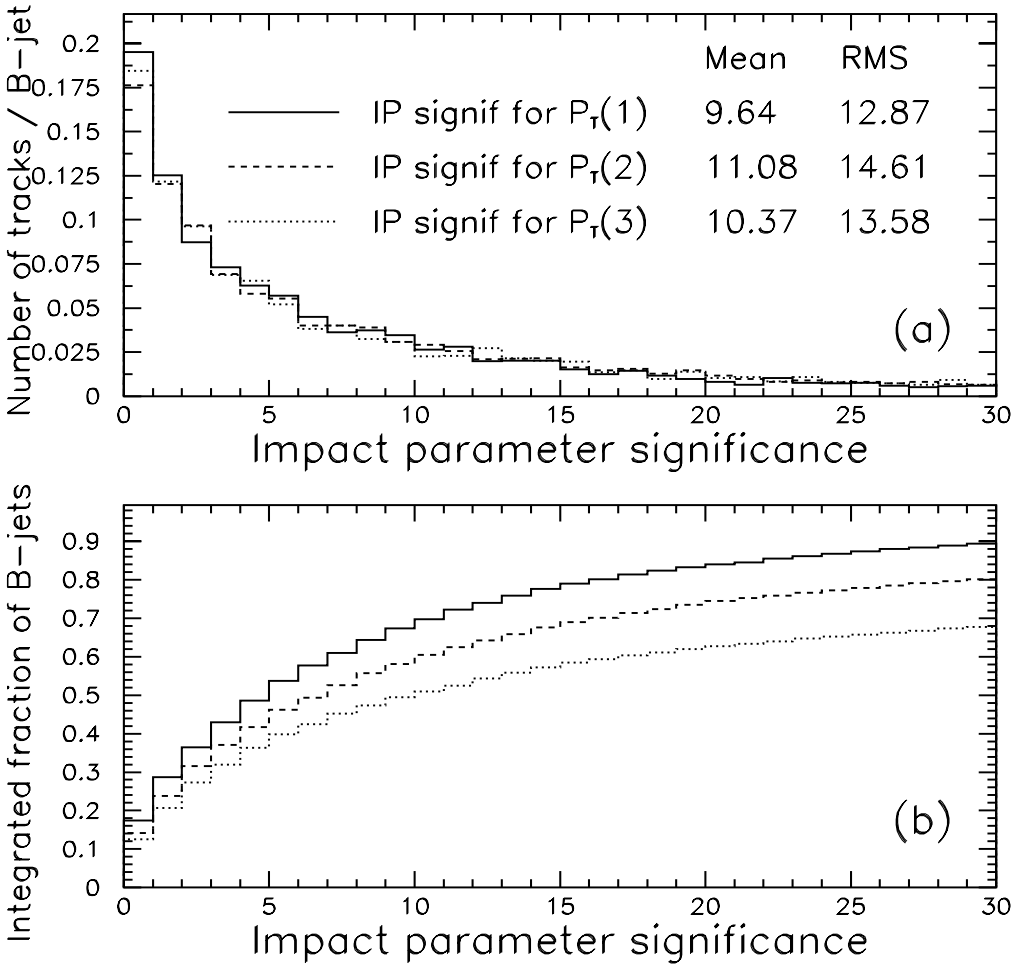

Figure 3.15: The differential (top) and integral (bottom) S_{d_0} distributions for the three highest P_T tracks. Only tracks from B and sequential charm decay are considered.

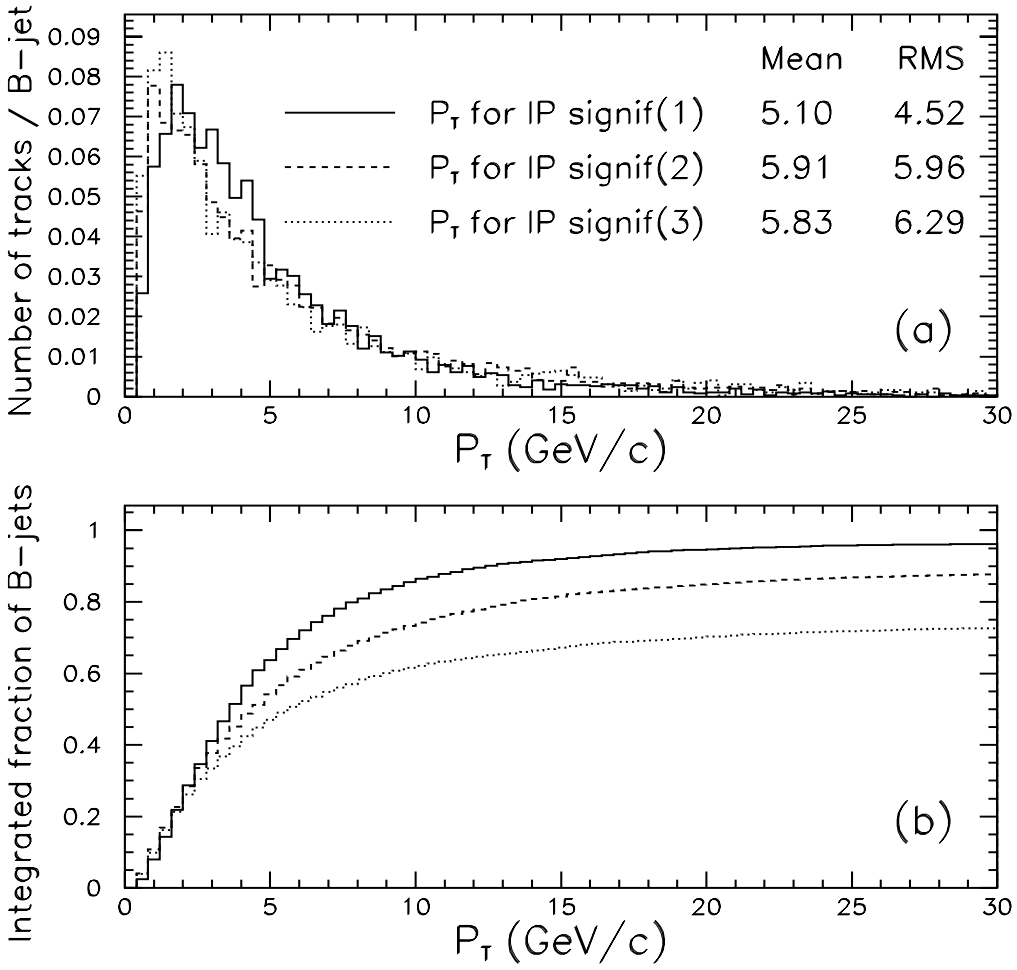

Figure 3.16: The differential (top) and integral (bottom) P_T distributions for the three most significantly displaced tracks. Only tracks from B and sequential charm decay are considered.

Systematic Investigations

The final states of B jets depend on the fragmentation and decay of the B hadron. Below we briefly describe the variations made to our default settings to systematically quantify the effects of changing the fragmentation and decay properties of the B hadron. The results are summarized in Table 3.5, where we observe that the overall B jet tagging efficiency (for a given set of cuts from Table 3.6) is only very marginally affected by these changes - varying by less than 5% relative.

As our default fragmentation model, we use the Peterson parameterization [49] with $\epsilon_b = 0.006$, which is determined by fitting LEP data [50]. To investigate what effect varying the fragmentation paramertrization has on the B jet kinematics we vary the Peterson parameter by $\pm 3\sigma$ about the LEP measured value. We consider the cases

softer fragmentation $\epsilon_b = 0.015$, $x(E_b) = 0.66$

default fragmentation $\epsilon_b = 0.006$, $x(E_b) = 0.70$

harder fragmentation $\epsilon_b = 0.001$, $x(E_b) = 0.75$.

We additionally investigate the effect of disabling initial state radiation (ISR). All these results are summarized in Table 3.5, where we find that they marginally affect the B jet kinematics.

As our default B hadron decay table we use the CLEO Monte Carlo [46]. We compare the B jet kinematics when we use the default PYTHIA decay table, JETSET. We find that the decay track multiplicity and mean P_T are affected at the 10% level, while the remaining distributions are unchanged. The effect of the decay tables is concluded to be small.

Lastly, we compare the kinematics of B jets using various Monte Carlo generators, which differ in their underlying event generation, fragmentation parameterization, and B hadron decay tables. We use PYTHIA as our default generator and compare to HERWIG [47] and ISAJET [48]. With each generator we make a $t\bar{t}$ sample

with a mass of 160 GeV/c^2. Again, the results are summarized in Table 3.5. The differences are small.

3.2.2 Monte Carlo Simulation of the SVX′ Detector

The prominent role played by the SVX in this analysis necessitates a faithful detector simulation. In this section, we develop an accurate simulation of charge deposition from a study of unbiased clusters on tracks. For our purposes, a cluster is any set of contiguous microstrips over charge threshold taken to signal the passage of a charged particle through the silicon. The distribution of charge among the strips included in the cluster is called the cluster profile. The purpose of this study is then the characterization of cluster charge and profile. Our assumption is that an accurate simulation of the detector at this fundamental level will naturally result in an accurate reproduction of the data at a more sophisticated level. As will be seen, this is born out. The importance of understanding cluster formation is underscored when we recall the results of our generator level study of B-tag efficiencies (cf. Table 3.6). We found that cluster sharing can reduce the B-tag efficiency by as much as 15%. Since we will ultimately have to trust a Monte Carlo to "measure" the B-tag efficiency in Top quark events, it is necessary that we trust that simulation at all levels.

We use the data to parameterize the fundamental characteristics of cluster formation. Cluster charge and profile are understood in terms of the microstrip geometry, ionization energy loss (dE/dx), particle pathlength, and secondary ionization processes (ie. $\delta-$rays) [53]. To account for noise and threshold variations across the detector, we use the CDF database to obtain real noise and threshold values from calibrations of the SVX′ detector.

Figure 3.17 depicts the passage of a charged track through a silicon wafer. The wafer is 300 μm thick with a strip pitch of 60 (55) μm on layers 0,1, and 2 (3). For each track we define the point at which the track intersects the silicon as x_{int} (the local $r\phi$ position on the ladder calculated at the center of the silicon wafer). We use an unbiased fitting procedure to estimate x_{int} with a resolution on the order of 8 μm. The two strips bounding the intersection point are called the "core strips".

The "left" core strip is that strip for which $x_{strip} - x_{int} < 0$, while the "right" core strip is that strip for which $x_{strip} - x_{int} > 0$. While it is always possible to define the core strips, a cluster does not necessarily include both these strips since a strip's charge need not exceed the charge threshold required for inclusion in the cluster. Thus, clusters are divided into two classes according to whether one or both of the core strips are above threshold.

Tracks at normal incidence tend to yield one or two strip clusters. The mechanisms for lengthening the cluster to include more than two strips are

- pathlength: particles traversing the silicon far from normal incidence deposit charge across more strips
- cross-talk: neighboring strips are capacitively coupled through the bulk silicon
- noise fluctuations: a strip can be added to a cluster if its noise fluctuates above threshold
- long range $\delta-$rays: a small fraction of the time secondary ionization is produced which is energetic enough to travel across multiple strips, which are then included in the cluster.
- cluster sharing: when two tracks are within 240 μm of each other, their clusters may merge to form a single, long cluster

For the purposes of this study, we assume that clusters shared by multiple tracks will be well modeled by the superposition of each individual track cluster. The total cluster charge distribution, Q_{TOT}, for shared clusters is compared in Figure 3.18 to the Q_{TOT} distribution of isolated clusters. As evidenced by the multiple peaks this assumption is a reasonable one. We then include in our study *only those clusters associated with well isolated tracks.* The cluster length and total cluster charge distributions are shown in Figure 3.19 for the tracks used in this study. To minimize the uncertainty in x_{int}, we study only layer 1 clusters associated to tracks with hits on all 4 silicon layers. The other 3 hits (layers 0, 2, and 3) are required to have

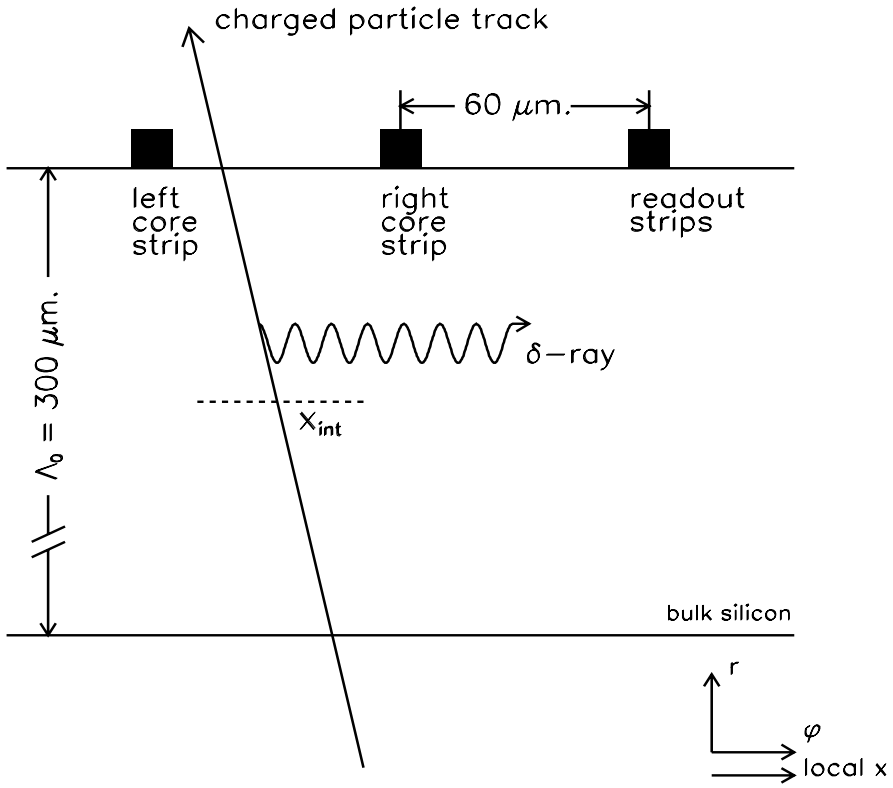

Figure 3.17: Schematic of a charged particle passing through one layer of the SVX. The silicon wafers used in the SVX are 300 μm thick with a strip pitch of 60 μm. The intersection point, x_{int}, of the track is measured at the wafer's center in the $r-\phi$ plane. We define the "core" strips as those bounding the intersection point. The "left" ("right") core strip has $x_L(x_R) - x_{int} < (>)0$.

$\leq$ 2 strips (for which the hit resolution is smallest) and $Q_{TOT} < 300$ ADC counts (an implicit isolation requirement). We use layer 1 clusters for two reasons:

- the errors on interpolating x_{int} into layers 1 and 2 are smaller than the errors on extrapolating x_{int} out to layers 0 and 3
- layer 1 is less affected by multiple scattering than layer 2.

To reduce further the effects of multiple scattering we require $P_T > 1$ GeV/c. To enhance further the track quality, we require that the SVX track stub match to a high quality CTC track stub. More stringent isolation requirements do not affect the cluster charge distributions or profiles. These requirements yield a sample of 150,000 layer 1 clusters.

From Figure 3.19(top) we observe that more than 85% of clusters have less than or equal to 2 strips. This can be readily understood by considering that:

(a) tracks generally intersect the silicon near normal incidence — $\Delta\phi < 15^\circ$ for 90% of the tracks (this corresponds to a pathlength difference of $\lambda/\lambda_0 = 1.04$)

(b) the intrinsic interstrip coupling capacitance is $< 1/10$ of the effective readout capacitance so that cross talk is a small effect

(c) the high signal to noise of the SVX allows a threshold of $> 2\sigma_{noise}$ so that noise fluctuations are infrequently included in the cluster

(d) the probability of emitting a long range $\delta-$ray is $< 5\%$ [54].

We then divide a cluster into two parts, alluded to earlier as, 1) the core strips and 2) the additional strips. The parameterization of each of these parts and their correlations with track parameters and with each other will be discussed separately in the following sections.

The Core Cluster

We begin with the sample of 150,000 layer 1 clusters selected as described in Section 3.2.2. We divide the sample into bins according to the incidence angles of the

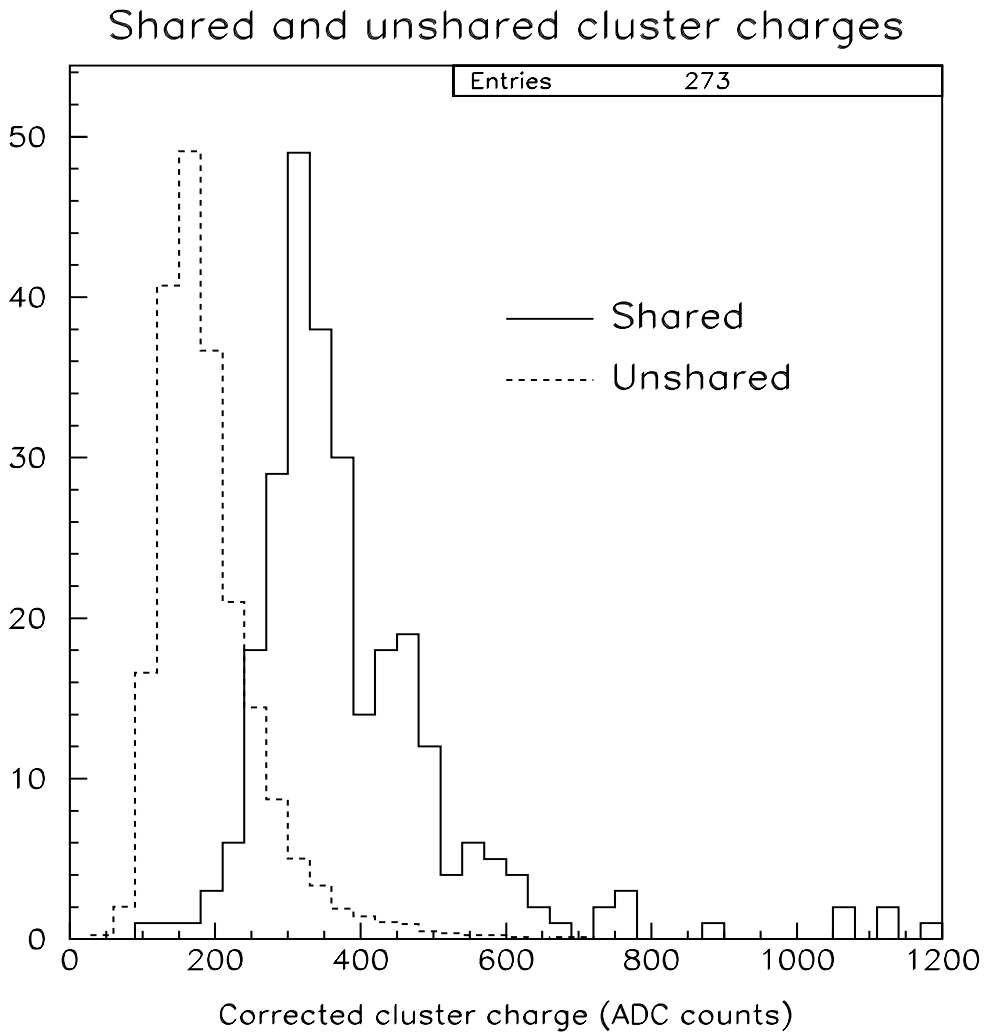

Figure 3.18: The total cluster charge, Q_{TOT}, corrected for the track pathlength through the silicon for shared clusters (solid) and for unshared clusters (dotted). The peaks in the shared cluster distribution occur every $\sim$ 150 ADC counts, which is the median charge deposition for a single track.

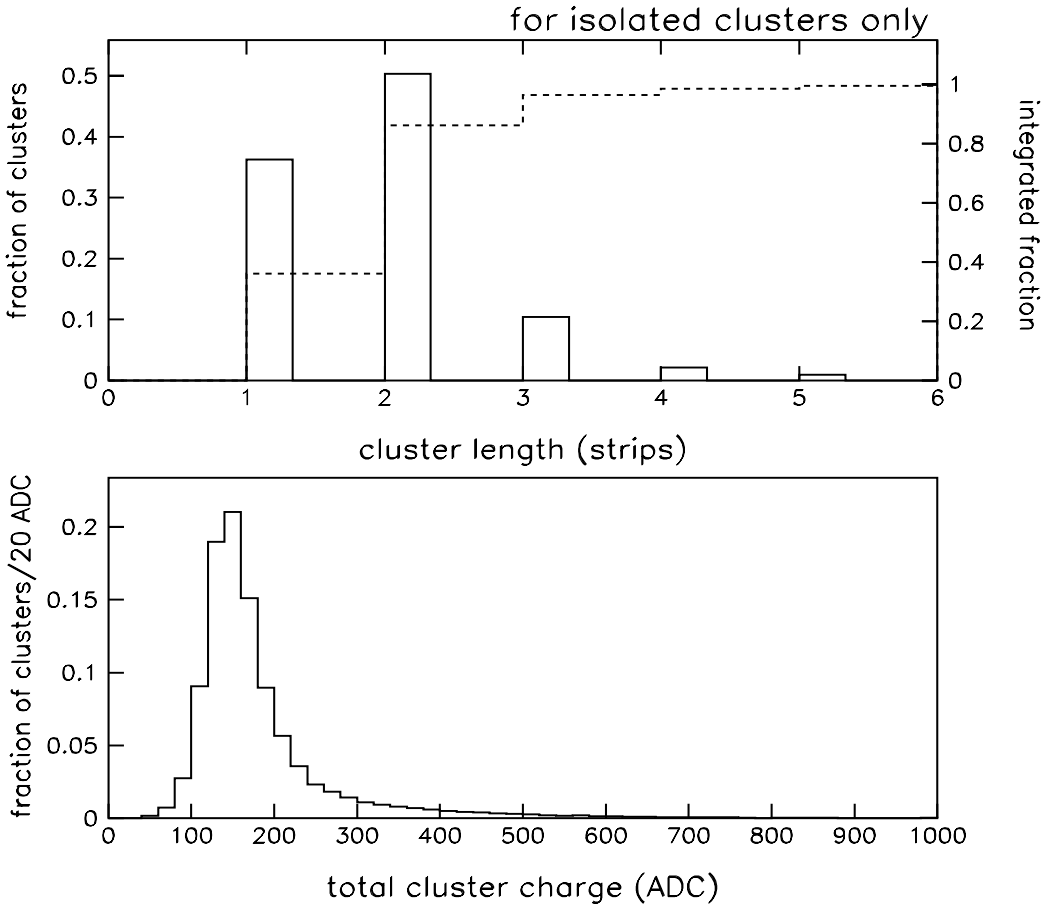

Figure 3.19: The total cluster length distribution for isolated tracks (top). Both the integral (dotted) and differential (solid) distibutions are shown. The total cluster charge corrected for pathlength, Q_{TOT}, for all clusters (bottom).

track. The angles are measured relative to the silicon wafer normal in the $r\phi$ ($\Delta\phi$) and rz ($\Delta\theta$) planes. We divide the $\Delta\phi$ ($\Delta\theta$) distribution into 4° (15°) bins. Note that $\Delta\phi$ rarely exceeds 15°, while values of $\Delta\theta > 45^\circ$ are not uncommon. We divide the core strip cluster formation into three pieces

Q_{core}: the total charge included on the core strips

$\mathcal{P}_1^{core}$: the probability that only one of the core strips is included in the cluster

F_L: the distribution of Q_{core} among the 2 core strips; given that *both* core strips are included in the cluster, we arbitrarily decide to parameterize the fraction of Q_{core} on the left core strip.

We discuss the parameterization of each of these pieces below.

To study the total charge included in the core strips, Q_{core}, in each $(\Delta\phi, \Delta\theta)$ bin, we divide the clusters into four groups according to whether there are 1 or 2 core strips and whether or not there are additional strips appended to the core strips. The Q_{core} distributions for normal incidence are shown in Figure 3.20. We parameterize the shapes of the distributions using the sum of a Gaussian plus exponential for the body and tail of the distribution respectively. The resulting shapes are also shown in Figure 3.20. Already, the effects of $\delta-$rays are made obvious. *A priori* we expect $\delta-$rays to have the following effects

- to increase the charge deposited on the core strips due to the secondary ionization they produce;
- when energetic enough to traverse across multiple strip widths, to append additional strips to the core strips.

A long range $\delta-$ray will generate a secondary ionization path with a component perpendicular to the track trajectory so that we further expect the additional strips to appear only to one side of the core strips. This in turn has the effect that the mean charge deposited on the core strip nearest the additional strips (ie. that core

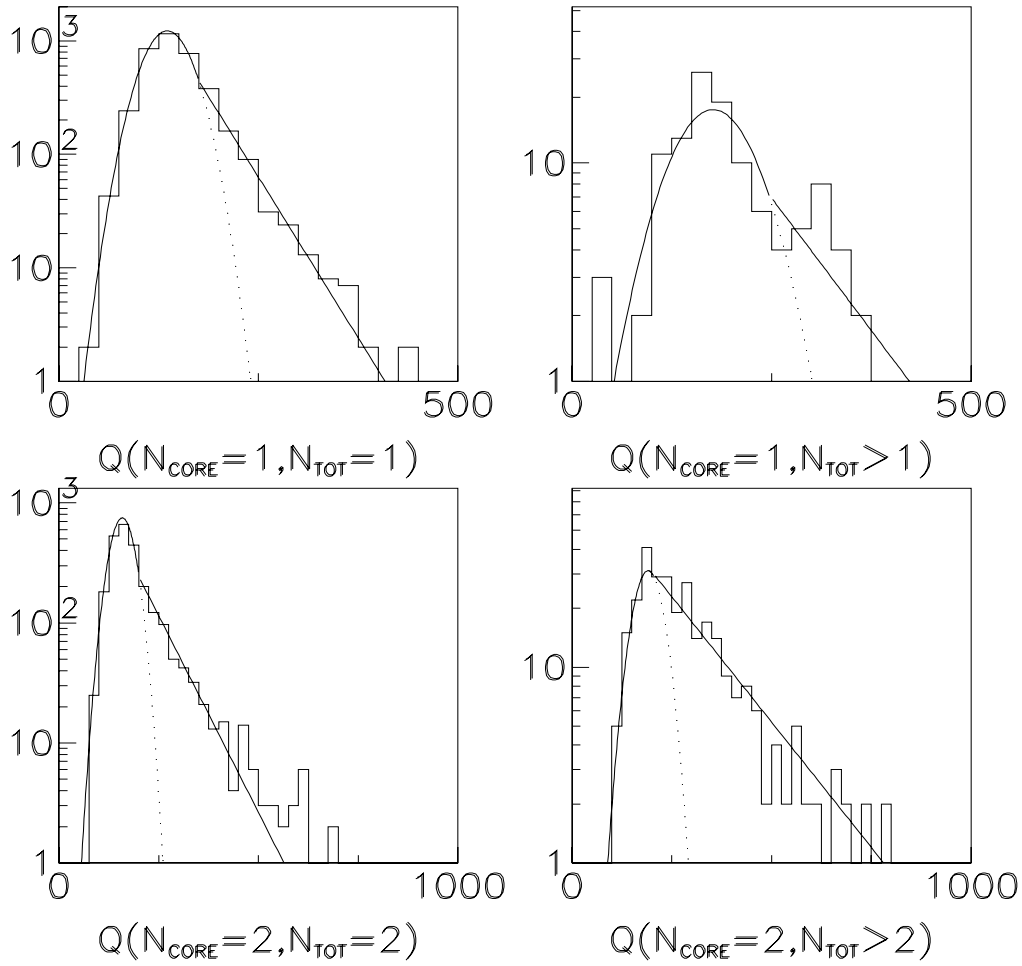

Figure 3.20: Core charge distributions for clusters where one core strip (top) or both core strips (bottom) are included in the cluster and where additional strips are absent (left) or present (right). The histograms are the data and the smooth curves are fits.

strip across whose boundaries the $\delta-$ray traveled) ought increase, while the charge distribution of the core strip farthest from the additional strips to ought remain unaffected. Our observations support these hypotheses.

For both 1 and 2 strip clusters, when additional strips are present, the tail of the core charge distribution is larger than when no additional strips are present. This is consistent with having a $\delta-$ray traverse multiple strip boundaries. We also find that additional strips are almost always appended to only one side of the cluster at a time . Finally, we observe that the additional charge appears only on that core strip near the additional strips. This is demonstrated in Figures 3.21 and 3.22.

In the top (bottom) plot of Figure 3.21 we compare the charge distribution of the core strip nearest (farthest) the track intersection point for the case in which additional strips are adjacent (points) to the case in which there are no additional strips (histogram). The enhanced tail, indicative of secondary ionization, is evident. In the top (bottom) of Figure 3.22 we compare the charge distribution of the core strip farthest (nearest) the track intersection point for the case in which additional strips are adjecent to the *other* core strip (points) to the case in which there are no additional strips (histogram). As expected, the charge on a core strip does not depend upon the presence of additional strips adjacent to the *other* core strip.

Fits to the four Q_{core} distributions of Figure 3.20 are made for all 16 $(\Delta\phi, \Delta\theta)$ bins. As expected, the Gaussian means are found to scale linearly with the pathlength of the track trajectory through the silicon. The exponential slope of the tail is observed to be constant as a function of incident angle, but the relative normalization is found to increase with pathlength. In light of our $\delta-$ray hypothesis, we understand this to mean that it is the *probability* that a $\delta-$ray is present, and *not* the $\delta-$ray *energy* spectrum, that varies with pathlength.

As mentioned above, both core strips are not always included in the cluster. We parameterize the probability that only one core strip is included in the cluster formation, $\mathcal{P}_1^{core}$, as a function of x_{int} and Q_{core} in each $(\Delta\phi, \Delta\theta)$ bin. Figure 3.23 plots $\mathcal{P}_1^{core}$ versus x_{int} for tracks near normal incidence. The three curves correspond

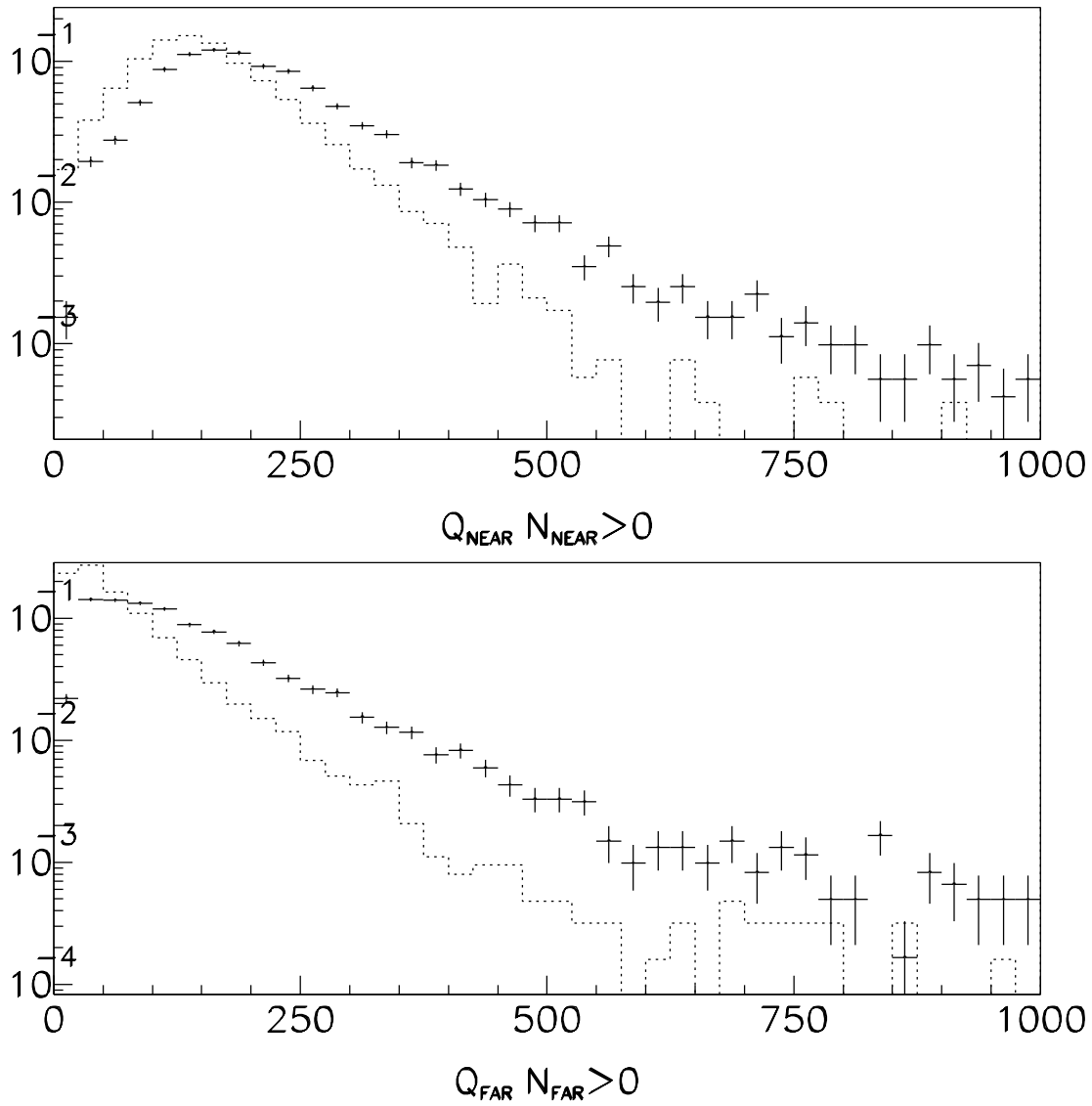

Figure 3.21: Top plot: Charge on core strip nearest the track intersection point when there are no adjacent additional strips (dotted) and when adjacent strips are present (points). Bottom plot: Charge on core strip farthest from track intersection point when there are no adjacent additional strips (dotted) and when adjacent strips are present (points).

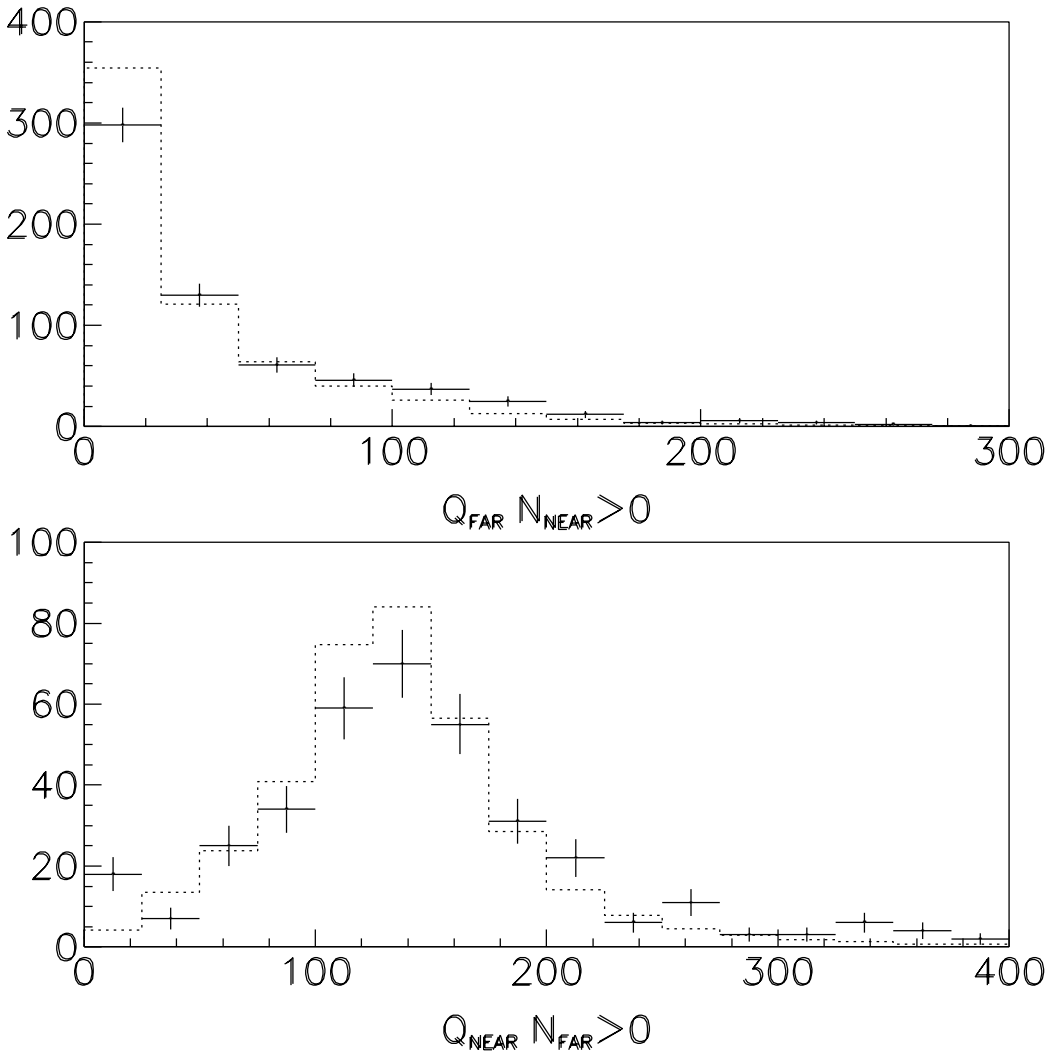

Figure 3.22: Top plot: Charge on core strip farthest from the track intersection point when there are additional strips adjacent to the *other* core strip (points) and when no additional strips are present (dotted). Bottom plot: Charge on core strip nearest the track intersection point when there are additional strips adjacent to the *other* core strip (points) and when no adjacent strips are present (dotted).

to different ranges of Q_{core}. For tracks passing very near the center of a readout strip, $\mathcal{P}_1^{core}$ is largest. As the track intersection point, x_{int}, moves towards the middle of the core strips, $\mathcal{P}_1^{core}$ is smallest. We additionally observe an inverse correlation between Q_{core} and $\mathcal{P}_1^{core}$ — for a given track incident angle and intersection point as Q_{core} increases, $\mathcal{P}_1^{core}$ decreases. This correlation can be qualitatively understood by postulating the presence of short range $\delta-$rays not energetic enough to traverse multiple strip boundaries, but which nevertheless, increase both the total charge deposition and the lateral distance over which that charge depostion takes place. The parameterization of $\mathcal{P}_1^{core}$ is repeated in each of the $(\Delta\phi, \Delta\theta)$ bins.

The final piece of the core cluster formation is the distribution of Q_{core} among the core strips. In the case that $N_{core} = 1$, the distribution is trivial. When both core strips are included in the cluster, we must understand how to distribute the charge between them. We arbitrarily choose to parameterize the fraction of core charge deposited on the left core strip, F_L. We parameterize F_L as a function of x_{int} and Q_{core}. Figure 3.24 shows the Q_{core} distribution (upper left), and the F_L profile distributions versus x_{int} for three different ranges of Q_{core}. For comparison, the distribution of the upper right plot is reproduced (dotted points) in the lower two plots.

We have now parameterized Q_{core} as a function of incident angle, $\mathcal{P}_1^{core}$ as a function of Q_{core}, x_{int}, and incident angle, and, when both core strips are included in the cluster, F_L as a function of Q_{core} and x_{int}. This completes our parameterization of the core cluster charges, we now consider the parameterization of the additional strips.

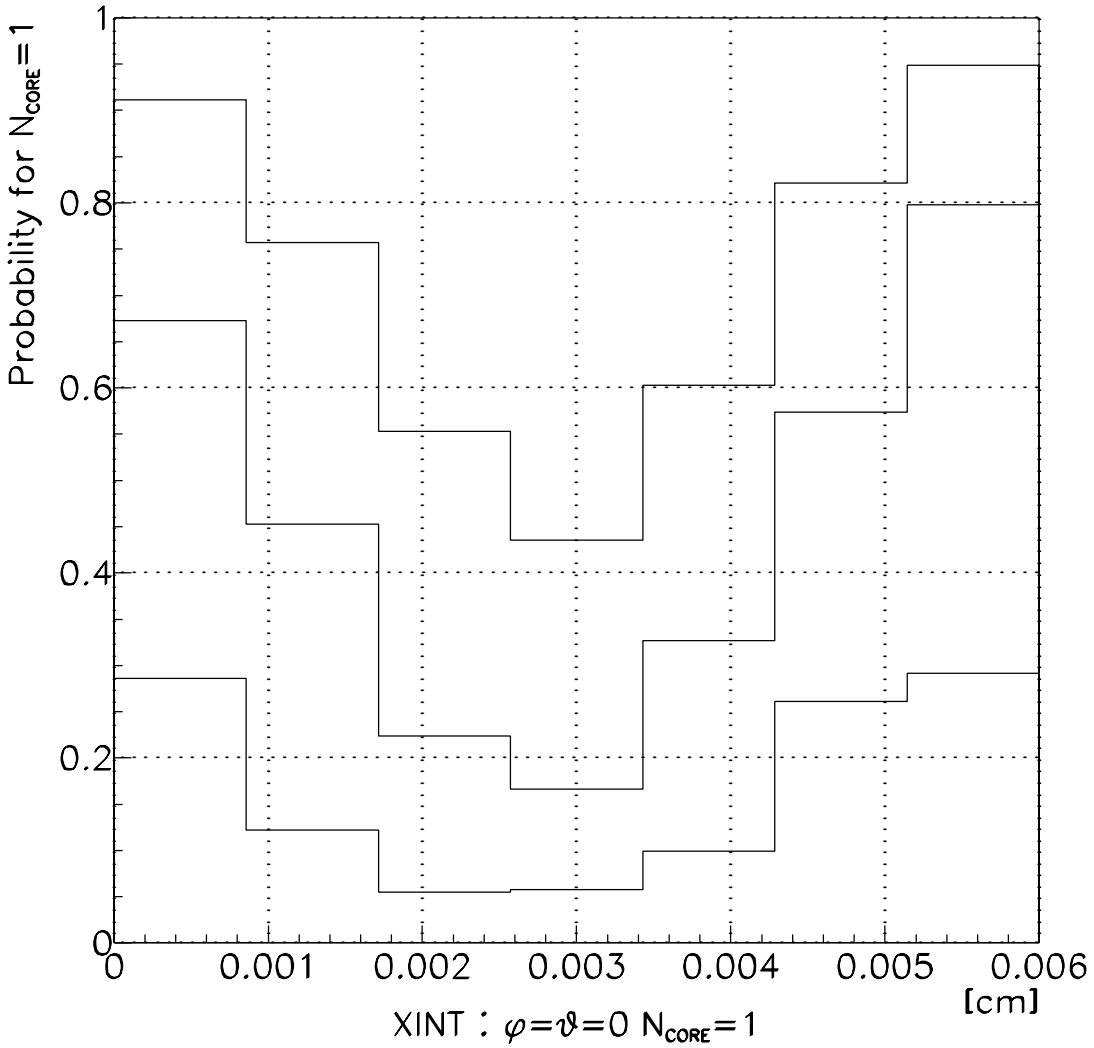

Figure 3.23: Probability for having only one core strip in a cluster as a function of the track's intersection point between the core strips for three different ranges of core charge, (from top to bottom) $Q_{core} \leq 150$ ADC, $150 < Q_{core} < 250$ ADC, and $Q_{core} \geq 250$ ADC. We take $x_{int} = 0$ to be centered on the left core strip and to increase in the direction of the right core strip.

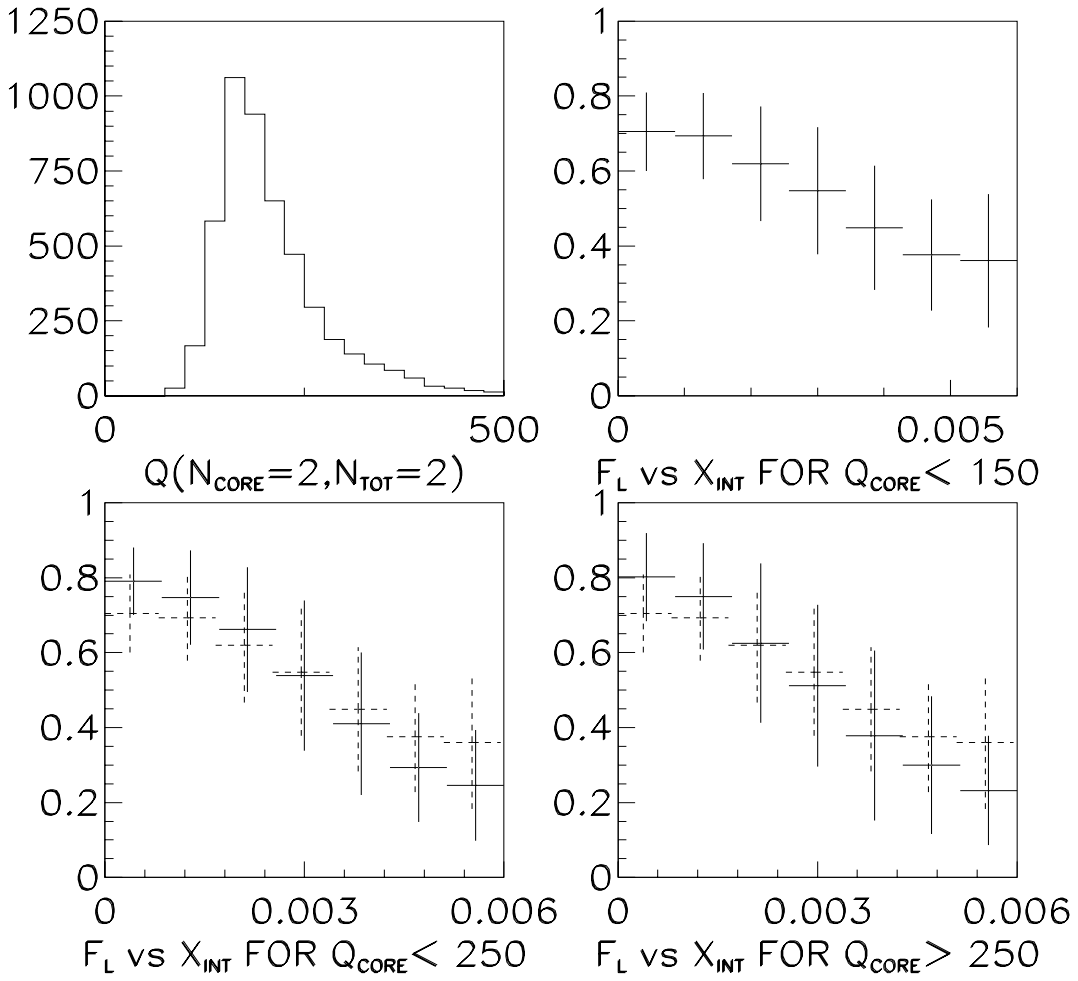

Figure 3.24: Clockwise from the upper left: The total core charge, Q_{core}, distribution and the fraction of that charge deposited on the left core strips, F_L, as a function of the track intersection point, x_{int}, measured relative to the left core strip for different ranges Q_{core}. The F_L profile distribution from the upper right plot is reproduced in the bottom plot (dotted) for comparison. The error bars correspond to the RMS of the F_L distribution in each bin.

Additional Strips in the Cluster

To complete our simulation of cluster formation we need to parameterize that part of the cluster that is in addition to the core strips. This parameterization is divided into two pieces:

- the frequency with which additional strips are included in the cluster;
- the charge distribution of the additional strips when present.

Before discussing each of these pieces, we consider the principle mechanisms for including addtional strips in the cluster. These mechanisms are 1) noise fluctuations and 2) long range $\delta-$rays. We assume that our modeling of the noise and thresholds using the CDF calibrations database, as discussed in Section 3.2.2, properly accounts for the contribution from noise fluctuations. We then concentrate on the modeling of the $\delta-$ray contribution. To do so, we require for clusters with only one additional strip that the charge on the additional strip be $Q^1 > 50$ ADC counts, where Q^i denotes the charge deposited on the ith additional strip. Typical mean values of the strip noise are 9 - 15 ADC counts, so this cut effectively removes the noise contribution. Since our threshold for inclusion in a cluster is $2\sigma_{noise}$, the probablility is very small that more than one additional strip is included in the cluster due to noise. Thus, clusters with more than one additional strip are due almost wholly to long range $\delta-$rays. (Recall that we are only using *isolated* tracks for this study).

The multiplicity of additional strips to the right (solid) and left (dotted) of the core strips is plotted in Figure 3.25. We can use this distribution to determine the frequency with which additional strips are added to the cluster. However, we first investigate some correlations.

In Figure 3.26 we investigate any correltations between the number of additional strips included to the left, N_L, and right, N_R, of the core cluster strips. No correlation is observed. Next, we investigate correlations between the number of additional strips included to the right or left of the core strips, $N_{R/L}$, and the charge on the

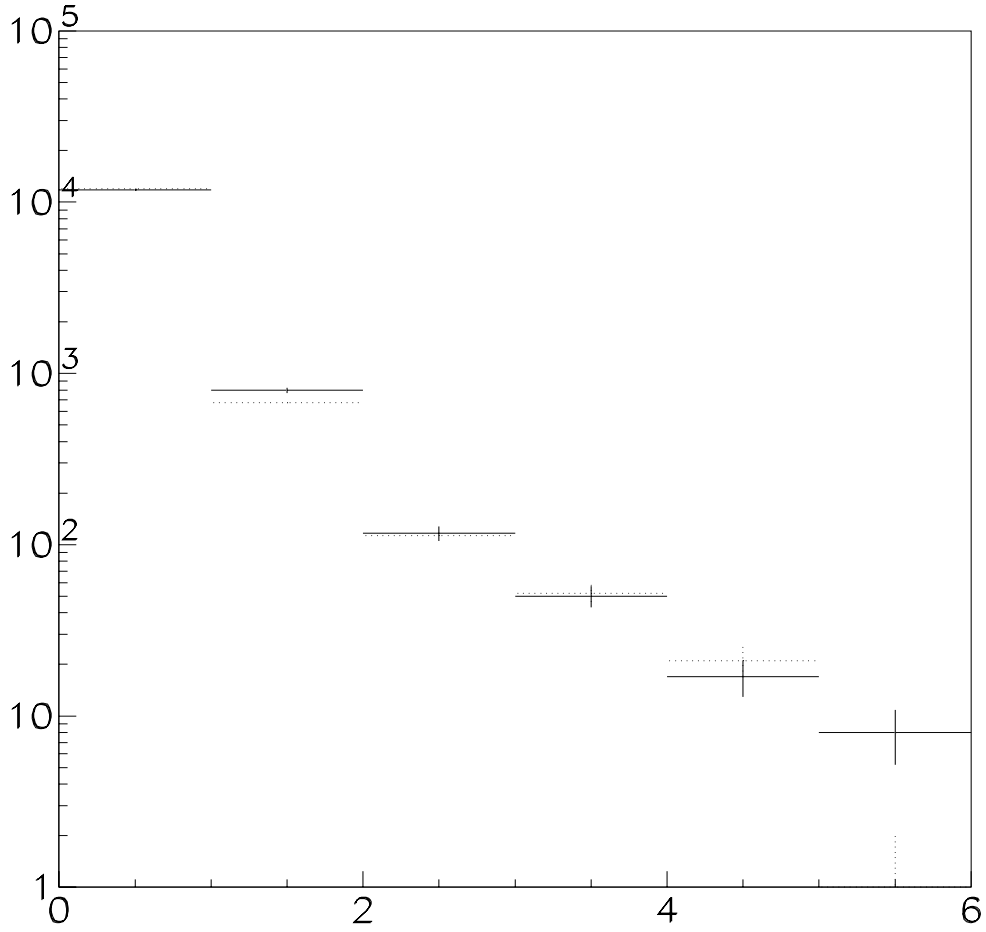

Figure 3.25: The multiplicity of additional strips to the right (solid) and left (dotted) of the core strips.

core strip adjacent to the additional strips, $Q_{R/L}$. Figure 3.27 shows the mean number of additional strips observed for all clusters versus the charge of the adjacent core strip. The correlation suggested in Figures 3.20 – 3.22 is made explicit. The presence of $\delta-$rays, as suggested by the presence of additional strips, is accompanied by an increase in the mean charge deposited on the core strip adjacent to the additional strips. Figure 3.28 is a similar plot but only includes clusters for which there is at least one additional strip. Here, no correlation between the number of additional strips, $N_{R/L}$, and the charge of the adjacent strip, $Q_{R/L}$, is observed. From these last two plots we conclude that while *presence* of $\delta-$rays *is* correlated with the charge of the core strips, the *range* of the $\delta-$rays is *not*.

Lastly, we investigate the charge distributions of the additional strips. The charge distribution of the first additional strip (Q^1), is plotted in Figure 3.29 for the case when $N_{add} = N_{L/R} = 1$ (top) and when $N_{L/R} > 1$ (bottom). The turn-on in the top plot is due to the contribution from noise fluctuations. We find that beyond 100 ADC counts, the slopes of the two distributions are the same. By normalizing the two distributions in the region $Q > 100$ ADC counts, we measure, for the $N_{L/R} = 1$ case, the excess in the region $Q < 50$ ADC counts. We then use this excess and estimate the probability for including a noise fluctuation as an additional strip in a cluster to be $\mathcal{P}_1^{noise} = 3\%$. Assuming a Gaussian noise distribution, a $2\sigma_{noise}$ threshold, and recalling that we're interested in the one sided probability, we calculate $\mathcal{P}_1^{noise} \sim 2.5\%$. Since the probability that two contiguous strips will fluctuate above threshold for inclusion in a cluster is negligible, we use the bottom distribution of Figure 3.29 to parameterize the charge distribution of the additional strips. In more detailed studies we find that this distribution is the same for all additional strips given that $N_{L/R} \geq 2$ strips. We find no correlation between the charge distributions of adjacent additional strips.

This completes our studies of the additional strips. We have characterized the frequency with which additional strips are added, $N_{L/R} > 0$, as a function of Q_{core}. Given that $N_{L/R} \geq 1$ we use Figure 3.25 to determine the number of additional strips

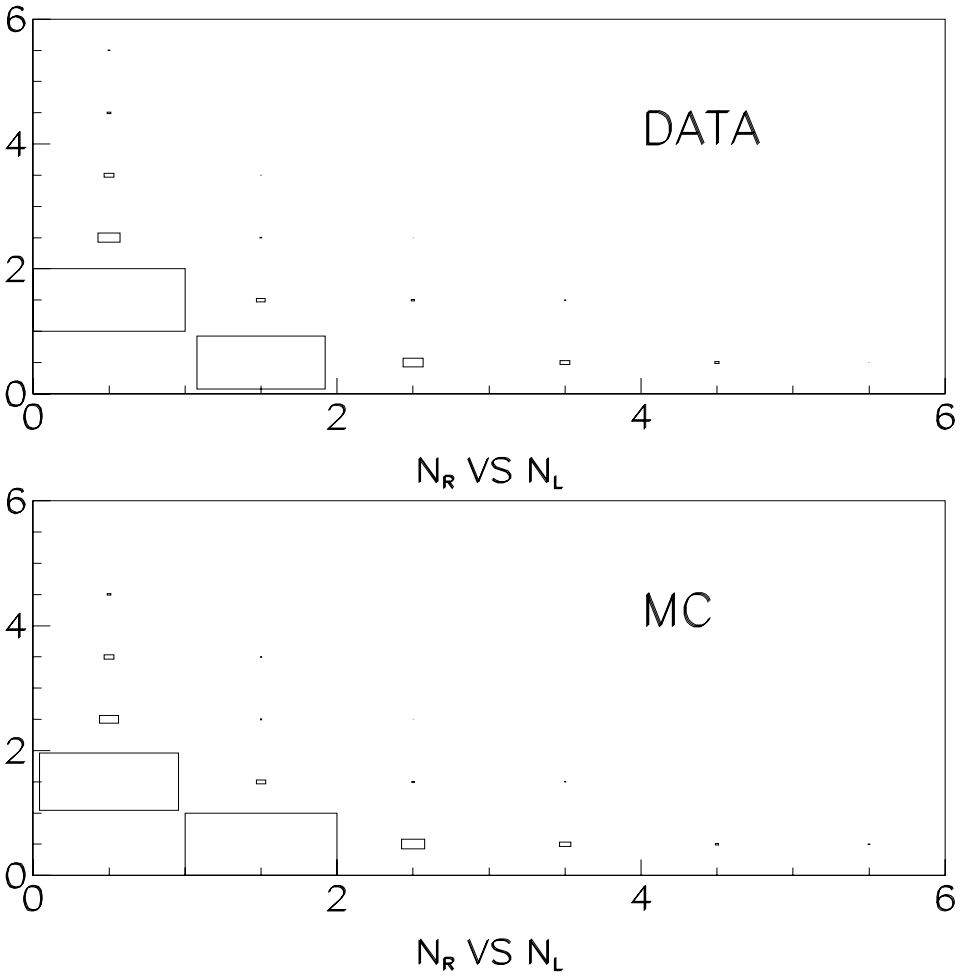

Figure 3.26: The number of additional strips to the right of the core cluster, N_R, versus the number of additional strips to the left, N_L. The area of each box is proportional to the number of entries in that bin. The very small number of diagonal entries demonstrates the independence of N_R and N_L.

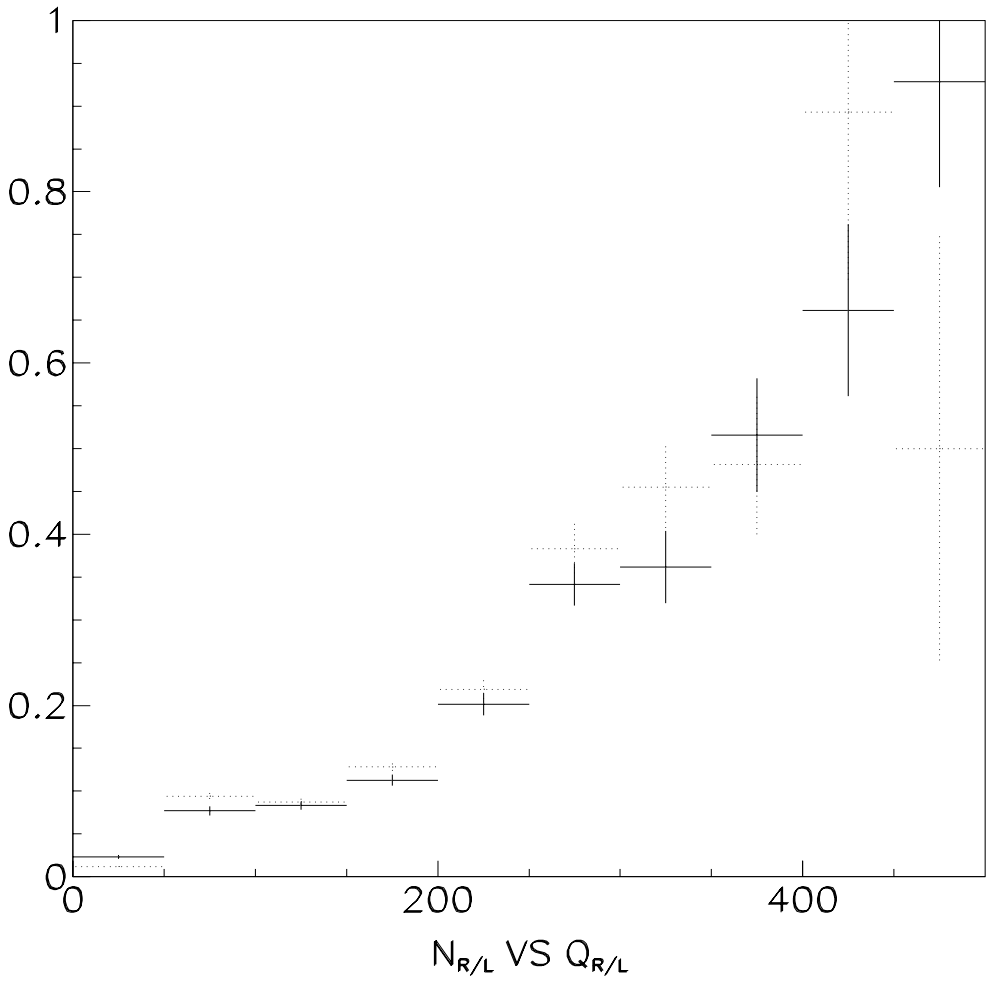

Figure 3.27: The mean number of additional strips to the right (left) of the core strips, $N_{R/L}$, for all clusters as a function of the charge deposited on the right (left) core strip, $Q_{R/L}$, for data (solid) and MC (dotted). The correlation is evident.

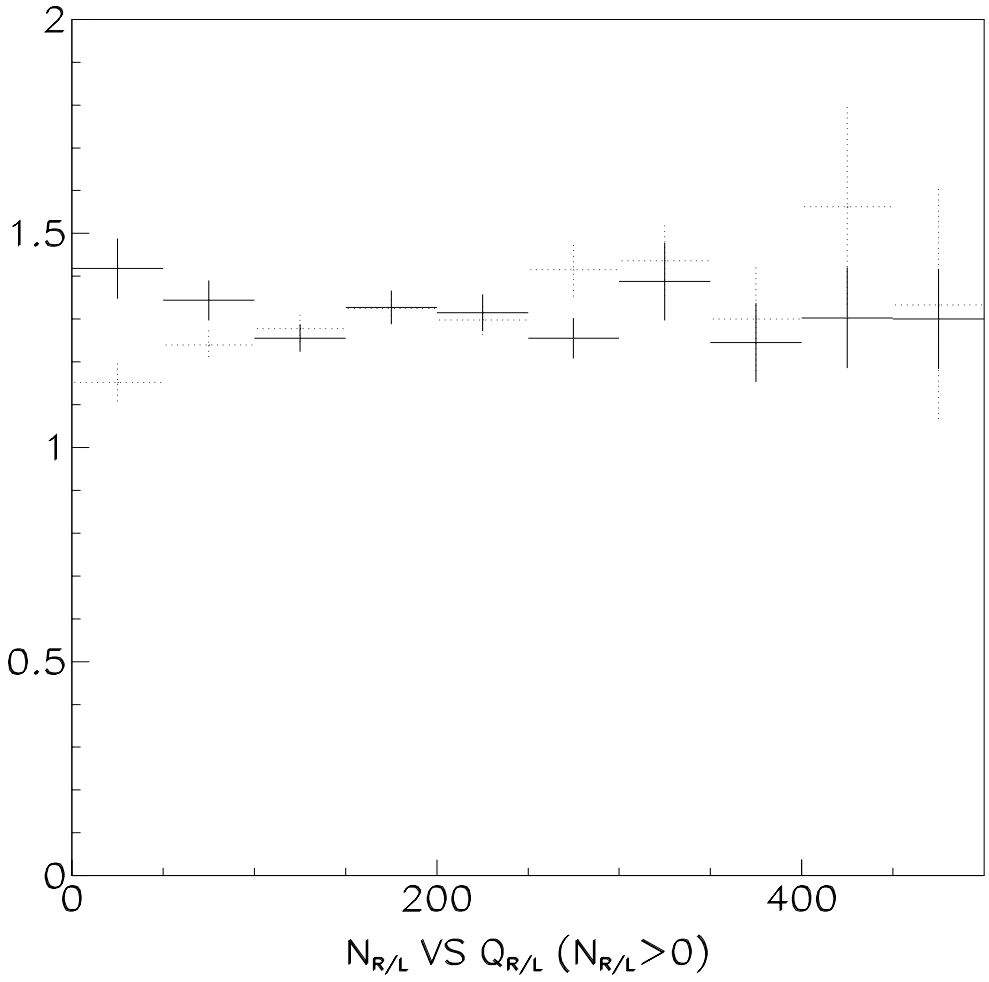

Figure 3.28: The mean number of additional strips, for all clusters *with at least one additional strip*, as a function of the charge deposited on the nearest core strip for data (solid) and MC (dotted). No significant correlation is observed.

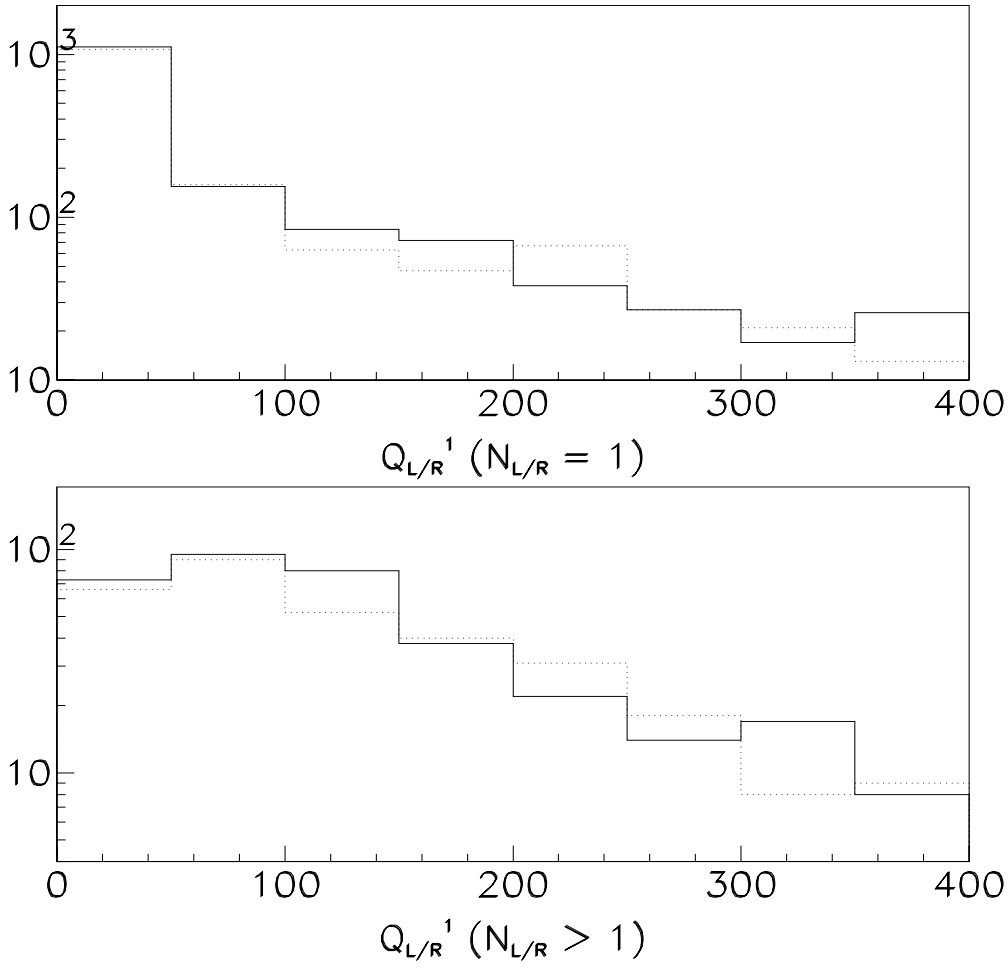

Figure 3.29: Charge distribution for the first additional strip when *only* one additional strip is present (top) and when there are *more than* one additional strips present (bottom) for data (solid) and MC (dotted).

and Figure 3.29 to distribute charge among those strips. With the characterization of both the core cluster strips and the additional cluster strips in hand, we turn to a comparison of MC and data.

Description of Simulation Algorithm

Using the above studies, we develop a quasi-phenomenological model for simulating the clusters of the SVX′ . All correlations are incorporated. As in the studies described in the previous sections, we divide the cluster simulation into two pieces 1) simulation of the core cluster strips and 2) simulation of the additional cluster strips. The simulation is summarized below.

We simulate a cluster at each layer of the SVX for each charged track fiducial to the SVX. We first construct the core of the cluster. We then allow for the addition of strips to the core strips. Finally, we account for noise and threshold fluctuations, and for dead strips. The core of the cluster is simulated as the sum of a Gaussian distributed piece (Q_{Gauss}) and an exponentially distributed piece (δQ). The former is ascribed to the energy loss of the primary particle track. Thus the Gaussian used to generate this charge is scaled according to pathlength through the silicon, the velocity of the charged particle, and the particle type. These last two scalings account for the relativistic rise and density effects of dE/dx in silicon [55] [56] [57]. The exponential piece is assumed to be the result of low energy secondary ionizing particles and is not always present. The probability for this piece to be added is measured to be 40% for normally incident tracks. We assume that this probability scales linearly with pathlength through the silicon.

Once a total core charge is obtained, we determine the number of core strips. We use the $\mathcal{P}_1$ distributions as a function of incident angle, Q_{core}, and x_{int}. For those clusters in which both core strips are included, we distribute the charge using the F_L distributions as a function of Q_{core} and x_{int}. This completes the construction of the core cluster strips.

With the core cluster strips in hand, we construct the additional cluster strips.

The probability of additional strips is correlated with the core charge and, in particular, the amount of charge on the nearest core strip. These correlations are accounted for using Figure 3.27. The multiplicity of additional strips and the charge distributions of those strips are then modelled using the data.

Comparison of the SVX′ Simulation and Data

In order to verify that the final cluster simulation is correct, we compare the simulated Monte Carlo (MC) clusters to those in data for a large number of distributions. In this section we present some of the more important comparisons. In particular, a number of clusters from tracks with the same track parameter distributions as the data are generated and analysed in exactly the same manner as the data. *No attempt is made to normalize the Monte Carlo distributions beyond the intial generation of an equal number of tracks.* For the majority of comparisons shown, tracks with $\Delta\phi < 4^\circ$ are used. Checks are done using tracks spanning the entire range of incident angles. The agreement is uniform across all $(\Delta\phi, \Delta\theta)$ bins and is well represented by the plots shown here.

In Figure 3.30 we compare data (solid) and MC (dotted) core charge distributions for clusters with ≤ 2 strips(top) and for all clusters (bottom). Figure 3.31 compares the charge distributions on the individual core strips closest to additional strips when the latter are present. In both cases agreement is excellent and gives us confidence in the MC modelling of the core cluster charge.

Figure 3.32 shows the fraction of charge on the left core strip, F_L, as a function of x_{int} for two different ranges of the total core charge, Q_{core}. The data (solid) and MC (dotted) distributions are in agreement so that we also trust the MC modelling of charge distribution among the core strips.

Finally we compare the simulation of clusters with additional strips to data. The additional strip multiplicity distributions for data (solid) and MC (dotted) are shown in Figure 3.33 and are found to agree. The MC correlation between the number of strips to the left (N_L) and right (N_R) of the core strips also agrees

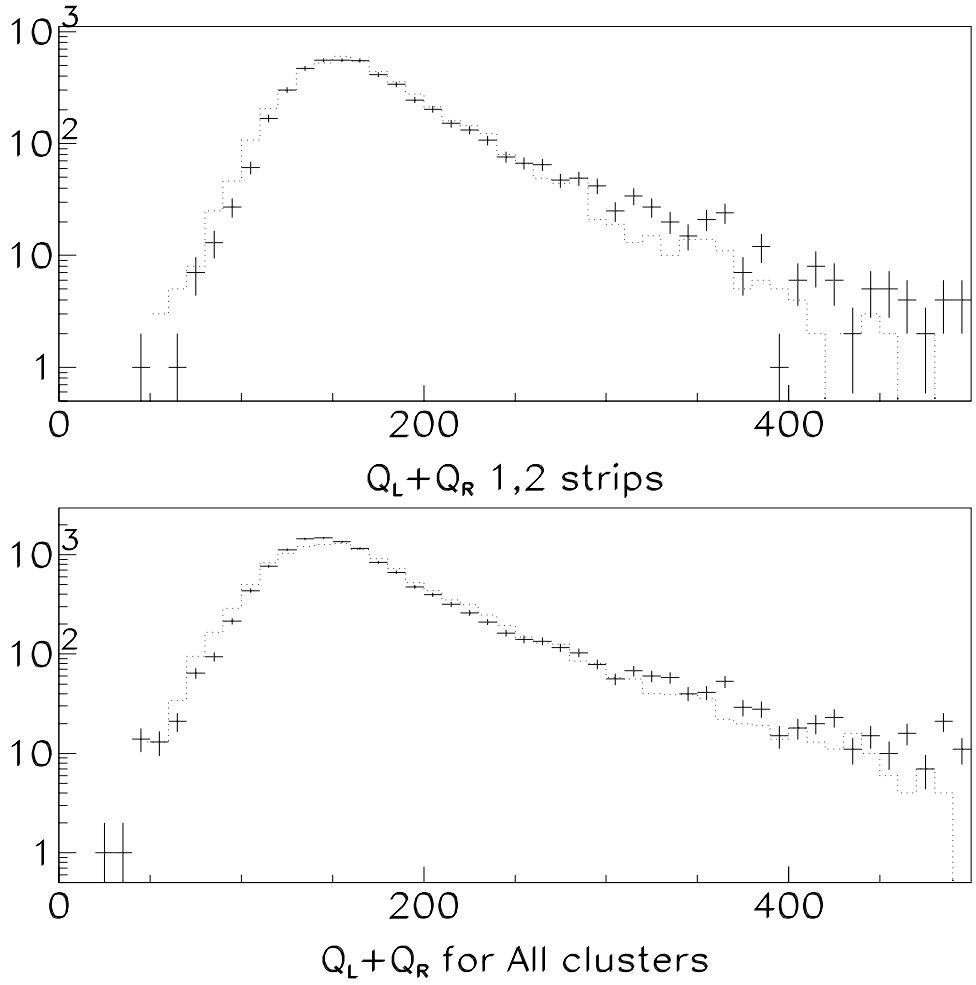

Figure 3.30: Core charge distributions ($Q_{core} = Q_L + Q_R$) for clusters with no additional strips, $N_{strip} \leq 2$ (top), and for all clusters (bottom) for data (solid) and MC (dotted).

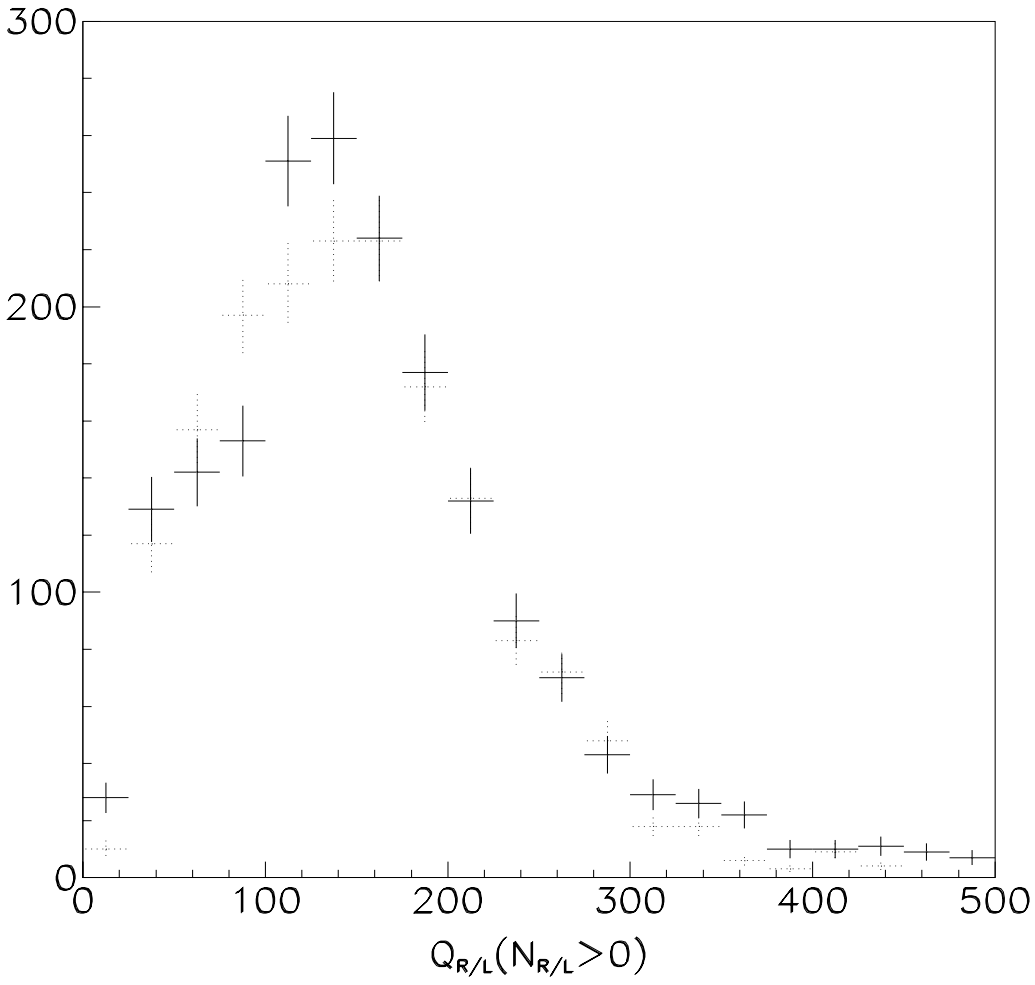

Figure 3.31: Charge distribution of core strip ($Q_{R/L}$) adjacent to additional strips when additional strips are present ($N_{R/L} > 0$) for data (solid) and MC (dotted).

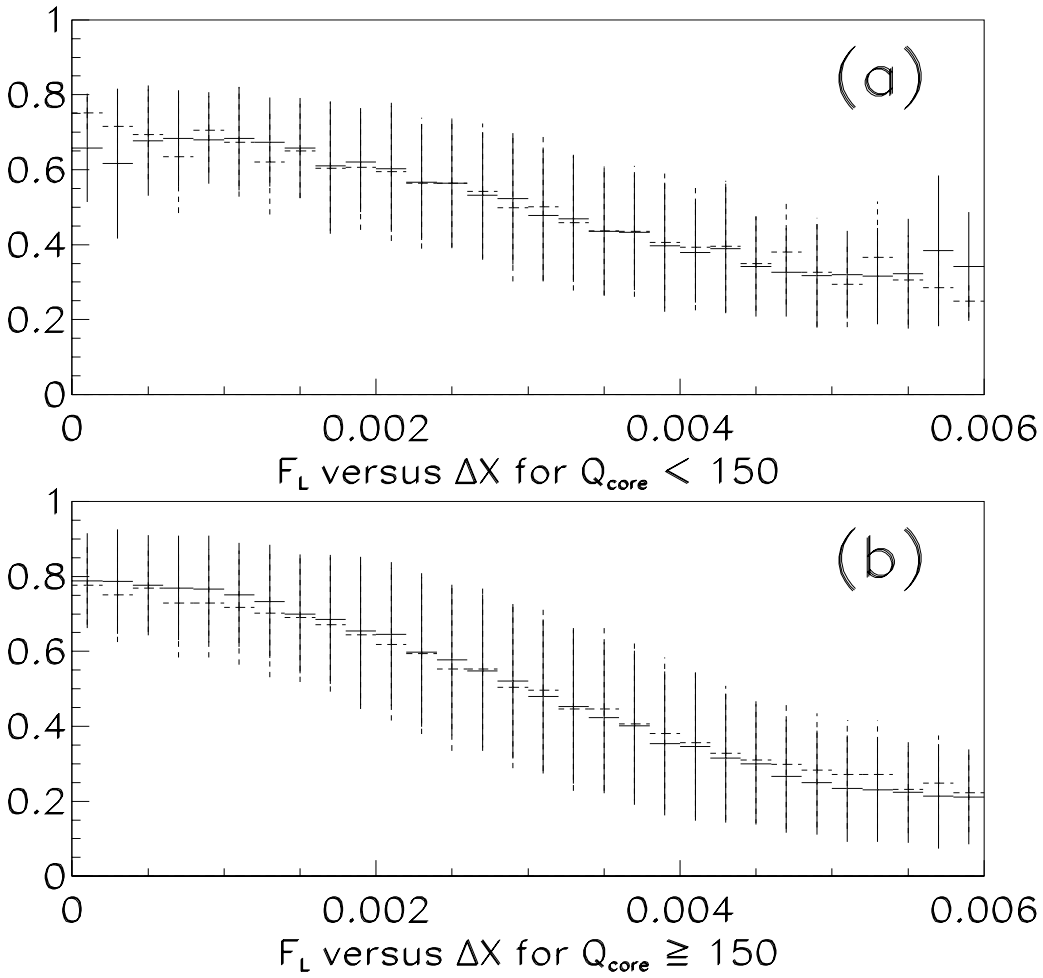

Figure 3.32: Fraction of core charge deposited on the left core strip as a function of Δx_{int}, measured from the center of that strip. Data (solid) and MC (dotted) distributions are compared for clusters with $Q_{core} < 150$ ADC (a) and with $Q_{core} \geq 150$ ADC (b). The error bars represent the RMS of the F_L distribution in each bin.

with the data as demonstrated in Figure 3.26. Figures 3.27 and 3.28 show MC (dotted) as well as data (solid) distributions for the correlation between $N_{L/R}$ and the core charge and are observed to be in good agreement. Figure 3.29 compares the charge distribution of the first additional strip when $N_{add} = N_{L/R} = 1$ strip (top) and $N_{L/R} > 1$ strip (bottom). Figure 3.34 compares the MC (dotted) and data (solid) charge distributions for the second through fifth additional strips when those are present. In all cases we find the distributions are faithfully reproduced in the MC giving us confidence in our modelling of noise fluctuations and the charge distributions of the additional strips. The total cluster length distribution for MC (solid) and data (dotted) is compared over a wide range of incident angles all shown in Figure 3.35. Again, the MC reproduces the data quite well.

After extensive comparison of the cluster simulation to data we conclude that we have in hand a Monte Carlo which faithfully reproduces the detector response at the fundamental level of cluster formation. It will be demonstrated in Section 3.5.4 that the agreement between the MC and data propogates to more sophisticated levels of analysis. We continue our development of a B-tag algorithm with a thorough understanding of signal formation in the SVX detector.

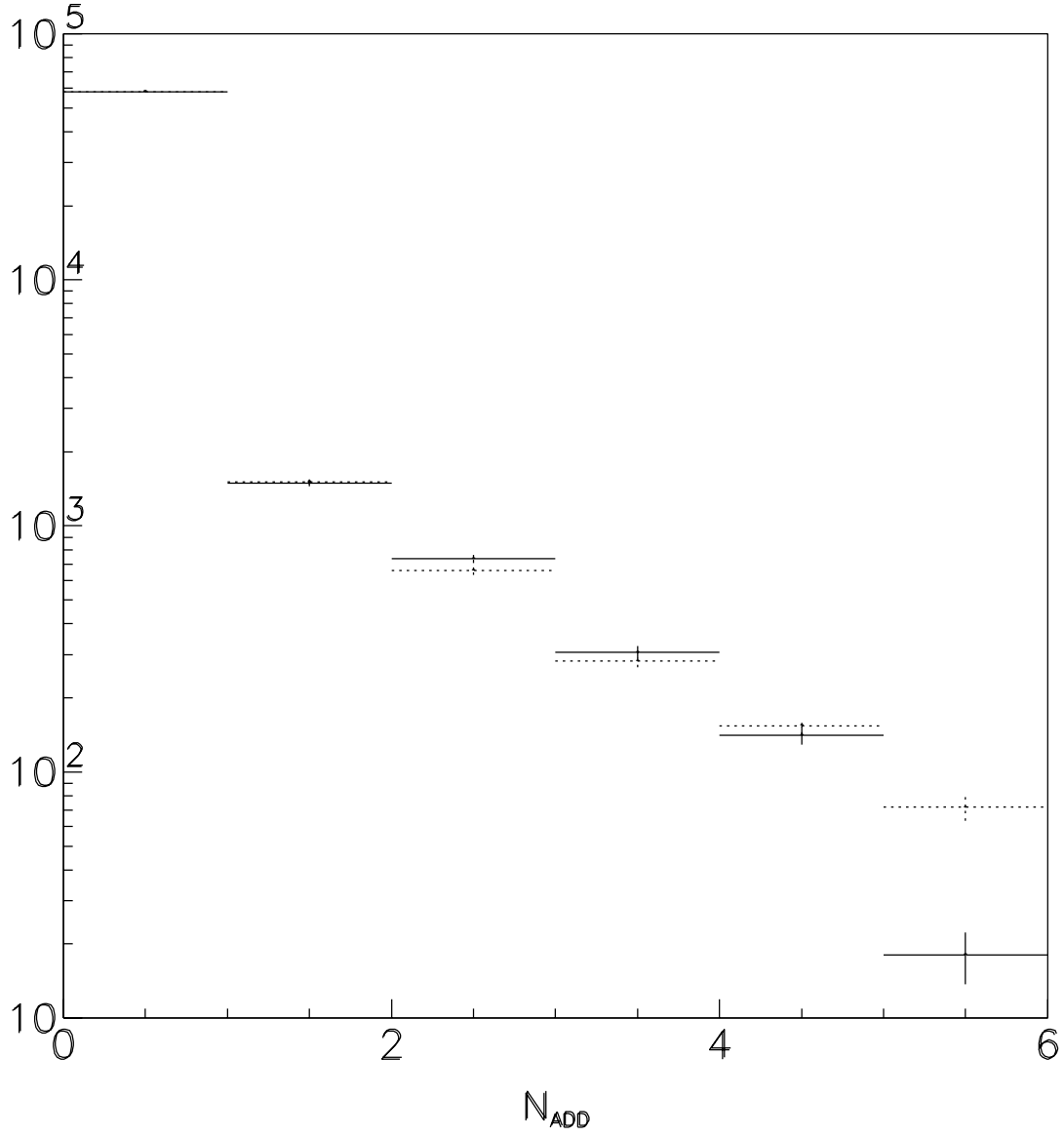

Figure 3.33: The multipliciy of additional strips, N_{add}, averaged over the right and left sides, for data (solid) and MC (dotted).

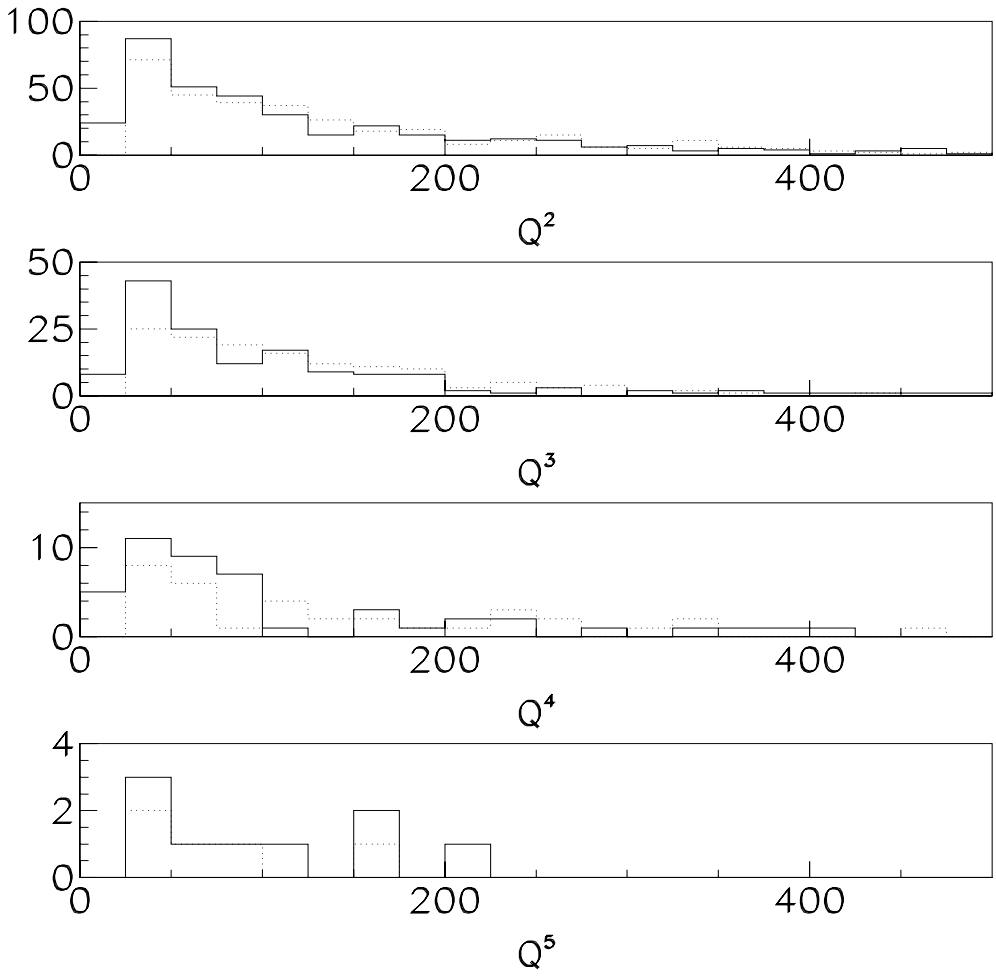

Figure 3.34: Charge distributions (in ADC counts) for the second through fifth additional strips, when present, for data (solid) and MC (dotted).

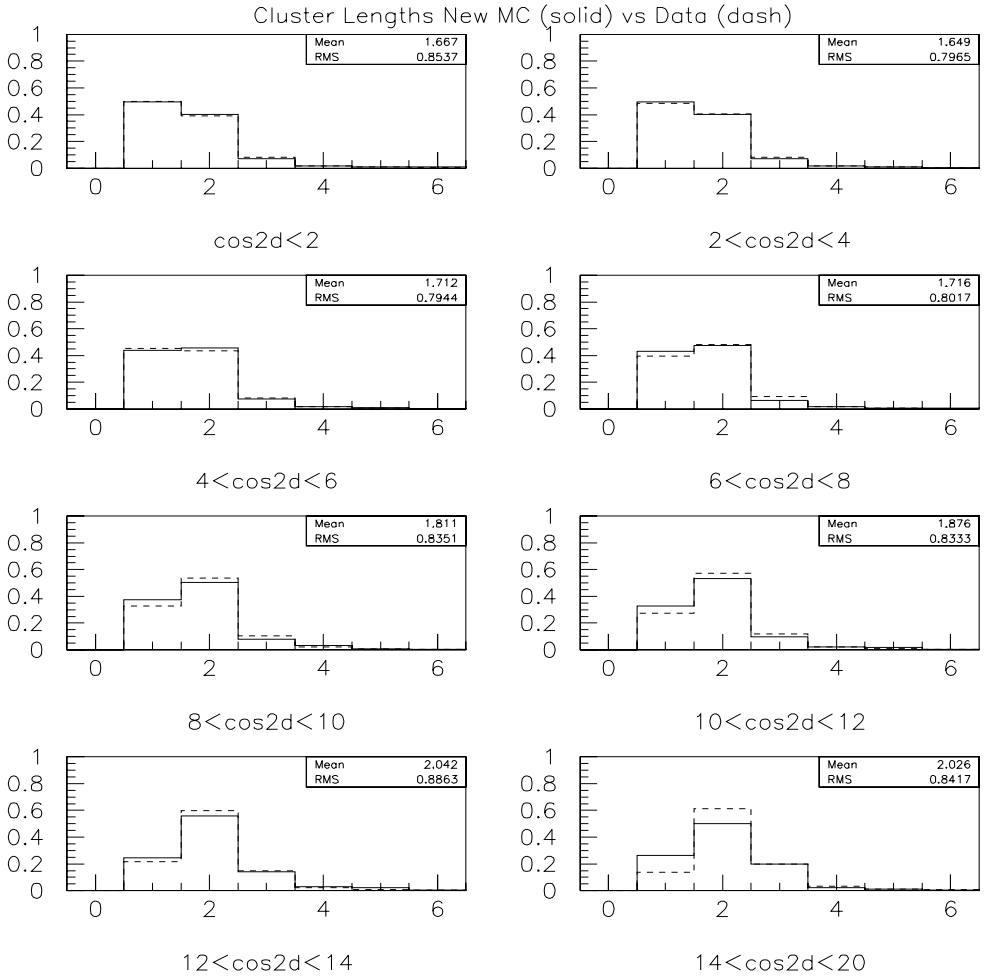

Figure 3.35: Distribution of the number of strips included in a cluster (ie. cluster length) for a variety of incidence angles in the $r - \phi$ plane for data (dashed) and MC (solid).

3.3 Algorithm Optimization

As discussed in Section 3.2, the primary goal in developing the SVX B-tag algorithm is to identify those tracks associated with the B decay vertex while discriminating against tracks *not* associated with the decay of a long lived particle. In optimizing the B-tag algorithm we first concentrate on understanding those characteristics which discriminate poorly measured tracks from good tracks. With this in hand we turn our attention to estimating the signal to noise ratio for the 2-pass algorithm alluded to in Section 3.2.1. We choose the final cuts of our algorithm based on "discovery potential".

3.3.1 Track Selection Studies

For any track based analysis, it is important to be able to discriminate poorly measured and fake tracks from real tracks. This is particularly true for our B-tag algorithm, for which fake tags are a major source of background. It is reasonable to assume that fake tracks, in combination with one another or with a single good track, give rise to fake tags. In order to quantitatively investigate the effect of various track selection cuts, we use an inclusive jet sample and assume the heavy flavor content is small. In general then, real tracks should originate at the primary vertex, while fake tracks should be more randomly distributed. We then define the track purity, or "pointback probability" as,

$$\mathbf{P} = N(S_{d_0} < 3\sigma)/N(total). \tag{3.2}$$

By maximizing the pointback probability we identify those track selection criteria which most readily discriminate real tracks from fake tracks.

It should be noted that real tracks originating from the decay of long lived particles are expected to have large values of S_{d_0} (cf. Figure 3.8). We estimate the heavy flavor content of the inclusive jet sample to be $< 7\%$. This is sufficiently small that we expect to introduce no bias by using pointback probability as our discriminator.

We find in Table 3.7 that the pointback probability is strongly correlated with the number of SVX hits associated with the track. Tracks with 4 SVX hits have the highest purity, 0.82, while tracks with only 2 SVX hits are most likely to be fakes, with a purity of 0.16. For this reason, the pointback probability for each cut is calculated separately for 2, 3, and 4 SVX hit tracks. The selection criteria considered are

P_T**:** the transverse momentum of the track

N_{shared}**:** the number of shared SVX clusters associated with the track

N_{bad}**:** the number of bad (excessively noisy or dead) strips associated with the track

cluster length: the largest number of strips included in a single cluster associated with the track

N_{good}**:** the number of "good" clusters associated with the track; a cluster is declared "good" if it is not shared, not bad, and includes ≤ 3 strips

N_{CTC}**:** the total number of axial and stereo CTC hits for the CTC track segment associated with the track

N_{SL}**:** the number of axial and stereo CTC superlayers traversed ($N_{hit}^{axial}/SL^{axial} \geq 4$, $N_{hit}^{stereo}/SL^{stereo} \geq 2$) by the CTC segment associated with the track

Q_{track}^{SVX}**:** the isolation of the track in the SVX, defined as the number of SVX clusters within 4σ of the SVX track segment.

For all cases we include the cuts χ^2_{fit} per degree of freedom < 6 and $|z_0 - z_{pvtx}| < 6\sigma_z$. We find that the pointback probability is most affected by the number of SVX hits associated, the number of CTC hits associated, and the quality of clusters associated. We observe little dependence on the P_T of the track for tracks with $P_T > 0.5$ GeV/c. For 2 SVX hit tracks, we find that additionally requiring the tracks to satisfy specific fiducial hit patterns the purity increases to $> 30\%$.

no. of SVX hits	F^j_{all}	$F^j_{S_{d_0}<3}$	$\mathbf{P}^j$
2	18%	4%	16%
3	25%	21%	50%
4	57%	75%	82%

Table 3.7: Breakdown of tracks according to the number of SVX hits associated with the track. We define F^j_{all} as the fraction of all SVX tracks with j SVX hits associated, $F^j_{S_{d_0}<3}$ as the fraction of all SVX tracks with $S_{d_0} < 3$ with j SVX hits associated, and $\mathbf{P}^j$ as the purity of tracks with j SVX hits associated.

We can identify those cut combinations which maximally discriminate good tracks by optimizing the S^2/B subject to efficiency constraints. The signal, S, is defined as the number of tracks with $S_{d_0} < 3$, while the background, B, is defined as the number of tracks with $S_{d_0} \geq 3$. The optimization is performed subject to the requirement that the fraction of tracks passing all the cuts remains $\geq 90\%$, or $\geq 75\%$, or subject to no additional constraint at all. We consider 576 cut combinations for 2, 3, and 4 hit tracks separately. The optimization is additionally allowed to ignore 2 or 3 SVX hit tracks completely. Table 3.8 lists the results. The optimization prefers to cut very lightly on 4 SVX hit tracks. For all SVX tracks, the prefered P_T cut is soft, > 0.75 GeV/c. The number of shared SVX hits and the maximum cluster length counted as a good cluster are also important. The optimizations choose either to ignore 2 hit tracks completely, or to cut harder on them by requiring they satisfy specific fiducial hit patterns*. The exercise is repeated using different optimization criteria and found to yield very similar results.

We now use the insights gained from the track selection optimization to help guide our optimization of the B-tagging algorithm.

*The 2 SVX hit tracks are required to 1) *not* cross SVX barrels, and 2) have both their hits in the inner two (hit pattern 0011) or outer two (hit pattern 1100) SVX layers.

criteria	N_{hit}^{SVX}	$P_T \geq$ (GeV/c)	$N_{share} \leq$ (hits)	cl.len. $\leq$ (strips)	$Q_{SVX} \leq$	$N_{SL}^{axial} \geq$ (hits)	$N_{SL}^{stereo} \geq$ (hits)
$\epsilon > 0.90$	2	0.75	0	4	2	no cut	2
	3	no cut	1	4	2	no cut	2
	4	no cut	no cut	no cut	no cut	no cut	no cut
$\epsilon > 0.75$	2	*eliminated*					
	3	0.75	1	4	2	3	2
	4	no cut	2	no cut	no cut	no cut	2
$\epsilon > 0.00$	2	*eliminated*					
	3	0.75	1	4	2	3	2
	4	no cut	2	no cut	no cut	no cut	2

Table 3.8: Results of optimizing pointback probability using the criteria S^2/B and subject to constraints on the efficiency, ϵ, defined as the fraction of all SVX tracks passing a given set of cuts. We consider the constraints $\epsilon > 0.90$, 0.75, and 0.00 - that is, no constraint at all. Note that the results for $\epsilon > 0.75$ and 0.00 are identicle and prefer to ignore all 2 hit tracks.

3.3.2 Final Algorithm Optimization

In Section 3.2.1 we performed a generator level study of a "two pass" B-tagging algorithm. In the "first pass" we apply loose track selection criteria and require at least three tracks in the vertex. If the first pass fails, we initiate a "second pass", which allows two track vertices, but requires tracks to satisfy stricter selection criteria. We use this as our skeleton algorithm and concentrate our optimization efforts on identifying a set of cuts, within this skeletal framework, which maximize the B-tagging efficiency while maintaining a small fake tag rate. Two independent optimizations are performed.

The first optimization concentrates on the track selection cuts and is guided by the track selection optimizations described in Section 3.3.1. Twenty-four sets of cuts are considered. For each cut set we calculate the quantity S^2/B. The results are shown in Figure 3.36 for two different optimization criteria. In the top plot we use an inclusive jet data set and define the signal as $S = N^{data}_{+tags} - N^{data}_{-tags}$, also known as the "positive excess". The background, B, is defined as the number of negative tags, N^{data}_{-tags}, in the same data set. Recall that negative tags are non-physical and are taken as an estimate of the number of fake tags, which are assumed to be symmetric about zero, on the positive side. By calculating the positive excess we are performing a first order background subtraction. In the bottom plot we define the signal as the positive excess from a Pythia Monte Carlo sample with a top quark mass of 160 GeV/c^2, and the background as the number of positive tags from the inclusive jet data. This criteria more nearly mimics the real signal and background estimates used in the final analysis. For both sets of criteria we observe little variation over the wide array of cut sets investigated. The final algorithm is shown as the solid square. The open circle is the algorithm used in the previous CDF top search analysis described in references [23] and [24].

The second optimization proceeds in a more general way and, in addition to track selection criteria, considers cuts on various vertex characteristics.

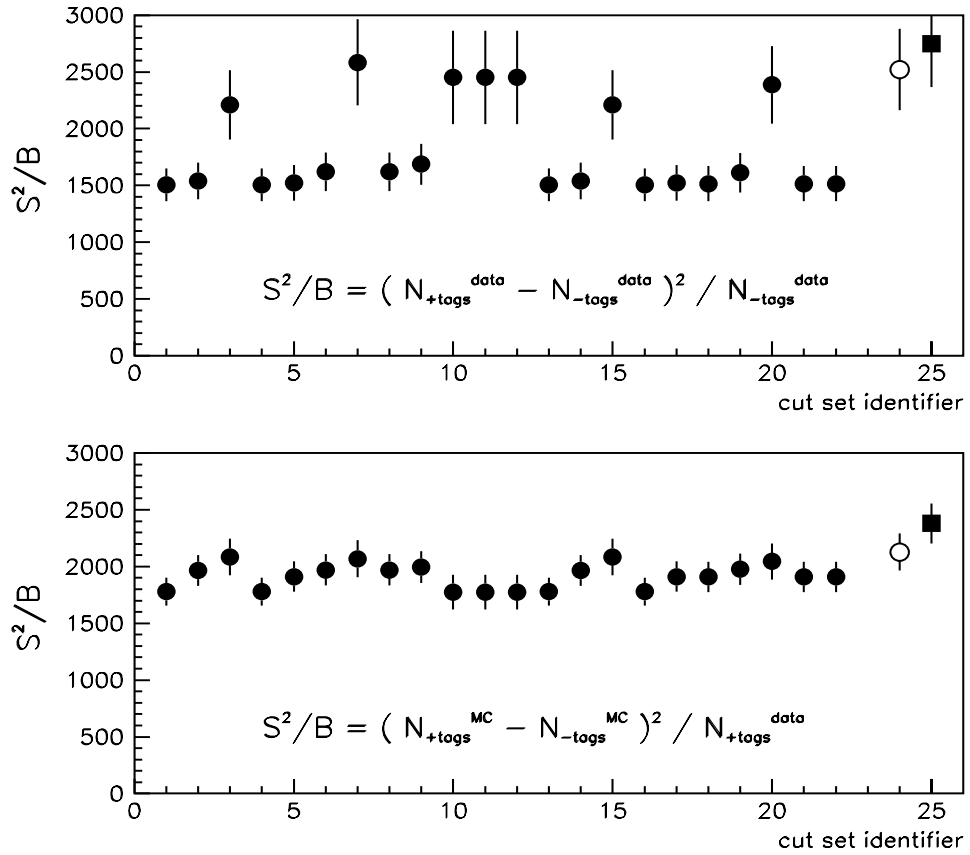

Figure 3.36: The optimization criteria, S^2/B, as a function of 24 sets of track selection cuts. The algorithm is seen to be relatively stable over a wide range of cuts.

Figure 3.37 plots the results of 27 different cut sets. Here the signal, S, is defined as the number of B-jet tags in a PYTHIA Monte Carlo with a top quark mass of 160 GeV/c^2 and the background, B, is defined as the number of positive tags in an inclusive jet data sample. In both Figures 3.36 and 3.37 we observe the algorithm to be relatively stable in S^2/B over a wide range of cut variations. This makes the final choice of cuts somewhat arbitrary. We base our final decision on the "discovery potential".

In making the final choice among the various cut sets we additionally consider that we expect our top yield to be small. This implies that in addition to considering the criteria S^2/B, the B-tag efficiency, ϵ_{B-tag}, ought also be considered. This is made more obvious if one considers an algorithm that applies very strict cuts, resulting in a very small fake tag rate and a correspondingly small B-tag efficiency. Such an algorithm might very well maximize S^2/B, but with a small data sample such an inefficient algorithm might yield a uselessly small number of top quark candidate events. Thus, in order to consider both these criteria simultaneously we calculate the "discovery potential" for a given set of cuts. For this last optimization we only consider three cut sets, known as options I, II, and III. These are those sets of cuts with highest efficiency and reasonable values of S^2/B. We then perform a statistical study to determine which of the three has the greatest potential for observing a significant excess of top quark candidate events assuming 50 pb^{-1} and 100 pb^{-1} data sets. For this optimization we assume a top quark mass of 170 GeV/c^2 and the corresponding theoretical production cross section of 6 pb. We employ a Pythia top quark Monte Carlo sample normalized to the production cross section and total integrated luminosity assumed. The Monte Carlo sample includes a full detector simulation and only those events passing the selection criteria described in Section 3.1 are considered. The mean number of background events is estimated by scaling the positive tag rate in an inclusive jet sample by the appropriate luminosity. This is analogous to the "method 1" background estimate described in references [24] and [23]. The results are plotted in Figure 3.38. Also shown are the

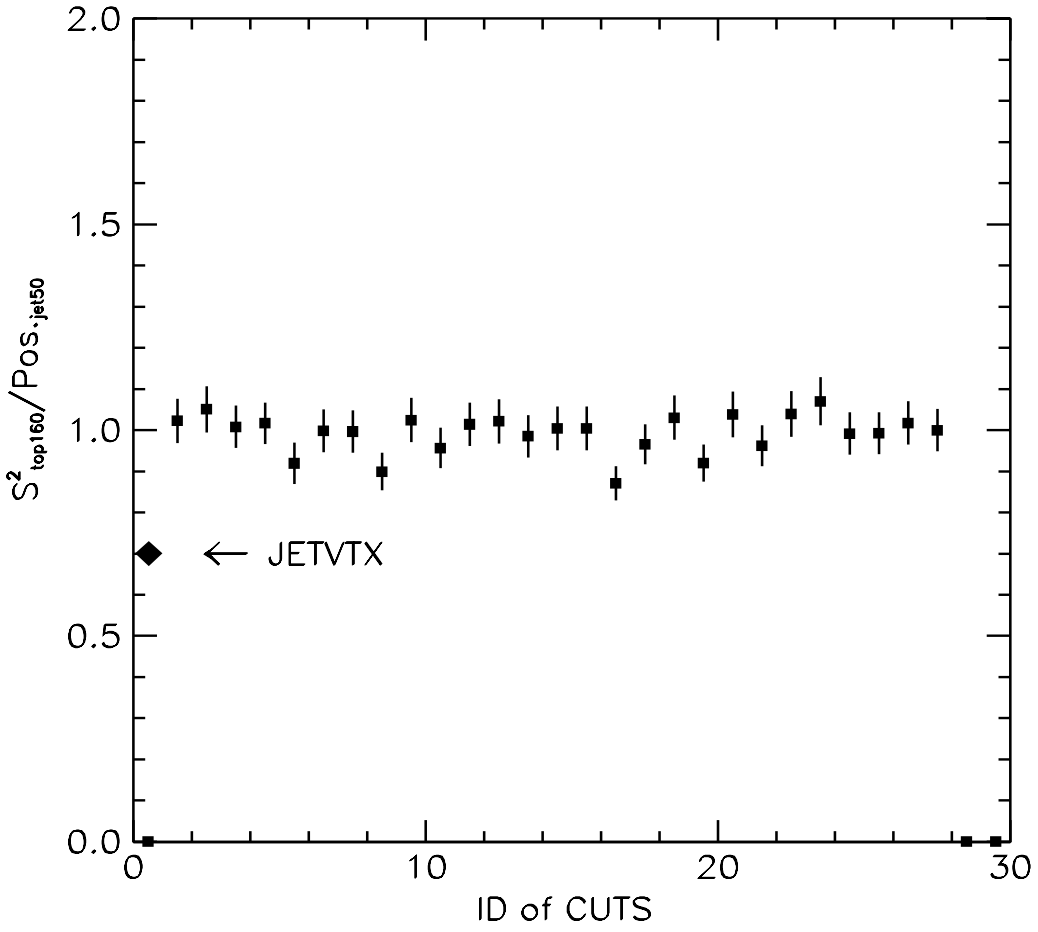

Figure 3.37: The optimization criteria, S^2/B, as a function of 27 sets of various track and vertex selection cuts. Again, the algorithm is seen to be relatively stable over a wide range of cuts.

results obtained when using the B-tag efficiencies measured using the B enriched inclusive electron sample. We observe that option III has a slight edge at smaller integrated luminosities. This becomes our default B-tagging algorithm. Figure 3.39 is a flow chart of the final algorithm. The final cuts are described in Figure 3.40.

3.4 Algorithm Performance in Control Samples

For any tagged jet we define the "$psuedo - c\tau$" as

$$psuedo - c\tau_{vtx} = \frac{L_{xy} \cdot M_{vtx}}{P_T^{vtx}} \tag{3.3}$$

where

$L_{xy} \equiv$ the transverse displacement of the secondary vertex from the primary interaction vertex as shown in Figure 3.3

$M_{vtx} \equiv$ the invariant mass of all tracks used in the vertex

$P_T^{vtx} \equiv$ the vector sum of the transverse momentum of all tracks used in the vertex.

The prefix "*psuedo*" recalls the fact that our algorithm does not completely reconstruct the decay vertex. In Figure 3.41 we compare the $psuedo - c\tau$ distribution of tagged electron jets in the B-enriched control sample discussed in Section 3.1.5 to the same distribution as measured in a Monte Carlo sample of $B \rightarrow eX$ decays. The data agree well with the Monte Carlo simulation of B-decay, which uses the world average B-hadron lifetime [51], and give us confidence that the algorithm really identifies B-jets. As discussed more thoroughly in Section 3.5.4, we estimate that approximately 40% of the electron jets in the B-enriched control sample are actually associated with the semi-leptonic decay of a B-hadron. The agreement in Figure 3.41 is curious, unless the algorithm tags B-jets much more efficiently than it tags charm-jets (D-jet) or non-heavy-flavor-jets (non-hf-jet). From Monte Carlo we determine that the ratio of tagging efficiencies is $\epsilon_B : \epsilon_D : \epsilon_{non-hf} \approx 40 : 10 : 1$. Thus, we expect a sample of tagged jets to have a large contribution from B-jets,

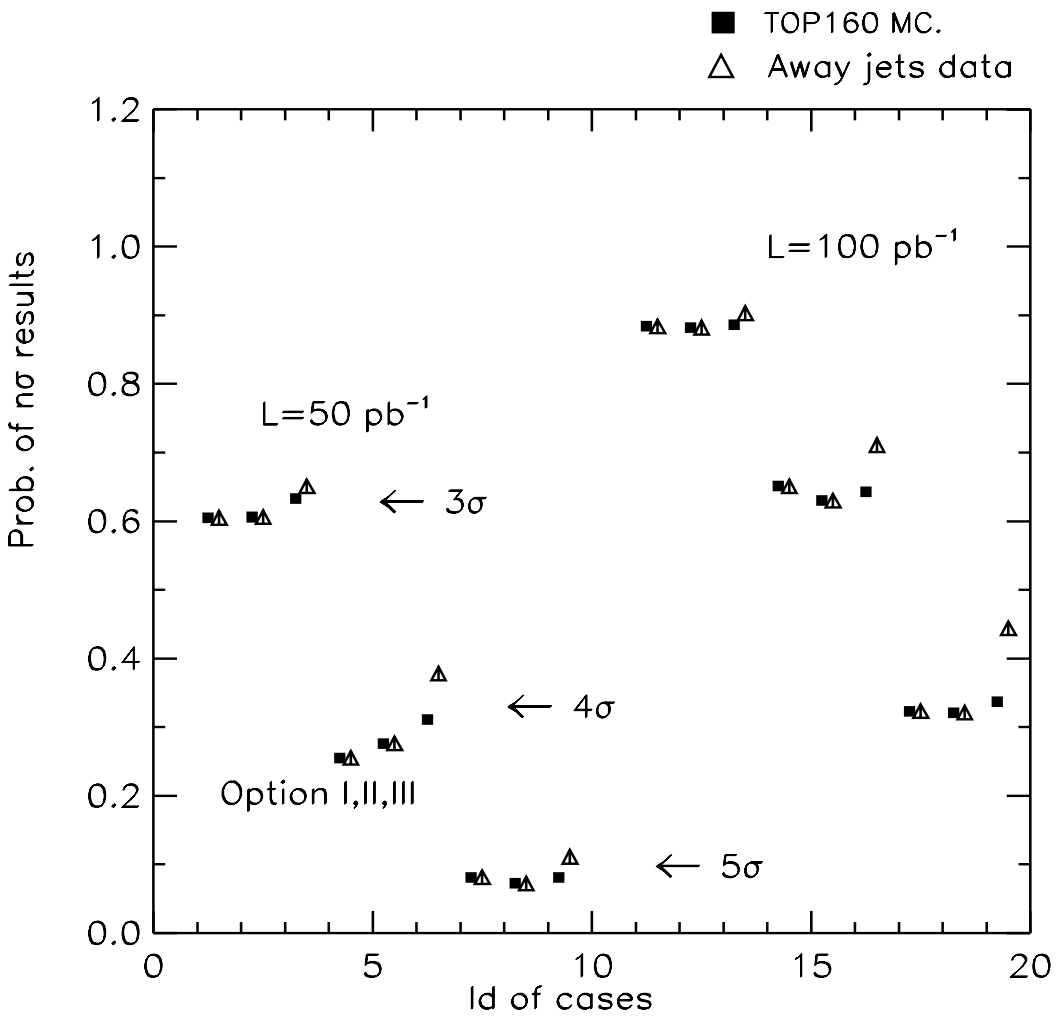

Figure 3.38: A comparison of the discovery potential for three sets of B-tag algorithm cuts. The probability for observing a 3, 4, or 5 σ excess, assuming a total integrated luminosity of 50 pb^{-1} or 100 pb^{-1}, is calculated for each of the three options using both data (triangles) and Monte Carlo (squares) as signal estimates.

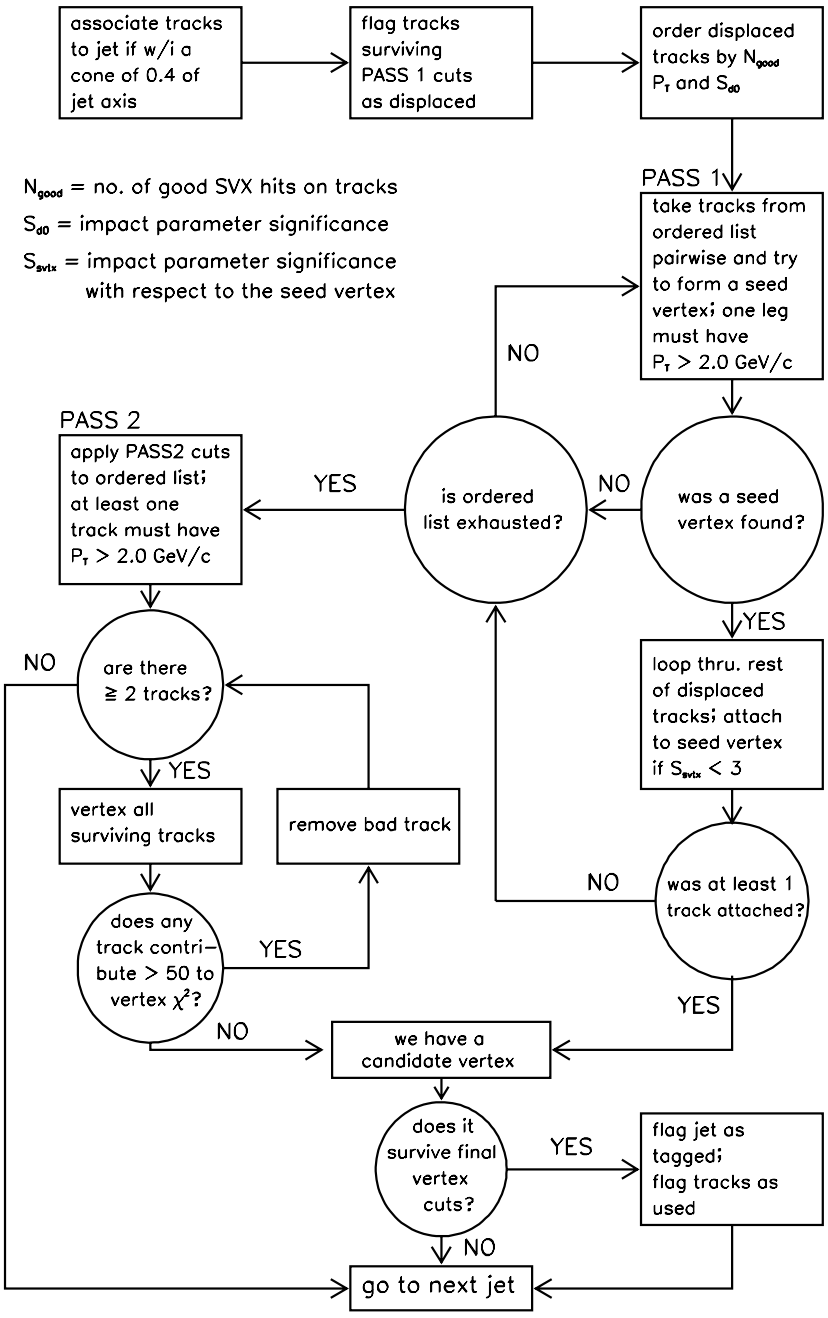

Figure 3.39: A flow chart of the final B-tag algorithm. The relevant cuts are given in Figure 3.40.

PASS 1 cuts

for all tracks within a
cone of 0.4 of a jet with
$E_T > 15$ GeV and $|\eta| < 2.0$:
- $S_{d0} > 2.5$
- $\chi^2/dof < 6$
- pass CTC cuts
- $|z_{trk} - z_{pvtx}| < 5$ cm
- $|d_0| < 0.15$ cm

for 3 or 4 hit SVX tracks :
- $P_T > 0.5$ GeV/c
- $N_{good} \geq 1$ hit

for 2 hit SVX tracks :
- $P_T > 1.5$ GeV/c
- $N_{good} = 2$ hits
- hit pattern 1100 or 0011

not used in a K^0 or Λ^0 vertex
not used in another
candidate B vertex

K^0_s and Λ^0 removal

tracks are flagged as being used
in a K^0 or Λ^0 vertex if they form
a vertex with an oppositely
charged track that passes CTC
cuts ; both legs must have
- $S_{d0} > 2.5$

the vertex must satisfy these cuts :
- using vertex constrained momenta, the vertex mass must be < 10 (6) MeV/c^2 away from the K^0 (Λ^0) mass
- the displacement of the vertex projected along the V−axis $> 10\sigma$
- the displacement of the vertex projected perpendicular to the V−axis $< 3\sigma$

PASS 2 cuts

for all tracks surviving
PASS 1 cuts :
- $S_{d0} > 3.0$
- $P_T > 1.0$ GeV/c

for 4 hit SVX tracks :
- $N_{good} \geq 1$ hit

for 3 hit SVX tracks :
- $N_{good} \geq 2$ hit

for 2 hit SVX tracks :
- not allowed

CTC cuts

for all tracks :
- must be 3−D

and have associated with them
- ≥ 2 axial layers with
- ≥ 4 hits in each layer

and
- ≥ 2 stereo layers with
- ≥ 2 hits in each layer

Good SVX hit cuts

an SVX cluster is good if :
- it is ≤ 3 strips long
- it contains no noisy strips
- it contains no dead strips
- it is not shared

Final vertex cuts

a candidate B vertex must have :
- ≥ 2 tracks
- $\chi^2_{max} < 50$
- $|L_{xy}| < 2.5$ cm
- $S_{Lxy} > 3$
- $|c\tau| < 1.0$ cm
- $|M_{vtx} - M_K| > 20$ MeV/c^2

where S_x = significance of the variable x, $|x / \sigma_x|$
N_{good} = number of good SVX hits

Figure 3.40: The list of cuts used in the final B-tag algorithm. A flow chart of the algorithm is given in Figure 3.39.

even if the pre-tagged parent sample has a very small contribution from B-jets. This is demonstrated in Figure 3.42, in which we plot the effective $c\tau$[†] distribution from a sample of generic jets collected with the 50 GeV trigger threshold. As discussed in Rerferences [24] and [52], we fit this distribution to a combination of effective $c\tau$ distributions from B-, D-, and non-hf-jets. The $c\tau$ shapes are determined from Monte Carlo. The fit gives the relative fraction of B:D:non-hf tags in the positive (negative) L_{xy} region to be approximately $40\% : 40\% : 20\%$ ($20\% : 20\% : 60\%$).

[†]The effective $c\tau$ includes a correction factor to account for those decay products which the algorithm fails to associate with the secondary vertex [24].

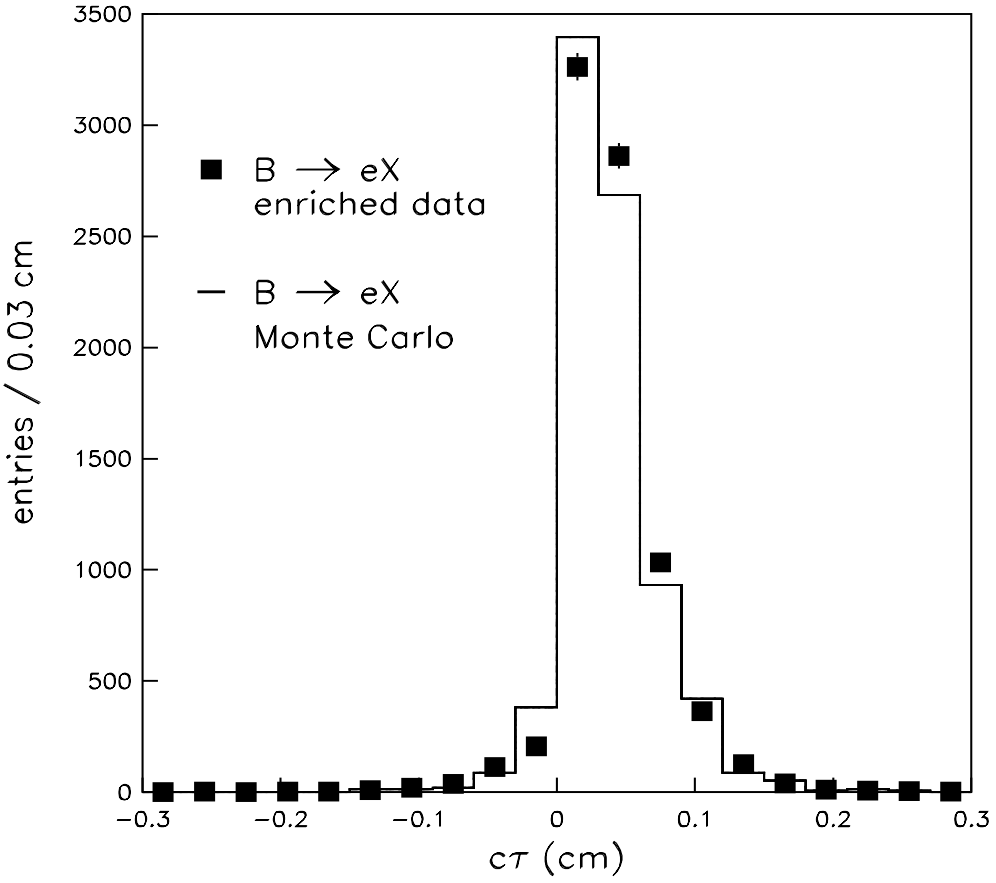

Figure 3.41: The $psuedo - c\tau$ distribution for tagged electron jets in a B-enriched data sample (points) and a Monte Carlo sample $B \to eX$ decays (histogram).

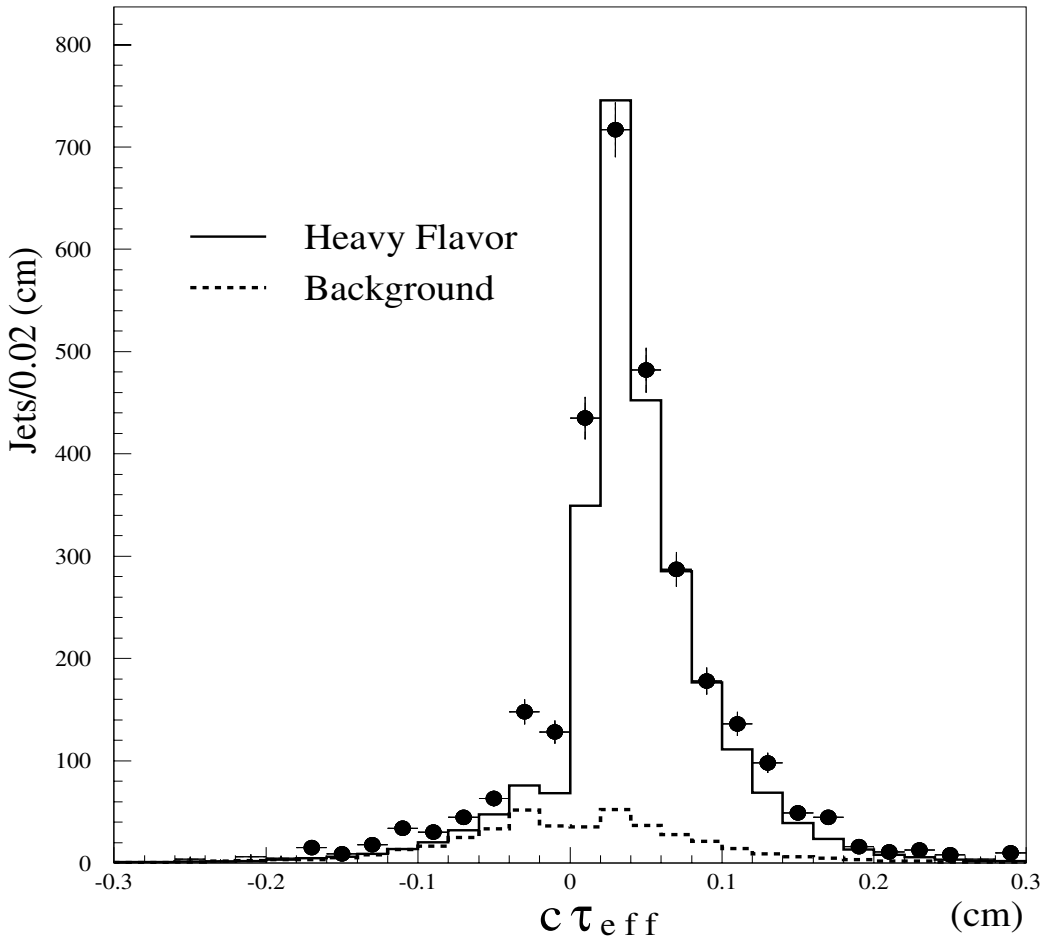

Figure 3.42: The $c\tau_{eff}$ distribution for a sample of generic jets collected with the 50 GeV trigger threshold (points). We fit the distribution to a combination of heavy flavor tags (B- and D- jet tags; solid) and background tags (non-hf-jets; dotted). The fit returns a ratio of heavy flavor to background tags in the positive L_{xy} region of $\approx 4:1$.

3.5 Acceptance for a Standard Model Top Quark

We use a combination of data and Monte Carlo to determine our efficiency for identifying a $t\bar{t}$ event. The Monte Carlo generator is PYTHIA, and Standard Model couplings are assumed. We consider the top quark masses $M_t = 150, 170$, and 190 GeV/c^2. We calculate the total event detection efficiency as follows

$$\epsilon_{t\bar{t}} = A_{t\bar{t}} \cdot \epsilon_{|z_{pvtx}|} \cdot \epsilon_{trig} \cdot \epsilon_{lepton\ id} \cdot \epsilon_{tag} \tag{3.4}$$

where

$A_{t\bar{t}} \equiv$ the fraction of $t\bar{t}$ events within the geometric acceptance of the CDF detector and passing the kinematic requirements of the event selection

$\epsilon_{|z_{pvtx}|} \equiv$ the efficiency of the cut $|z_{pvtx}| < 60$ cm

$\epsilon_{trig} \equiv$ the trigger efficiency for identifying high P_T leptons

$\epsilon_{lepton\ id} \equiv$ the efficiency of the lepton identification cuts

$\epsilon_{tag} \equiv$ the efficiency for tagging at least one jet in the event.

We discuss each piece separately below.

3.5.1 Determination of $A_{t\bar{t}}$

The geometric and kinematic acceptance is calculated as follows.

$$A_{t\bar{t}} = \epsilon_{geom} \cdot \epsilon_{kin} \cdot \epsilon_{\not\!\!E_T} \cdot \epsilon_{iso} \tag{3.5}$$

where

$\epsilon_{geom} \equiv$ the fraction of fiducial $t\bar{t}$ events, defined as the fraction of all generated $t\bar{t}$ events with ≥ 1 lepton with $P_T > 15$ GeV/c and $|\eta| < 3.0$

$\epsilon_{kin} \equiv$ the fraction of fiducial $t\bar{t}$ events with ≥ 1 one good electron or muon, defined as an electron (muon) with E_T (P_T) > 20 GeV/c and $|\eta| < 2.0$ and ≥ 3 jets ($E_T > 15$ GeV, $|\eta| < 2.0$).

$\epsilon_{\not\!\!E_T} \equiv$ the fraction of $t\bar{t}$ events with ≥ 1 good electron or muon, ≥ 3 jets and with $\not\!\!E_T > 20$ GeV

$\epsilon_{iso} \equiv$ the fraction of $t\bar{t}$ events having ≥ 1 good lepton, ≥ 3 jets and passing the $\not\!\!E_T$ requirements in which the high P_T lepton additionally passes the isolation requirement, $I_{cal} < 0.1$.

Each of these efficiencies is conditional upon the previous one.

We assign a $\pm 5\%$ and $\pm 2\%$ (relative) systematic error due to uncertainties in the modelling of initial state (ISR) and final state (FSR) radiation, respectively. These errors are estimated by taking half the difference in $A_{t\bar{t}}$ between Monte Carlo samples with the ISR and FSR turned off separately and that obtained using the default Monte Carlo parameters. We additionally assign a $\pm 2\%$ (relative) error due to detector resolution effects and a $\pm 7\%$ (relative) error due to uncertainties in the jet energy scale. Finally, we assign a $\pm 1\%$ (relative) error due to the dependence of ϵ_{iso} on the number of multiple interactions in an event. This last uncertainty is estimated by measuring the efficiency of the $I_{cal} < 0.1$ cut on a sample of $W \rightarrow \mu\nu$ events as a function of the instantaneous luminosity. This is shown in Figure 3.43. We assume the distribution is flat and estimate a systematic by taking half the difference assuming the $\pm 1\sigma$ slope variations convoluted with the instantaneous luminosity distribution of events in our signal region. Table 3.9 shows $A_{t\bar{t}}$ for several masses of the top quark. The first error is statistical and the second is the quadrature sum of all systematic errors.

3.5.2 Determination of ϵ_{trig} and $\epsilon_{lepton\ id}$

As discussed in Sections 3.1.2 and 3.1.3, we measure the trigger and lepton identification efficiencies using $Z \rightarrow \ell\ell$ ($\ell = e$ or μ) events. The results are given in Table 3.10. For $\epsilon_{lepton\ id}$ we *exclude* the explicit isolation cut, I_{cal}, which is included as part of the $A_{t\bar{t}}$ calculation discussed in Section 3.5.1. Taking the average efficiency over all detector components weighted by their relative acceptances yields

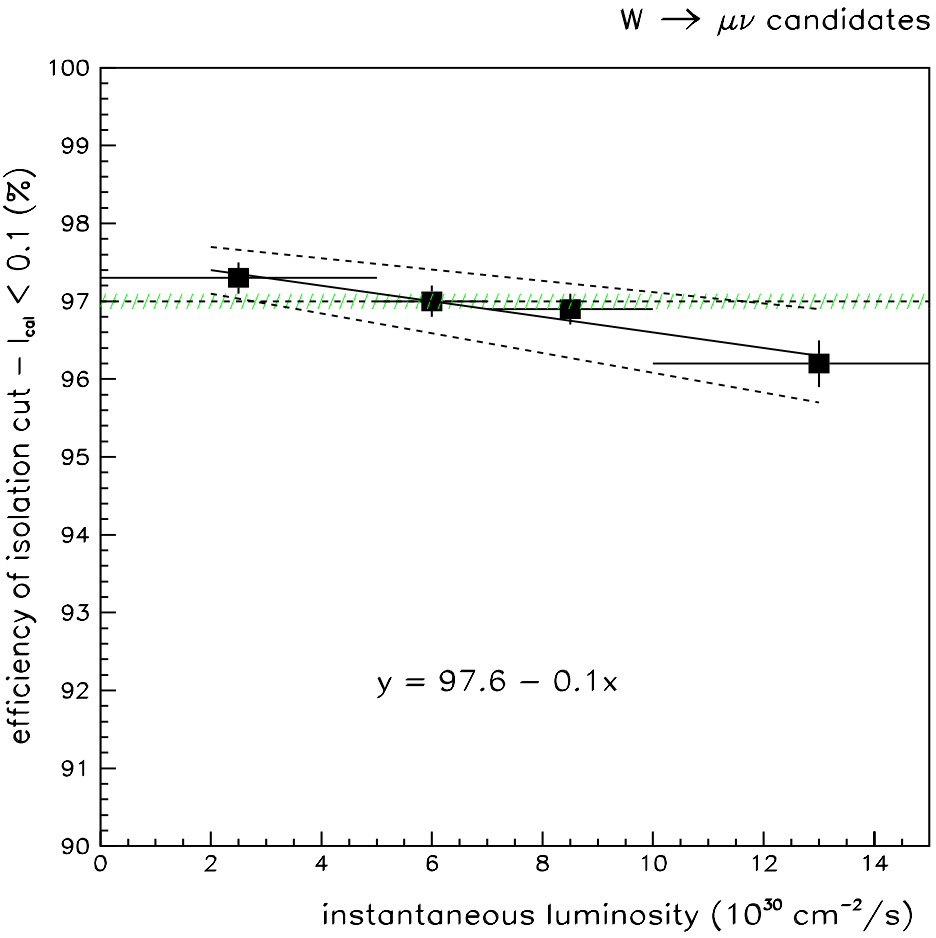

Figure 3.43: The efficiency of the isolation cut, $I_{cal} < 0.1$, as a function of the instantaneous luminosity in the event. We use $W \rightarrow \mu\nu$ events and assume the distribution is the same for electron events. The result of a fit to a sloped line is given and displayed (solid line). The $\pm 1\sigma$ variation on the slope is also displayed as the dashed lines. The $\pm 1\sigma$ bounds assuming no dependence are given by the hatched region.

$A_{t\bar{t}} = \epsilon_{geom} \cdot \epsilon_{lepton} \cdot \epsilon_{\not\!\!E_T} \cdot \epsilon_{iso}$

M_t :	150 GeV/c^2	170 GeV/c^2	190 GeV/c^2
$A_{t\bar{t}}$:	$0.105 \pm 0.003 \pm 0.010$	$0.116 \pm 0.002 \pm 0.011$	$0.122 \pm 0.003 \pm 0.012$

Table 3.9: Combined geometric and kinematic acceptances for $t\bar{t}$ events at various assumed top quark masses, M_t. The first error is statistical, the second is the quadrature sum of all systematic errors.

$\epsilon_{trig} = 0.854 \pm 0.014$ and $\epsilon_{lepton\ id} = 0.903 \pm 0.008$ for leptons with $P_T > 20$ GeV/c. The lepton samples used to measure the above efficiencies have isolation environments different from leptons in $t\bar{t}$ events. We measure the dependence of $\epsilon_{trig} \cdot \epsilon_{id}$ as a function of the isolation variable, I_{cal}, and the number of jets in the event, N_{jet}, using a sample of $W \rightarrow \mu\nu$ events required to pass all the event selection criteria of Section 3.1. We fit the resulting distributions, shown in Figure 3.44, to a sloped line and recalculate the trigger efficiency using the resulting $\pm 1\sigma$ slope variations convoluted with the appropriate distribution for leptons in fiducial $t\bar{t}$ events. We set the systematic error equal to half the difference between these variations and the value obtained assuming no dependence on isolation or jet multiplicity. The resulting systematic error is 5%.

3.5.3 Determination of $\epsilon_{|z_{pvtx}|}$

An additional fiducial requirement is that the z co-ordinate of the primary event vertex be within 60 cm of the nominal interaction point, $|z_{pvtx}| < 60$ cm. We use $W \rightarrow \mu\nu$ events passing the lepton identification criteria discussed in Section 3.1.2 to measure the efficiency of this cut. We measure $\epsilon_{|z_{pvtx}|} = 0.949 \pm 0.001$, where the error is statistical only. The z_{pvtx} distribution for all of run 1B is shown in Figure 3.45. Since the TeVatron parameters are changing during the course of the run, we investigate for a possible time dependence by plotting $\epsilon_{|z_{pvtx}|}$ as a function

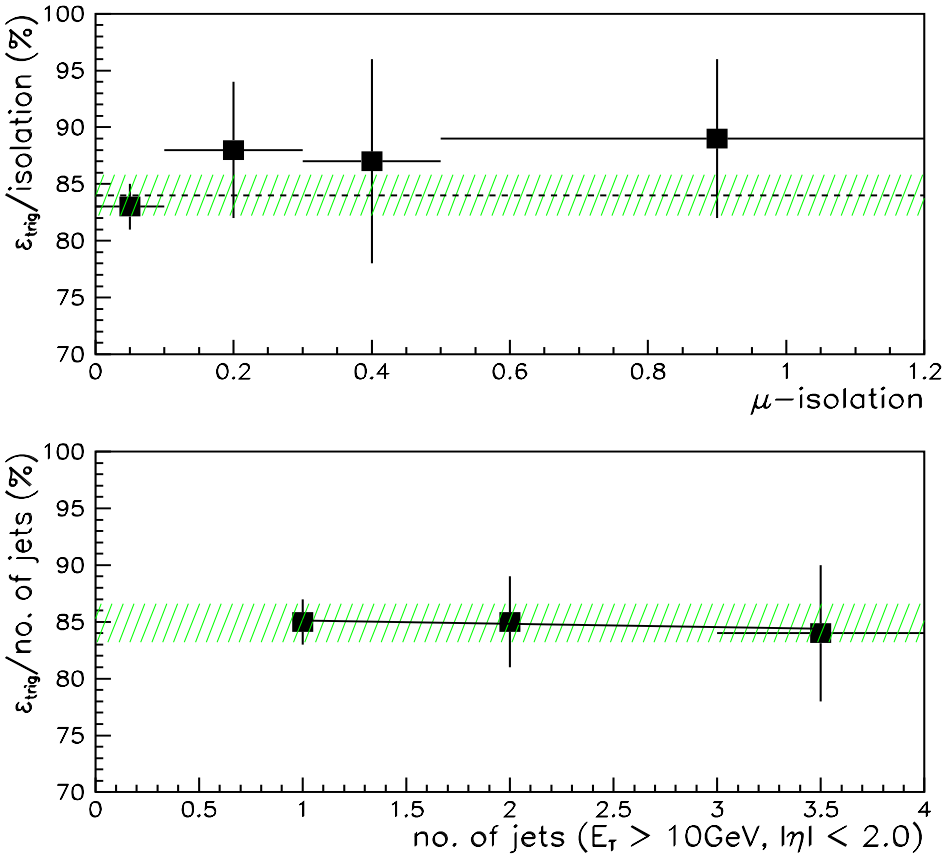

Figure 3.44: The CMUP trigger efficiency as a function of the muon isolation, I_{cal} (top), and the number of jets ($E_T > 10$ GeV and $|\eta| < 2.0$) in the event, N_{jet} (bottom). We assume the shapes of these distributions are the same for all triggers used in analysis.

ϵ_{trig} and $\epsilon_{lepton\ id}$

	muons	electrons
ϵ_{trig}	$0.871^{+0.061}_{-0.091}$ (CMNP)	
	$0.834^{+0.021}_{-0.023}$ (CMUP)	0.928 ± 0.002 (CEM)
	$0.696^{+0.045}_{-0.049}$ (CMX)	
$\epsilon_{lepton\ id}$	$0.953^{+0.026}_{-0.044}$ (CMNP)	
	$0.971^{+0.008}_{-0.011}$ (CMUP)	0.837 ± 0.012 (CEM)
	$0.943^{+0.016}_{-0.021}$ (CMX)	

Table 3.10: The trigger and lepton identification efficiencies as measured using $Z \rightarrow \ell\ell$ ($\ell = e$ or μ) events. The errors are statistical only.

of the total integrated luminosity as shown in Figure 3.46. It is observed to be flat to within 1%. To determine whether or not the distribution is biased by requiring ≥ 3 jets ($E_T > 15$ GeV/c, $|\eta| < 2.0$) we measure $\epsilon_{|z_{pvtx}|}$ as a function of the number of jets in the event, N_{jet}. This is also shown in Figure 3.46 and is flat to within 2%.

We assign a systematic error of $\pm 0.8\%$ and $\pm 2.3\%$ to our assumptions that $\epsilon_{|z_{pvtx}|}$ is flat as a function of total integrated luminosity and the number of jets in the event, respectively. These are estimated by fitting the appropriate curve in Figure 3.46 to a sloped line and taking half the maximum difference assuming the $\pm 1\sigma$ variations of the fit parameters.

3.5.4 Determination of ϵ_{tag}

We define our efficiency for tagging at least one jet in $t\bar{t}$ events passing all other event selection criteria as

$$\epsilon_{tag} = \epsilon^{event}_{B-tag} + \epsilon^{event}_{mistag} - \epsilon^{event}_{B-tag} \cdot \epsilon^{event}_{mistag} \tag{3.6}$$

where

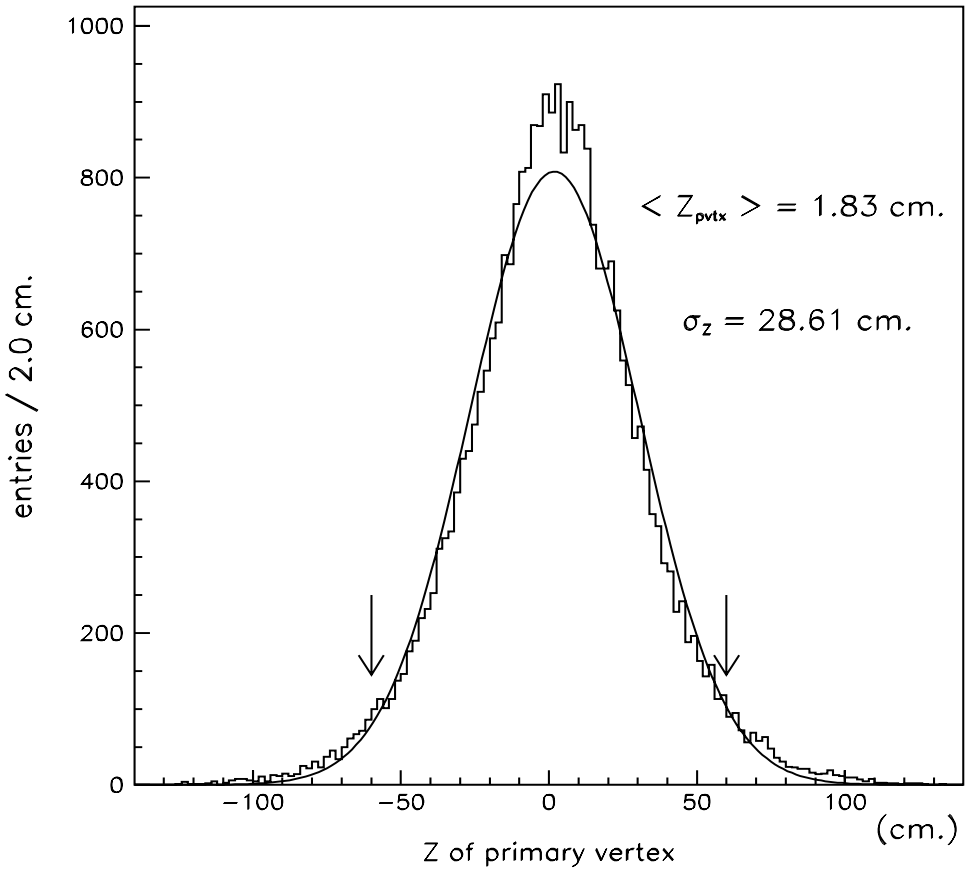

Figure 3.45: The z_{pvtx} distribution for all run 1B data. The results of a fit to a Gaussian are also displayed. The arrows indicate the cut value of ± 60 cm.

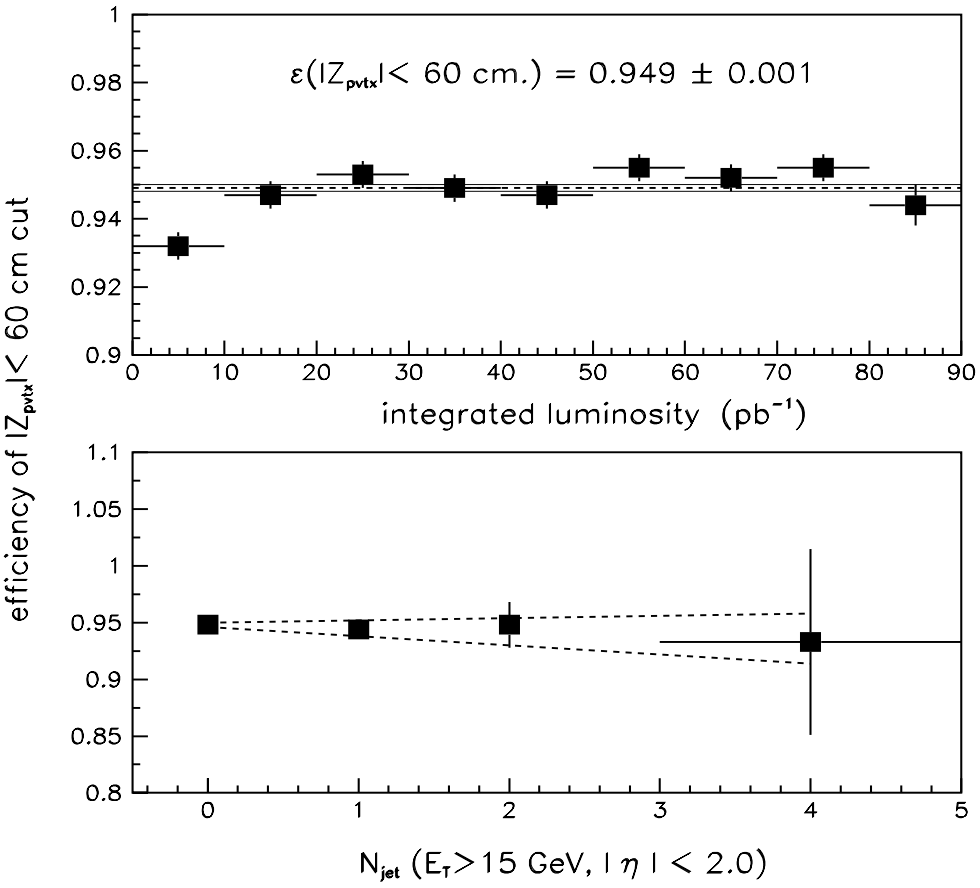

Figure 3.46: The $\epsilon_{|z_{pvtx}|}$ as a function of the total integrated luminosity (top) is flat to within 1% and yields an average efficiency of $\epsilon_{|z_{pvtx}|} = 0.949 \pm 0.001$ (shaded region). The $\epsilon_{|z_{pvtx}|}$ as a function of the number of jets in the event, N_{jet}, is fit to a sloped line (bottom). The $\pm 1\sigma$ variations of the slope are shown as dashed lines.

$\epsilon^{event}_{B-tag} \equiv$ the fraction of $t\bar{t}$ events passing all event selection criteria with ≥ 1 tagged B-jet

$\epsilon^{event}_{mistag} \equiv$ the fraction of $t\bar{t}$ events passing all event selection criteria with ≥ 1 tagged nonB-jet.

We discuss each separately below.

Determination of $\epsilon^{event}_{mistag}$

We estimate the fraction of $t\bar{t}$ events in which at least one non-B-jet is tagged using Monte Carlo. We find $\epsilon^{event}_{mistag} = 1 \pm 1\%$, where the error is dominated by the systematic uncertainty derived by comparing various Monte Carlo simulations.

Determination of ϵ^{event}_{B-tag}

The efficiency for tagging ≥ 1 B-jet in a $t\bar{t}$ event passing all event selection criteria is calculated using a mixture of data and Monte Carlo. From the data we measure the efficiency for tagging *semileptonic* B-decays. We then rely on a Monte Carlo simulation to extrapolate the measured B-tagging efficiency for semileptonic B-decays to that expected for the generic B-decays in $t\bar{t}$ events. This extrapolation requires that we scale the measured Monte Carlo tagging efficiency by the efficiency observed in data. We call this the B-tagging scale factor, SF. The determination of the semileptonic B-decay tagging efficiency and of the data to Monte Carlo scale factor is described below. The measurements discussed all use run 1B data unless otherwise specified. We consider differences between run 1A and run 1B data at the end of this Section.

We use the B-enriched, low P_T, inclusive electron data set described in Section 3.1.5 to help determine the efficiency *per jet* of the B-tagging algorithm described in Section 3.3.2. Two different methods are employed, and each yields the B-tagging efficiency for *semileptonic* B-decays.

For each event we define the "electron jet" (or "ejet") as that jet closest to the electron in $\eta - \phi$ space and require

$$E_T^{ejet} > 10 \text{ GeV}$$
$$|\eta^{ejet}| < 2.0$$
$$\Delta R_{ele-jet} = \sqrt{\Delta\eta^2_{ele-jet} + \Delta\phi^2_{ele-jet}} < 0.4.$$

We define the "away jet" (or "ajet") as that jet opposite the electron jet and require

$$\Delta R_{ejet-ajet} > 2.5$$
$$E_T^{ajet} > 15 \text{ GeV}$$
$$|\eta^{ajet}| < 2.4.$$

We also require that the away jet be "taggable". A taggable jet has associated with it ≥ 2 good tracks within the SVX fiducial volume. A good track is defined as any track passing all "pass 1" cuts, *excluding the* S_{d_0} *cut*, described in Figure 3.40.

The first method employed to measure the B-tagging efficiency uses the expression

$$\epsilon_{B-tag}^{method\ 1} = \left(\frac{P_{ejet} - N_{ejet}}{T_{ejet}}\right) \cdot \left(\frac{1}{F_B}\right) \tag{3.7}$$
$$= (XS_{ejet}) \cdot \left(\frac{1}{F_B}\right) \tag{3.8}$$

where

$P_{ejet} \equiv$ the number of positively tagged electron jets (there is *no away tag requirement*)

$N_{ejet} \equiv$ the number of negatively tagged electron jets (there is *no away tag requirement*)

$T_{ejet} \equiv$ the number of taggable electron jets (there is *no away tag requirement*)

$F_B \equiv$ the fraction of electron jets associated with a real semileptonic B-decay

$XS_{ejet} = (P_{ejet} - N_{ejet})/T_{ejet} \equiv$ the positive excess tagging rate in the electron jets.

Since we only consider tags in the electron jets — that is, we require no away jet tag — we call this the "single tag" method.

In determining the electron jet tagging efficiency, we subtract the negative tagged electron jets. This is a small background subtraction of order 5% . The positive excess tagging rate for all electrons jets with $E_T^{ejet} > 10$ GeV is $XS_{ejet} = 12.0 \pm 0.1$ %. The correction factor, F_B, is required to account for the B-purity of the pre-tagged electron jets. We measure F_B by looking for a nearby, low P_T muon ($\Delta R_{\mu-ejet} < 0.4$, and $P_T^{\mu} > 2$ GeV/c) associated with the semileptonic sequential decay of a charmed hadron, $B \to eDX \to e^{\pm}\mu^{\mp}X$. We use the following expression to calculate F_B

$$F_B = \left(\frac{OS_{e-\mu} - SS_{e-\mu}}{\epsilon_{\text{soft }\mu}}\right) \cdot \left(\frac{1}{T_{ejet}}\right) \tag{3.9}$$

where

$OS(SS)_{e-mu} \equiv$ the number of opposite (same) sign $e - \mu$ pairs

$\epsilon_{\textbf{soft }\mu} \equiv$ the efficiency for finding the muon associated with the sequential charm decay.

$T_{ejet} \equiv$ the number of taggable electron jets (there is *no away tag requirement*)

The largest background in the determination of F_B is due to fake leptons. The number of same-sign $e - \mu$ pairs provides a calibration of this background. Gluon splitting is not expected to contribute significantly to the opposite-sign sample. The fraction of all $b\bar{b}$ events which come from gluon splitting is predicted to be $\sim 25\%$. The cone cut of $\Delta R_{ele-jet} < 0.4$ and the isolation cuts implicit in the electron identification reduce this to $< 10\%$. Therefore, the excess of opposite-sign over same-sign events, $OS_{e-\mu} - SS_{e-\mu}$, is a clean signature for sequential semileptonic

B-decays. The distribution of the $e-\mu$ invariant mass, $M_{e-\mu}$, after background subtraction, is shown in Figure 3.47 for all electron jets with an away jet tag and is consistent with the $M_{e-\mu}$ distribution derived from a $B \to eDX \to e^{\pm}\mu^{\mp}X$ Monte Carlo.

The efficiency for finding the sequential μ in the electron jet is calculated as

$$\epsilon_{\text{soft }\mu} = F(B \to eDX \to e\mu X; P_T^{\mu} > 2 \text{ GeV}/c) \cdot \epsilon_{\mu \text{ find}} \tag{3.10}$$

where

$F \equiv$ the fraction of $B \to eDX$ decays that also have a μ from the sequential charm decay with $P_T > 2.0$ GeV/c; the μ is required to be within a cone of 0.4 from the electron jet axis in $\eta - \phi$ space, $\Delta R_{\mu-ejet} < 0.4$

ϵ_{μ} **find** $\equiv$ the efficiency for finding a muon with $P_T > 2.0$ GeV/c.

Using a Monte Carlo of $b\bar{b}$ events, passing all the same event selection criteria used in the data, we measure $F = 0.028 \pm 0.002$, where the error is statistical only. The muon finding efficiency, $\epsilon_{\mu \text{ find}}$, is measured separately for each central muon detector component (CMU, CMP, and CMX) as a function of P_T^{μ} using $Z \to \mu\mu$ and $J/\psi \to \mu\mu$ data events [32]. We then calculate $\epsilon_{\mu \text{ find}}$ as the average over all central muon detector components weighted by their relative acceptance and by the P_T spectrum of the sequentially decaying muons as determined in the Monte Carlo. We find, within the limited statistics available, $\epsilon_{\mu \text{ find}}$ is independent of E_T^{ejet} and is given as $\epsilon_{\mu \text{ find}} = 0.866 \pm 0.087$. This yields a soft muon finding efficiency of $\epsilon_{\text{soft }\mu} = 0.024 \pm 0.003$, which is also independent of E_T^{ejet}. We measure for all electron jets with $E_T^{ejet} > 10$ GeV that $F_B = 39 \pm 5$ % and $\epsilon_{B-tag}^{method\ 1} = 31 \pm 4$ %, where the error is dominated by the uncertainty in $\epsilon_{\mu \text{ find}}$.

The second method employed to measure the B-tagging efficiency uses the expression

$$\epsilon_{B-tag}^{method\ 2} = \left(\frac{P_{ejet}^{atag}}{T_{ejet}^{atag}}\right) \cdot \left(\frac{P_{ajet}}{P_{ajet} - N_{ajet} \cdot (1 - F_B)}\right) \tag{3.11}$$

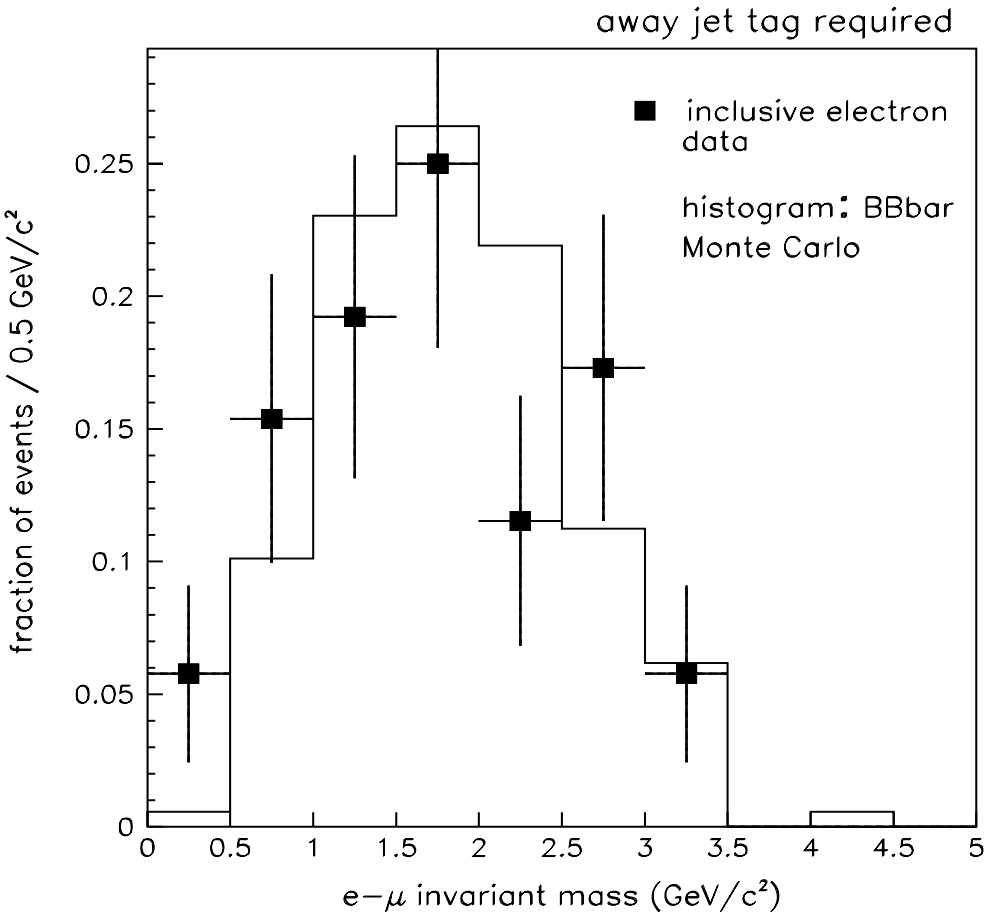

Figure 3.47: The $e-\mu$ invariant mass distribution for all electron jets with an away side tag required. The data points include a background subtraction.

$$= R \cdot \left(\frac{1}{1 - F_{non-B}} \right) \tag{3.12}$$

where

$P_{ejet}^{atag} \equiv$ the number of positively tagged electron jets with a *positively tagged away jet required* on the opposite side (this increases the B-purity by a factor of ~ 2 on the electron jet side)

$T_{ejet}^{atag} \equiv$ the number of taggable electron jets with a *positively tagged away jet required* on the opposite side

$P_{ajet} \equiv$ the number of positively tagged away jets

$N_{ajet} \equiv$ the number of positively tagged away jets as predicted using the tag rate parameterization discussed in Section 3.7.2

$F_B \equiv$ the fraction of electron jets from B decay as determined above

$R \equiv$ the electron jet tagging rate

$F_{non-B} \equiv$ an estimate of the non-B fraction of electron jets with an away jet tag required

For all electron jets with $E_T^{ejet} > 10$ GeV we measure $R = 29 \pm 1$ %. The factor F_{non-B} is required as a small background subtraction and is of order 15%. Since an away jet tag is required in both the numerator and denominator of the electron jet tagging rate, R, we call this the "double tag" method. For all electron jets with $E_T^{ejet} > 10$ GeV we find $\epsilon_{B-tag}^{method\ 2} = 34 \pm 2$ %, where the error is statistical only.

In Figure 3.48(top) we plot $\epsilon_{B-tag}^{method\ 1}$ and $\epsilon_{B-tag}^{method\ 2}$ as a function of E_T^{ejet}. They are consistent to within 1.5σ of each other in all but the first bin ($10 < E_T^{ejet} < 15$ GeV), where they differ by 2σ. This difference could be due to simultaneous statistical fluctuations in the number of both double and single tagged events or due to an undiscovered dependence on E_T^{ejet} of some element used in determining the efficiencies. In particular, in the single tag method one might expect $\epsilon_{\mu\ \mathrm{find}}$, since it

depends on the P_T^{μ}, to likewise depend on the E_T^{ejet}. As previously mentioned, this dependence might be masked by the limited statistics of the available Monte Carlo sample. We should note that in $t\bar{t}$ events we only consider jets with $E_T > 15$ GeV for tagging. Our reason for including this lower E_T bin in this study becomes more obvious when we discuss the determination of the scale factor in the next section.

We also note in Figure 3.48(top) that the efficiency as determined using the single tag method is systematically lower than the efficiency as determined using the double tag method. We discuss this in the next Section.

Determination of the Scale Factor

We compare the Btag efficiency measured in data with the same efficiency determined using Monte Carlo. A $b\bar{b}$ Monte Carlo is used and is required, after a full detector simulation, to pass all the same event selection criteria as the data. We calculate the ratio of data to Monte Carlo tagging efficiency for the electron jet as a function of the electron jet E_T,

$$SF = \left(\frac{\epsilon_{B-tag}^{data}}{\epsilon_{B-tag}^{MC}} \right) \cdot R_{taggable} \tag{3.13}$$

where

$\epsilon_{B-tag}^{data} \equiv$ the efficiency for tagging a B-jet as measured in the data; we take the weighted average of single and double tag methods

$\epsilon_{B-tag}^{MC} \equiv$ the efficiency for tagging a B-jet as measured in a $b\bar{b}$ Monte Carlo

$R_{taggable} \equiv$ the data to Monte Carlo ratio of the fraction of jets which are taggable

The correction $R_{taggable}$ is required since we normalize our tagging efficiencies to the number of taggable jets (cf. equations 3.12 and 3.8). It is measured to be 0.990 ± 0.002 independent of jet E_T. We assume this to be flat during the course of the run and assign a 1.2% (relative) systematic derived by fitting the distribution in Figure 3.51 to a sloped line and taking half the difference assuming the $\pm 1\sigma$ slope

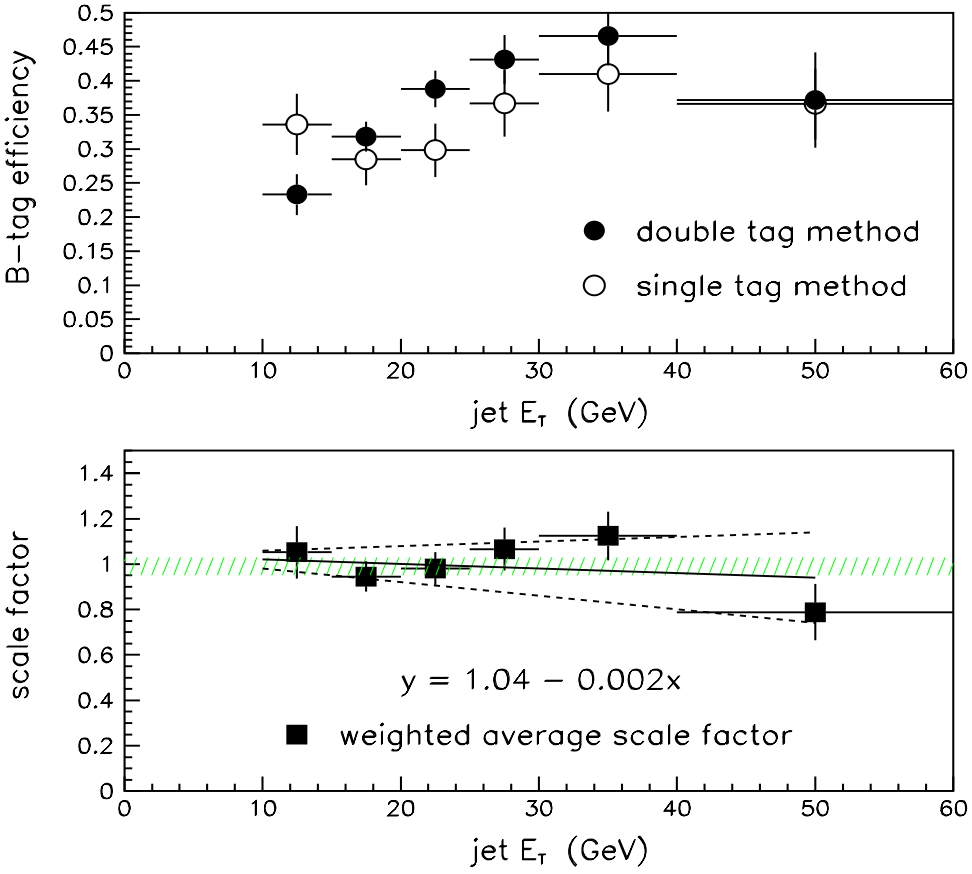

Figure 3.48: The B-tag efficiency, as determined using the two methods described in Section 3.5.4, is plotted versus the E_T^{ejet} (top). The weighted average scale factor as a function of E_T^{ejet} is also plotted (bottom). The result of a fit to a sloped line is given and is displayed as the solid line. The $\pm 1\sigma$ variations of the slope are given as dashed lines. The shaded region is the $\pm 1\sigma$ bounds of a fit assuming no dependence on E_T^{ejet}.

variations. Figure 3.48(bottom) shows SF as a function of jet E_T. The distribution is consistent with being flat to within $\sim 5\%$. In each E_T bin we determine ϵ_{B-tag}^{data} by taking the weighted average of ϵ_{B-tag} as determined using the single and double tag methods. Averaging over all jet $E_T > 10$ GeV yields $SF = 0.98 \pm 0.04$. We also find good agreement between the kinematic features of the tags in the data and $b\bar{b}$ Monte Carlo as shown in Figures 3.49 and 3.50. We compare the number of tracks included in the secondary vertex tag, N_{trk}, the summed P_T and invariant mass of those tracks (P_T^{vtx} and M_{vtx} respectively), and the "psuedo-cτ" $= \frac{L_{xy} \cdot M_{vtx}}{P_T^{vtx}}$ of the vertex for both the semileptonic B-decay tags in electron jets (with an away tag) and for the generic B-decay tags in away jets. The discrepancy in the 2 track bin of the N_{trk} distribution for away jets is consistent with an expected $\sim 7 - 10\%$ contribution from mistags. These comparisons give us confidence that the scale factor is appropriate for arbitrary B-decays.

To determine the appropriate scale factor for $t\bar{t}$ events, we assume that SF is independent of E_T^{jet} and measure for all $E_T^{jet} > 10$ GeV that $SF = 0.98 \pm 0.04$, where the error is statistical. To obtain the systematic error we fit the SF versus E_T^{jet} distribution to a sloped line and convolute the fit result, assuming the $\pm 1\sigma$ variations on the slope, with the E_T distribution of B-jets in Monte Carlo $t\bar{t}$ events passing all event selection criteria. Half the difference between this result and the result assuming the scale factor is flat in E_T^{jet} is taken as the systematic error, which is of order 13% (relative) for all assumed top masses.

We check for other variations of the SF by measuring the tagging efficiencies as a function of the instantaneous luminosity, L_{inst}, and total integrated luminosity, L_{total}. We worry the tagging rate might be affected by the increased track multiplicity of events with high L_{inst} — such an affect would manifest itself as a dependence of the tagging rate on the instantaneous luminosity. Additionally, we worry that radiation damage to the SVX detector might also affect the tagging rates — this would manifest itself as a dependence of the tagging rate on the total integrated luminosity. Figure 3.52 shows $\epsilon_{B-tag}^{method\ 2}$ as a function L_{inst} and L_{total}. Both distri-

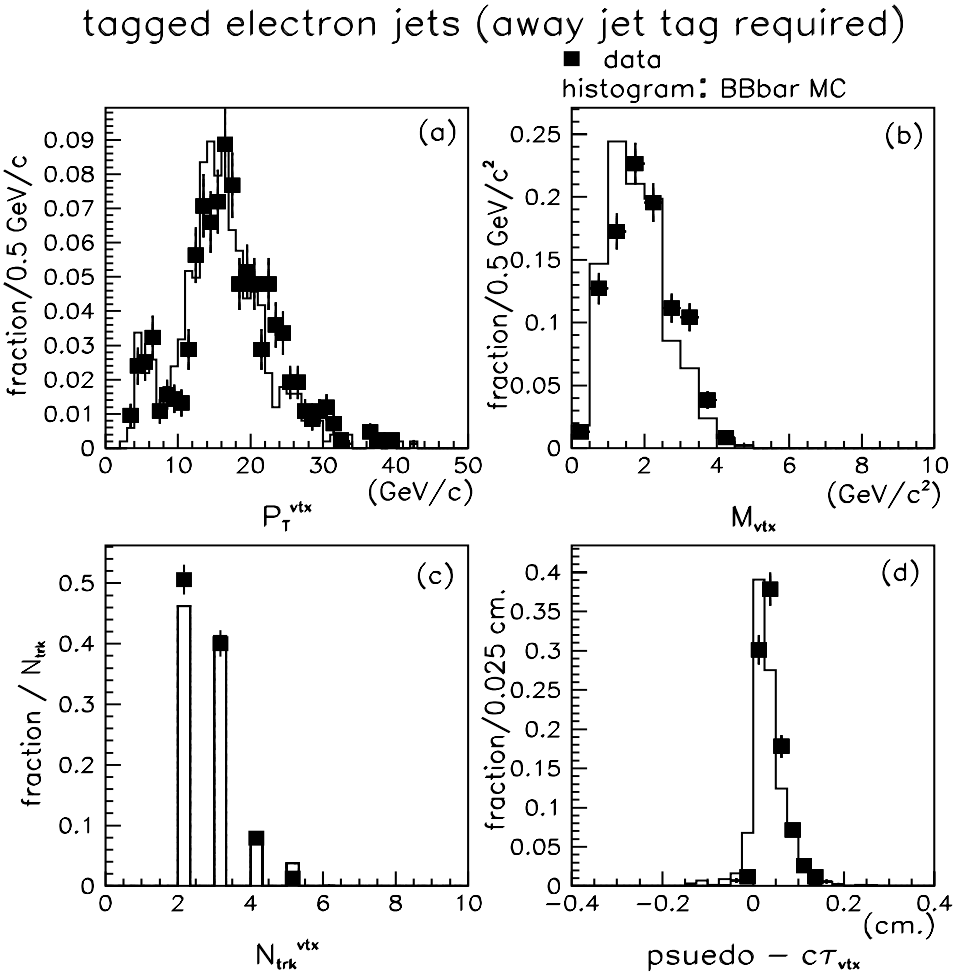

Figure 3.49: A comparison between tags in electron jets with an away tag required (points) and $b\overline{b}$ Monte Carlo (histogram) for various kinematic properties of the tracks included in the secondary vertex tag.

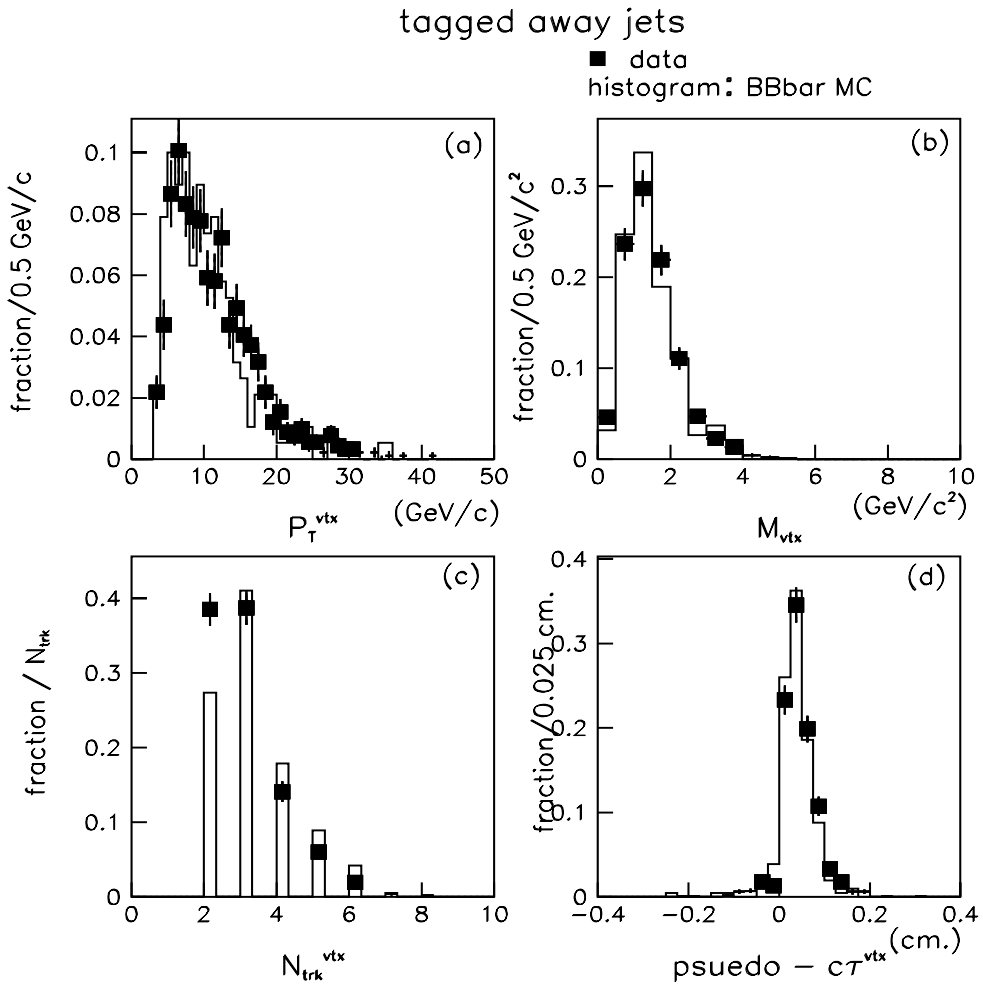

Figure 3.50: A comparison between tags in away jets (points) and $b\bar{b}$ Monte Carlo (histogram) for various kinematic properties of the tracks included in the secondary vertex tag.

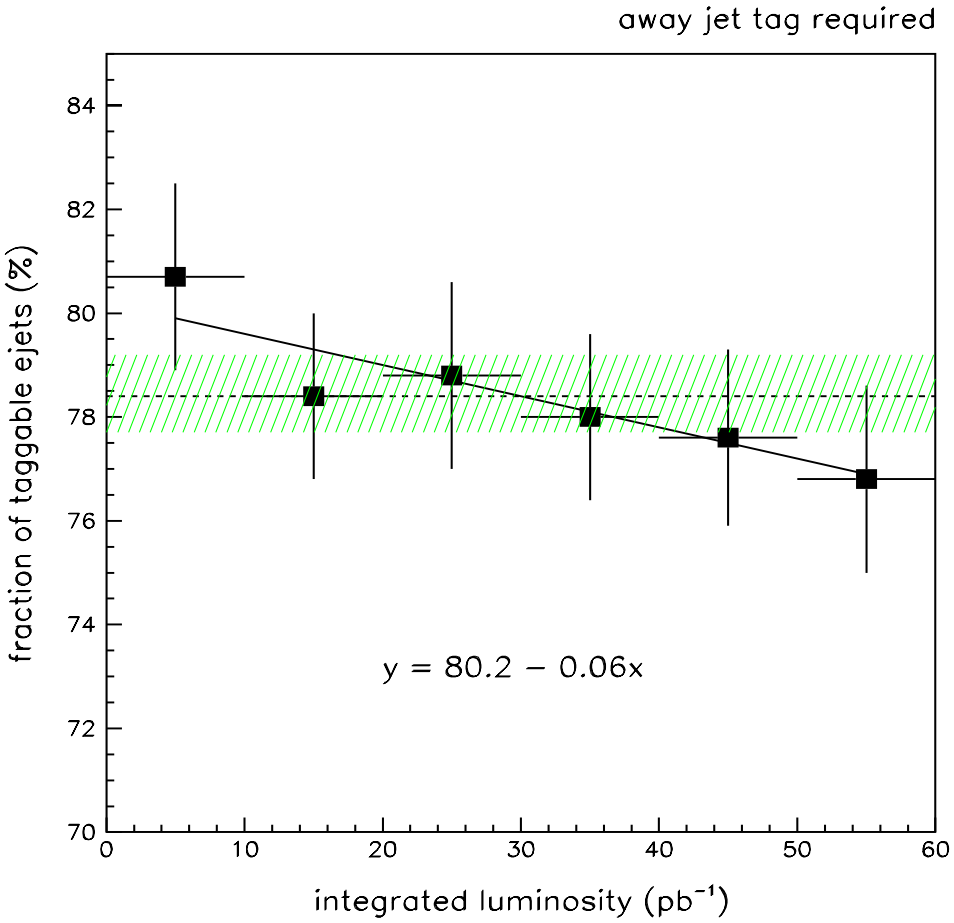

Figure 3.51: The fraction of taggable electron jets (with an away tag required) as a function of the total integrated luminosity. The average is given as a dotted line and the $\pm 1\sigma$ bounds are given by the shaded band. The results of a fit to a sloped line are also given and drawn as a solid line.

butions are consistent with being flat. As a second check, we take advantage of the large statistics available in the single tag sample and make no corrections for F_B, which has large errors associated with it. Since we use the same selection criteria independent of L_{inst} and L_{total}, we do not expect F_B to vary as a function of these variables. As demonstrated in Figure 3.53, this is indeed the case. In Figure 3.54 we plot XS_{ejet} as a function of L_{inst} and L_{total}. Each distribution is fit to a sloped line. Even if we conservatively assume the $\pm 1\sigma$ slope parameters, the excess tagging rate is affected by $< 1\%$ over the entire range of both L_{inst} and L_{total}. A variation of this size is wholly accounted for by the assigned systematic error.

As mentioned in the previous section, the efficiencies determined using the single tag method appear to be systematically lower than those determined using the double tag method as shown in Figure 3.48(top). As described in Reference [32], the background subtraction in Equation 3.9 may be an underestimate, which would, in turn, lead to an underestimate in the single tag efficiency, $\epsilon_{B-jet}^{method\ 1}$. If we incorporate the background subtraction as discussed in Reference [32], the method 1 B-tag efficiency on average changes by $+8\%$. The resulting scale factor is 1.05 ± 0.04. We take half the difference between this result and the result discussed above as an additional systematic of 3%.

Differences in Run 1A Data

Since the SVX detector used in run 1A is radiation soft, we might expect the tagging rates in run 1A to be more affected by radiation damage. We investigate this by looking for a run dependence of the excess tagging rate in electron jets, XS_{ejet}, in a B-enriched sample selected using the same criteria as for the run 1B sample. We measure the B-fraction of the run 1A sample, $F_B^{run\ 1A} = 37 \pm 8\%$, to be consistent with the run 1B fraction, $F_B^{run\ 1B} = 39 \pm 5\%$. This facilitates a direct comparison of the run 1A and run 1B excess tagging rates. Figure 3.55 shows $XS_{ejet}^{run\ 1A}$ as a function of run number. The points are normalized to the first bin. There is a clear run dependence. We determine the average run 1A B-tagging efficiency by taking

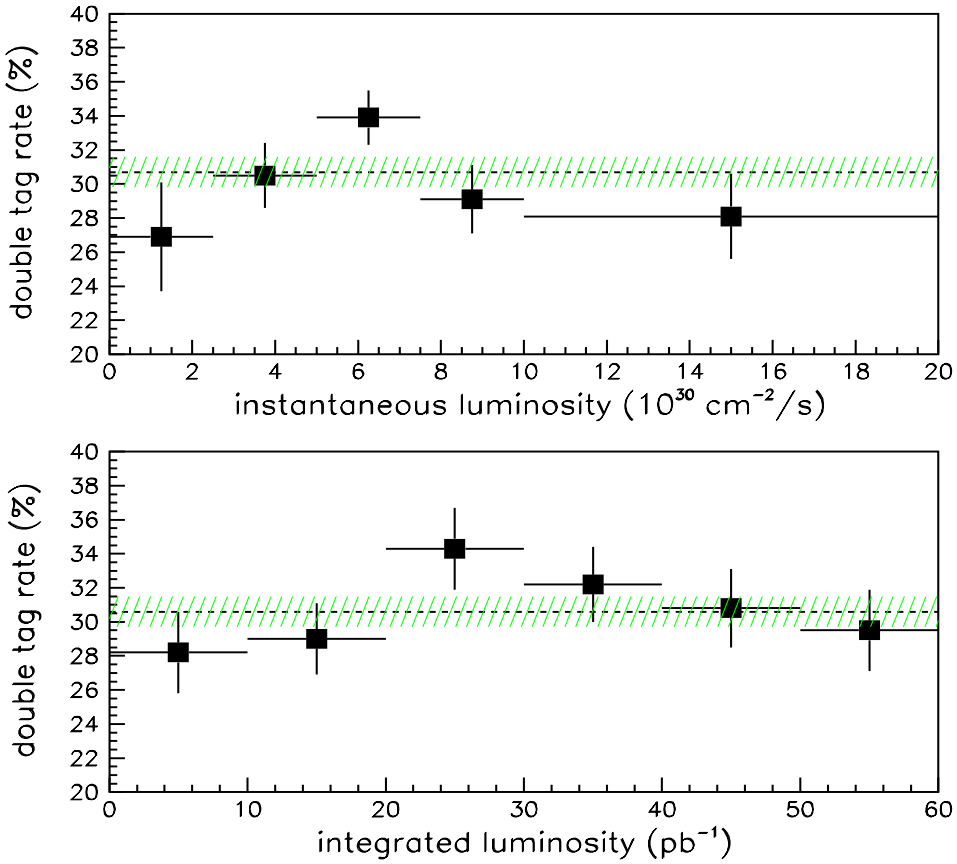

Figure 3.52: The double tag rate, $\epsilon_{B-tag}^{method\ 2}$, is plotted as a function of the instantaneous luminosity (top) and the total integrated luminosity (bottom). Both distributions are consistent with being flat. The weighted average is displayed as a dashed line. The shaded region indicates the $\pm 1\sigma$ bounds.

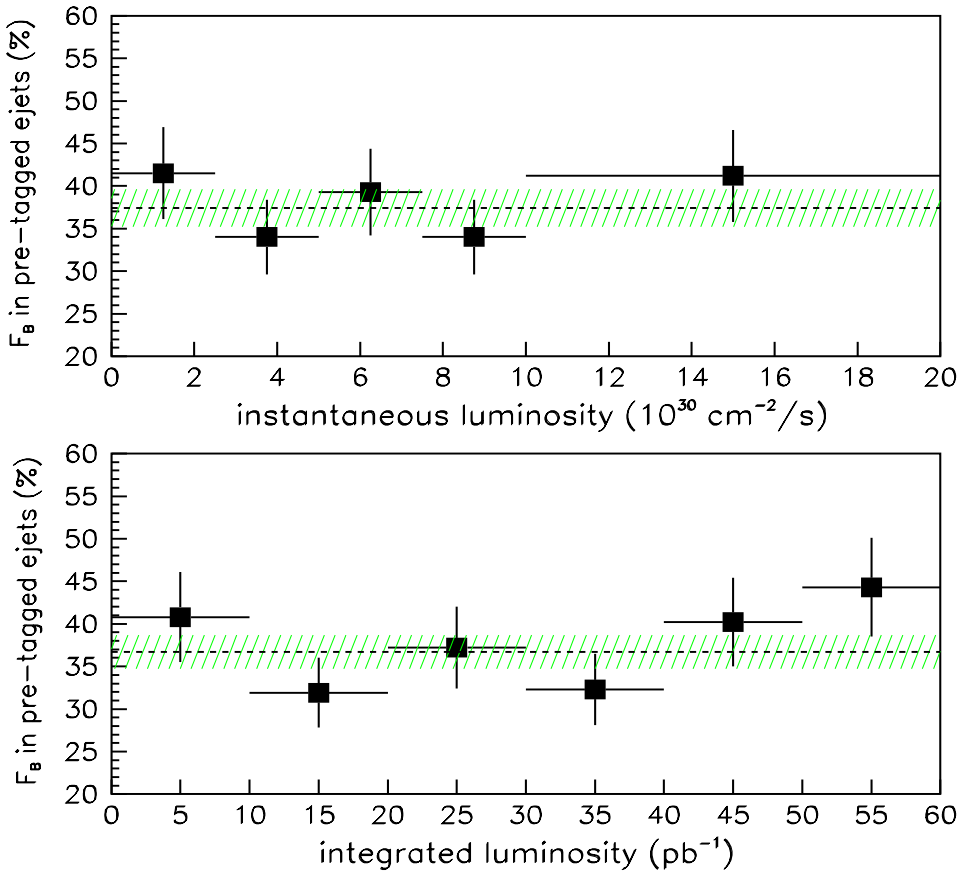

Figure 3.53: The estimated fraction of pre-tagged electron jets that are B-jets, F_B, as a function of the instantaneous luminosity (top) and the total integrated luminosity (bottom). The hatched bands represent the $\pm 1\sigma$ bounds of the weighted average F_B in each plot.

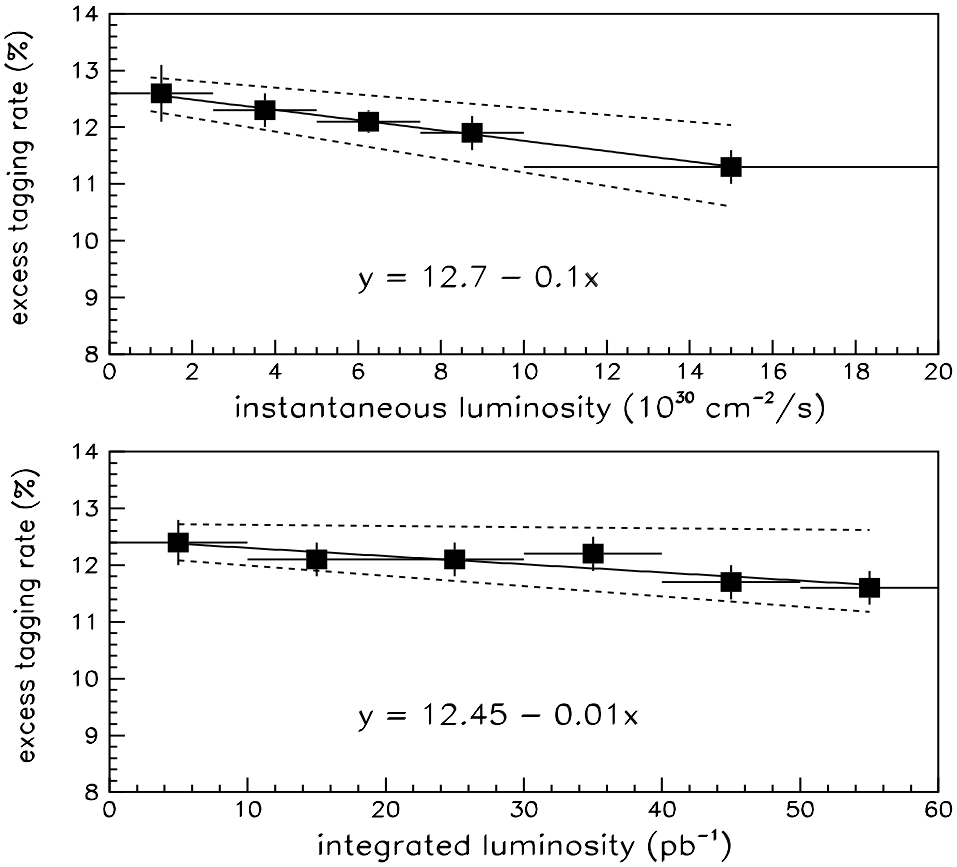

Figure 3.54: The excess tagging rate, XS_{ejet}, is plotted as a function of the instantaneous luminosity (top) and the total integrated luminosity (bottom). Each distribution is fit to a sloped line. The fit results are displayed and drawn as a solid line. The $\pm 1\sigma$ variations of the fit parameters are drawn as dashed lines.

the luminosity weighted average over all points. We measure

$$\epsilon_{B-tag}^{run\ 1A} = (0.855 \pm 0.044) \cdot \epsilon_{B-tag}^{run\ 1B}. \tag{3.14}$$

We determine the average run 1A plus run 1B B-tagging efficiency by taking the luminosity weighted average of $\epsilon_{B-tag}^{run\ 1A}$ and $\epsilon_{B-tag}^{run\ 1B}$. The resulting run averaged B-tagging efficiency is a factor of 0.971 ± 0.009 smaller that the run 1B-only rates determined above. In calculating the $t\bar{t}$ detection efficiency, we diminish all tagging efficiencies by this factor.

Determination of ϵ_{B-tag}^{event} for $t\bar{t}$ Events

We use the following expression to determine ϵ_{B-tag}^{event} for $t\bar{t}$ events passing all the event selection criteria.

$$\epsilon_{B-tag}^{event} = F_{2B} \cdot \epsilon_{B-tag} \cdot SF \cdot (2 - \epsilon_{B-tag} \cdot SF) + F_{1B} \cdot \epsilon_{B-tag} \cdot SF \tag{3.15}$$

where

$F_{2B} \equiv$ the fraction of $t\bar{t}$ events passing all event selection criteria that contain 2 taggable B-jets

$F_{1B} \equiv$ the fraction of $t\bar{t}$ events passing all event selection criteria that contain only 1 taggable B-jet

$\epsilon_{B-tag} \equiv$ the *per jet* B-tagging efficiency as determined from the Monte Carlo

$SF \equiv$ the data to Monte Carlo scale factor.

Table 3.11 gives the resulting ϵ_{B-tag}^{event} for the assumed top masses 150, 170, and 190 GeV/c^2. Our total $t\bar{t}$ event detection efficiency is given in Table 3.12.

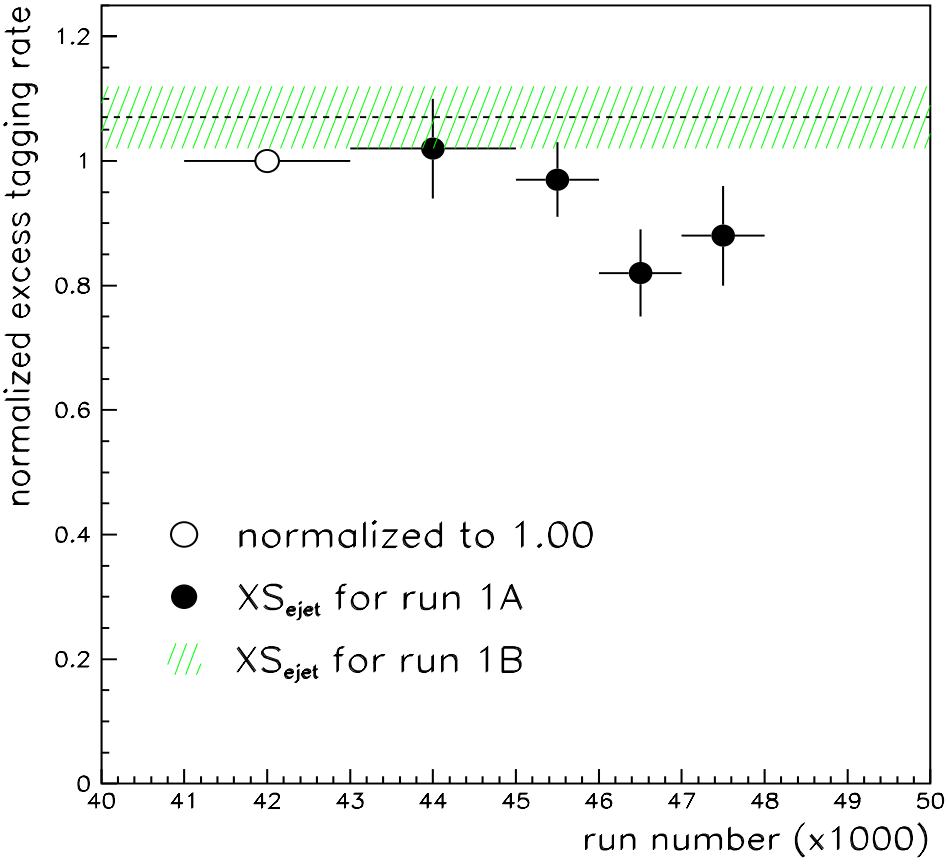

Figure 3.55: The excess tagging rate for a run 1A B-enriched sample as a function of run number. A clear run dependence is observed. The dotted line is the average run 1B excess tagging rate. The hatched band indicates the $\pm 1\sigma$ bounds on the run 1B rate.

	$M_t = 150$ GeV/c^2	$M_t = 170$ GeV/c^2	$M_t = 190$ GeV/c^2
F_{1B} :	0.327 ± 0.017	0.302 ± 0.007	0.279 ± 0.015
F_{2B} :	0.320 ± 0.017	0.341 ± 0.007	0.378 ± 0.018
ϵ_{B-tag} :	0.561 ± 0.004	0.561 ± 0.004	0.561 ± 0.004
SF :	0.98 ± 0.15	0.98 ± 0.15	0.98 ± 0.15
ϵ^{event}_{B-tag} :	0.42 ± 0.05	0.43 ± 0.04	0.44 ± 0.040
$\epsilon^{event}_{mistag}$:	0.010 ± 0.010	0.010 ± 0.010	0.010 ± 0.010
ϵ_{tag} :	0.43 ± 0.05	0.44 ± 0.04	0.45 ± 0.040

Table 3.11: The fraction of $t\bar{t}$ events passing all event selection criteria with at least one tagged B-jet. All uncertainties include statistical and systematic errors added in quadrature.

	$M_t = 150$ GeV/c^2	$M_t = 170$ GeV/c^2	$M_t = 190$ GeV/c^2
$A_{t\bar{t}}$:	0.105 ± 0.010	0.116 ± 0.011	0.122 ± 0.012
$\epsilon_{\lvert z_{pvtx}\rvert}$:	0.949 ± 0.023	0.949 ± 0.023	0.949 ± 0.023
ϵ_{trig} :	0.854 ± 0.045	0.854 ± 0.045	0.854 ± 0.045
$\epsilon_{lepton\ id}$:	0.903 ± 0.008	0.903 ± 0.008	0.903 ± 0.008
ϵ_{tag} :	0.43 ± 0.05	0.44 ± 0.04	0.45 ± 0.04
$\epsilon_{t\bar{t}}$:	0.033 ± 0.006	0.037 ± 0.006	0.040 ± 0.006

Table 3.12: The total $t\bar{t}$ event detection efficiency. All uncertainties include statistical and systematic errors added in quadrature.

	$W + n$ jet multiplicity bin			
quantity	1 jet	2 jets	3 jets	≥ 4 jets
N_{event}	9531	1469	231	65
N_{tag} events	61	43	22	18
N_{tag} jets	61	38	17	15

Table 3.13: B-tagging results using 100 pb^{-1} of data.

3.6 Results

As discussed in Section 3.1, we search for $t\bar{t}$ pair production and assume the Standard Model decay $t\bar{t} \rightarrow W^+bW^-\bar{b}$. We require one of the W bosons to decay leptonically, the other hadronically. A candidate top quark event would then have a high P_T lepton (an electron or muon) and lots of missing transverse energy — from the neutrino of the leptonically decaying W, and ≥ 3 jets — from the hadronization of the two b-quarks and the hadronically decaying W. We further require that at least one jet in the event is tagged by our B-tagging algorithm. The results from 100 pb^{-1} of run 1A + run 1B data is given in Table 3.13. We divide the events according to their jet multiplicity. For each multiplicity bin we count the number of events in the sample prior to tagging, N_{event}, and the number of events with ≥ 1 tagged jet. Since it is possible to tag more than one jet in an event, we also give the total number of tagged *jets*. Note that an event with 2 tagged jets, a "double tagged" event, is much more likely to contain real heavy flavor jets than not. We observe 40 tagged jets in 32 events. There are 8 double tagged events and no triple tagged events. The derivation of our background estimate is discussed in detail in Section 3.7 and the significance of the result is discussed in Section 3.7.6. We compare the kinematic distributions of the tagged events with expectations from a $t\bar{t}$ + background Monte Carlo sample in Section 3.8.

3.7 Background Estimate

Even in the absence of any $t\bar{t}$ events, we still expect tags in the W plus jets data samples. The primary sources of these "background" tags are W + heavy flavor events and mistags. Specifically we consider the following backgrounds:

$Wb\bar{b}$, $Wc\bar{c}$ $\equiv$ higher order W production in association with heavy quark pair production via gluon splitting (cf. Figure 1.6)

mistags $\equiv$ false secondary vertex tags due to detector resolution effects in events containing no heavy flavor

$Wc \equiv$ flavor excitation processes yielding a W in association with a charm quark, primarily $sg \rightarrow Wc$

WW, $WZ \equiv$ diboson production in which one boson decays to real heavy flavor via $W \rightarrow c\bar{s}$ or $Z \rightarrow b\bar{b}$, $c\bar{c}$

$Z \rightarrow \tau\tau$ $\equiv$ tauonic decay of a Z boson in which one of the taus generates a tag due to the tau lifetime

non-W $\equiv$ non-W events which contain heavy flavor, primarily $q\bar{q} \rightarrow b\bar{b}$ events, passing the event selection criteria.

The first 2 sources constitute $\sim$ 65% of the total background, while the first 3 make up $>$ 80%. We use Monte Carlo to calculate the *relative* contribution to each jet multiplicity bin for the $Wb\bar{b}$, $Wc\bar{c}$, and Wc background sources. We then scale these relative rates according to the number of *observed* events (prior to tagging) in each bin. In this manner we do not rely on Monte Carlo for the absolute normalization of the background rate. The mistag contribution is estimated using a parameterization of the mistag rate derived from inclusive jet data. The remaining background estimates utilize a combination of data and Monte Carlo techniques. We discuss the estimate of each background source separately below.

3.7.1 Estimate of the $Wb\bar{b}$, $Wc\bar{c}$, and Wc Contributions

For a given background source, b ($= Wb\bar{b}$, $Wc\bar{c}$, Wc), we estimate the number of tags in a given jet multiplicity bin, j, using the following expression

$$N_b^j = N^j \cdot \left(1 - F_{non-W}^j\right) \cdot F_b^j \cdot k \cdot \epsilon_b^j \cdot SF \tag{3.16}$$

where

$b \equiv$ corresponds to one of the W plus heavy flavor background sources, $Wb\bar{b}$, $Wc\bar{c}$, or Wc

$N_b^j \equiv$ the estimated number of background tags due to background source b in jet multiplicity bin j

$N^j \equiv$ the number events passing all event selection criteria in jet multiplicity bin j *prior* to tagging

$F_{non-W}^j \equiv$ fraction of events in jet multiplicity bin j originating from non-W sources (primarily $b\bar{b}$)

$F_b^j \equiv$ the fraction of events with jet multiplicity j originating from background source b

$k \equiv$ a correction factor discussed more thoroughly below

$\epsilon_b^j \equiv$ the efficiency for tagging ≥ 1 jet in events from background source b in jet multiplicity bin j

$SF \equiv$ the data to Monte Carlo scale factor discussed in Section 3.5.4.

The correction F_{non-W}^j is required to account for that fraction of events passing all selection criteria which are not real W events. It is on the order of 10% for all jet multiplicity bins and is discussed in Section 3.7.3. Below, we specifically discuss the determination of $N_{Wb\bar{b}}^j$. Unless otherwise noted, the same methods are used to determine $N_{Wc\bar{c}}^j$ and N_{Wc}^j.

We use a HERWIG Monte Carlo sample of W + multijet events to determine the fraction of events with jet multiplicity j containing a $b\overline{b}$ pair

$$F^j_{Wb\overline{b}} = \frac{N^j\left(\text{ events with } b\overline{b} \text{ pair }\right)}{N^j\left(\text{ all } W\text{+j jet events }\right)}. \tag{3.17}$$

In the 1 jet bin, we compute the inclusive $Wb\overline{b}$ and $Wc\overline{c}$ production rates and compare the results to those obtained using the full leading-order matrix element calculation described in Reference [58]. They are consistent to well within the $\pm 40\%$ uncertainty assigned to the renormalization scale [58]. To be conservative we choose the upper bound of this range and require the two methods to yield consistent $Wb\overline{b}$ $+1$ and $Wc\overline{c}$ $+1$ jet rates. This requires a correction factor, $k = 1.4$, for the HERWIG prediction, which is applied to all jet multiplicity bins.

As a check of this method we repeat this study for a sample of generic jets selected as described in Section 3.1.5. We compare the excess tagging rate as measured in the data to the tagging rate predicted using a HERWIG Monte Carlo sample of generic QCD multijet events. The dominant production diagram for these generic multijet events is given in Figure 3.56. As with $W+$ heavy flavor events, $b\overline{b}$ and $c\overline{c}$ pairs predominantly result from gluon splitting. We compare the tag rates as a function of jet multiplicity and require the Monte Carlo tags to be associated with a heavy flavor jet. Figure 3.57 shows the results. The two rates are consistent and give us confidence in the heavy quark production rate predicted by HERWIG. We also verify that the HERWIG rates are consistent with a full next-to-leading-order matrix calculation of the heavy flavor fraction of generic jet events. We assign a 60% (relative) error to the correction factor, k, which is determined by varing the heavy flavor fraction in HERWIG until it disagrees by $\pm 1\sigma$ with the observed excess tagging rate in generic jet data.

For the fraction of $W + 1$ jet events due to Wc we again use the HERWIG Monte Carlo program. The dominant production mechanism is shown in Figure 3.58. The uncertainty in the strange sea content of the proton is estimated by generating a variety of HERWIG samples utilizing a variety of structure functions [59] and is

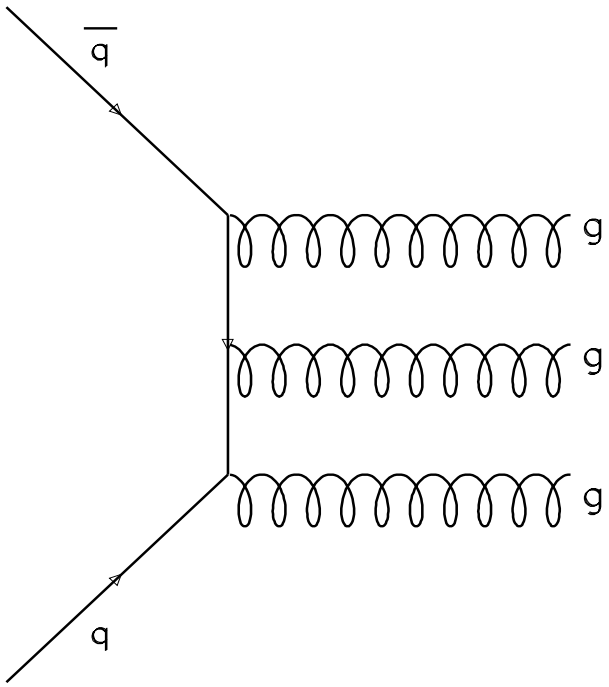

Figure 3.56: Tree level diagram of a generic multijet event. A heavy flavor quark pair results from a gluon splitting to a $b\overline{b}$ or $c\overline{c}$ pair.

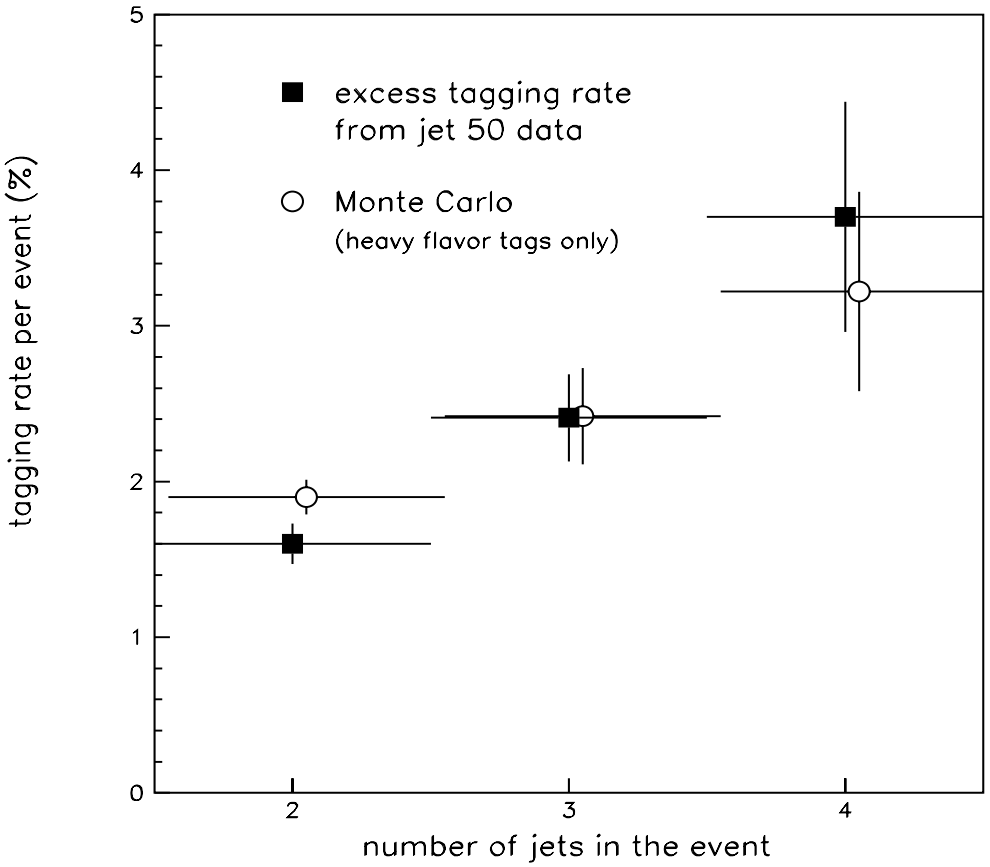

Figure 3.57: We compare the heavy flavor tagging rate (per event) observed in data and measured in a HERWIG Monte Carlo sample of generic jets.

$\sim 30\%$ (relative). To facilitate a large statistics study over a wide range of structure functions, we use an idealized detector simulation. To account for detector resolution effects we need to scale the resulting rates by a correction factor. We determined this factor by performing a full detector simulation on a single Monte Carlo sample and comparing results to that obtained using the idealized simulation. We require a correction of $k_{Wc} = 1.1 \pm 0.3$.

The tagging rate, $\epsilon^j_{Wb\bar{b}}$, is also determined from Monte Carlo. To avoid double counting mistags, only tags in B-jets are considered. We use expression 3.15 to determine the efficiency for tagging ≥ 1 B-jet in an event. We do this as a function of jet multiplicity. When determining the tagging rates for $Wc\bar{c}$ and Wc events, we require the tag to be associated with a charm jet. We use the scale factor determined in Section 3.5.4, $SF = 0.98 \pm 0.15$, and assume it is the same for charm jets.

Table 3.14 gives the values for F^j_b, k, and ϵ^j_b for the background sources $b = Wb\bar{b}$, $Wc\bar{c}$, and Wc.

3.7.2 Estimate of Mistag Contribution

We use a heavy flavor depleted generic jet sample to parametrize the mistag rate *per jet* as a function of the jet E_T, $|\eta|$, number of associated SVX-tracks, and the event ΣE^*_T , which is defined as the scalar sum over all jets in the event with $E_T > 15$ GeV and $|\eta| < 2.0$. The bins used in the parametrization are given in Table 3.15. We parameterize the mistag rate using a generic jet sample with a 50 GeV threshold because the event kinematics (ie. jet E_T and event ΣE^*_T) have distributions similar to those of the $W+ \geq 3$ jets signal sample. The resulting mistag rate parameterization is then applied to the jets in the $W+$ multijet sample to yield an estimate of the mistag contribution to the background. As a check of this procedure, we compare the number of negative tags predicted using the parameterization to the number observed in a variety of control samples, including a variety of generic jet samples requiring different jet thresholds, and a sample of events with $\Sigma E_T > 300$ GeV, where the sum is over *all* jets in the event. The results

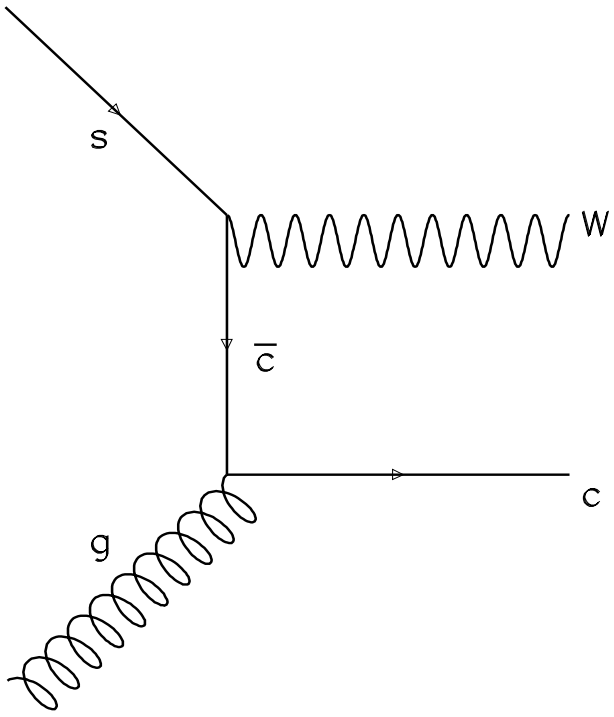

Figure 3.58: Tree level diagram for Wc production. This is dominated by the process $sg \to Wc$, with a $\sim 10\%$ contribution from $dg \to Wc$.

background source (b)	jet multiplicity (j)	F_b^j	k	ϵ_b^j
$Wb\bar{b}$	1	0.005 ± 0.002	1.4 ± 0.8	0.228 ± 0.005
	2	0.010 ± 0.001	1.4 ± 0.8	0.350 ± 0.015
	3	0.021 ± 0.003	1.4 ± 0.8	0.359 ± 0.030
	≥ 4	0.025 ± 0.012	1.4 ± 0.8	0.359 ± 0.030
$Wc\bar{c}$	1	0.012 ± 0.001	1.4 ± 0.8	0.051 ± 0.004
	2	0.025 ± 0.001	1.4 ± 0.8	0.093 ± 0.012
	3	0.035 ± 0.005	1.4 ± 0.8	0.086 ± 0.034
	≥ 4	0.027 ± 0.015	1.4 ± 0.8	0.086 ± 0.034
Wc	1	0.053 ± 0.013	1.1 ± 0.3	0.048 ± 0.005
	2	0.075 ± 0.015	1.1 ± 0.3	0.061 ± 0.010
	3	0.080 ± 0.015	1.1 ± 0.3	0.078 ± 0.015
	≥ 4	0.080 ± 0.015	1.1 ± 0.3	0.078 ± 0.015

Table 3.14: Summary of numbers used in estimating the $W+$ heavy flavor background contribution as a function of jet multiplicity.

parameter	bins
E_T of the jet (GeV)	15, 25, 35, 45, 60, 75, 90, 120, 150, $>$ 150
N_{trks}	2, 3, 4, 5, 6-7, 8-9, 10-13, $\geq$ 14
event ΣE_T^* (GeV)	0, 80, 140, $>$ 140

Table 3.15: The parameters and binning used to parameterize the mistag rate.

are given in Table 3.16, where we observe discrepancies of $\leq 10\%$ in all samples. As a further check, we compare the predicted and observed mistag rates as a function of variables thought to be correlated with tracking confusion, but *not* used in the parameterization. The variables investigated are

$N_{vtx} \equiv$ the number of interaction vertices in the event; note that due to the high luminosity conditions of run 1B there are on average ~ 2 interactions per event

$|\Delta Z|_{min} \equiv$ the minimum separation between the primary interaction vertex and any other interaction vertex in the event

$\Delta R_{min} \equiv$ the minimum separation in $\eta - \phi$ space between a given jet and any other jet in the event

$|\Delta\phi|_{min} \equiv$ the minimum azimuth separation between a given jet and any other jet in the event.

Since the ΣE_T^* of events in the $W+ \geq 3$ jets sample ($\langle \Sigma E_T^* \rangle \sim 150$ GeV) is considerably smaller than that of events in the $\Sigma E_T > 300$ GeV sample ($\langle \Sigma E_T^* \rangle > 200$ GeV), we take this latter sample as an extreme case in which to make these comparisons. The results are given in Table 3.17. We observe that the mistag rate is flat as a function of all variables investigated and that whatever correlations might exist are acurrately modeled by the mistag parameterization within $10-20\%$. Based on this, we assign a systematic error of $\pm 20\%$ (relative) to the mistag prediction.

3.7.3 Estimate of F_{non-W} Contribution

We determine the non-W contribution using the data. We assume that the event $\not\!\!E_T$ and lepton isolation I_{cal} are independent. We then release the cuts on $\not\!\!E_T$ and isolation in the sample selection and divide the data into four regions as shown in Figure 3.59. Note that regions A and B are background dominated, while region D is our signal region. We then estimate the fraction of non-W events in the signal

data sample	no. of negative tags observed	predicted
jets (20 GeV thresh.)	108	120
jets (50 GeV thresh.)	541	564
jets (70 GeV thresh.)	371	365
jets (100 GeV thresh.)	538	500
jets (140 GeV thresh.)	270	272
$\Sigma E_T > 300$ GeV	434	391

Table 3.16: Comparison of the number of observed negative tags to the number predicted using the mistag parameterization in a variety of control samples.

region using the expression

$$F_{non-W} = N_C \cdot \left(\frac{N_A}{N_B}\right) \cdot \frac{1}{N_D} \tag{3.18}$$

where

$N_I \equiv$ the number of events, *prior* to tagging, in region I.

This is done separately for electrons and muons. The results are given in Table 3.18. We estimate the final background contribution to the signal region by applying the tagging rate measured in region A to the events in region D and scaling by F_{non-W}.

3.7.4 Estimate of WW, WZ and $Z \to \tau\tau$ Contributions

We estimate the remaining background contributions using the following expression

$$N_b^j = \sigma_b \cdot (BR)_b \cdot \mathcal{L}_{total} \cdot A_b^j \cdot \epsilon_b^j \cdot SF \tag{3.19}$$

where

bin	N_{jet}^{total}	$N_{jet}^{taggable}$	N_{-tag}^{obs}	N_{-tag}^{pred}	ratio	$\epsilon_{-tag}(\%)$
$N_{vtx} = 1$	35426	20558	189	171	1.11 ± 0.08	0.92 ± 0.07
$N_{vtx} = 2$	23319	13544	137	114	1.20 ± 0.10	1.01 ± 0.09
$N_{vtx} = 3$	11034	6432	45	50	0.90 ± 0.13	0.70 ± 0.10
$N_{vtx} \geq 4$	12446	7115	63	56	1.13 ± 0.14	0.89 ± 0.11
$\lvert\Delta Z\rvert_{min} \leq 5$ cm	5362	3045	30	24	1.25 ± 0.23	0.99 ± 0.18
$5 < \lvert\Delta Z\rvert_{min} \leq 10$	6414	3684	40	30	1.33 ± 0.21	1.09 ± 0.17
$10 < \lvert\Delta Z\rvert_{min} \leq 20$	10853	6320	51	53	0.96 ± 0.13	0.81 ± 0.11
$20 < \lvert\Delta Z\rvert_{min} \leq 30$	8001	4512	37	37	1.00 ± 0.16	0.82 ± 0.13
$30 < \lvert\Delta Z\rvert_{min}$	16169	9530	87	77	1.13 ± 0.12	0.91 ± 0.10
$\Delta R_{min} \leq 0.5$	1694	1033	8	7	1.14 ± 0.40	0.77 ± 0.27
$0.5 < \Delta R_{min} \leq 0.7$	12334	7736	72	55	1.31 ± 0.16	0.92 ± 0.11
$0.7 < \Delta R_{min} \leq 0.9$	9910	6059	59	42	1.40 ± 0.18	0.97 ± 0.13
$0.9 < \Delta R_{min} \leq 1.1$	8211	4895	35	34	1.03 ± 0.17	0.72 ± 0.12
$1.1 < \Delta R_{min} \leq 1.5$	13031	7468	57	51	1.12 ± 0.15	0.76 ± 0.10
$1.5 < \Delta R_{min} \leq 2.0$	12130	6684	59	49	1.20 ± 0.16	0.88 ± 0.11
$2.0 < \Delta R_{min}$	14653	6994	48	49	0.98 ± 0.14	0.69 ± 0.10
$\lvert\Delta\phi\rvert_{min} \leq 10^o$	9045	4700	46	28	1.64 ± 0.24	0.98 ± 0.14
$10 < \lvert\Delta\phi\rvert_{min} \leq 20$	8588	4782	40	31	1.29 ± 0.20	0.84 ± 0.13
$20 < \lvert\Delta\phi\rvert_{min} \leq 30$	9512	5615	54	41	1.32 ± 0.18	0.96 ± 0.13
$30 < \lvert\Delta\phi\rvert_{min} \leq 40$	9024	5319	46	39	1.18 ± 0.17	0.86 ± 0.13
$40 < \lvert\Delta\phi\rvert_{min} \leq 50$	6814	3975	37	29	1.29 ± 0.021	0.93 ± 0.15
$50 < \lvert\Delta\phi\rvert_{min}$	28920	16454	114	121	0.94 ± 0.09	0.69 ± 0.06

Table 3.17: A comparison between the number of negative tags observed, N_{-tag}^{obs}, and predicted, N_{-tag}^{pred}, as a function of several variables in the $\Sigma E_T > 300$ GeV sample. In each bin we calculate the mistag rate, $\epsilon_{-tag} = N_{-tag}^{obs}/N_{jet}^{taggable}$, and the ratio of observed to predicted mistags, $N_{-tag}^{obs}/N_{-tag}^{pred}$.

		jet multiplicity		
		1	2	≥ 3
F_{non-W}	e	0.088 ± 0.007	0.102 ± 0.016	0.112 ± 0.036
	μ	0.052 ± 0.004	0.065 ± 0.009	0.091 ± 0.027
	ave.	0.073 ± 0.005	0.084 ± 0.012	0.100 ± 0.030

Table 3.18: The fraction of non-W, F_{non-W}, events passing all event selection criteria as a function of jet multiplicity. The errors are statistical only.

background source	jet multiplicity	total acceptance	tagging efficiency
$WW \rightarrow e\nu c\overline{s}$ $(\sigma \cdot BR = 0.703 \pm 0.052\ pb)$	1	0.110 ± 0.005	0.040 ± 0.004
	2	0.116 ± 0.005	0.052 ± 0.004
	≥ 3	0.023 ± 0.002	0.071 ± 0.010
$WZ \rightarrow e\nu b\overline{b}$ $(\sigma \cdot BR = 0.052 \pm 0.008\ pb)$	1	0.094 ± 0.005	0.24 ± 0.03
	2	0.099 ± 0.005	0.49 ± 0.06
	≥ 3	0.022 ± 0.002	0.51 ± 0.06
$Z \rightarrow \tau\tau \rightarrow e\nu\nu + 3$ prong + X $(\sigma \cdot BR = 10.0 \pm 1.0\ pb)$	1	0.0029 ± 0.0003	0.08 ± 0.02
	2	0.0008 ± 0.0001	0.10 ± 0.02
	≥ 3	0.001 ± 0.00005	0.12 ± 0.02

Table 3.19: The total event acceptances and per event tagging efficiencies used to estimate the WW, WZ, and $Z \rightarrow \tau\tau$ background contributions.

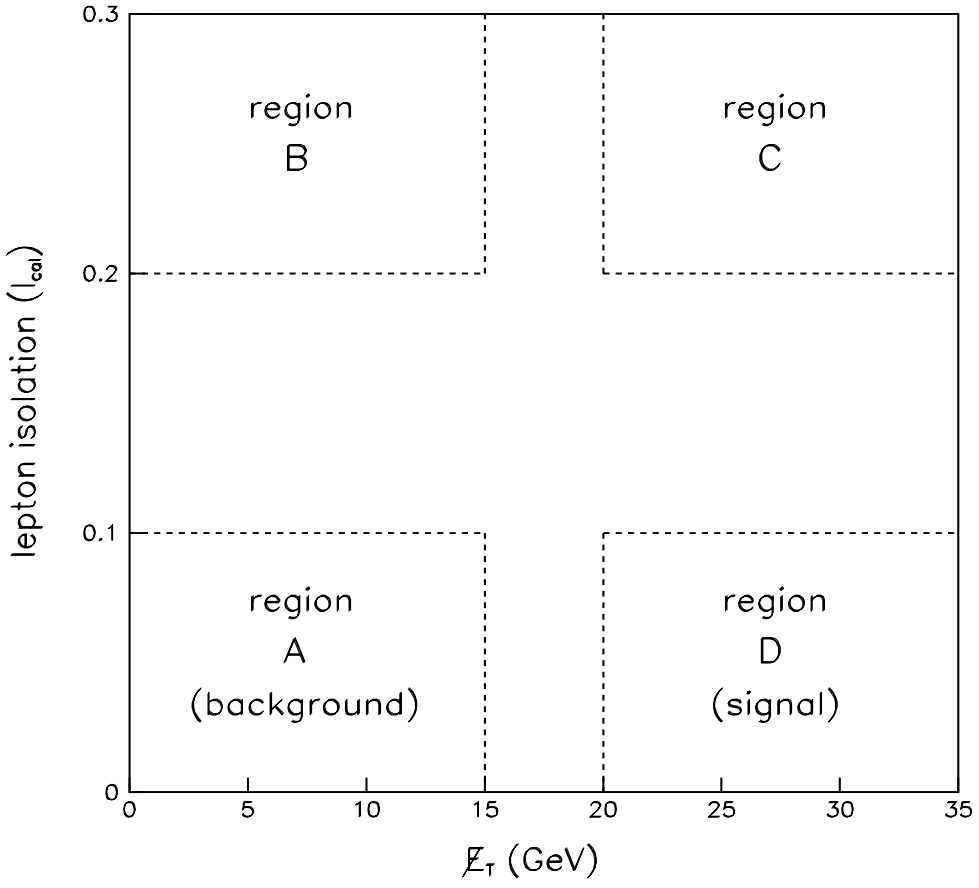

Figure 3.59: Regions used to determine the fraction of events in the signal region (D) due to non-W sources such as $b\bar{b}$.

$b \equiv$ specifies a particular background source, WW, WZ, or $Z \rightarrow \tau\tau$

$\sigma_b \equiv$ the production cross section for background source b from References [60] [61]

$BR_b \equiv$ the branching ratio for background source b to a final state including a high P_T electron or muon and the heavy flavor decay of one of the bosons

$\mathcal{L}_{total} \equiv$ the total integrated luminosity

$A_b^j \equiv$ the total event acceptance for jet multiplicity bin j, including trigger, lepton identification, and event selection efficiencies, for background source b

$\epsilon_b^j \equiv$ the efficiency for tagging ≥ 1 heavy flavor jet in an event with jet multiplicity j; to avoid double counting mistags, we require the tag to be in a B-, D-, or $\tau-$ jet.

$SF \equiv$ the data to Monte Carlo scale factor discussed in Section 3.5.4.

The numbers used in the calculation are given in Table 3.19. We use PYTHIA Monte Carlo samples to estimate both the acceptance and tagging efficiency. The Monte Carlo samples included only $W \rightarrow e\nu$. In order to account for the $W \rightarrow \mu\nu$ contribution we scale the above numbers by the ratio of muon to electron events in the $W + 1$ jet bin, $1 + \left(N_\mu^1/N_e^1\right) = 1.76$.

Table 3.20 summarizes the total background estimate as a function of jet muliplicity. Figure 3.60 graphically compares the background estimate to the observed number of tagged jets as a function of jet multiplicity. We observe that in the control region, $W+ \leq 2$ jets, the data and background estimate are in reasonable agreement. In the signal region, $W+ \geq 3$ jets, we observe a large excess over the expected background contribution. The significance of this excess is discussed in the next section.

$W+$ multijet sample

background source	W + 1 jet	W + 2 jets	W + 3 jets	W + $\geq$4 jets
(1) $Wb\bar{b}$, $Wc\bar{c}$	20.6 ± 13.8	11.5 ± 7.2	2.9 ± 1.9	0.85 ± 0.68
(2) mistags	20.4 ± 4.1	7.3 ± 1.5	1.9 ± 0.4	0.70 ± 0.14
(3) Wc	22.9 ± 6.5	6.3 ± 1.7	1.3 ± 0.6	0.38 ± 0.17
(4) non-W (including $b\bar{b}$)	9.3 ± 2.7	3.8 ± 1.3	1.2 ± 0.5	0.37 ± 0.16
(5) WW, WZ, $Z \to \tau\tau$	1.2 ± 0.2	1.2 ± 0.2	0.33 ± 0.06	0.10 ± 0.03
(6) **Total**	74.4 ± 16.0	30.1 ± 7.7	7.6 ± 2.1	2.4 ± 0.7
N_{event} **prior to tagging**	9531	1469	231	65
N_{tag} **events observed**	61	38	17	15
N_{tag} **jets observed**	61	43	22	18

Table 3.20: The expected number of tagged *jets* for each background source. Estimates and observations based on 100 pb^{-1} of CDF data.

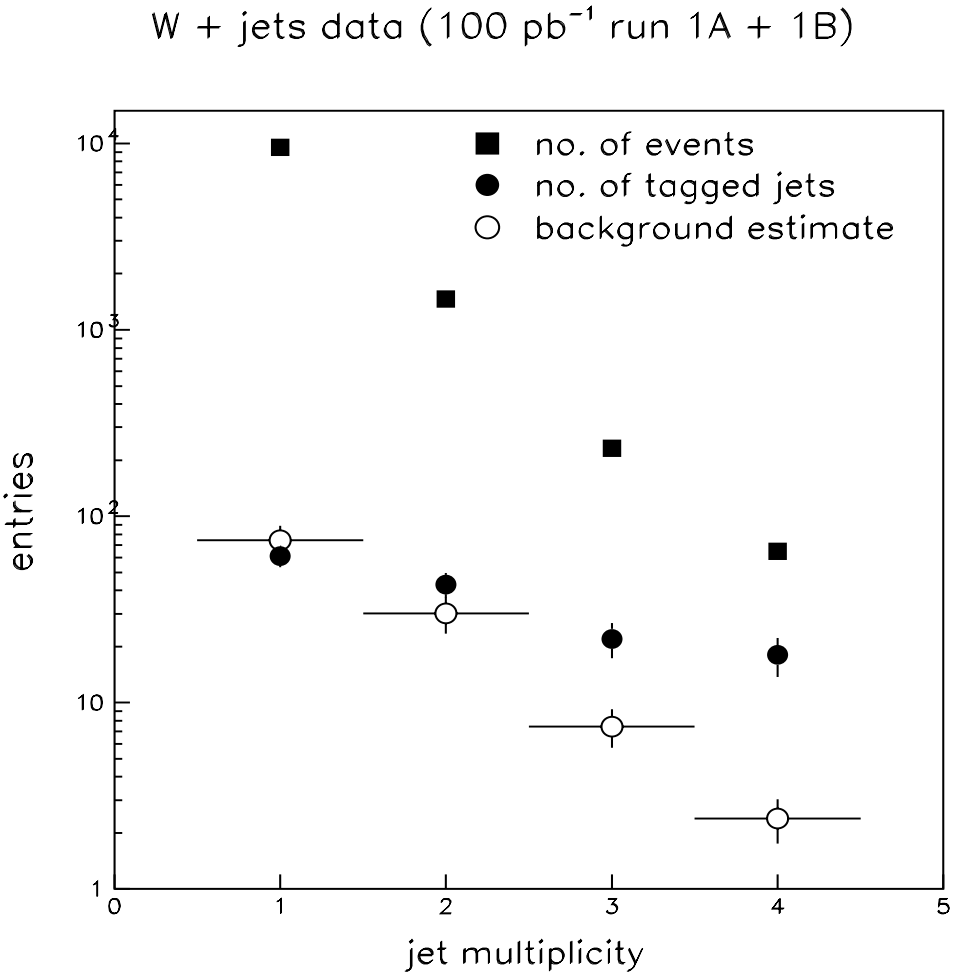

Figure 3.60: B-tagging results using 100 pb^{-1} of data. The $W+ \leq 2$ jets bins are expected to have a very small $t\bar{t}$ contribution. The $W+ \geq 3$ jets bins are our search region, where Standard Model $t\bar{t}$ production might significantly contribute.

3.7.5 Additional Checks of Background Estimate

As additional checks of the background estimate described above, we place upper limits on the number of residual tags from the following sources:

- $K_s^0 \to \pi^+\pi^-$ decays
- $\Lambda^0 \to p\pi^-$ decays
- $\gamma \to e^+e^-$ conversions
- an asymmetry of the mistag $c\tau$ shape.

We discuss these separately below.

For the "V-decays" ($K_s^0 \to \pi^+\pi^-$ and $\Lambda^0 \to p\pi^-$) we employ the removal algorithm described in Figure 3.40. In short, we forbid the use of a given track in a tag if it forms, with an oppositely charged track, a vertex with an invariant mass within 10 (6) MeV/c^2 of the K_s^0 (Λ^0) mass. At least one of the tracks must pass the CTC cuts described in Figure 3.40. Prior to V-removal there are two types of V-decays which can generate a secondary displaced vertex tag

Type-I: V-decays in which both decay tracks are reconstructed to form a secondary displaced vertex tag

Type-II: V-decays in which one decay track is lost, while the other intersects a mis-measured track to form a secondary displaced vertex tag.

Type-I tags will lie within the mass window and are removed with 100% efficiency. The rate at which Type-II tags occur is strongly correlated to the track finding efficiency of the CTC. If we very conservatively assume that every unpaired V-daughter track yields a positive tag, then we can place an upper limit on the number of residual tags originating from a V-decay. By imbedding Monte Carlo tracks from $K_s^0 \to \pi^+\pi^-$ decay into data events we measure the CTC trackfinding efficiency to be greater than 95% for tracks with $P_T > 250$ MeV/c and $|\eta| < 1.0$ [62]. We

use a HERWIG Monte Carlo sample of inclusive jets, with a trigger threshold of 50 GeV, to estimate that 80% of the V-daughter tracks have $P_T > 250$ MeV/c and $|\eta| < 1.0$. If we conservatively assume that the efficiency for finding those tracks not passing these cuts is zero, then we can place a lower bound on the CTC track finding efficiency of $\epsilon_{CTC} > 75\%$. By turning off V-removal in the B-tagging algorithm an additional 57 jets are tagged in a generic jet sample, where 30 ± 8 fall within a mass peak (ie. are Type-I tags). We place an upper bound on the number of residual V-decay tags by calculating

$$N_{II}^{res} \leq N_{II}^{rem} \cdot \left(\frac{1}{\epsilon_{II}} - 1\right) \tag{3.20}$$

where

$N_{II}^{res} \equiv$ the number of residual Type-II tags

$N_{II}^{rem} \equiv$ the number of Type-II tags removed by the V-removal algorithm; this is estimated by subtracting from the total number of removed tags the number within a mass peak; for our sample this yields $50 - (30 \pm 8) = 27 \pm 8$

$\epsilon_{II} \equiv$ the efficiency for finding the second leg of a V-decay given that the first leg passes all the CTC quality cuts; this is approximately given by the CTC track finding efficiency and has a lower bound of 75%.

Since we use the negative tag rate to estimate the number of mistags in the positive L_{xy} region, we calculate by what fraction we need to increase the mistag estimate in order to account for this residual contribution. We find that

$$F_{II}^{res} \leq \frac{N_{II}^{res}}{\text{total no. of negative tags}} \tag{3.21}$$

$$= 25 \pm 8\%. \tag{3.22}$$

In our signal region this corresponds to increasing the mistag contribution by 0.65 tags. This is negligible compared to the systematic error of 2.8 tags assigned to the total background.

The problem of $\gamma \to e^+e^-$ conversions yielding false displaced vertices is largely avoided by requiring the 2-D decay length to be well inside the 1st silicon layer, $L_{xy} < 2.5$ cm, and by cutting harder on the quality of tracks used in 2-track tags (cf. Figure 3.40). Knowing that the K/π ratio is of order 1/10 and that, averaged over its fiducial volume, the SVX is less than 1% of a radiation length we estimate that, even if the track finding efficiency for the electron tracks from photon conversions is half that for the V-decay tracks discussed above, the number of residual tags which originate from $\gamma \to e^+e^-$ conversions is less than 1/5 of those originating from V-decay. Again this is a negligible contribution compared to the assigned systematic error on the total background in our signal region.

We have assumed that the shape of the L_{xy} distribution from non-heavy flavor jets is symmetric about zero. We check this assumption by requiring, in a sample of generic jet tags, that all tracks used in a tag have $\chi^2 > 3$ and that at least one track in each tag have $\chi^2 > 5$. Since the average χ^2 of tracks passing the CTC cuts and having $P_T > 0.5$ GeV/c is less than 2.5, (and less than 10% have $\chi^2 > 5$) these tracks are most likely mismeasured tracks and thus yield a sample that is largely mistags. Note that the tag rate is reduced by more than 2 orders of magnitude. The ratio of positive tags to negative tags is 1.3 ± 0.2. Conservatively assuming that mistags are asymmetrically distributed requires increasing the mistag estimate of the background in the signal region by 0.78 tags. This is wholly accounted for by the systematic error on the total background estimate.

As a final check of our background predictions, we compare the observed and predicted number of tags in a $Z+$ multijet sample. Since the production mechanisms for $Z+$ multijet are very similar to those of $W+$ multijet, and since the top contribution is expected to be very small, this is an excellent sample in which to look for an anamolous source of background tags. Table 3.21 shows the results. The data and background prediction are in excellent agreement over all jet multiplicity bins.

$Z+$ multijet sample

	1 jet	2 jets	≥ 3 jets
N_{event}	896	119	19
N_{tag} jets observed	6	3	1
N_{tag} jets predicted	8.4 ± 0.84	2.3 ± 0.23	0.94 ± 0.09

Table 3.21: B-tagging results from a $Z+$ multijet sample using 100 pb^{-1} of CDF data.

3.7.6 Significance of Observed Excess

An excess of tagged events is observed in the search region. To determine the significance of the excess we employ a toy Monte Carlo in which we assume the data contains *only background* (i. e. we assume the "null hypothesis") and compute the probability of observing ≥ 40 tagged jets. This probability is estimated by performing a large number (100 million) of background-only "experiments" and counting the number which yield *at least* 40 tags total. We choose to count tagged jets, instead of tagged events, in order to account for the double tagged events. In each experiment we throw for the number of pre-tagged $Wb\overline{b}$, $Wc\overline{c}$, and Wc events from a Poisson distribution with a Gaussian smeared mean to account for the uncertainties. We constrain the total number of events to be what we observe, 296, so that the number of pre-tagged $W + non-hf$ events is given by

$$N_{W+non-hf} = 296 - (N_{Wb\overline{b}} + N_{Wc\overline{c}} + N_{Wc}) \tag{3.23}$$

The number of single and double tagged events is determined by applying the appropriate *per event* tagging efficiency for each background source. The $Wb\overline{b}$, $Wc\overline{c}$, and Wc tagging efficiencies are determined using MC and are calculated from "first principles" as

$$\epsilon_1 \quad = \quad f_1 \cdot \epsilon_{jet} + 2 \cdot f_2 \cdot \epsilon_{jet} \cdot (1 - \epsilon_{jet}) \tag{3.24}$$

$$\epsilon_2 = f_2 \cdot \epsilon_{jet}^2 \tag{3.25}$$

where

$\epsilon_1 \equiv$ the efficiency for tagging one heavy flavor jet per event

$\epsilon_2 \equiv$ the efficiency for tagging two heavy flavor jets per event

$f_1 \equiv$ the fraction of events passing all event selection criteria and containing 1 taggable heavy flavor jet

$f_2 \equiv$ the fraction of events passing all event selection criteria and containing 2 taggable heavy flavor jets

$\epsilon_{jet} \equiv$ the tagging efficiency per taggable heavy flavor jet.

The tagging efficieny, ϵ_{jet}, is corrected by a data to Monte Carlo scale factor, which is thrown from a Gaussian distribution with $\mu \pm \sigma = 0.98 \pm 0.15$ (cf. Section 3.5.4). Additionally, we include a mistag component and allow for each event to be mistagged, double mistagged, and double tagged with one heavy flavor tag plus one mistag. We express these per event mistag contributions to the tagging efficiency as

$\epsilon_{mtag} \equiv$ the efficiency per event for mistagging a jet

$\epsilon_{hf+mtag} \equiv$ the efficiency per event for heavy flavor tagging one jet and mistagging another jet to yield a double tagged event

$\epsilon_{2mtag} \equiv$ the efficiency per event for mistagging two jets.

We estimate ϵ_{mtag} from the data using the mistag parameterization discussed in Section 3.7.2.

$$\epsilon_{mtag} = \frac{\text{no. of predicted mistags in search region}}{\text{total no. of events in search region}} \tag{3.26}$$

$$= \frac{3.7 \pm 0.7}{296} = 0.013 \pm 0.003. \tag{3.27}$$

The double tag efficiencies are estimated by assuming for each background source that ϵ_1 is independent of ϵ_{mtag}. We then take the per event mistag contribution to the double tags as

$$\epsilon_{2mtag} = \epsilon_{mtag}^2 \tag{3.28}$$

$$\epsilon_{hf+mtag} = \epsilon_1 \cdot \epsilon_{mtag} \tag{3.29}$$

The total probability that an event is tagged is then given by

$$\epsilon_{\geq 1 tag} = \epsilon_{single\ tag} + \epsilon_{double\ tag} \tag{3.30}$$

where

$\epsilon_{single\ tag} = \epsilon_1 + \epsilon_{mtag}$

$\epsilon_{double\ tag} = \epsilon_2 + \epsilon_{2mtag} + \epsilon_{hf+mtag}$

For each MC experiment, we account for the uncertainties of each component, f_1, f_2, ϵ_{jet}, and ϵ_{mtag} by smearing their mean value with a Gaussian. Table 3.22 lists the input values for the parameters used in calculating ϵ_1 and ϵ_2 for each of the background sources. Table 3.23 compares the mean values yielded from the first principles calculation of ϵ_1 and ϵ_2 (as given in equation 3.24) to the values measured directly from Monte Carlo samples specific to each background source. The excellent agreement assures us that any unaccounted for correlations are smaller than the uncertainties assigned to the event tagging efficiencies.

Finally, we include a contribution from WW, WZ, $b\overline{b}$, and $Z \rightarrow \tau\tau$ sources by throwing for the number of tags from a Poisson distribution with a Gaussian smeared mean. The probability of a pure background sample fluctuating to yield ≥ 40 tags is then given by

$$\mathbf{P_{\geq 40}} \equiv \frac{\text{no. of experiments with } N_{tag} \geq 40 \text{ tags}}{\text{total no. of MC experiments performed}} \tag{3.31}$$

$$= 2.8 \times 10^{-6} \tag{3.32}$$

This corresponds to $\sim 4.5\sigma$ on a Gaussian distribution. Figure 3.61 shows, for all background Monte Carlo experiments, the distribution of N_{tag}. The arrow indicates

parameter	background source		
	$Wb\overline{b}$	$Wc\overline{c}$	Wc
f_1	0.410 ± 0.040	0.350 ± 0.044	0.384 ± 0.030
f_2	0.155 ± 0.022	0.183 ± 0.030	0.014 ± 0.005
ϵ_{jet}	0.450 ± 0.011	0.123 ± 0.008	0.123 ± 0.008

Table 3.22: The input parameters used to calculate the per event tagging efficiencies expressed in equation 3.24. They are measured from Monte Carlo samples specific to the various background sources. The errors are statistical only.

background sources	ϵ_1^{fp}	ϵ_1^{obs}	ϵ_2^{fp}	ϵ_2^{obs}
$Wb\overline{b}$	0.261 ± 0.026	0.270 ± 0.025	0.031 ± 0.004	0.039 ± 0.012
$Wc\overline{c}$	0.083 ± 0.009	0.073 ± 0.019	0.0027 ± 0.0004	$0.0000^{+0.0076}_{-0.0000}$
Wc	0.050 ± 0.005	0.052 ± 0.010	0.0002 ± 0.0001	$0.0000^{+0.0032}_{-0.0000}$

Table 3.23: We compare the per event tagging efficiencies yielded from the "first principles" calculation from equation 3.24 and the numbers given in Table 3.22, ϵ^{fp}, to those observed directly from the Monte Carlo, ϵ^{obs}.

where our data lie. Also shown is the distribution for the number of double tags for all background experiments. Note that the mean number of tags is 11, which is in reasonable agreement with the number estimated in Table 3.20 ($N_{tag}^{bkgnd} = 10.0 \pm 2.8$). We interpret the excess in the signal region as evidence for $t\bar{t}$ production. This hypothesis is strengthened by comparing the kinematic distributions of the data to those expected from a $t\bar{t}$ Monte Carlo.

3.8 Kinematic Distributions of Candidate Events

We make several comparisons between the data and a PYTHIA $t\bar{t}$ + background Monte Carlo. Before we proceed with the comparisons, we first correct our background estimate for a top contribution.

Recall that in Section 3.7 all background estimates are calculated assuming *no* $t\bar{t}$ *contribution*. In particular, the background estimates for $Wb\bar{b}$, $Wc\bar{c}$, and Wc (the $W+$ heavy flavor backgrounds) are scaled from the number of pre-tagged events in the data. If we assume the excess in the signal region is due to $t\bar{t}$ production, then the background is overestimated, since some of the pre-tagged events are then $t\bar{t}$ events. Note that some portions of the background estimate (WW, WZ, $Z \to \tau\tau$, and non-W) are not affected by our assuming the null hypothesis. We correct for the $t\bar{t}$ contribution using the iterative procedure depicted in Figure 3.62. In brief, we assume the excess in the $W+ \geq 3$ jets region is due solely to $t\bar{t}$ production, unfold the efficiency for tagging a $t\bar{t}$ event — this yields the the number of pre-tagged $t\bar{t}$ events — and scale the $W+$ heavy flavor component of the background estimate to account for this contribution. The procedure quickly converges and yields that $80 \pm 7\%$ ($75 \pm 7\%$) of the tagged jets (events) are from $t\bar{t}$ production.

We compare some kinematic properties of the tagged events in the signal region to expectations from Monte Carlo. The Monte Carlo distributions include a $t\bar{t}$ and background contribution, each normalized to their relative contribution as determined using the iterative procedure described above. The top mass assumed

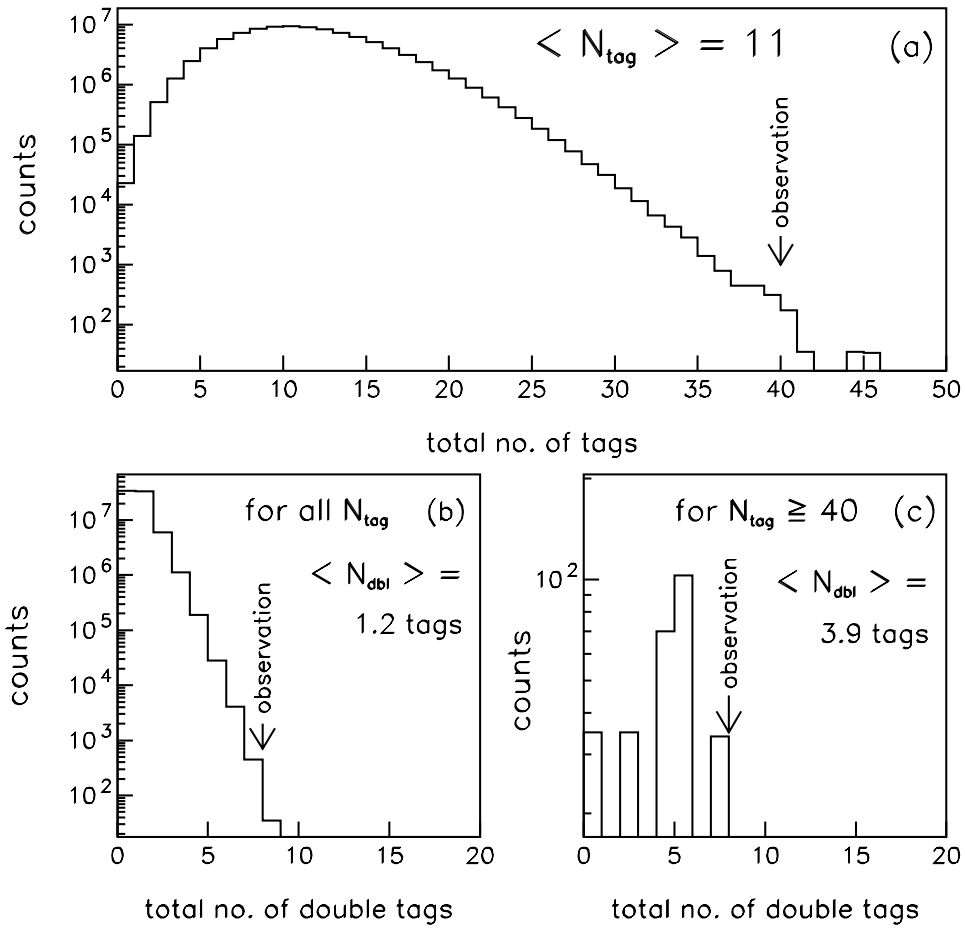

Figure 3.61: The distributions are (A) the total number of tags from 100 million Monte Carlo background experiments, (B) the total number of double tags from all experiments, and (C) the total number of double tags in experiments with at least 40 tags total. The arrows indicate where our data lie.

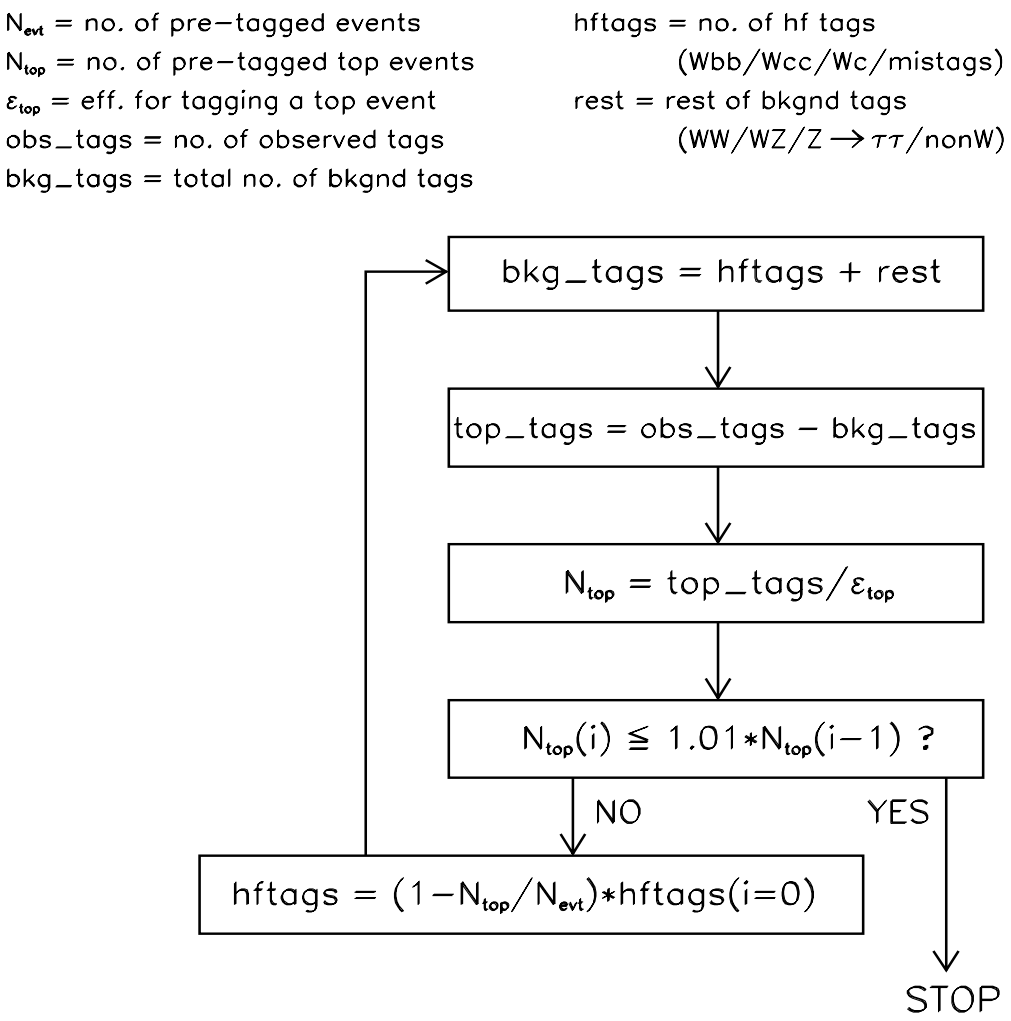

Figure 3.62: Flow chart describing the iteration procedure used to correct the background estimate of Section 3.7 for a $t\bar{t}$ contributions. The procedure yields that $80 \pm 7\%$ ($75 \pm 7\%$) of the tagged jets (events) are from $t\bar{t}$ production.

in the Monte Carlo is 175 GeV/c^2. The background distributions include contributions from $Wb\bar{b}$, $Wc\bar{c}$, Wc, WW, WZ, and $Z \rightarrow \tau\tau$ sources, each normalized to their relative contribution to the total background. Figure 3.63 compares the $c\tau$ distribution of the tagged jets, where we've calculated the $c\tau$ as

$$c\tau = \frac{L_{xy} \cdot M_{vtx}}{P_T^{vtx}} \cdot \frac{1}{F_{corr}} \tag{3.33}$$

where F_{corr} is a correction factor required since the B-decay vertex is not completely reconstructed. It is on the order of 0.8 for jets with $E_T > 50$ GeV and rises to ~ 0.9 for jets with $15 < E_T < 20$ GeV. Figure 3.64 compares the jet E_T distribution for the tagged jets. Figure 3.65 compares the number of tracks used in the vertex. Since this distribution is sensitive to the performance of the SVX, we only use run 1B data since the SVX Monte Carlo is tuned using run 1B data. Figure 3.66 compares the transverse mass of the tagged events. For the Monte Carlo shape we require that the lepton originate from a leptonically decaying W. The data are consistent with the Monte Carlo and provide qualitative evidence for W production in the tagged events. Finally, in Figure 3.67, we compare the total event energy as characterized by the variable

$$\mathbf{H} = \Sigma E_T^* + \not\!\!E_T + P_T^{lep} \tag{3.34}$$

where P_T^{lep} is the transverse momentum of the primary lepton in the event. For a heavy top quark we expect the **H** distribution to be significantly harder than for the dominant backgrounds $Wb\bar{b}$, $Wc\bar{c}$, and Wc. In all cases the two distributions are in good agreement. This strengthens our hypothesis that the excess in the signal region is due to $t\bar{t}$ production.

In these comparisons we have taken the background shape from Monte Carlo. This has the disadvantage that the mistag contribution is neglected. This is a very difficult background to model. As a check, we repeat the above comparisons taking all background distributions from the $W + 1$ jet bin. Note that this is not an ideal solution either since the relative mix between $Wb\bar{b}$, $Wc\bar{c}$, and Wc is very different between the $W + 1$ jet and $W + \geq 3$ jets regions. We find that while the background

shapes varied some, the resulting top + background distributions, because they are so dominated by the $t\bar{t}$ contribution, change imperceptibly.

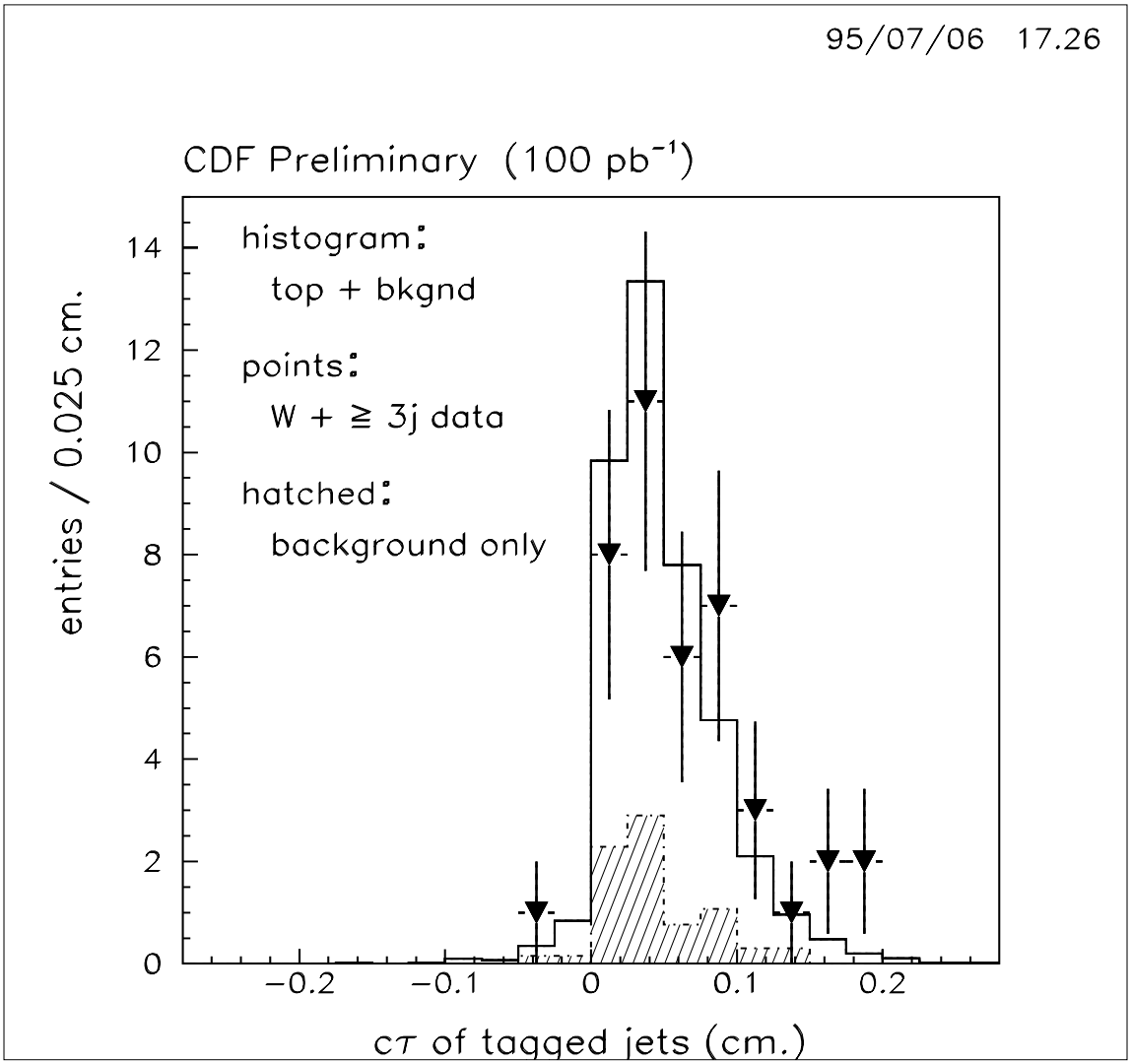

Figure 3.63: The solid histogram is the $c\tau$ of tagged jets in the signal region for a $t\bar{t}$ + background Monte Carlo. The points are the data. The two distributions are normalized to the same number of events. The hatched histogram is the background shape normalized to its relative contribution.

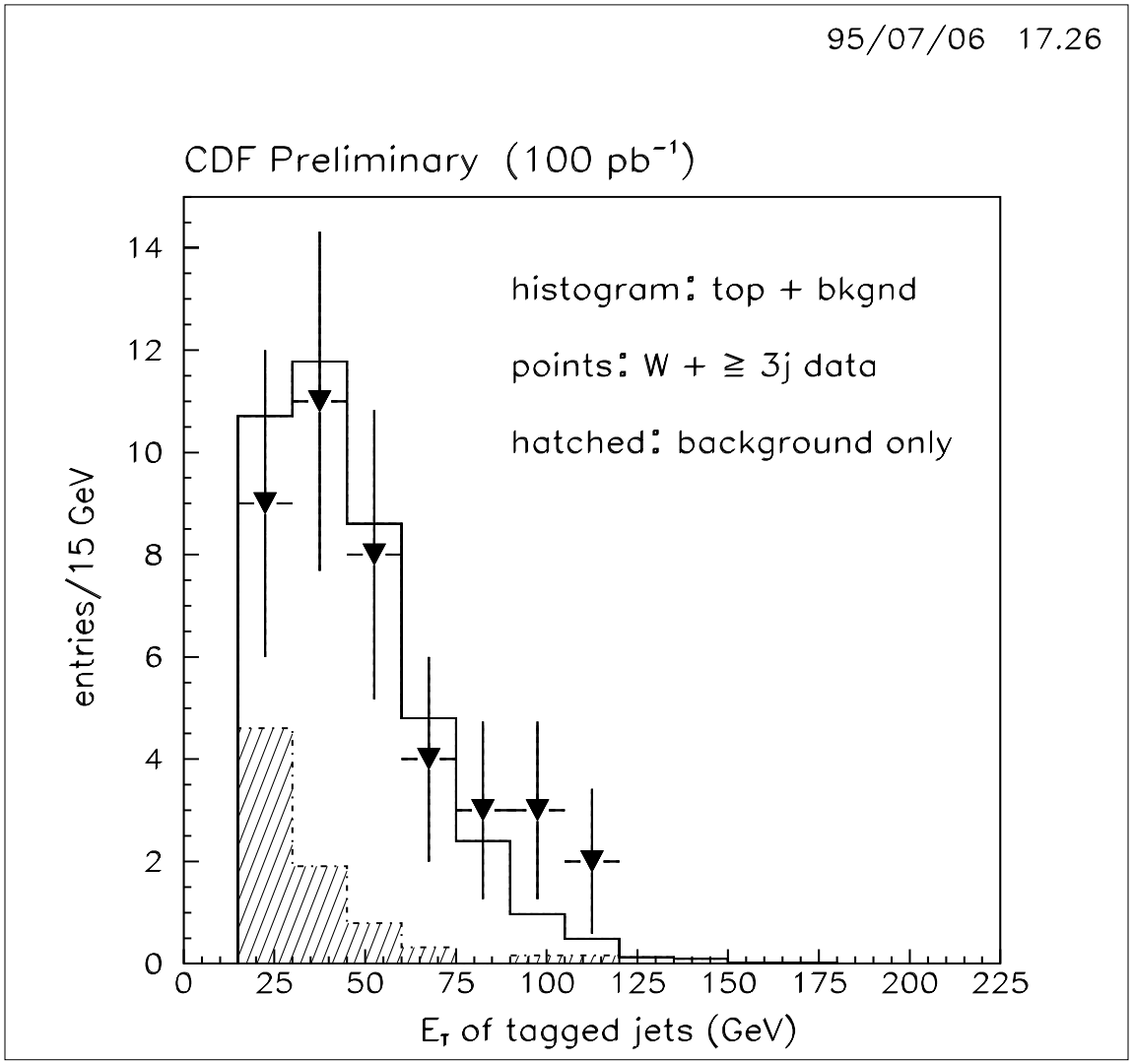

Figure 3.64: The solid histogram is the E_T of tagged jets in the signal region for a $t\bar{t}$ + background Monte Carlo. The points are the data. The two distributions are normalized to the same number of events. The hatched histogram is the background shape normalized to its relative contribution.

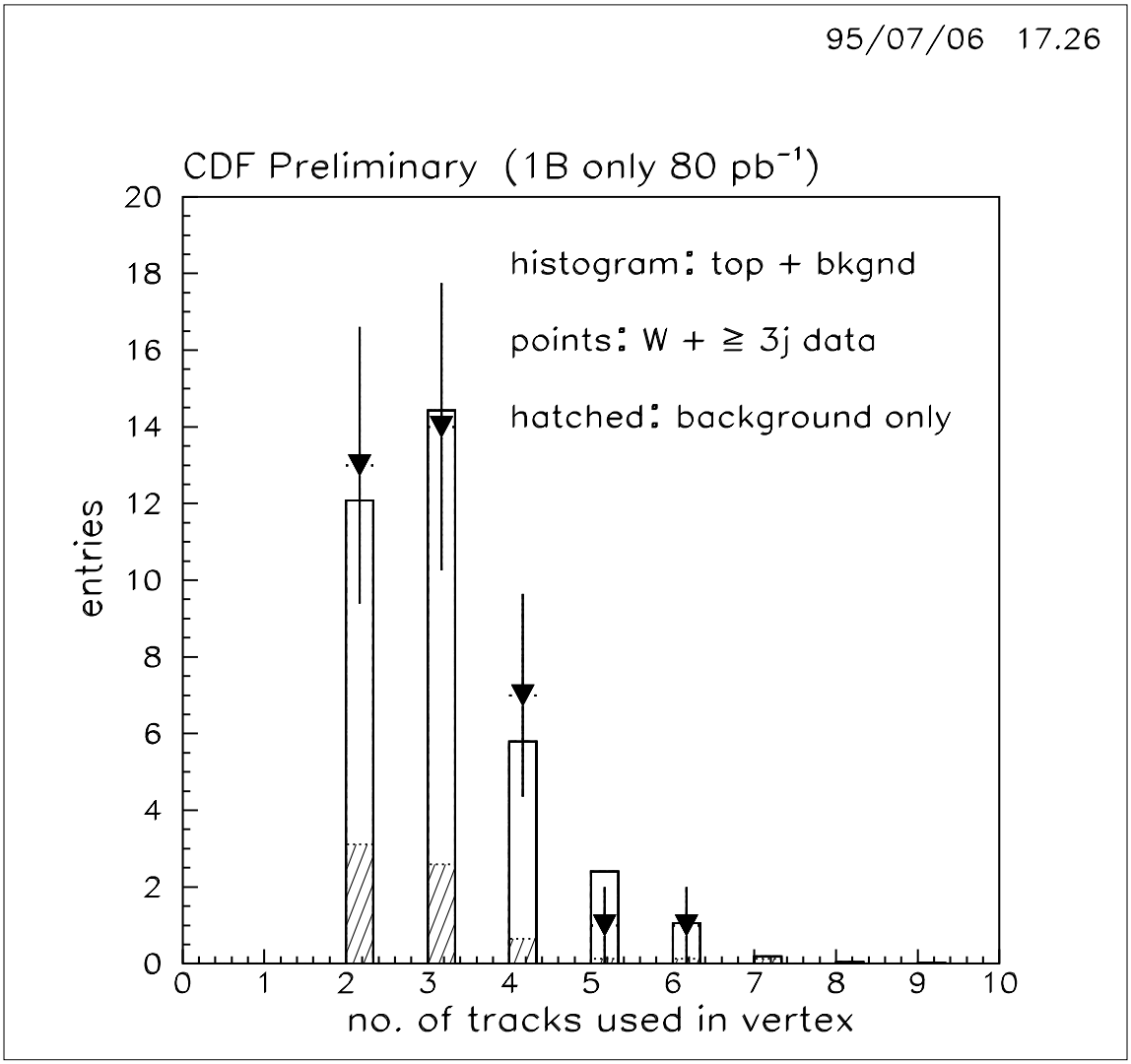

Figure 3.65: The solid histogram is the number of tracks included in the vertex for tagged jets in the signal region for a $t\bar{t}$ + background Monte Carlo. The points are the data. The two distributions are normalized to the same number of events. The hatched histogram is the background shape normalized to its relative contribution.

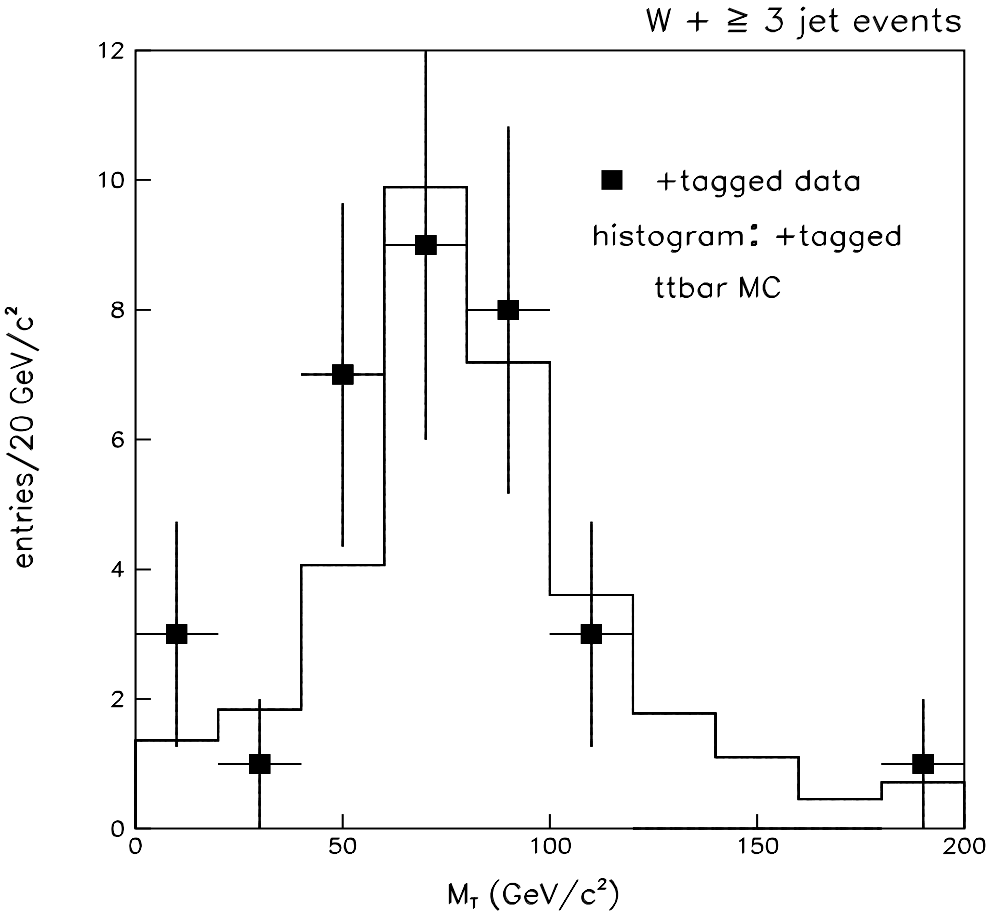

Figure 3.66: The histogram is the transverse mass distribution of the lepton and neutrino (whose momentum is estimated using the missing E_T vector) for a $t\bar{t}$ Monte Carlo. The points are the data. The two distributions are normalized to the same number of events. The last bin includes overflows.

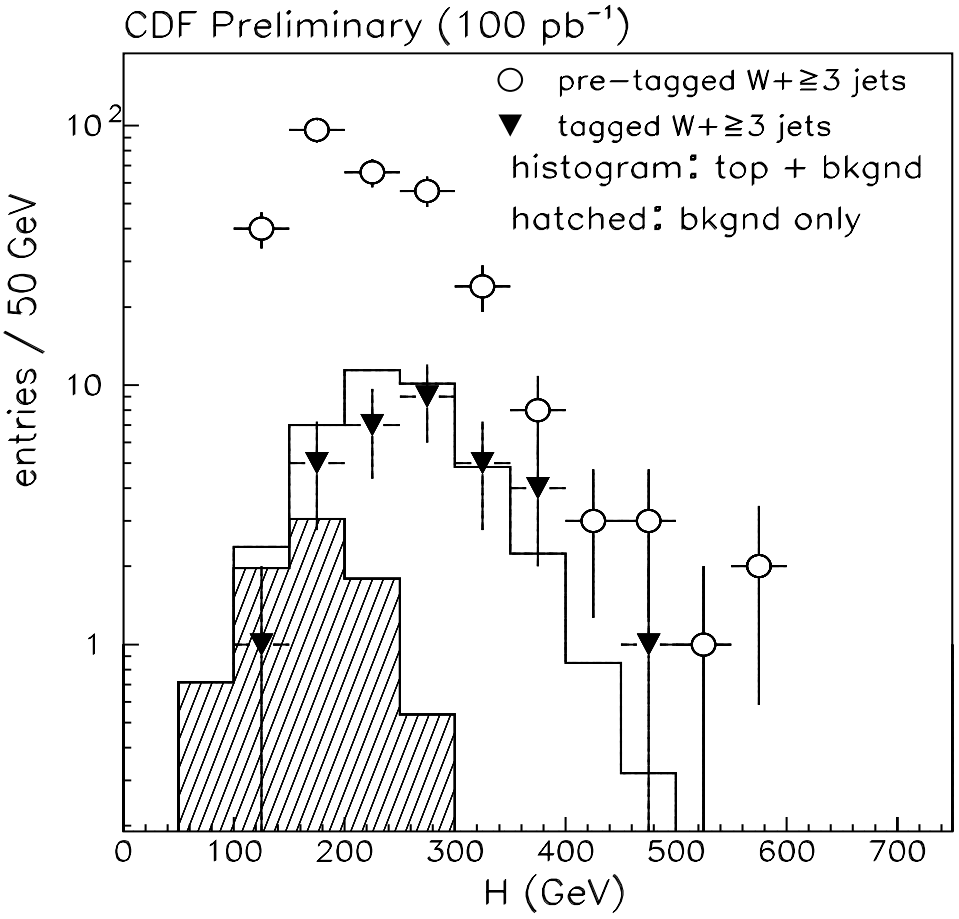

Figure 3.67: The solid histogram is the **H** distribution $\left(= \Sigma E_T^* + \not\!\!E_T + P_T^{lep}\right)$ for tagged events in the signal region for a $t\bar{t}$ + background Monte Carlo. The open points are the pre-tagged data and the solid points are the tagged data. The two tagged distributions are normalized to the same number of events. The hatched histogram is the background shape normalized to its relative contribution.

3.9 Cross Section Measurement

Assuming the excess in the $W+ \geq 3$ jets signal region is due to Standard Model $t\bar{t}$ production and using the acceptances and efficiencies discussed in Section 3.5, we calculate the $t\bar{t}$ production cross section using the expression

$$\sigma_{t\bar{t}} = \frac{N_{obs} - b}{\epsilon_{t\bar{t}} \cdot \int \mathcal{L}dt} \tag{3.35}$$

where

$N_{obs} \equiv$ the number of observed tagged *events* in the $W+ \geq 3$ jets signal region (32)

$b \equiv$ the number of estimated tagged background *events* in the signal region

$\epsilon_{t\bar{t}} \equiv$ the fraction of all $t\bar{t}$ events surviving all event selection criteria with ≥ 1 tagged jet

$\int \mathcal{L}dt \equiv$ the total integrated luminosity of the data sample $\left(100 \pm 8 \text{ pb}^{-1}\right)$.

It should be noted that our background estimate of Section 3.7 yields the number of tagged *jets* **assuming the null hypthesis**. This requires our making two corrections before proceeding with the cross section calculation. First, we correct for the $t\bar{t}$ contribution to the background estimate using the iterative procedure described in Section 3.8. Second, to get the tagged *event* background estimate we determine from Monte Carlo that it is necessary to correct the tagged *jet* background estimate by a factor of 0.97 ± 0.01. Note that since the $t\bar{t}$ per event tagging efficiency changes as a function of top mass, the number of background events after all corrections, b, also changes as a function of top mass. We use the $t\bar{t}$ tagging efficiencies, ϵ_{tag}, and detection efficiencies, $\epsilon_{t\bar{t}}$, listed in Table 3.12 as a function of top mass to calculate the total $t\bar{t}$ production cross section for $\bar{p}p$ collisions at $\sqrt{s} = 1.8$ TeV. The results are given in Table 3.24. The uncertainty on the number of background events includes a contribution from the iterative procedure due to the uncertainty in the $t\bar{t}$ tagging efficiency. For comparison we superimpose our measured results over the theoretical calculations given in Reference [29]. This is shown in Figure 3.68.

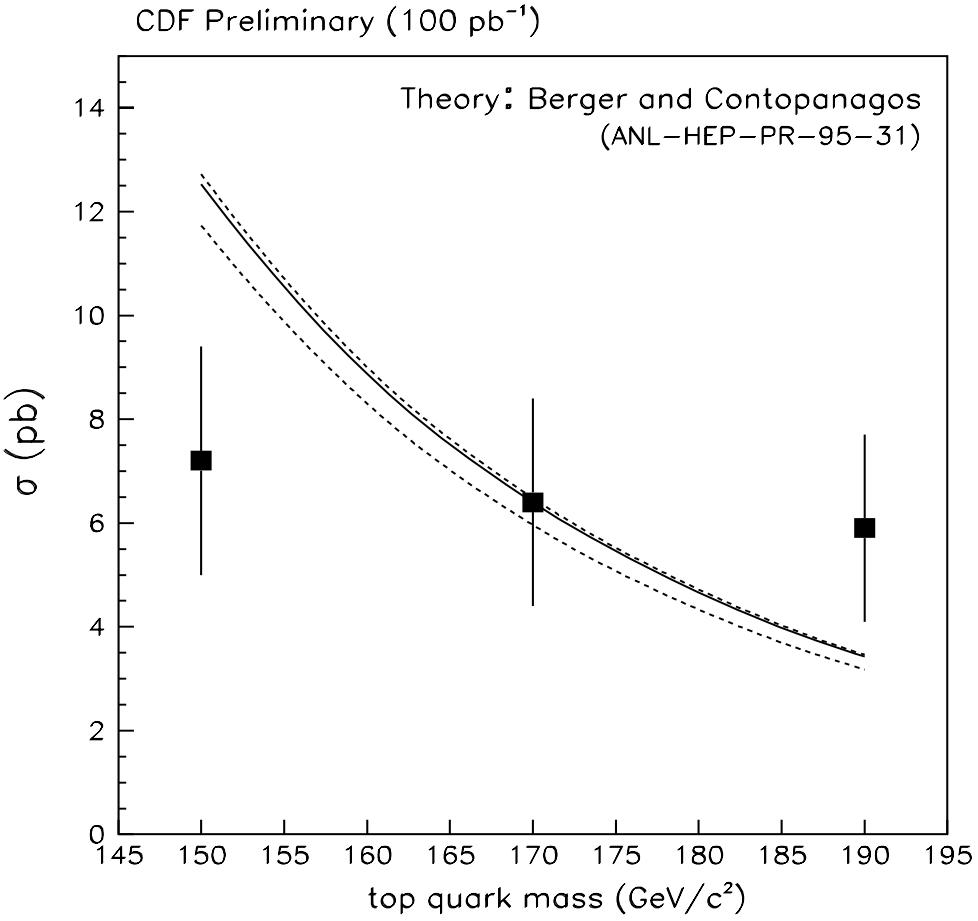

Figure 3.68: Total $t\bar{t}$ production cross section for $\overline{p}p$ collisions at $\sqrt{s} = 1.8$ TeV as a function of top mass as measured (points) and calculated in Reference [29] (solid curve). Estimates of the theoretical uncertainty are given as dashed lines.

	M_t (GeV/c^2)		
	150	170	190
N_{obs} :	32	32	32
b :	8.2 ± 2.5	8.3 ± 2.5	8.3 ± 2.5
ϵ_{tag} :	0.43 ± 0.05	0.44 ± 0.04	0.45 ± 0.05
$\epsilon_{t\bar{t}}$:	0.033 ± 0.006	0.037 ± 0.006	0.040 ± 0.006
$\sigma_{t\bar{t}}$:	7.2 ± 2.2 pb	6.4 ± 2.0 pb	5.9 ± 1.8 pb

Table 3.24: The total $t\bar{t}$ production cross section, $\sigma_{t\bar{t}}$, as a function of top quark mass, M_t, for $\overline{p}p$ collisions at $\sqrt{s} = 1.8$ TeV.

3.10 Direct Determination of the Top Quark Mass

Using a constrained-fitting procedure, it is possible to directly determine the top quark mass, M_t, using the events in the $W+ \geq 3$ jets region. This measurement is non-trivial and requires a thorough discussion. The author regrets not having had the opportunity to more fully participate in this measurement and, for the sake of completeness, summarizes the method and results below. A more complete discussion can be found in Reference [24].

The Standard Model decay

$$t\bar{t} \rightarrow \ell\nu b_1 + q\bar{q}b_2 \tag{3.36}$$

is assumed. At least 4 jets in the event are required in order to allow a one-to-one matching between jets and final state quarks. To increase the acceptance for $t\bar{t}$ events in the B-tagged sample of $W+ \geq 3$ jets described in Section 3.1.4 the selection criteria for the fourth jet is relaxed to $E_T > 8$ GeV and $|\eta| < 2.4$. Excluding the B-tagging requirement, there are 132 events passing the 4 jet criteria. To reduce combinitorics and help improve the jet-quark assignments, at least one B-tagged jet is also required. Both SVX-tags, as described in Section 3.2, and "SLT-tags", as described in References [23] [24] [32] are allowed. The SLT tagging algorithm searches for an additional soft lepton, e or μ, with $P_T > 2$ GeV, consistent with having originated from the semi-leptonic decay of a B hadron. The probability of finding an additional e or μ in a $t\bar{t}$ event passing all the event selection criteria is $20 \pm 2\%$ [23]. In the $W+ \geq 3$ jets signal region there are 40 SLT tags with an estimated background of 23.8 ± 3.8 (assuming the null hypothesis — to account for the $t\bar{t}$ contribution to the pre-tagged event sample, scale this number by ~ 0.80). Table 3.25 lists the final event counts. There are 35 events passing the 4 jet criteria and containing at least one B-tagged jet. A likelihood function is used to estimate that the background in this sample is 10.4 ± 3.0 events [24].

The following is assumed

sample	N_{events}
$W+ \geq 3$ jets	296
and with 4th jet	132
and ≥ 1 B-tag	35
and SVX-tagged	21
and SLT-tagged	20
double tagged	7

Table 3.25: Number of events surviving various cuts used to isolate a sample from which to directly determine the top quark mass.

$$
\begin{aligned}
\overline{p}p &\rightarrow t_1 + t_2 + X \\
t_1 &\rightarrow W_1 + b_1 \\
t_2 &\rightarrow W_2 + b_2 \\
W_1 &\rightarrow \ell\nu \\
W_2 &\rightarrow q\overline{q}'
\end{aligned}
$$

The measured energy and angle of each of the four jets are used to infer the 4-momenta of the primary quarks. The W mass is required to be consistent with $M_W = 80.2$ GeV/c^2 within the uncertainties due to the jet energy resolution and the W width [63]. The quantity X represents the system recoiling against the $t\overline{t}$ pair. The total energy of the $\overline{p}p$ system is taken to be 1.8 TeV with a net momentum of zero. This allows for the first two components of X (the $\hat{x}$ and $\hat{y}$ components) to be determined by vectorially subtracting from zero the event $\not\!\!E_T$, the E_T of the four jets used in the fit, and the E_T of the primary lepton as measured by the calorimeter tower through which the lepton passes. The remaining components are left as unknowns. The ν momentum is also left as an unknown in the fit and is determined from the kinematic constraints. Because the longitudinal component of

the total event energy is not measured, there are two possible solutions for the $\hat{z}$ component of the ν momentum.

A fit is made for every possible configuration of the jet-quark assignments. To reduce the combinatorics, only the four highest E_T jets are considered. A B-tagged jet is assigned as having originated from one of the final state b quarks in Equation 3.36. In the absence of any B-tag information, there are then 12 possible configurations, each with a two-fold ambiguity in the $\hat{z}$ component of the ν momentum, for a total of 24 solutions. If there exists only 1 B-tagged jet in the event, the total number of solutions is reduced to 12. Double tagged events have only 4 possible solutions. The solution with the lowest fit χ^2_{fit} is used subject to the constraint that $\chi^2_{fit} < 10$. Thirty-two of the 35 B-tagged 4 jet events survive this cut and are used to determine the top quark mass.

A variety of corrections are applied to the jet energies as measured by the calorimeters. These corrections account for detector non-linearities, reduced calorimeter response at detector boundries, detector-dependent energy thresholds, contributions from multiple interactions, out-of-cone losses, undetected energy carried by μs and νs, and fragmentation effects. There are two sets of corrections, the first being a standard set of corrections, the other being specific to Standard Model $t\bar{t}$ production and decay according to Equation 3.36. The standard corrections are fully described in References [41] and [64] and typically increase the jet energy by $\sim 30\%$. As a check of the energy scale set by these corrections, a sample of photon + one jet events is used to calculate

$$\Delta_{E_T} = \frac{\left(E_T^{photon} - E_T^{jet}\right)}{E_T^{photon}} \tag{3.37}$$

where the quantity E_T^{jet} includes the jet corrections. The candidate photon energy is required to be fully contained in the CEM, where the energy scale is well understood. Figure 3.69 plots the resulting Δ_{E_T} distribution. The average imbalance is measured to be 2.7%. The second set of corrections is used to account for energy sharing between jets and for the presence of B-jets, which require corrections specific for the

decay of B-jets in Standard Model $t\bar{t}$ events. This latter set of corrections is more fully described in Reference [24] and is determined from Monte Carlo. It has a loose dependence on the assumed top quark mass of the Monte Carlo sample. Figure 3.70 demonstrates the improvement in M_t after inclusion of the $t\bar{t}$ specific jet energy corrections.

A Monte Carlo sample assuming $M_t = 170$ GeV/c^2 is used to test the procedure. The sample is passed through a full detector simulation and the full analysis path including all jet energy corrections. The resulting M_t distribution is given in Figure 3.71 and has a mean of 168 GeV/c^2 and a $\sigma = 23$ GeV/c^2. The fitting method correctly makes all four jet-quark assignments 31% of the time. In 22% of the events, the 4 final states quarks fragment into the 4 highest E_T jets, but the lowest χ^2_{fit} solution does not correctly assign the jets. In the remaining 47% of the events, at least one of the 4 highest E_T jets is not readily associated with one of the 4 final state quarks. For comparison, the resulting M_t distribution for that subset of events in which all jet-quark assignments are correctly made is superimposed in Figure 3.71 and has a $\sigma = 12$ GeV/c^2.

A Monte Carlo sample of $W+$ multijet events, passed through a full detector simulation and the full analysis path, fit to the $t\bar{t}$ hypothesis yields the distribution of Figure 3.72, which is very broad and centered at 140 GeV/c^2. This distribution is used as the background shape of the reconstructed mass distribution.

The observed reconstucted mass distribution is fit to the sum of the expected mass distributions from $t\bar{t}$ decay, assuming a given top quark mass, M_T, and from $W+$ multijet background events using the maximum likelihood method discussed in Reference [24]. The likelihood function, L, is defined as

$$\begin{aligned} L &= \mathbf{G}\left(N_b, \sigma_b; n_b\right) \cdot \mathbf{P}\left(n_t + n_b, N_{obs}\right) \\ &\quad \times \prod_{i=1}^{N_{obs}} \frac{n_b \cdot f_b\left(m_i\right) + n_t \cdot f_t\left(m_i, M_t\right)}{\left(n_b + n_t\right)} \end{aligned}$$

where

$N_{obs} \equiv$ the number of observed B-tagged 4 jet events (32)

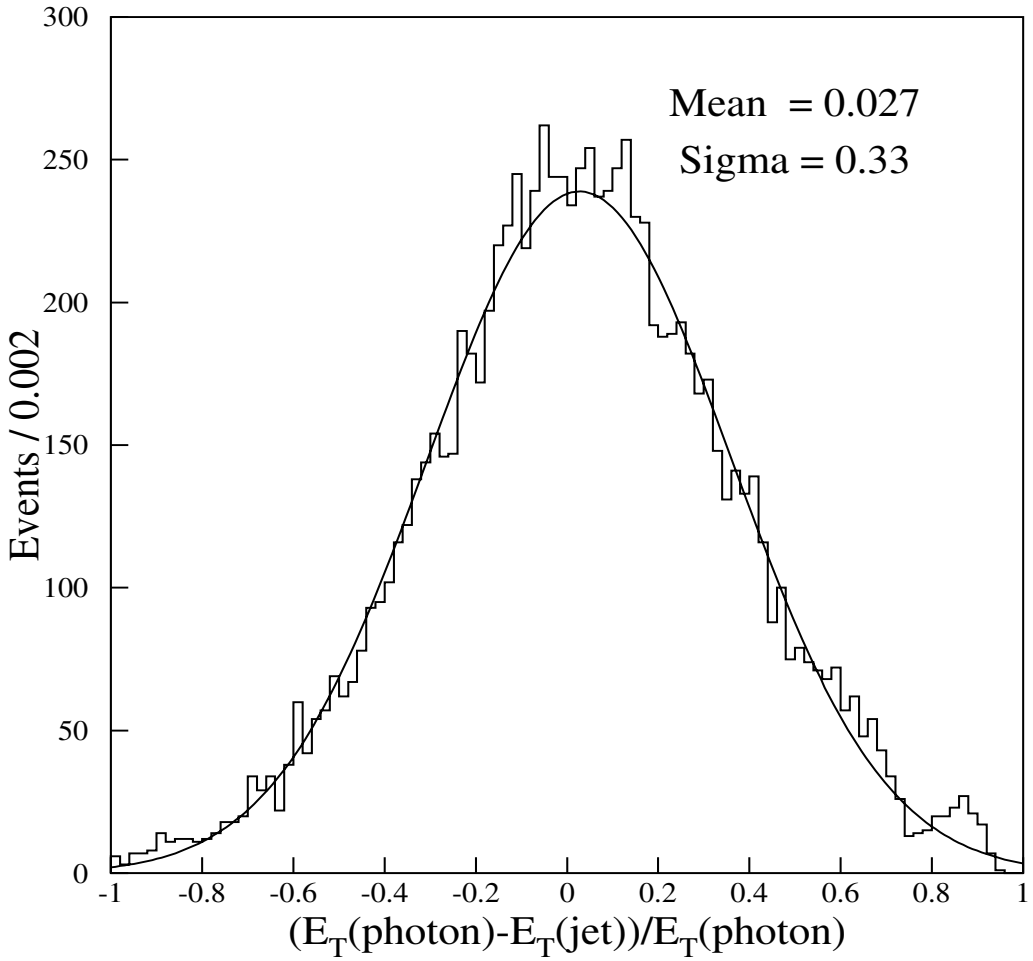

Figure 3.69: Jet energy balancing after the application of jet energy corrections, $\Delta_{E_T} = \frac{\left(E_T^{photon} - E_T^{jet}\right)}{E_T^{photon}}$.

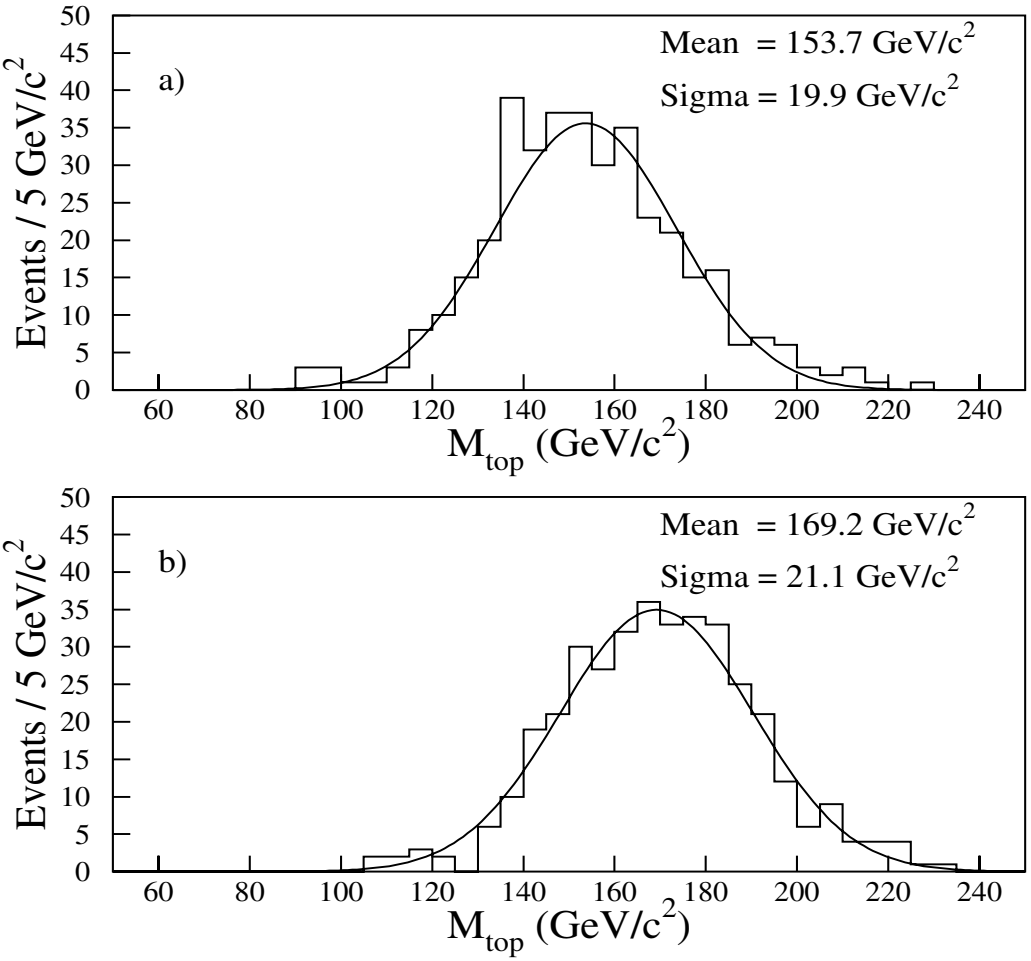

Figure 3.70: The resulting M_t distribution from a Monte Carlo sample generated assuming a top mass of 170 GeV/c^2 using the standard jet corrections (top) and additionally including those jet corrections specific to top decay (bottom).

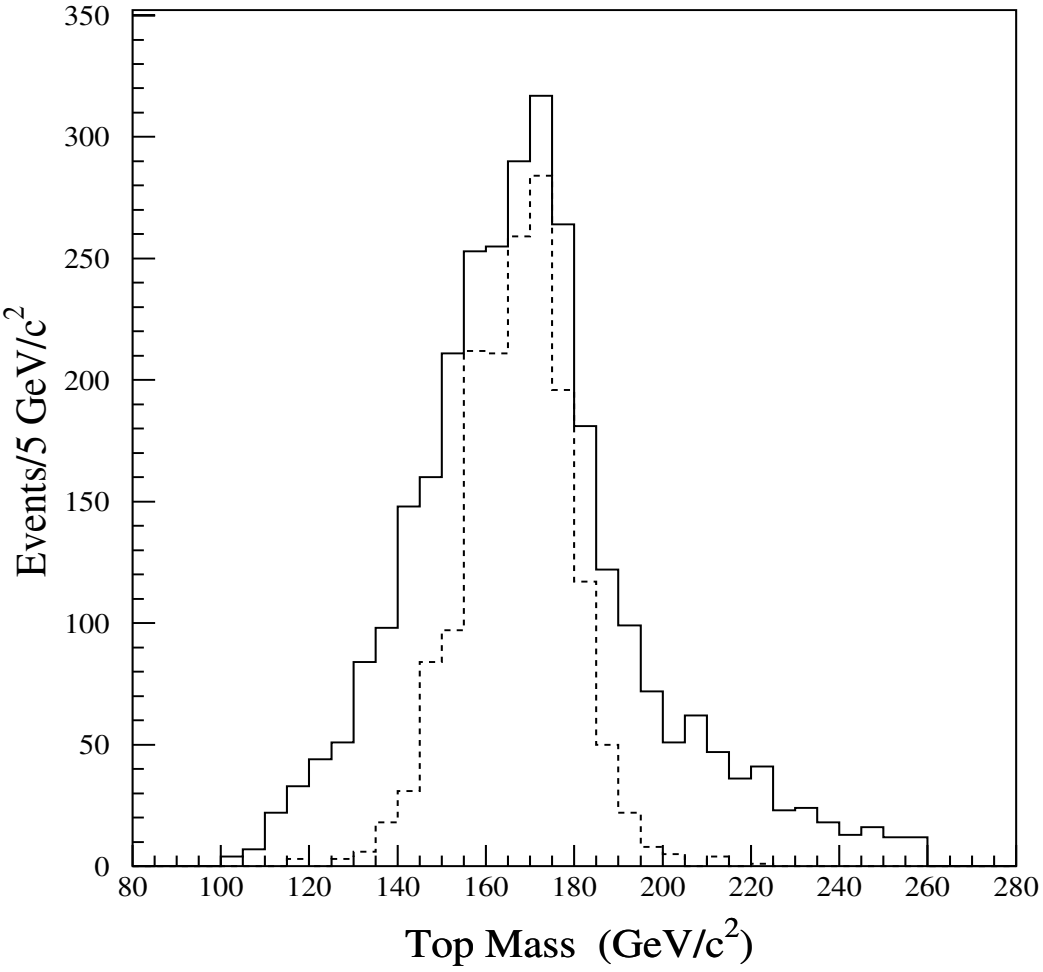

Figure 3.71: The resulting reconstructed M_t distribution using the fitting procedure described in the text on a Monte Carlo sample of $t\bar{t}$ events passing all the event selection criteria (solid). The subset of events in which the fitting procedure makes all the correct jet-quark assignments is also shown (dashed). The Monte Carlo assumes a top mass of 170 GeV/c^2.

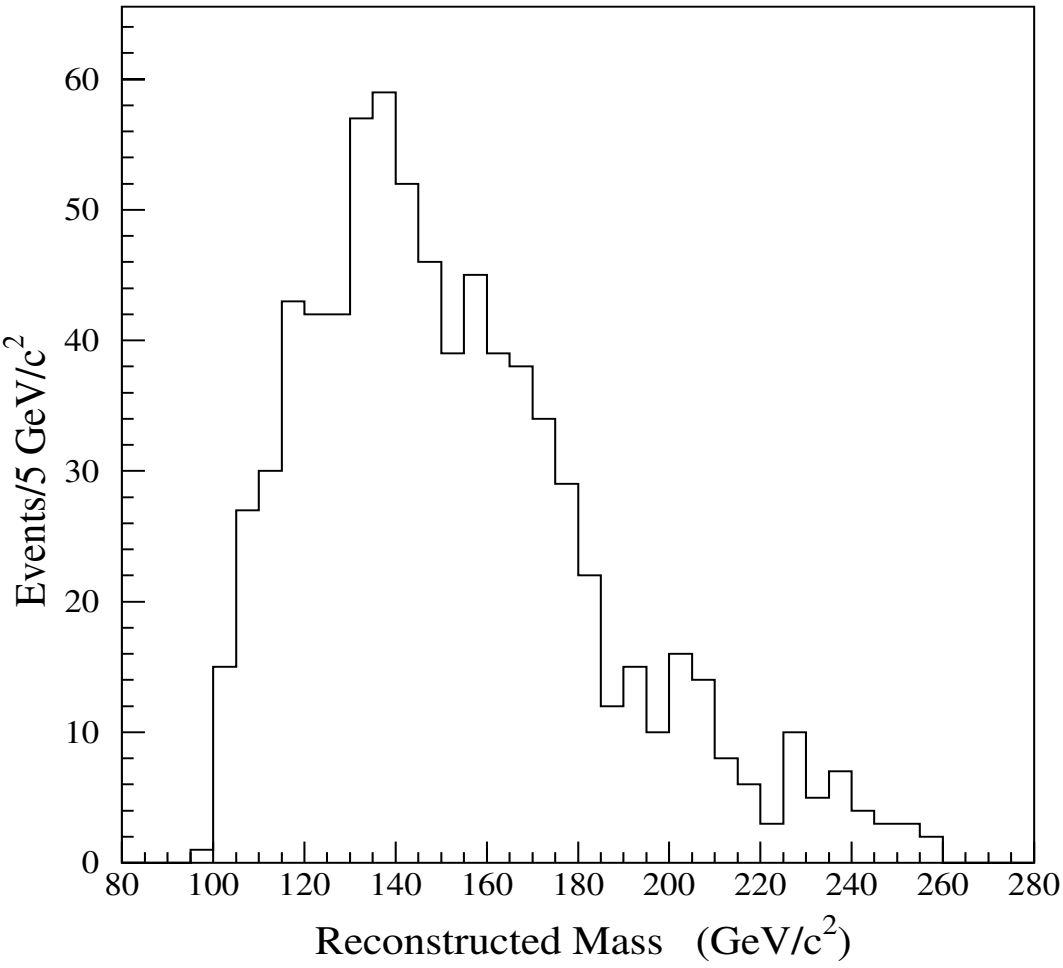

Figure 3.72: The resulting reconstucted mass distribution for a $W+$ multijet Monte Carlo sample. This is used as the background shape in the fitting procedure described in the text.

$\mathbf{G}\,(N_b, \sigma_b; n_b) \equiv$ the Gaussian distributed probablity that the sample really contains n_b background events given that N_b are expected with an uncertainty of σ_b $(N_b \pm \sigma_b = 10.4 \pm 3.0)$

$n_t \equiv$ the number of $t\bar{t}$ events in the data sample

$\mathbf{P}\,(n_t + n_b, N_{obs}) \equiv$ the Poisson distributed probablity that N_{obs} events are observed if $n_t + n_b$ are expected on average

$m_i \equiv$ the reconstructed mass value of the lowest χ^2_{fit} solution for data event i

$f_b\,(m_i) \equiv$ the normalized $W+$ multijet Monte Carlo reconstucted mass distribution evaluated at the reconstructed mass value of m_i (cf. Figure 3.72)

$f_t\,(m_i, M_t) \equiv$ the normalized $t\bar{t}$ Monte Carlo reconstructed mass distribution, assuming a top quark mass of M_t, evaluated at the reconstructed mass value of m_i (cf. Figure 3.71).

A range of top quark masses is considered and at each assumed value of M_t the likelihood function is maximized with respect to n_b and n_t. Figure 3.73 shows the reconstucted mass distribution of the B-tagged data events. The inset is the resulting $-\ln L$ distribution as a function of assumed M_t. The smoothed $-\ln L$ distribution has a minimum at 175 GeV/c^2. The vertical error bars reflect the uncertainty on the value of L due to the statistics of the Monte Carlo samples used to estimate f_t and f_b. A more complete discussion of the fitting procedure is given in Reference [24]. The uncertainty in M_t is estimated by allowing L to change by 0.5 units and, in combination with the uncertainty due to Monte Carlo statistics, is 6 GeV/c^2.

A variety of checks on the construction of the likelihood function, fitting procedure, shape of the background $W+$ multijets reconstructed mass distribution, assumed number of background events, and biases introduced by B-tags are also discussed in detail in Reference [24] and are used to assign the systematic errors given in Table 3.26. Adding all the systematic errors in quadrature yields a final value for the top quark mass of

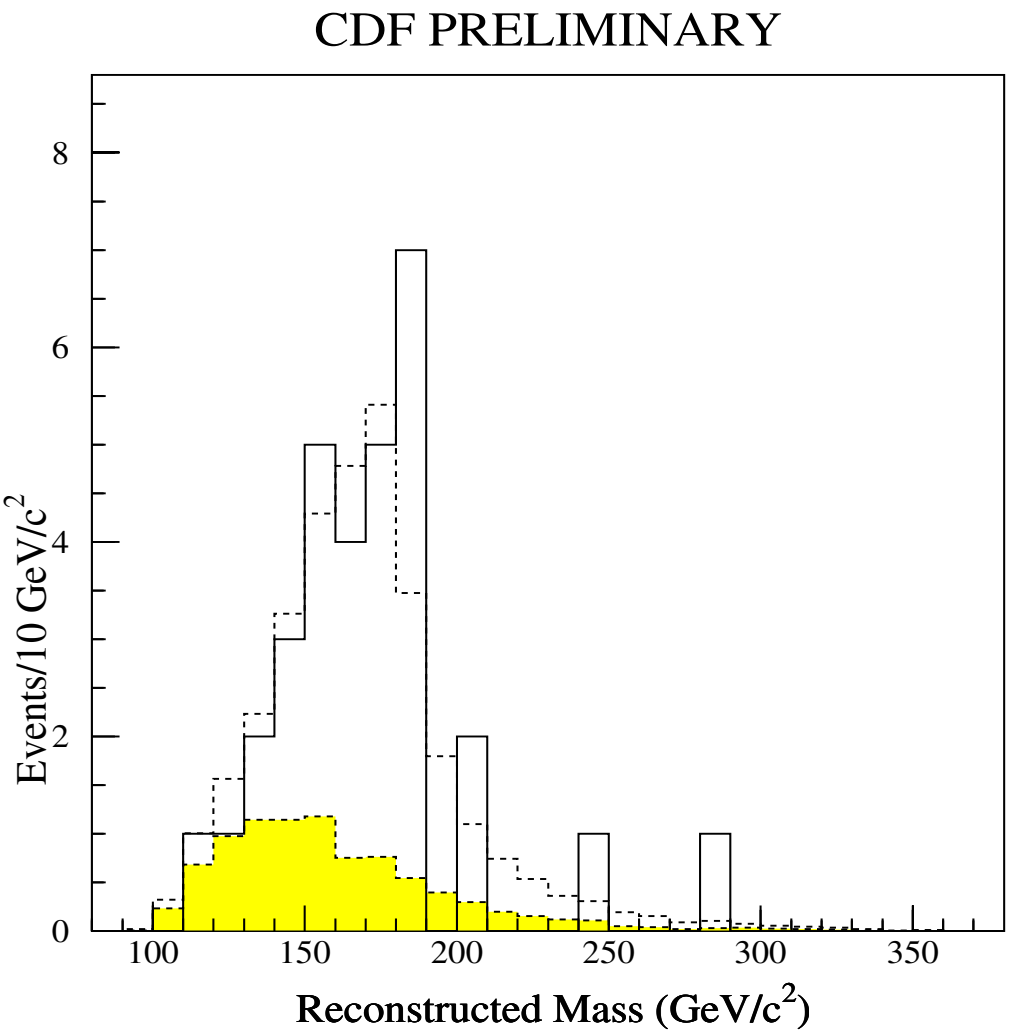

Figure 3.73: The resulting mass distribution of the B-tagged $W+4$ jet events (solid) assuming the $t\bar{t}$ hypothesis. The dashed histogram is derived from a $t\bar{t}$ Monte Carlo with $M_t = 170$ GeV/c^2. The shaded region is the background distribution, derived from a $W+$ multijet Monte Carlo. The Monte Carlo distributions are normalized to their relative contributions as determined in the fit.

Systematic Uncertainty	(%)
a. Jet energy scale (detector effects)	1.8
b. Gluon radiation effects on quark energy	4.4
c. B-tag bias to $t\bar{t}$ distribution	1.3
d. B-tag bias to background distribution	< 0.1
e. Shape of background distribution	0.9
f. Varying likelihood functions	0.9
g. Varying fit used to determine minimum $-\ln L$	0.7

Table 3.26: Systematic uncertainties investigated in direct determination of top quark mass using B-tagged $W+ \geq 4$ jet data.

$$M_t = 175 \pm 6 \pm 9 \text{ GeV}/c^2.$$

Using the acceptances and efficiencies as calculated from a $t\bar{t}$ Monte Carlo with a top quark mass of 175 GeV/c^2, we repeat the cross section measurement of Section 3.9 to obtain

$$\sigma_{t\bar{t}} = 6.2 \pm 1.9 \text{ pb}.$$

This result is consistent with the theoretical calculation of Reference [29] as demonstrated in Figure 3.74.

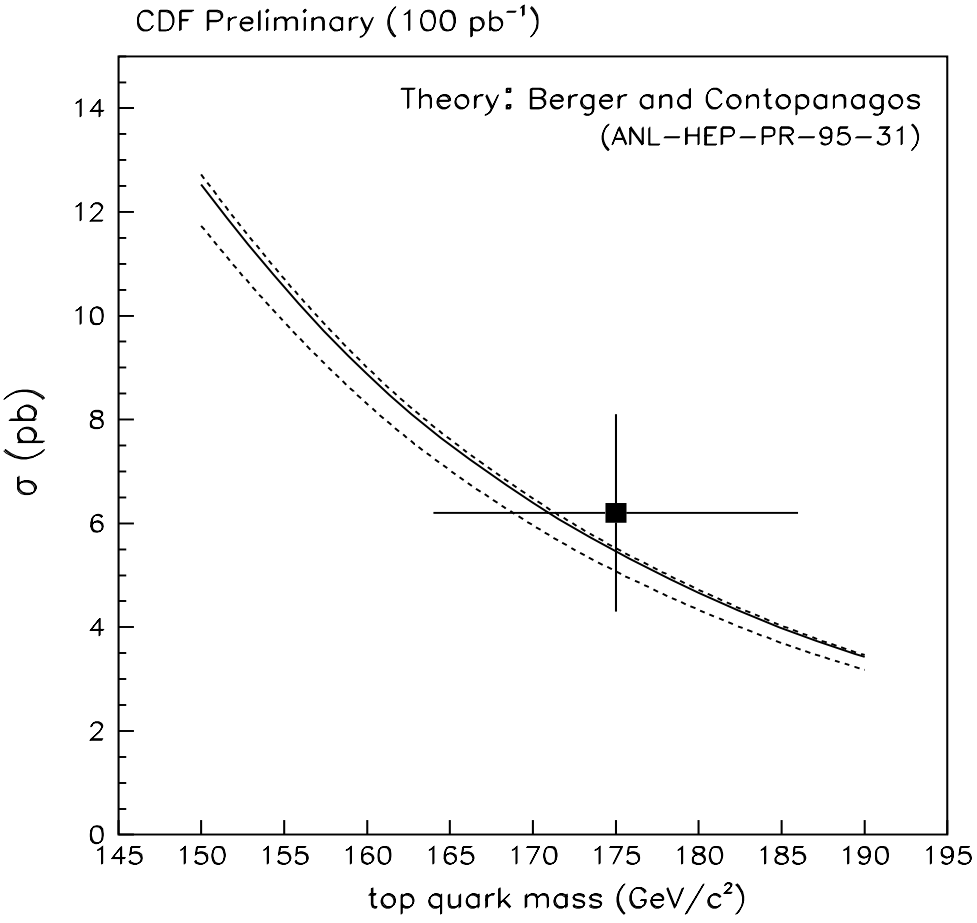

Figure 3.74: The total $t\bar{t}$ production cross section, $\sigma_{t\bar{t}}$, evaluated at the measured value of the top quark mass, $M_t = 175 \pm 6 \pm 9$ GeV/c^2 (point), and theory curve of Reference [29] (solid curve). Estimates of the theoretical uncertainties are drawn as dashed lines.

3.11 Conclusion

We search for $t\bar{t}$ production in $\overline{p}p$ collisions at $\sqrt{s} = 1.8$ TeV using the Fermilab TeVatron collider and the CDF detector. We assume Standard Model decays and couplings and look for an excess of events consistent with the $\overline{p}p \to t\bar{t} \to W^+bW^-\overline{b}$ hypothesis. We require a high P_T electron or muon, large missing transverse energy, and at least three high E_T jets in the event. We additionally require that at least one jet in the event be identified as a B-jet by identifying within it a secondary displaced vertex (a B-tag). Using 100 pb^{-1} of data we observe 40 B-tags in 32 events with 10.0 ± 2.8 tags expected from background. The probability that a statistical fluctuation of the background can account for the excess is 2.8×10^{-6}, which corresponds to 4.5σ on a Gaussian distribution. Kinematic distributions of the B-tagged events are consistent with expectations derived from a $t\bar{t}$ plus background Monte Carlo.

These data establish the existence of the top quark. We use B-tagged four jet events to directly determine the mass of the top quark. Using a maximum likelihood method we measure $M_t = 175 \pm 6 \pm 9$ GeV/c^2. The $t\bar{t}$ total production cross section assuming the measured mass is calculated to be $\sigma_{t\bar{t}} = 6.2 \pm 1.9$ pb. Both the mass and the cross section measurements are consistent with the Standard Model expectations [25] [28] [29].

Bibliography

[1] S.L. Gashow, Nucl. Phys. **22**, 579 (1961).

[2] S. Weinberg, Phys. Rev. Lett. **19**, 1264 (1967).

[3] A. Salam, *Elementary Particle Theory; Relativistic Groups and Analyticity (Nobel Symposium No. 8)*, ed. N. Svartholm, Almqvist and Wiksell, Stockholm, 1968.

[4] S.L. Gashow, J. Illiopoulos, and L. Maiani, Phys. Rev. D **2**, 1285 (1970).

[5] M. Kobayashi and M. Maskawa, Prog. Theor. Phys. **49**, 652 (1973).

[6] I.J.R. Aitchison and A.J.G. Hey, *Gauge Theories in Particle Physics*, IOP Publishing Ltd., Bristol, 1989.

[7] D.H. Perkins, *Introduction to High Energy Physics*, Addison-Wesley Publishing Company, Inc., Menlo Park, 1987.

[8] R.N. Cahn and G. Goldhaber, *Experimental Foundations of Particle Physics*, Cambridge University Press, Cambridge, 1989.

[9] S.H. Neddermeyer and C.D. Anderson, Phys. Rev. **51**, 884 (1937); J.C. Street and E.C. Stevenson, Phys. Rev. **52**, 1003 (1937).

[10] M.L. Perl *et al.*, Phys. Rev. Lett. **35**, 1489 (1975).

[11] F. Reines and C.L. Cowan Jr., Phys. Rev. **113**, 273 (1959); G. Danby et al., Phys. Rev. Lett. **9**, 36, (1962).

[12] R.W. McAllister and R. Hofstadter, Phys. Rev. **102**, 851 (1956);
E.D. Bloom *et al.*, Phys. Rev. Lett. **23**, 930 (1969).

[13] The discovery of the s quark was, perhaps, a bit serendipitious; the first observation of "strangeness-carrying" hadrons was not immediately recognized as the "discovery" of a new quark, especially since, at the time, quarks were not on a firm theoretical foundation. See for example Chapter 3 of Cahn and Goldhaber, *Experimental Foundations of Particle Physics* (1989).

[14] J.J. Aubert *et al.*, Phys. Rev. Lett. **33**, 1404 (1974);
J.-E. Augustin *et al.*, Phys. Rev. Lett. **33**, 1406 (1974).

[15] S.W. Herb *et al.*, Phys. Rev. Lett. **39**, 252 (1977).

[16] G. Hanson *et al.*, Phys. Rev. Lett. **35**, 1609 (1975).

[17] R. Bandelic *et al.*, Phys. Lett. **86B**, 243 (1979); D.P. Barber *et al.*,
Phys. Rev. Lett. **43**, 830 (1979); Ch. Benser *et al.*, Phys. Lett. **86B**, 418 (1979);
W.. Bartel *et al.*, Phys. Lett. **91B**, 142 (1980).

[18] G.S. LaRue *et al.*, Phys. Rev. Lett. **38**, 1011 (1977); **46**, 967 (1981).

[19] M. Breidenbach *et al.*, Phys. Rev. Lett. **23**, 935 (1969);
A. Bodeck *et al.*, Phys. Rev. D **20**, 1471 (1979);
T. Eichten *et al.*, Phys. Lett. **46B**, 274 (1973).

[20] R.P. Feynman, *Photon-Hadron Interactions*, Bejamin, Reading, 1972.

[21] W. Bartel *et al.*, Phys. Lett. **146B**, 437 (1984); D. Decamp *et al.*,
Phys. Lett. **263B**, 325 (1991).

[22] S. Abachi *et al.*, Phys. Rev. Lett. **72**, 2138 (1994).

[23] F. Abe *et al.*, Phys. Rev. Lett. **73**, 226 (1994).

[24] F. Abe *et al.*, Phys. Rev. D **50**, 2966 (1994).

[25] LEP Electroweak Working Group, B. Pietrzyk, Laboratoire de Physique des Particules Report No. LAPP-EXP-94.07, 1994 (unpublished).

[26] M. Gluck, J.F. Owens and E. Reya, Phys. Rev. D **17**, 2626 (1978); B.L. Combridge, Nucl. Phys. **B151**, 429 (1979); J. Babcock, D. Sivers and S. Wolfram, Phys. Rev. D **18**, 162 (1978); K. Hagiwara and T. Yoshino, Phys. Lett. B **80**, 282 (1979); L.M. Jones and H. Wyld, Phys. Rev. D **17**, 782 (1978); H. Georgi *et al.*, Ann. of Phys. **114**, 273 (1978).

[27] P. Nason, S. Dawson, and R. K. Ellis, Nucl. Phys. **B303**, 607 (1988); W. Beenakker, H. Kuijf, W.K. van Neerven, and J. Smith, Phys. Rev. D **40**, 54 (1989); G. Altarelli, M. Diemoz, G. Martinelli, and P. Nason, Nucl Phys. **B308**, 724 (1988).

[28] E.Laenen, J. Smith, and W.L. van Neerven, Phys. Lett. B **321**, 254 (1994); E.Laenen, J. Smith, and W.L. van Neerven, Nucl. Phys. **B339**, 543 (1992).

[29] Berger, and Contopanagos, ANL-HEP-PR-95-31 (1995).

[30] R.K. Ellis and S. Parke, Phys. Rev. D **46**, 3785 (1992); D.O. Carlson and C.-P. Yuan, Phys. Lett. B **306**, 386 (1993).

[31] M. Kruse, Ph.D. thesis, Purdue Universiy, 1996.

[32] D. Kestenbaum, Ph.D. thesis, Harvard Universiy, 1996.

[33] P. Azzi, Ph.D. thesis, Padova Universiy, 1996.

[34] F. Abe *et al.*, Phys. Rev. Lett. **71**, 3421 (1993); **72**, 3456 (1994).

[35] S. D. Holmes, Fermilab-conf-91/141, 1991 (unpublished).

[36] S. D. Holmes, Fermilab-conf-87/160, 1987 (unpublished).

[37] Livingston and Blewett, *Particle Accelerators*, McGraw-Hill Book Co., Inc., New York, 1962.

[38] F. Abe *et al.*, Nucl. Inst. Meth. **A269**, 93 (1988).

[39] P. Derwent, CDF internal note CDF/PHYS/CDF/CDFR/2361, 1994 (unpublished).

[40] F. Abe *et al.*, Nucl. Inst. Meth. **A271**, 378 (1988).

[41] F. Abe *et al.*, Phys. Rev. D **45**, 1448 (1992).

[42] H.-U. Bengtsson and T. Sjöstrand, Comput. Phys. Commun. **46**, 43 (1987).

[43] T. Sjöstrand, Comput. Phys. Commun. **39**, 347 (1986).

[44] T. Sjöstrand and M. Bengtsson, Comput. Phys. Commun. **43**, 367 (1987).

[45] T. Sjöstrand and M. van Zijl, Phys. Rev. D **36**, 2019 (1987).

[46] P. Avery, K. Read, and G. trahern, Cornell Internal Note CSN-212, 1985 (unpublished).

[47] G. Marchesini and B.R. Webber, Nucl. Phys. **B310**, 461 (1988); G. Marchesini *et al.*, Comput. Phys. Commun. **67**, 465 (1992).

[48] F. Paige and S.D. Protopopescu, BNL Report No. 38034, 1986 (unpublished).

[49] C. Peterson, D. Schlatter, I. Schmitt, P.M. Serwas, Phys. Rev. D **27**, 105 (1983).

[50] R. Akers *et al.*, Z. Phys. C **61**, 209 (1994).

[51] W. Venus, in *Lepton and Photon Interactions*, Proceedings of the XVI International Symposium, Ithaca, New York, 1993, edited by P. Drell, D. Rubin (AIP, New York, 1994).

[52] P. Koehn, Ph.D. thesis, University of Rochester, 1996.

[53] W.R. Leo, *Techniques for Nuclear and Particle Physics Experiments*, Springer-Verlag, Berlin, 1987.

[54] Mika Huhtinen, HU-SEFT-1992-06, (1992).

[55] Particle Data Group, Phys. Rev. D **50**, 1173 (1994).

[56] G. Hall, Nucl. Instr. and Meth. **220**, 356 (1984).

[57] R.M. Stermeimer, Phys. Rev. **145**, 247 (1966).

[58] M.L. Mangano, Nucl. Phys **B405**, 536 (1993).

[59] H. Plothow-Besch, Comp. Phys. Commun. **75**, 396 (1993); J. Botts *et. al.*, Phys. Lett. B **304**, 159 (1993); A.D. Martin, W.J. Stirling, and R.G. Roberts Phys. Rev. D **47**, 867 (1993).

[60] J. Ohnemus *et. al.*, Phys. Rev. D **44**, 1403 (1991);
S. Frixione, Nucl. Phys. **B410**, 280 (1993).

[61] J. Ohnemus *et. al.*, Phys. Rev. D **44**, 3477 (1991);
S. Frixione, P. Nason, G. Ridolfi, Nucl. Phys. **B383**, 3 (1992).

[62] J.B. Gonzalez, J.G. Heinrich, and N.S. Lockyer, CDF internal note CDF/BOTTOM/ANAL/CDFR/3010, 1995 (unpublished).

[63] K. Hikasa *et al.*, Phys. Rev. D **45**, S1 (1992).

[64] F. Abe *et al.*, Phys. Rev. D **47** 4857 (1993).

Vita

The author was born in Kankakee, Illinois to Dennis and Mary Glenzinski on February 8, 1968. He attended St. Joseph Grade School for eight years and Bishop Martin D. McNamara High School for four years. In June of 1990, he received a Bachelor of Art degree from Northwestern University in Evanston, Illinois, where he majored in Physics. In September 1990, he came to The Johns Hopkins University to pursue graduate studies. In 1992 he joined the CDF collaboration at Fermilab in Batavia, Illinois. Under the guidance of Professor Bruce A. Barnett, he participated in the design and construction of the SVX′ detector, and in all phases of the CDF top quark search. In November of 1995, this work culminated in a doctoral dissertation, *Observation of the Top Quark in Proton-Antiproton Collisions at a Center of Mass Energy of 1.8 TeV.*